Spatial and Contrast Enhancement in Photoacoustic Imaging

Abdulrhman Alshaya

Ultrasound Group
School of Electronic and Electrical Engineering

University of Leeds

A thesis submitted for the degree of

Doctor of Philosophy

September 2019

The candidate confirms that the work submitted is his own, except where work which has formed part of jointly authored publications has been included. The contribution of the candidate and the other authors to this work has been explicitly indicated below. The candidate confirms that appropriate credit has been given within the thesis where reference has been made to the work of others.

Chapter 5 contains materials from (Alshaya *et al.*, 2016).

Chapter 6 contains materials from (Alshaya *et al.*, 2017).

Acknowledgements

First of all, I am thankful to my God for helping me throughout the years to complete my PhD research. Then, my great thanks to King Abdulaziz City for Science and Technology (KACST) for sponsoring my study. Also, my thanks are extended to the Saudi Ministry of Education through the Saudi Arabian Cultural Bureau in the U.K. for being available at any time to support me during my stay in Leeds.

I would like to thank my supervisor Prof. Steven Freear for his guidance, encouragement and support, helping me overcome all difficulties during my PhD research. A huge thanks to my co-supervisor Dr. Sevan Harput for his extensive support during the second year of my PhD. Also, I am thankful to my great fellows in the Ultrasound Group for helping me and sharing their knowledge over the past four years. My special thanks to my friend Luzhen Nie for assisting me in preparing this thesis.

I am grateful to my mother and my father for their prayers and their emotional support which were crucial to help me go through all these years. Special thanks to my wife Alhanoof for being with me and supporting me. Also, not to forget to thank my sons Abdulaziz and Fares for their endless love. I would like to thank my brothers and sisters for their presence around whenever I need their help. Also, my thanks are extended to my friends for their continuous advice and support.

Abstract

Photoacoustic imaging have advantages in terms of imaging targets inside a biological tissue and differentiating tissue types. In photoacoustic imaging, a solid-state laser delivers a laser pulse on the target object. This type of laser source is expensive, bulky and it consumes significant power. To facilitate photoacoustic equipment for a wider use in clinical diagnostics, a more portable form is required. To overcome this limitation pulse laser diodes (PLDs) will be investigated. PLDs have advantages over the solid-state laser in terms of price, size and pulse repetition frequency (PRF). However, PLDs suffer from low output energy, generating the acoustic signal with a low signal to noise ratio (SNR) and limiting the imaging depth. Researchers have used some techniques to deal with this issue. For instance, multiple PLDs have been used to increase the output optical energy. The averaging technique has also been used to reduce noise. In addition, some types of coded excitations have been used to investigate the high PRF and reduce noise.

In this thesis, the required number of PLDs to generate photoacoustic emissions with a specific SNR was estimated. This technique was compared with the Nd:YAG laser based on the generated photoacoustic emission. This calculation limited the applications of PLDs for superficial imaging. In addition, in this thesis, the photoacoustic unipolar golay code was developed to reduce the number of transmitted pulse sequences from four to two with little effects on its performance. This developed unipolar golay code improved the code gain when the noise level was high. Moreover, in this thesis, a weak photoacoustic emission was extracted, despite limited bandwidth, and was recovered by using the miro-Doppler technique. This technique has been performed by using a linear array transducer.

Delay and sum (DAS) is one of the most popular beamforming techniques in photoacoustic imaging due to its simplicity. However, the photoacoustic image is significantly affected by side lobes, clutter and phase aberration when the DAS beamfomer is used. All of these reduce the spatial resolution, SNR and contrast of the image. Researchers have used some adaptive beamforming techniques to reduce these effects. In this thesis, the filter delay multiply and sum (FDMAS) beamformer is applied to photoacoustic imaging. This beamformer that depends on the cross correlation between the delayed RF signals provided photoacoustic images with improved resolution and SNR. The FDMAS beamformer was used also in 3D photoacoustic imaging in conjunction with a linear array transducer. This beamformer showed improvement in the elevation resolution out of the focal point. In this thesis, the dynamic filter delay multiply and sum (D-FDMAS) beamformer was produced to reduce the contrast difference between imaging targets and reduce the computation time. This beamformer improves monitoring biopsy needle and sentinel lymph node (SLN) to be co-located. In addition, the D-FDMAS beamfomer was linearized to study the effect of the non-linearity of the D-FDMAS beamformer in multispectral photoacoustic imaging (MIP). This study showed that there was not significant difference between the MIP images when using the linear and non-linear D-FDMAS beamformers.

Abbreviations

ALN	Axillary Lymph node
CD	Contrast difference
CF	Coherence factor
CR	Contrast Ratio
CW	Continuous wave
DAS	Delay and sum
D-FDMAS	Dynamic filter delay multiply and sum
DMAS	Delay multiply and sum
D-sDMAS	Dynamic sign delay and multiply and sum
FDMAS	Filter delay multiply and sum
FL	Focal line
FM	Frequency modulation
FOV	Field of view
FWHM	The full width at half maximum
ICG	Indocyanine green
LAN	Low noise amplifier
MB	Methylene Blue dye
M-FDMAS (3D)	FDMAS (3D) beamformer with multiplication combination
MIP	Maximum intensity projection
MPE	Maximum permissible exposure
MPI	Multispectral photoacoustic imaging
MV	Minimum variance
PGA	Programmable gain amplifier
PLD	Pulse laser diode

PPM	Pulse position modulation
PRF	Pulse repetition frequency
RMS	Root mean square
SA-FDMAS	Subarray Average delay multiply and sum
sDMAS	Signed delay multiply and sum
S-FDMAS (3D)	FDMAS (3D) beamformer with sum combination
SLN	Sentinel lymph node
SNR	Signal to noise ratio
Sub-FDMAS	FDMAS beamformer with sub-group of elements
UARPII	Ultrasound Array Research Platform II
VP	Velocity potential
3D	Three dimensions

List of Symbols

a	Radius of the spherical object
a_k	The value of pulse at k
a_{min}	The radius of the smallest object that will be detected
A	The stress confinement coefficient
A_e	The absorbed optical energy per unit volume of the object
$A_e(j)$	The energy per unit volume of grid element (J/m^3)
$A(k)$	The transmitted A sequence
$A_{max}(k)$	The received sequence of photoacoustic waves from the highest pulse number of positive or negative A sequence
A_{mic-d}	The amplitude of the modulated signal
$A_r(k)$	The received sequence of photoacoustic waves due to transmitted A sequence
A_R	The amplitude of the reference ultrasound signal shifted by 90 degree
$A(X,i)$	The Apodization for transducer element number i and position X
B	Isothermal bulk modulus
$B(k)$	The transmitted B sequence
$B_{max}(k)$	The received sequence of photoacoustic waves from the highest pulse number of positive or negative B sequence
$B_r(k)$	The received sequence of photoacoustic waves due to transmitted B sequence
c	The speed of the ultrasound wave on a medium
$C_{\text{HbR}}(X,Y)$	The molar concentration of deoxy-hemoglobin
$C_{\text{HbO}_2}(X,Y)$	The molar concentration of oxy-hemoglobin
C_p	The specific heat
CR	The contrast ratio
d	The diameter of the object
f	The band pass filter
f_d	The Doppler frequency
f_{de}	The elevation focus depth
f_{max}	The maximum frequency on the transducer bandwidth

f_{mic-d}	The frequency of the micro-doppler signal
f_o	The frequency of the carrier signal
f_{se}	The size of the focus point
f_t	The transmitted ultrasound signal
F	The optical fluence at depth z
F_d	The depth of the focal point
F_o	The optical fluence on the surface of the medium
g	Anisotropy value
g_s	The group size of delayed RF signals
G_{dUGC}	The code gain of developed unipolar golay code
G_{LS}	The code gain of lagendre code sequence
G_{PPM}	The code gain of PPM coded excitation
G_{UGC}	The gain of the unipolar golay code
h	The height of transducer element
h_{kj}	Function is used to take the element which are in the simulation curve
$h_{PA}(k)$	The response for laser pulses
H	The complex conjugate
k	the point of the photoacoustic pressure
k_d	A constant value depends on the type of apodization
k_s	The adiabatic compressibility
$K_{\text{D-DMAS}}(X,Y)$	The apodization and ultrasound attenuation that result from the multiplication of D-FDMAS beamforming without applying bandpass filter
L	The sub-group size of transducer elements
M	The number of scanning planes in the elevation direction
M_{FDMAS}	The number of multiplication of FDMAS beamformer
$M_{\text{Sub-FDMAS}}$	The number of multiplication of Sub-FDMAS beamformer
n_1	Refractive index of the first medium
n_2	Refractive index of the second medium

$n(k)$	The noise signal
N	The number of transducer elements
N_{Average}	Averaged background noise
N_L	The code length
N_{Lmax}	The maximum code length of PPM to get the highest gain
$NU_{\text{D-FDMAS}}$	Number of multiplication of D-FDMAS beamforming technique
$NU_{\text{SA-FDMAS}}$	Number of multiplication of SA-FDMAS beamforming technique
P	Pressure (Pa)
P_o	The increasing in the object pressure
$P_o(X,Y,\lambda)$	The initial photoacoustic pressure
$P_{peak}(t)$	The peak photoacoustic pressure
$P(t)$	The generated pressure signal in term of time
R	Reflected optical energy to the first medium
R_{kj}	The distance between the transducer element and grid element (j)
r_j	The coordinate of the grid element
r_k	The coordinate of the transducer
R_d	The diameter of the blood vessel
$RF_i(t,T_i)$	The delayed RF signal for element ith
$R(k)$	Noise
RMS_{noise}	The root mean square of the noise signal
RMS_{signal}	The root mean square of the acoustic signal
R_{out}	The output of the covariance matrix
$S_i(t)$	The delayed RF signals for transducer element i
S_{ij}	The multiplication between the delayed RF-signal of transducer element i and j
$S_j(t)$	The delayed RF signals for transducer element j
$SS_{ji}(t)$	The delayed RF signals that is received by the element ith in the jth scanning plane

SNR_{dB}	The SNR of the acoustic wave in dB scale
S_{peak}	The maximum intensity of the target signal
t_k	The distance between the transducer and the simulation curve
t_p	The width of the transmitted optical pulse
t_s	The width of the object in term of time
T	Transmitted optical energy to the second medium
T_{dUGC}	The time of receiving photoacoustic wave sequences from developed unipolar golay coded excitation
T_i	Time delay for focusing photoacoustic signal for transducer elements that its position at (x_i, z_i) to imaging point at (x, z)
T_{LS}	The time of receiving photoacoustic wave sequences from lagendre code sequence
T_{tp}	The transpose of the vector
T_{PPM}	The time of receiving photoacoustic wave sequences from PPM coded excitation
T_{UGC}	The time of receiving photoacoustic wave sequences from unipolar golay coded excitation
V	The speed of blood flow in the blood vessel
V_{PH}	The vibration of the blood vessel due to the thermoelastic expansion
w_{kj}	Transducer specifications
$X_l(t)$	The sub-group of transducer elements
Y_1	The beamformed data of the first step of FDMAS (3D) beamformer
Y_2	The beamformed data of the second step of FDMAS (3D) beamformer
y_{DAS}	The output of DAS beamforming technique
$Y_{\mathrm{DAS}}(X, Y, \lambda)$	The output of DAS beamforming technique
$y_{\mathrm{D\text{-}FDMAS}}$	The output of D-FDMAS beamforming technique
$y_{dUGC}(k)$	The generating photoacoustic signal by using developed unipolar golay code

y_{FDMAS}	The output of FDMAS beamforming technique
$y_{LS}(k)$	The received photoacoustic signal by using legendre code sequence
$y_{\text{M-FDMAS (3D)}}$	The output of multiplication of the two beamforming steps of FDMAS (3D) beamformers
$y_{PPM}(k)$	The received photoacoustic signal by using PPM coded excitation technique
$y_{\text{SA-FDMAS}}$	The output of SA-FDMAS beamforming technique
$y_{UGC}(k)$	The generating photoacoustic signal by using unipolar golay code
z	The depth of the object inside the medium
z_a	The maximum depth for photoacoustic imaging
α	The primitive root of K
α_s	The specification of the receiving system
α_t	The ultrasound attenuation coefficient
β	Thermal expansion
Γ	Grueneisen parameter
Δt	Time step of the hardware
ΔV	Volume of the grid element
$\epsilon_{\text{HbO}_2}(\lambda_i)$	The molar extinction coefficient of oxy-hemoglobin at wavelength λ_i
$\epsilon_{\text{HbR}}(\lambda_i)$	The molar extinction coefficient of deoxy-hemoglobin at the wavelength λ_i
θ	The angle between the incident ultrasound signals and the blood vessel
θ_2	Angle of transmitted laser light in the second medium
θ_1	Angle of transmitted laser light in the first medium
$\frac{\theta}{2}$	The divergence angle in the elevation direction
λ	The wavelength at the centre frequency of the transducer
μ_a	Absorption coefficient
$\mu_{\text{Background}}$	The mean of the background
μ_{eff}	Optical attenuation coefficient for the medium
μ_s	Scattering coefficient
$\mu_s^{'}$	Reducing scattering coefficient

μ_{Signal}	The mean of the target signal
ρ	Density of the object (Kg/m^3)
$\sigma_{\text{background}}$	The standard deviation of the background noise
τ	The relaxation time
τ_a	The peak to peak photoacoustic emission length
τ_{delay}	The time delay
τ_E	The time of flight of the photoacoustic wave from the deepest target
τ_L	The pulse repetition interval
τ_s	The increment in time delay between pulses
ϕ	Velocity potential (m^2/s)

Contents

List of Figures

LIST OF FIGURES

Chapter 1

Introduction

The photoacoustic effect was discovered by Alexander Bell in 1880 (Manohar & Razansky, 2016). When Bell dis-continually shined a light on different solid materials, ultrasound waves were generated. These waves were called photoacoustic emissions. The photoacoustic effect was first applied to the medical field in 1964 by L Amar and his colleagues when laser pulses were delivered to rabbit eyes (Manohar & Razansky, 2016). By emitting a short laser pulse on a target which will absorb the optical energy, the temperature and pressure of the target will increase. Due to thermoelastic expansion, ultrasound waves will be generated (De Montigny, 2011; Xu & Wang, 2006). These waves can be recorded by an ultrasound transducer to create a photoacoustic image. Photoacoustic imaging has advantages over other imaging modalities such as optical coherence tomography (OCT), diffuse optical tomography (DOT), and ultrasound imaging. For example, the imaging depth of photoacoustic imaging (> 5 cm) is higher than that of OCT (~ 1 mm). This is because the high scattering of optical light limits the imaging depth of the OCT. This is unlike the photoacoustic imaging, which depends on generating ultrasound signals due to thermoelastic expansion. These ultrasound signals are much less scattered than the light in the tissue, thus resulting in increased imaging depth (Kim *et al.*, 2010a; Xu & Wang, 2006). In addition, the spatial resolution of the photoacoustic image is much higher than that of DOT, the depth of which is measured on a centimetre scale. This is because the resolution of photoacoustic imaging is within the ultrasound resolution while the resolution of DOT is optical resolution (Kim *et al.*, 2010a). Moreover, photoacoustic imaging has advantages over ultrasound imaging in terms of differentiation between types of tissues. This is because the photoacoustic im-

age depends on the wavelength of the absorbed laser light while the ultrasound image depends on the mismatch impedance. (Chan & Perlas, 2011; Deng & Li, 2016; Kim *et al.*, 2010a; Sivasubramanian *et al.*, 2018)

The photoacoustic image is used to provide anatomical and functional information of the biological tissue using the endogenous contrast agents such as oxy-hemoglobin, deoxy-hemoglobin and melanin (Xia *et al.*, 2014). All of these contrast agents have a specific optical absorption spectrum (Mallidi *et al.*, 2011). The optical absorption of endogenous agents is higher than that of normal tissue in visible and near infrared bands. In addition, the physiological specifications of these agents are not affected when they absorb the optical light to generate photoacoustic emissions (Zhang *et al.*, 2011). Some exogenous contrast agents, such as Indocyanine green (ICG) dye (Kim *et al.*, 2010c), Methylene blue (MB) (Mansik Jeon, 2014; Song *et al.*, 2008) and gold nanoparticles (Li & Chen, 2015), are used in photoacoustic imaging. These exogenous agents are used to enhance the imaging contrast where the concentration of endogenous contrast agents is low. In addition, they assist in tracking antibodies which are integrated with them (Wang & Yao, 2016; Zhang *et al.*, 2011).

In photoacoustic imaging, the pulse length of the laser should be short, typically nanosecond to maintain the thermal and stress confinement coefficients (Allen *et al.*, 2005; Jacques, 2004; Wang, 2008). The Neodymium-doped Yttrium Aluminum Garnet (Nd:YAG) laser is one of the most popular laser sources in photoacoustic imaging as its output optical energy is high (100 mJ) even with a short laser pulse length (5-7 nm). However, there are some disadvantages of this laser source. For instance, it has a low pulse repetition frequency (PRF) (10 Hz to 20 Hz). As a result, it is not suitable for medical applications that need a high frame rate. The associated equipment has a large size that needs a large space and, in addition, it is expensive (Zeng *et al.*, 2012). To address the need of a high-frame-rate laser system, the portable and relatively cheap pulse laser diode (PLD) was developed for photoacoustic imaging (Allen & Beard, 2006; Daoudi *et al.*, 2014; Upputuri & Pramanik, 2015). However, the PLD has some drawbacks. For example, its output optical energy is low (1.45 mJ) when compared with the Nd:YAG laser (100 mJ) (Upputuri & Pramanik, 2018), however, this drawback can be overcome by using averaging techniques and coded excitations (Beckmann *et al.*, 2012; Mienkina *et al.*, 2010). In this thesis, the PLD will be studied as to whether it can take place of the Nd:YAG laser in photoacoustic imaging.

There are different types of ultrasound transducers used to record photoacoustic emissions. The linear array transducer is popular in photoacoustic imaging and can be used to combine an ultrasound image with a photoacoustic image, when operated in two imaging modes. It is also advantageous as it is hand-held, useful for maneuvering for optimal clinical view (Li *et al.*, 2015; Wang *et al.*, 2016b). When the delay and sum (DAS) beamforming technique is used to produce the photoacoustic image with the emissions received by a linear array transducer, the photoacoustic image will be affected by clutter noise, side lobes and phase aberration. As a result, the spatial resolution, signal to noise ratio (SNR) and contrast of the photoacoustic image will be degraded. Thus, other advanced beamforming techniques (Alles *et al.*, 2014; Park *et al.*, 2008b; Zemp *et al.*, 2007) are being proposed to address these issues. In this thesis, the filter delay multiply and sum (FDMAS) beamformer and the Dynamic filter delay multiply and sum (D-FDMAS) beamformer will be applied to photoacoustic imaging to investigate their effects on spatial resolution, SNR and contrast difference (CD) between imaging targets. In addition, the FDMAS beamformer will be applied to 3-D photoacoustic imaging to study its effects on elevation resolution.

1.1 Motivation

The PLD has been investigated in photoacoustic imaging due to its higher PRF, smaller size and affordability. However the main limitation of the PLD is its lower optical energy when compared with the solid-state laser (Allen *et al.*, 2005; Wang *et al.*, 2014). Therefore, the PLD is typically used for superficial imaging (Wang *et al.*, 2014; Zeng *et al.*, 2013, 2014). One of the ways to deal with this limitation is the use of multiple PLDs combined with each other to increase the output optical energy (Allen & Beard, 2006). The determination of the required number of PLDs to achieve a specific SNR of the photoacoustic emission can be realized by using a specific programming code.

In photoacoustic imaging, when the PLD is used, the generated photoacoustic emission from the target is very weak due to a low-level of transmitted optical energy (Kolkman *et al.*, 2006). To improve the SNR of the photoacoustic emission, an averaging technique is typically used (Kolkman *et al.*, 2006). However, the number averaged is limited by the acoustic wave's time of flight (Wei *et al.*, 2015). To deal with this limitation and investigate the high-PRF PLD, coded excitations are used which are no longer

limited by the time of flight of the acoustic wave. Many types of coded excitations, such as the unipolar golay code, pulse position modulation and Legendre code sequence, have been utilised in photoacoustic imaging (Beckmann & Schmitz, 2013; Beckmann *et al.*, 2010; Mienkina *et al.*, 2010). The unipolar golay code has an advantage over other coded excitations, without the generation of the coded artefact in the extracted photoacoustic emissions. However, with the unipolar golay code, four sequences of pulses will be transmitted separately, reducing the frame rate when compared against other coded excitations that transmit one or two sequences of pulses (Mienkina *et al.*, 2010). Therefore, when using the unipolar golay code, there is a need to reduce the number of the transmitted pulse sequences without reducing its performance.

When laser pulses propagate through the biological tissue, some parts of the optical energy will be reflected due to the difference in reflective index for different tissue layers. Whereas, other parts will be absorbed and scattered by the biological tissue (Vo-Dinh, 2003). If the imaging target is deep, the optical energy slightly reaches it. As a result, a photoacoustic emission with a low SNR will be generated (Andreev *et al.*, 2003). There are some techniques for improving the SNR of the received photoacoustic emissions. For example, the eliminated surface is covered with a reflective material to enhance the eliminated surface with reflective optical energy. This results in the increase of optical energy absorbed by the target, thereby improving the SNR of photoacoustic emissions (Wang *et al.*, 2012). In addition, the SNR of the photoacoustic emissions can be improved by transmitting two laser pulses with a short time delay between them. The first pulse is used to change the thermal properties of the biological tissue, which will improve the SNR of the photoacoustic emission that is generated by the second pulse (Tian *et al.*, 2015). Moreover, the SNR of the photoacoustic image can be improved by overlapping the photoacoustic emissions with ultrasound signals (McLaughlan *et al.*, 2014). By using an ultrasound signal, the enhanced SNR can be also achieved by modulating the micro-vibration of the imaging target due to the photoacoustic effect (micro-Doppler technique) (Gao *et al.*, 2016). In this technique, the photoacoustic emission is extracted by demodulating the received signal. In this thesis, the micro-Doppler technique will be utilised in 2-D photoacoustic imaging by using a linear array transducer which has not been investigated before.

By using the DAS beamformer, the photoacoustic image will be significantly affected by phase aberration, side lobes and clutter, mainly resulting in the reduced spatial

resolution and SNR. Advanced techniques, such as the coherence factor weight (CF), minimum variance (MV) and short-lag beamformers, are used to reduce the effects of these issues (Alles *et al.*, 2014; Park *et al.*, 2008b; Zemp *et al.*, 2007). Recently, another beamforming technique, named filter delay multiply and sum (FDMAS), was proposed (Matrone *et al.*, 2015). It is based on the correlation operation of the delayed RF data, enhancing the high correlated signals. It is developed from the delay multiply and sum (DMAS) beamformer, which was originally applied to radar microwave imaging to detect early-stage breast cancer (Lim *et al.*, 2008). The FDMAS beamformer has improved SNR and lateral resolution when it is applied to ultrasound imaging (Matrone *et al.*, 2015). Therefore, it is encouraging to apply the FDMAS beamforming technique in photoacoustic imaging and study its effects on SNR and spatial resolution of the photoacoustic image.

When performing 3-D photoacoustic imaging by mechanically moving a 1-D linear array transducer, the photoacoustic image has a poor elevation resolution. This can be improved by inserting a metal slice with a hole at the focal point in the elevation direction which will increase the aperture size in the elevation direction. As a result, the elevation resolution will be improved after beamforming (Wang *et al.*, 2016b). In addition, the resolution can be enhanced when bi-directional scanning is used and the beamformed RF data in each scanning direction is combined (Schwarz *et al.*, 2015). A CF weight with a focal line (FL) beamforming technique can be also used to improve the elevation resolution of 3-D photoacoustic imaging (Wang *et al.*, 2016a). In this thesis, the use of the FDMAS beamformer to improve the elevation resolution and SNR of 3-D photoacoustic imaging will be investigated with a linear array transducer.

In photoacoustic imaging, the FDMAS beamforming technique could affect the image contrast difference between imaging targets. This is because the FDMAS beamformer depends on the correlation operation (Alshaya *et al.*, 2016; Matrone *et al.*, 2015). The result of the correlation operation is affected by the shape of the RF signals. For instance, if the FDMAS beamformer is used for localising the sentinel lymph node (SLN) and tracking the biopsy needle, the contrast difference between the needle and SLN will be high due to the different shapes of the RF signals for the needle and SLN. In addition, the time consumption of FDMAS is much higher than that of DAS. For instance, if the number of transducer elements was 128, the FDMAS beamformer would sum 8,128 delayed RF-signals, while the DAS beamformer would sum 128 delayed RF-signals only

to create photoacoustic image (Matrone *et al.*, 2015). Therefore, it is encouraging to reduce the contrast difference between the imaging targets and computation time by using the dynamic filter delay multiply and sum (D-FDMAS) beamformer. In this beamforming technique, only the delayed RF data from a subgroup of elements will be correlated with each other. For example, if the number of transducer elements was 128 and the sub-group size was 32 elements, the D-FDMAS would reduce the number of summing delayed RF-signals to 3,600 when compared with FDMAS (8,128).

FDMAS is a nonlinear beamforming technique (Matrone *et al.*, 2015). The linearised version of FDMAS, signed delay multiply and sum (sDMAS), has been applied to multispectral photoacoustic imaging (MPI) (Kirchner *et al.*, 2018). This motivates the linearization of the D-FDMAS non-linear beamforming technique and its utilisation in MPI.

1.2 Principles of Generating Photoacoustic Emissions

1.2.1 Propagation of Light inside Biological Tissue

When the laser beam propagates from one medium to another, the original incident laser beam will be refracted at the boundary of the second medium. The refraction angle can be calculated by using Snell's law as given in equation 1.1 (Vo-Dinh, 2003):

$$\sin(\theta_2) = \frac{n_1}{n_2} \sin(\theta_1), \tag{1.1}$$

where θ_2 is the incident angle of the laser beam in the second medium (refraction angle), θ_1 is the original incident angle of the laser beam, n_1 is the refractive index of the first medium and n_2 is the refractive index of the second medium. When the angle of the incident beam from the first medium to the second one is 90°, the amount of the optical energy that pass from the first medium to the second medium (T) is calculated by using equation 1.2 (Vo-Dinh, 2003):

$$T = \frac{4n_1 n_2}{(n_1 + n_2)^2}. \tag{1.2}$$

In addition, the amount of the optical energy (R) that is reflected back to the first medium is calculated by using equation 1.3 (Vo-Dinh, 2003):

$$R = 1 - T = \frac{(n_1 - n_2)^2}{(n_1 + n_2)^2}.$$ (1.3)

The amount of optical energy that is scattered in the tissue can be calculated by using the scattering coefficient, with the scattering points assumed to have a homogeneous distribution (Vo-Dinh, 2003). The direction of scattering depends on the anisotropy value which has a range between -1 and 1. For example, if the anisotropy value is positive, scattering will be forward. However, if the anisotropy value is zero, scattering will be isotropic. In contrast, if the anisotropy value is negative, scattering will be backward (Ansari & Mohajerani, 2011). The anisotropy value will affect the scattering coefficient and the effect can be calculated by using equation 1.4 (Vo-Dinh, 2003):

$$\mu_s^{'} = (1 - g)\mu_s,$$ (1.4)

where $\mu_s^{'}$ is the reduced scattering coefficient, g is the anisotropy value and μ_s is the scattering coefficient. The amount of light that is absorbed by tissue is calculated by using the absorption coefficient when the absorbed points are a homogeneous distribution (Vo-Dinh, 2003). This coefficient depends on the tissue type and the wavelength of the laser beam as shown in figure 1.1 (Jacques *et al.*, 2014).
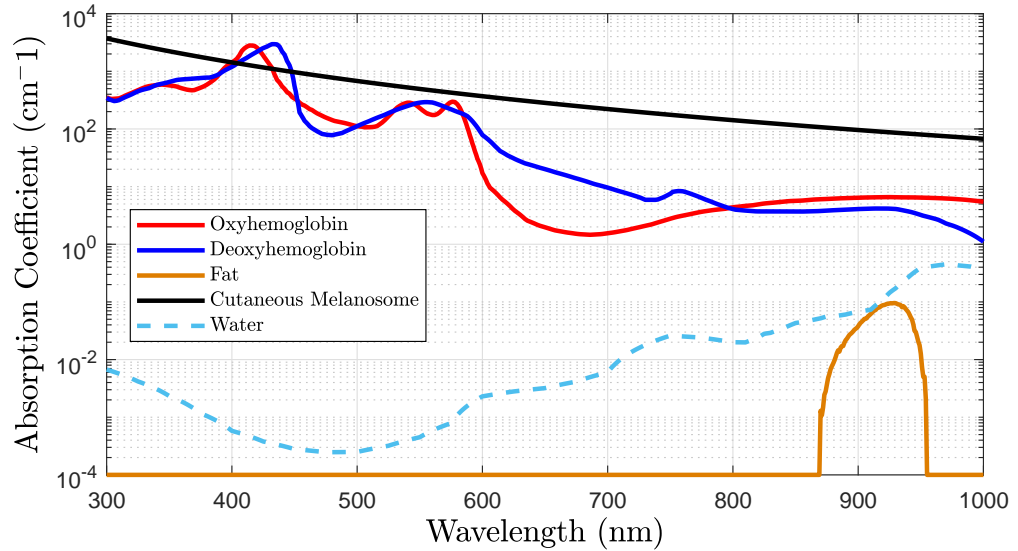
Figure 1.1: Absorption coefficients of different biological materials (Jacques *et al.*, 2014).

1.2.2 Photoacoustic Effect

The photoacoustic effect can be generated by delivering the laser light on the object that absorbs it. The absorbed optical energy is transferred to heat, increasing the local temperature and, as a result, the local pressure will be increased leading to the generation of an acoustic wave that can be detected using an ultrasound transducer (figure 1.2 (De Montigny, 2011)). However, the characteristics of the laser pulse that is applied to the object, and the characteristics of the ultrasound transducer, will have certain effects on the received photoacoustic signal such as the shape of the received signals.
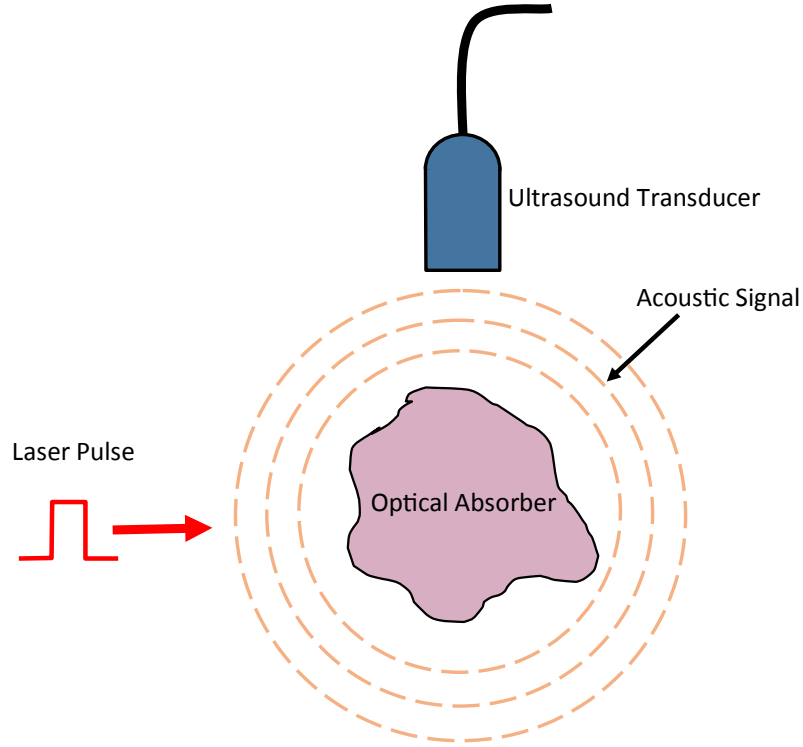
Figure 1.2: Generating an acoustic signal due to the photoacoustic effect (De Montigny, 2011).

Specifications of the Laser Source

The safe exposure level of the utilised laser for tissue imaging is regulated by professional organisations such as the American National Standards Institute (Mallidi *et al.*, 2011). The fluence that reaches the target depends on the depth of the object inside the medium, and can be calculated by using equation 1.5 (Andreev *et al.*, 2003):

$$F = F_o e^{-\mu_{eff} z}, \tag{1.5}$$

where F is the optical fluence at depth z, F_o is the optical fluence on the surface of the

medium and μ_{eff} is the optical attenuation coefficient inside of the medium. μ_{eff} can be calculated through equation 1.6 (Mallidi *et al.*, 2011):

$$\mu_{eff} = \sqrt{3\mu_a(\mu_a + \mu_s')}, \tag{1.6}$$

where μ_a is the absorption coefficient. There are limitations for the length of the transmitted optical pulse to obtain a reasonable resolution. The optical pulse length is supposed to be much smaller than the size of imaging target. If the shape of the object is assumed spherical, the pulse length should satisfy the condition in equation 1.7 (Jacques, 2004):

$$t_p \ll \frac{d}{c}, \tag{1.7}$$

where t_p is the length of the transmitted optical pulse, d is the diameter of the object and c is the speed of sound in the medium. Equation 1.7 illustrates the stress confinement condition where the optical pulse length should be very short when compared with the size of the target object (Jacques, 2004). For example, if the diameter of the object was 0.2 mm and the speed of sound in the medium was 1520 m/s, the laser pulse should be much less than 131 ns. This condition can be achieved by using Nd:YAG (5-7 ns).

Effects of The Laser Pulse Length on Photoacoustic Emissions

The shape of the generated photoacoustic emission is affected by the optical pulse length. For example, when the length of the pulse laser is increased, the amplitude of the received acoustic wave will be increased, whereas, the spatial resolution will be reduced (Allen & Beard, 2006). The amplitude increase of the acoustic wave is determined by the stress confinement coefficient which can be calculated by using equation 1.8 (Allen *et al.*, 2005; Jacques, 2004):

$$A = \frac{(1 - e^{-\tau})}{\tau}, \tag{1.8}$$

where A is the stress confinement coefficient, and τ is the relaxation time which can be calculated by equation 1.9 (Allen *et al.*, 2005):

$$\tau = \frac{t_p}{t_s} = \mu_a c t_p, \tag{1.9}$$

where t_s is the width of the object in terms of time. From equations 1.8 and 1.9, it is noticed that when the laser pulse length or the absorption coefficient is increased, the stress confinement coefficient reduces. The reduction of the stress confinement coefficient will affect the peak pressure of the photoacoustic emission (Allen *et al.*, 2005; Jacques, 2004). When the beam width of the laser source is assumed infinite, the relation between the stress confinement coefficient and the peak pressure of the photoacoustic emission is given by equation 1.10 (Allen *et al.*, 2005):

$$P_{peak}(t) = \frac{B\beta}{\rho C_p} F_o \mu_a A, \tag{1.10}$$

where $P_{peak}(t)$ is the peak photoacoustic pressure, B is the isothermal bulk modulus, β is the thermal expansion, ρ is the density of the medium and C_p is the specific heat. From equations 1.9 and 1.10, it can be seen that when the laser pulse length is increased, the stress confinement coefficient is reduced. As a result, the percentage of the increased peak pressure of the photoacoustic emission is reduced (Allen *et al.*, 2005).

Specifications of The Ultrasound Transducer

A broadband transducer is required to detect the photoacoustic emissions. However, an increased transducer bandwidth will lead to the increased thermal noise. As a result, the bandwidth of the ultrasound transducer that is used for photoacoustic imaging is calculated based on the size of the imaging target. For example, the maximum required frequency f_{max} is calculated based on the radius of smallest object a_{min} that needs to be detected, as given in 1.11 (Andreev *et al.*, 2003):

$$f_{max} = \frac{1.5c}{a_{min}}. \tag{1.11}$$

For instance, if the radius of the smallest object in the imaging area was 0.1 mm and the speed of sound in the medium was 1520 m/s, the highest frequency part of the ultrasound transducer should be at least 22.8 MHz to detect the boundary of the imaging targets (Andreev *et al.*, 2003).

Characteristics of the Photoacoustic Emission

The photoacoustic emission has an N-shape (figure 1.3 (Andreev *et al.*, 2003)). The structure of this shape depends on a number of factors including the size of the object, among others. If the shape of the object is assumed to be spherical and the optical pulse length satisfies the stress confinement condition, the relationship between the peak to peak photoacoustic emission length and the radius of the target object is given by equation 1.12 (Andreev *et al.*, 2003):

$$\tau_a = \frac{2a}{c}, \tag{1.12}$$

where τ_a is the peak to peak photoacoustic emission length and a is the radius of the spherical object. When the laser light is applied to the object, the local pressure will increase. The increase of the pressure P_o can be calculated by using equation 1.13 (Wang, 2008):

$$P_o = \Gamma A_e, \tag{1.13}$$

where Γ is the Grueneisen parameter and A_e is the absorbed optical energy per unit volume. The Grueneisen parameter can be calculated using equation 1.14 (Wang, 2008):

$$\Gamma = \frac{c^2 \beta}{C_p}. \tag{1.14}$$

The absorbed optical energy per unit volume is calculated using equation 1.15 (Wiendelt, 2013):

$$A_e = \mu_a F. \tag{1.15}$$
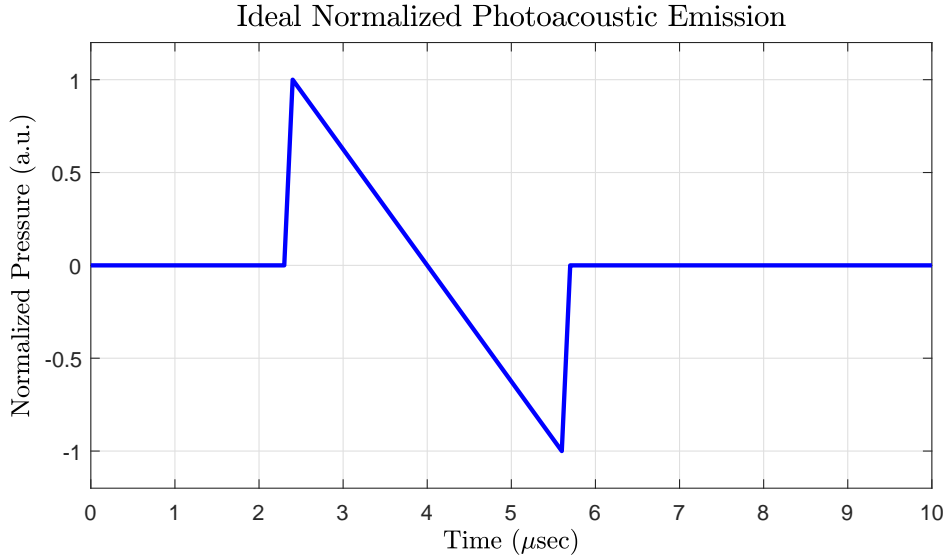
Figure 1.3: Shape of the acoustic wave due to the photoacoustic effect (Andreev *et al.*, 2003).

The pressure amplitude of the photoacoustic emission (P) depends on both its velocity potential (ϕ) and the density of the medium (ρ), as illustrated in equation 1.16 (Jacques, 2004; Paltauf *et al.*, 2002):

$$P = -\rho \frac{d\phi}{dt}. \tag{1.16}$$

The shape of the negative velocity potential when the object is spherical is shown in figure 1.4 (Jacques, 2004). The velocity potential (ϕ) can be calculated by using equation 1.17 (Paltauf *et al.*, 2002):

$$\phi = -\frac{\beta}{4\pi\rho C_p} \frac{\Delta V}{\Delta t} \sum_j \frac{A_e(j)h_{kj}}{R_{kj}} w_{kj}, \tag{1.17}$$

where ΔV is the volume of the grid element, Δt is the sampling period of the hardware, $A_e(j)$ is the energy per unit volume for the grid element, R_{kj} is the distance between

13
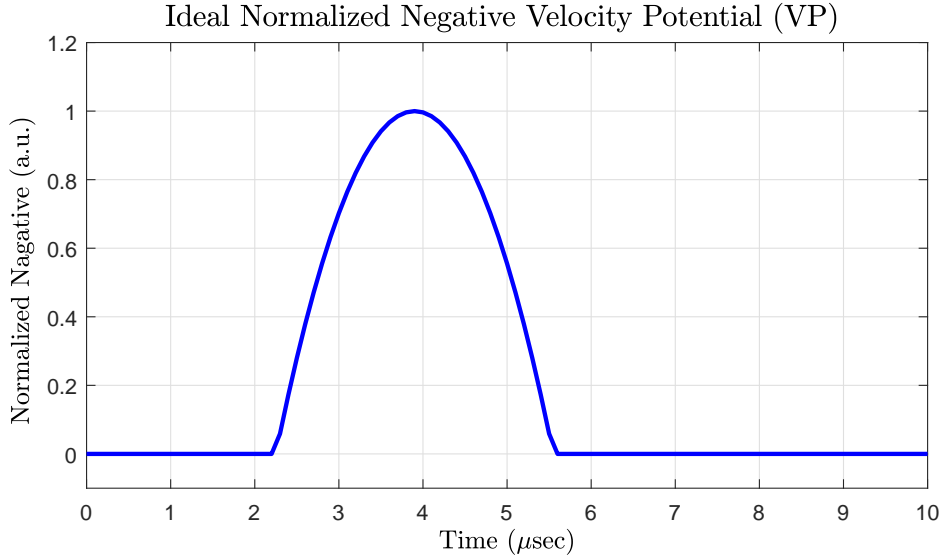
Figure 1.4: Shape of the negative velocity potential when the object is spherical (Jacques, 2004).

the transducer element and grid element (j), h_{kj} is the function that is used to take the grid elements that have the same distance to the transducer element (simulation curve) and w_{kj} is the transducer specification.

The distance between the transducer element and grid element (j) can be calculated by using equation 1.18 (Paltauf *et al.*, 2002):

$$R_{kj} = |r_k - r_j|, \tag{1.18}$$

where r_k is the coordinate of the transducer and r_j is the coordinate of the grid element. The grid element that is on the simulated curve can be determined using equation 1.19 (Paltauf *et al.*, 2002):

$$h_{kj} = \begin{cases} 1, & \text{if } |t_k - \frac{R_{kj}}{c}| < \frac{\Delta t}{2} \\ 0, & \text{else} \end{cases} \tag{1.19}$$

14

where t_k is the distance between the transducer and the simulation curve. The photoacoustic pressure can be calculated by subtracting two values of the negative potential velocity, as shown in equation 1.20 (Jacques, 2004, 2014):

$$P(k) = \rho \frac{-\phi(k+1) - (-\phi(k))}{\Delta t}, \tag{1.20}$$

where k is a sample of the photoacoustic wave.

1.3   Organisations of the Thesis

The shape of the generated photoacoustic emissions is affected by some factors such as the properties of tissue and the ultrasound transducer specifications (Andreev *et al.*, 2003; Ansari & Mohajerani, 2011; Vo-Dinh, 2003). The principle of generating photoacoustic emissions was explained in Chapter 1. The number of PLDs required for a specific SNR of the generated photoacoustic emissions will be calculated and compared with the SNR of the photoacoustic emissions generated using the Nd:YAG laser in Chapter 2. In Chapter 3, the unipolar golay code will be developed to reduce the number of the required pulse sequences for photoacoustic imaging. The micro-Doppler technique that modulates the photoacoustic emissions by using ultrasound signals (Gao *et al.*, 2016) will be investigated for photoacoustic imaging in Chapter 4.

The FDMAS beamforming technique is investigated for enhanced photoacoustic imaging with improved SNR and resolution in Chapter 5. In addition, the effects of the lateral step size on side lobes and main lobes are also analysed. This study has been published in the following paper:

- A. Alshaya, S. Harput, A. M. Moubark, D. M. J. Cowell, J. McLaughlan, S. Freear, "Spatial resolution and contrast enhancement in photoacoustic imaging with filter delay multiply and sum beamforming technique", IEEE Int. Ultrasonics Symposium (IUS), 2016, pp. 1-4

The elevation resolution of 3-D photoacoustic imaging is improved by using the FDMAS beamformer in Chapter 6. The relevant results have been published in the following paper:

- A. Alshaya, S. Harput, D. M. J. Cowell, T. Carpenter, J. McLaughlan, S. Freear, "Elevation resolution enhancement in 3D photoacoustic imaging using FDMAS beamforming", IEEE Int. Ultrasonics Symposium (IUS), 2017, pp. 1-4

- A. Alshaya, S. Harput, D. M. J. Cowell, T. Carpenter, J. McLaughlan, S. Freear, "Improvement of Spatial Resolution in 3D photoacoustic imaging using FDMAS beamforming" (In process)

The D-FDMAS beamformer is investigated for photoacoustic imaging to reduce the contrast difference between imaging targets in Chapter 7. In addition, this beamformer has been compared with other photoacoustic beamforming techniques in terms of contrast difference, SNR and lateral resolution. The subarray average delay multiply and sum (SA-FDMAS) beamformer is also investigated for photoacoustic imaging. The relevant results will be published in the following paper:

- A. Alshaya, Luzhen Nie, D. M. J. Cowell, T. Carpenter, J. McLaughlan, S. Freear, "Monitoring Needle Biopsy of Sentinel Lymph Nodes Using Photoacoustic Image with Dynamic-FDMAS Beamformer", IEEE Int. Ultrasonics Symposium (IUS), 2019, pp. 1-4

- A. Alshaya, Luzhen Nie, D. M. J. Cowell, T. Carpenter, J. McLaughlan, S. Freear, "Enhancing Performance of the FDMAS Beamformer in Photoacoustic Imaging by Using Dynamic Elements " (In process)

In Chapter 8, the D-FDMAS, a non-linear beamforming technique, is linearised and applied to MPI. MPI, when using the linearised and non-linearised D-FDMAS beamformers, are also compared.

Chapter 2

Pulse Laser Diodes to Generate Photoacoustic Emissions

Abstract

The required number of PLDs to achieve a specific SNR for photoacoustic emissions was calculated and compared with the SNR of the photoacoustic emissions generated using the Nd:YAG laser. This comparison was achieved by using simulations and experimental measurements. The Monte Carlo simulation was used to simulate the absorbed optical energy inside the biological tissue and in this simulation, the photoacoustic pressure was generated from the velocity potential. The shape of the generated photoacoustic wave was affected by the transducer bandwidth (For example, OLYMPUS-V384 that its centre frequency was 3.5 MHz and its bandwidth was 65.29 %). In addition, this photoacoustic wave was attenuated and noise was added to it. In experiments, the peak output optical power of PLDs was compared with that of the Nd:YAG laser, based on the SNR of the generated photoacoustic emission from a gelatine phantom. Based on the simulation, a SNR of 10.02 dB $\pm$ 1.58 dB can be achieved by using 190 PLDs. However, by using 190 PLDs, it achieved 7.5 dB $\pm$ 0.3 dB SNR in experiments.

2.1 Introduction

The practical applications of photoacoustic imaging are limited due to a number of reasons. Firstly, an expensive pulse laser source, such as the Q-switched Nd:YAG laser, is used. This is because this type of pulse laser source provides a high output optical

17

2. PULSE LASER DIODES TO GENERATE PHOTOACOUSTIC EMISSIONS

power. The physical size of this laser source is large and this would cause issues for clinical applications (Allen *et al.*, 2005; Wang *et al.*, 2014). Moreover, cooling equipment will be needed when this type of laser is used (Wang *et al.*, 2014). Furthermore, the PRF of this type of laser is low. Therefore, researchers are attempting to reduce these limitations by replacing the large pulse laser source with the PLD. The PLD has a number of attractive features. For instance, its size is smaller with a more affordable price (Allen *et al.*, 2005; Wang *et al.*, 2014). However, a major drawback is that the peak output optical power of the PLD is lower compared with the solid-state laser. This results in the reduced SNR of the received acoustic signal when PLDs are used for photoacoustic imaging (Allen *et al.*, 2005; Kolkman *et al.*, 2006).

The high noise level in the received photoacoustic emissions can be reduced by using averaging (Kolkman *et al.*, 2006). This is because the PRF of the PLD is higher when compared with a solid-state laser (Allen *et al.*, 2005). However, the number of averaging is limited by the time of flight of the acoustic wave (Wei *et al.*, 2015). This means that the pulse repetition time should be equal or longer than the time for the acoustic wave travelling from the target object to the receiving ultrasound transducer (Mienkina *et al.*, 2010). Furthermore, the transmitted pulse energy should be reduced when the PRF is increased due to safety concerns (Wei *et al.*, 2015). The improvement in SNR due to averaging is calculated by the square root of the number of averaging. This is because the averaging technique will reduce the amplitude of uncorrelated signals (Noise signals) when compared with that of correlated signals (Target signals) (Kolkman *et al.*, 2006).

Researchers have used PLDs to generate the photoacoustic effect. For example, in 2005, T. Allen and his colleagues experimentally and theoretically presented the relationship between the peak to peak photoacoustic pressure and the laser pulse length (Allen *et al.*, 2005). Also, the relationship between the peak to peak photoacoustic pressure and the absorption coefficient was illustrated. The results of these experiments showed that when the absorption coefficient of the object was increased, the amount of the increased peak to peak photoacoustic pressure when the laser pulse length was increased was reduced. Moreover, the stress confinement coefficient was decreased when the absorption coefficient of the target was increased.

In 2006, R. Kolkman and his colleagues generated the photoacoustic effect for blood vessels using PLD (Kolkman *et al.*, 2006). For that experiment, the diameter of the blood vessel was around 1 mm. In addition, with the 112-ns laser pulses, photoacoustic

images were reconstructed for two blood vessels that were in close proximity. The SNRs of the photoacoustic emissions by using PLD and the Nd:YAG laser were compared. The experiment shows that it is possible to generate the photoacoustic emission with the same level of SNR by using both PLD and the Nd:YAG laser. However, multiple transmissions are needed when using PLD to average the received photoacoustic signals. The number of acquisitions for averaging depends on the difference of the transmitted energy between these two types of laser sources.

In 2006, T. Allen and P. Beard investigated the effects of increasing the laser pulse length on the photoacoustic emissions with PLD used as the laser source (Allen & Beard, 2006). Two types of Laser pulses were applied to the absorbent where one of these pulses satisfied the stress confinement, while the other did not. As a result, when the duration of the transmitted pulse satisfied the stress confinement, the SNR was low, while the spatial resolution was high. However, when the duration of the transmitted pulse did not satisfy the stress confinement, the spatial resolution was low, while the SNR was high.

In 2007, T. Allen and P. Beard used the PLD to measure the amount of oxy-haemogl- -obin and deoxy-haemoglobin in blood (Allen & Beard, 2007). Two different wavelengths of 905 and 850 nm were used. The percentage of oxy-haemoglobin and deoxy-haemoglobin were measured for arteries and veins in a thumb digit. This study shows that it is possible to measure the percentage of oxygen in blood although with a low level of accuracy. This was due to only two laser wavelengths were used and the fluctuation of the laser fluence was not taken in account.

In 2013, L. Zeng and his colleagues designed a photoacoustic microscopy with an optical resolution by using PLD (Zeng *et al.*, 2013). This optical resolution helped reduce the number of averaging to receive photoacoustic signals with a high SNR. The optical resolution means that the lateral resolution depends on focusing the laser light on the targets image. This is unlike the ultrasound resolution, where the lateral resolution depends mainly on the bandwidth of the ultrasound transducer. The optical resolution is used on the photoacoustic microscopy because the laser light can only be focused in shallow depth ($\sim$ 1 mm) (Zeng *et al.*, 2013, 2014). Furthermore, in 2014, L. Zeng and his colleagues used this photoacoustic microscopy to perform 3-D photoacoustic imaging (Zeng *et al.*, 2014). In 2014, T. Wang and his colleagues used

the PLD in optoacoustic microscopy (Wang *et al.*, 2014). A spatial resolution of 7μm and a SNR of 15 dB were achieved.

In 2014, K. Daoudi and his colleagues designed an array transducer for ultrasound and photoacoustic imaging (Daoudi *et al.*, 2014). In this design, an array of PLDs with a wavelength of 805nm were used. In addition, a cylindrical lens was used to control the fluence of the laser pulse on the surface of the target object. The centre frequency and bandwidth of the ultrasound array transducer were 7.5 and 100 %, respectively, and the laser pulse length was 130 ns which produced a laser energy of 0.56 mJ. A 15 mm imaging depth was demonstrated in phantoms. In addition, the maximum frame rate was 20 Hz for the depth of 4 to 5 mm.

In this chapter, the number of PLDs for generating photoacoustic emission with a specific SNR is calculated. In this calculation, the Monte Carlo simulation is investigated. Moreover, the peak optical outputs of the PLD and the Nd-YAG laser are compared experimentally based on the SNR of the received photoacoustic emission.

2.2 Simulations

2.2.1 Light Propagation Inside Tissue

The Monte Carlo simulation was used to simulate the propagation of light inside the biological tissue. This Monte Carlo simulation code was written by Steven Jacques and his colleagues (Jacques *et al.*, 2014; Jacques, 2014). The structure and properties of the biological tissue used in this simulation are shown in figure 2.1 (Jacques, 2014) and Table 2.1 (Jacques *et al.*, 2014; Jacques, 2014), respectively.
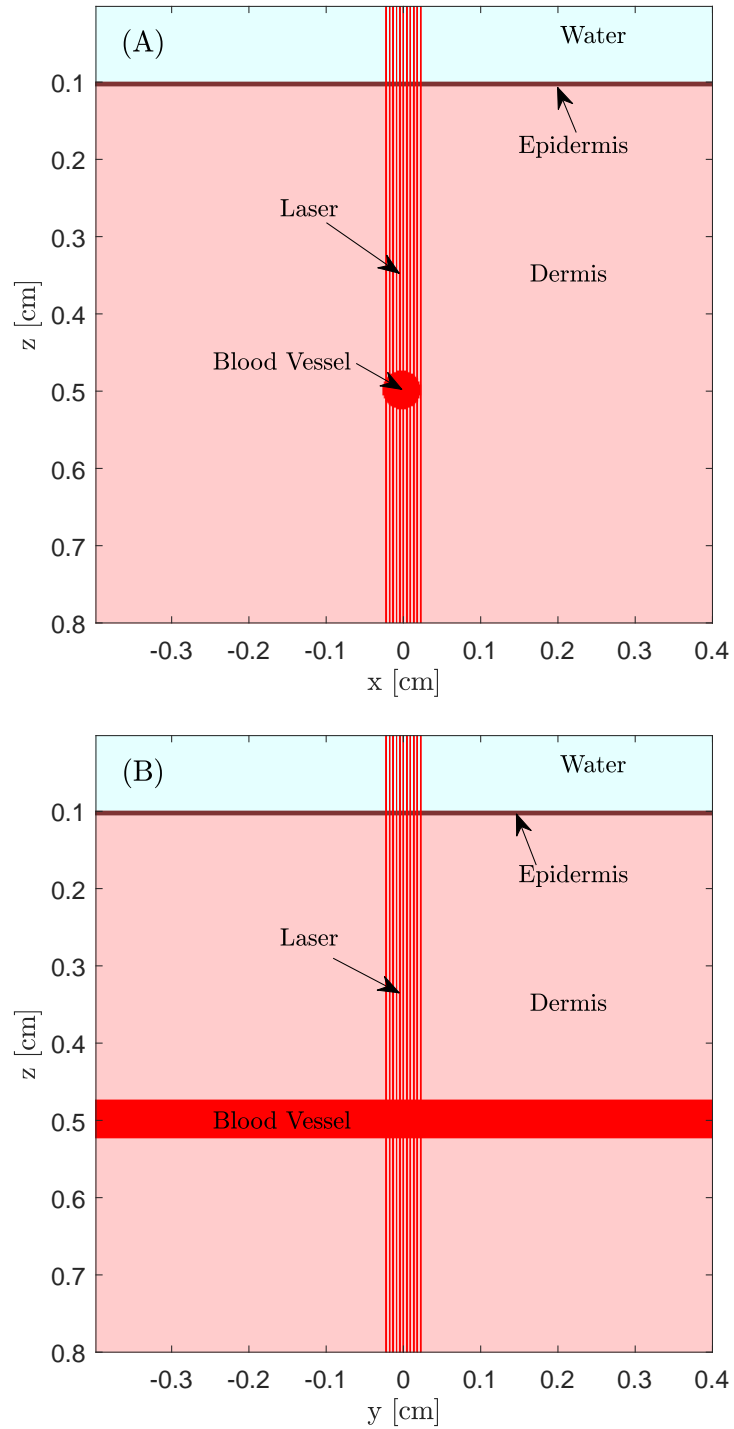
Figure 2.1: Structure of the biological tissue, (A) the right view of the biological structure (Z, X), and (B) the left view of the biological structure (Z,Y).

2. PULSE LASER DIODES TO GENERATE PHOTOACOUSTIC EMISSIONS

Water	
Space	0.1 cm
Absorption coefficient	0.0004 cm^{-1}
Scattering coefficient	100 cm^{-1}
Anisotropy	1
Epidermis	
Thickness	60μm
Absorption coefficient	2.8779 cm^{-1}
Scattering coefficient	221 cm^{-1}
Anisotropy	0.9
Dermis	
Thickness	0.694 cm
Absorption coefficient	0.0572 cm^{-1}
Scattering coefficient	113.5 cm^{-1}
Anisotropy	0.9
Blood Vessel	
Radius	250μm
Absorption coefficient	5.9458 cm^{-1}
Scattering coefficient	55.2 cm^{-1}
Anisotropy	0.9

Table 2.1: Specifications of the biological tissue (Jacques *et al.*, 2014; Jacques, 2014).

The output optical energy from a PLD was assumed to be 15.7μJ in the simulation. This output energy was measured from the pulsed PLD (905D3s3J09S) with an input current of 30 A and a laser pulse length of 150 ns. The simulated wavelength was 905 nm. The beam width of this type of laser source was 235μm $\times$ 400μm (Laser-Components, 2015). The shape of the laser beam was assumed circular in the simulation. The maximum fluence in this simulation was 49.97 mJ/cm^2 which is smaller than the limit of 51.4 mJ/cm^2 (Laser-Safety, 2014). The relevant parameters of this simulation are given in Table 2.2.

Specifications	
Wavelength	905 nm
Diameter of the beam	Based on the maximum transmitted energy
Number of bins	400
Bin size	0.002 cm
Place of the laser source (Y,X,Z)	(0,0,0)
Place of the vessel centre	0.4 cm under the skin
Simulation time	10 min
Speed of sound (Jacques, 2014)	1500 m/s
Thermal expansion (Jacques, 2004)	$2.29 \times 10^{-4} \text{c}^{-1}$
Specific Heat capacity (Jacques, 2004)	4184 J/Kg
Density(Jacques, 2004)	1000 Kg/m^3
Acoustic attenuation (Jacques, 2014)	(90 dB/m)$\times$(frequency/1MHz)$^{1.1}$

Table 2.2: Simulation specifications for laser light propagation in the biological tissue.

The absorbed optical energy inside the biological tissue is shown in figure 2.2. It can be seen that the laser pulse propagated inside the biological tissue due to light scattering inside the biological tissue. In addition, the epidermis layer absorbed higher optical energy than other places in the tissue due to its shortest distance to the laser source. Also, this layer had a larger absorption coefficient than the dermis layer and water. Moreover, more optical energy was absorbed inside the blood vessel due to blood having a larger absorption coefficient than the dermis layer.
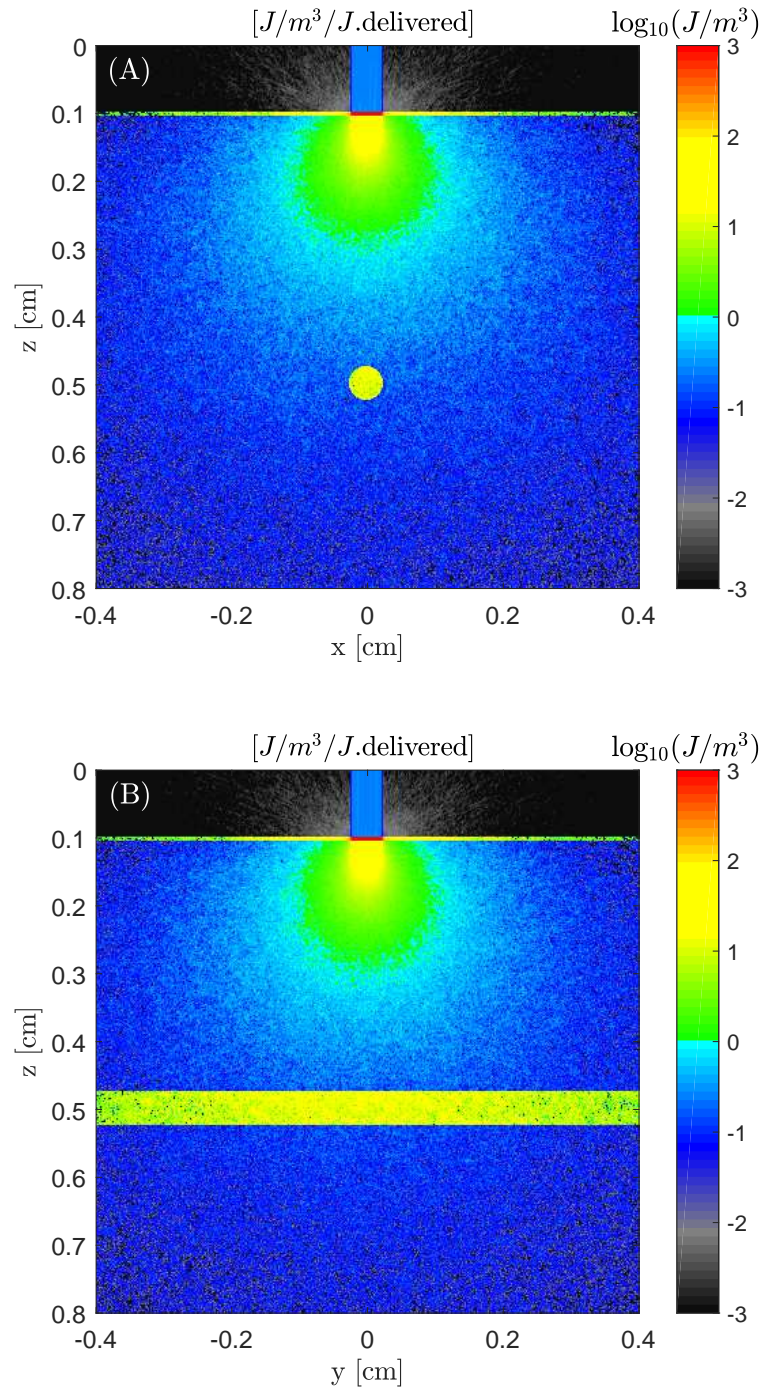
Figure 2.2: Absorbed optical energy inside the biological tissue, (A) Right view of the absorbed optical energy, and (B) Left view of the absorbed optical energy.

2.2.2 Effects of Transducer Specifications on Photoacoustic Emission

From this absorbed optical energy, the photoacoustic emission was generated through velocity potential (Paltauf *et al.*, 2002). When the bandwidth of the simulated transducer was infinite and no attenuation was applied, the photoacoustic wave using five PLDs is shown in figure 2.3. It is clear that the first two peaks delineate the epidermis layer (First photoacoustic wave) followed by a blood vessel (Second photoacoustic wave). The photoacoustic wave from the blood vessel (Second photoacoustic wave) cannot be seen in figure 2.3 (A). This is because the photoacoustic wave generated by the blood vessel was very weak when compared with the photoacoustic wave generated by the epidermis layer (First photoacoustic wave). Figure 2.3 (B) shows only the photoacoustic wave from the blood vessel. These measurements were close to the real size due to the ideal simulation. The shape of the photoacoustic wave was affected by the transducer bandwidth and acoustic attenuation. When using the specifications as shown in Table 2.3 (OLYMPUS, 2015), the photoacoustic wave as shown in figure 2.4 was obtained. This figure shows that the photoacoustic wave becomes wider with the 3.5 MHz transducer. This was a result of the high frequency components of the photoacoustic wave being lost due to the finite bandwidth. As a result, the spatial resolution of the photoacoustic image was degraded. However, when a high frequency single element transducer is used, The boundaries of the target signal which have high frequency parts are detected. This is because the photoacoustic emission is a broadband signal. As a result, the spatial resolution of the imaging target (size of the target) will not significantly be reduced while the low frequency parts of the signal will be lost (Chen *et al.*, 2009). For example, when using a 15 MHz single element transducer, whose specifications are shown in Table 2.4 (OLYMPUS, 2015), the corresponding photoacoustic wave is shown in figure 2.5. This figure illustrates that the spatial resolution was improved when compared with that when using the 3.5 MHz single element transducer. However, the use of a high frequency transducer incurs higher acoustic attenuation, thereby decreasing the penetration depth. It is worth noting when comparing the signals from the two transducers that the amplitude of the photoacoustic wave from the epidermis layer, when using the 15 MHz, was higher than that when using the 3.5 MHz transducer. This occurred as the peak energy of the ideal photoacoustic signal was approximately at 12.03 MHz, as shown in figure 2.6.
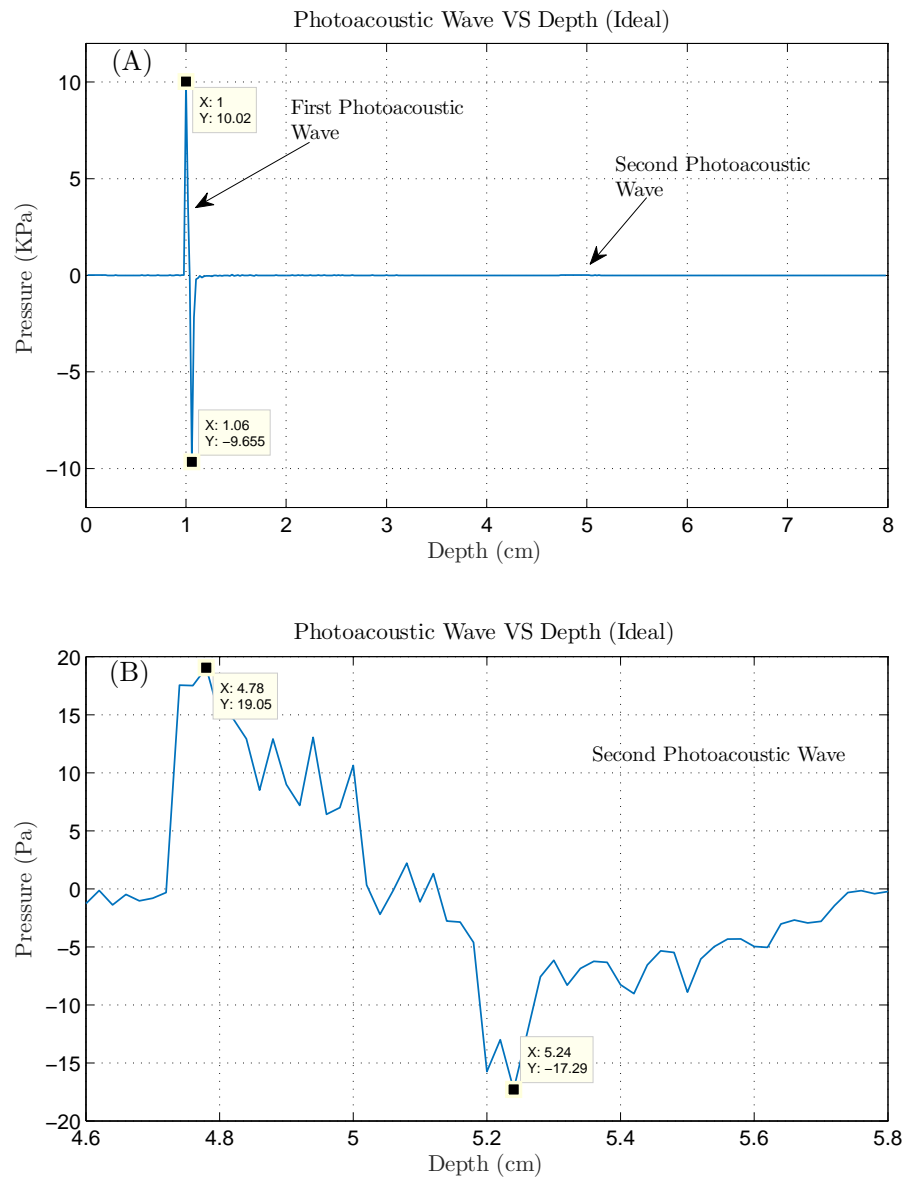
Figure 2.3: Photoacoustic wave when the bandwidth of the simulated transducer was infinite and no attenuation was applied. (A) The pressure wave from the epidermis (First photoacoustic wave) and blood vessel layers (Second photoacoustic wave). (B) The pressure wave from the blood vessel.

Specifications of the Single Element Transducer	
Centre frequency	3.5 MHz
Diameter of the element	6.3 mm
Length of the near field	23 mm
Location of the focus point	17 mm
Bandwidth of the transducer (-6 dB)	65.29%
Origin of the transducer (Y,X,Z) (Assumption)	(0,0,0)
Sensitivity of the transducer (Assumption)	270 mV/MPa
Frequency of attenuation (Assumption)	4.6 MHz
Noise source (Assumption)	Lab experiment

Table 2.3: Specifications of the transducer used to detect the photoacoustic emission (OLYMPUS, 2015).

Specifications of the Single Element Transducer	
Centre frequency	15 MHz
Diameter of the element	6.3 mm
Length of the near field	99.9mm
Location of the focus point	19.5 mm
Bandwidth of the transducer (-6 dB)	57.6%
Origin of the transducer (Y,X,Z) (Assumption)	(0,0,0)
Sensitivity of the transducer (Assumption)	270 mV/MPa
Frequency of attenuation (Assumption)	19.32 MHz
Noise source (Assumption)	Lab experiment

Table 2.4: Specifications of the transducer used to detect the photoacoustic emission (OLYMPUS, 2015).
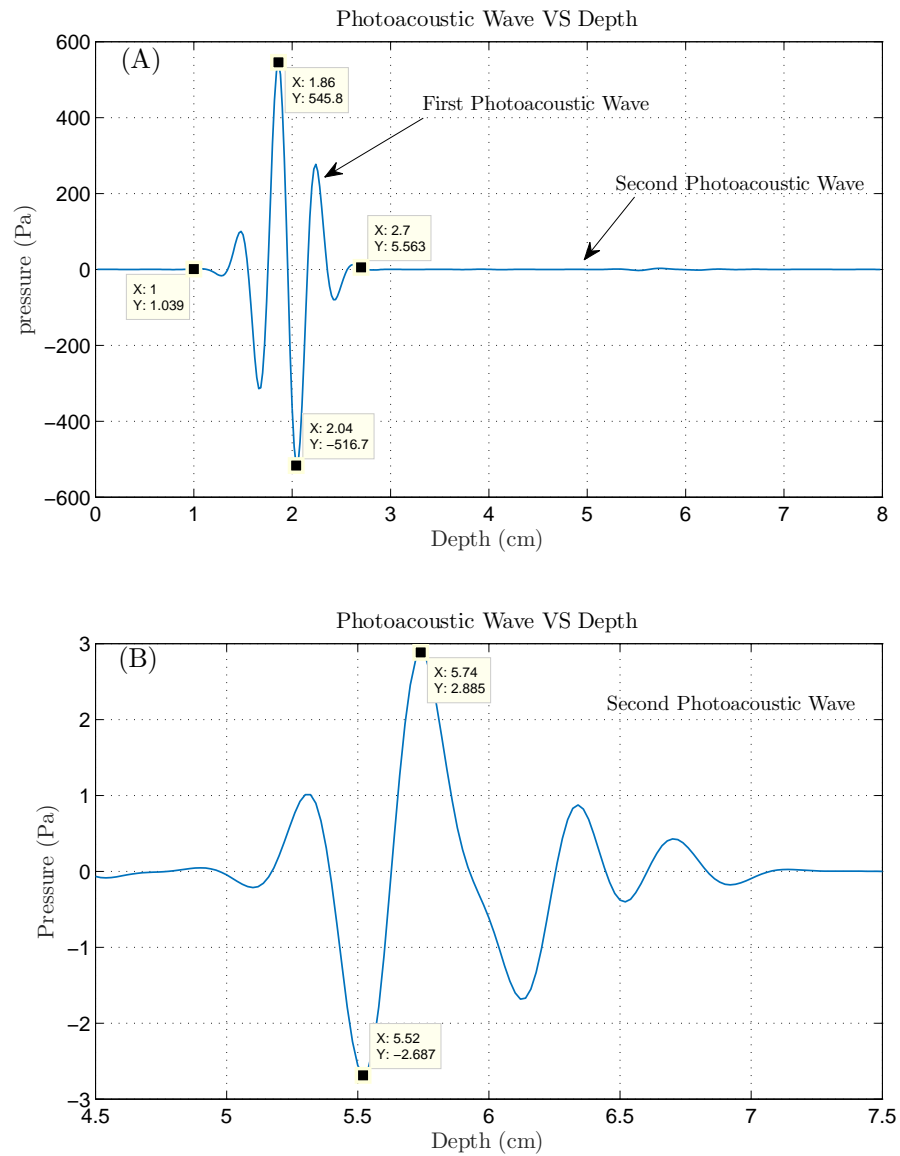
Figure 2.4: Photoacoustic wave when the centre frequency and transducer bandwidth (-6 dB) were 3.5 MHz and 2.27 MHz, respectively. In this simulation, attenuation was applied to the photoacoustic wave. (A) The pressure wave from the epidermis (First photoacoustic wave) and blood vessel layers (Second photoacoustic wave). (B) The photoacoustic wave from the blood vessel.
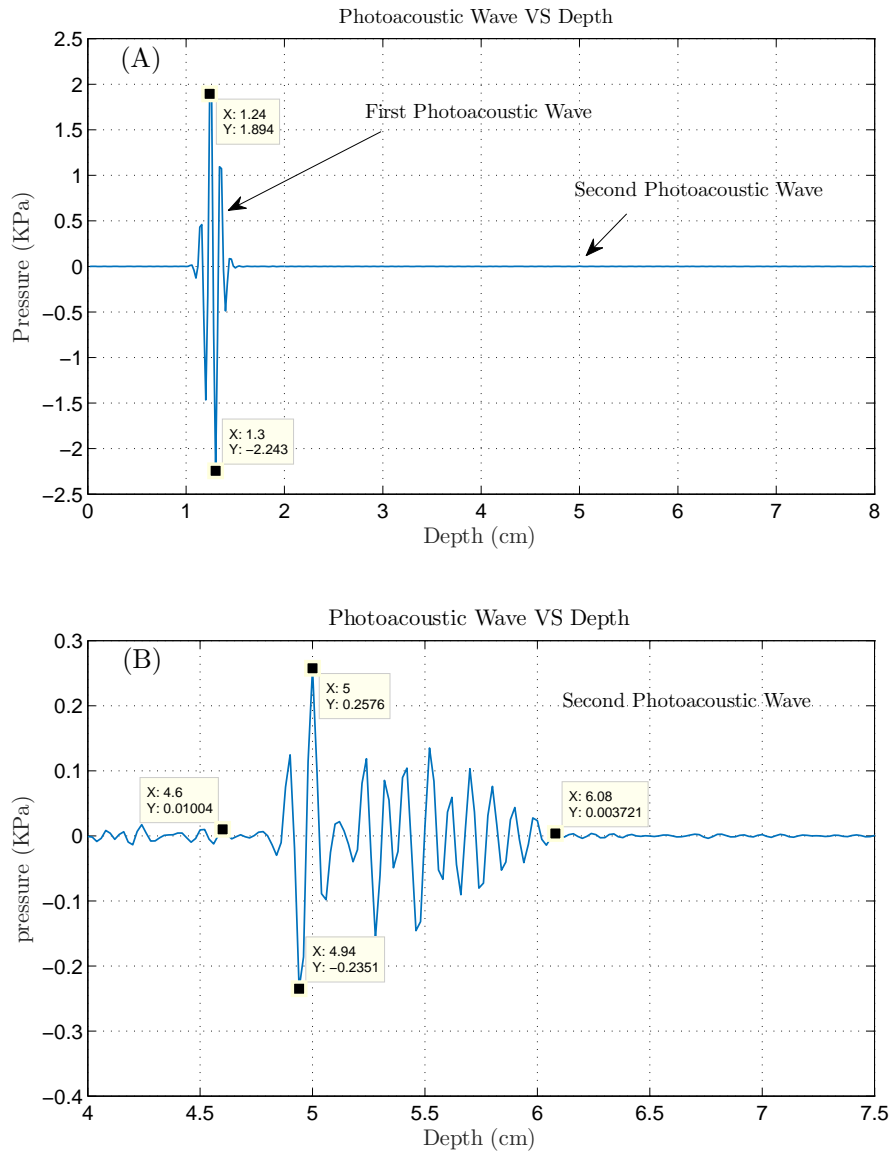
Figure 2.5: Photoacoustic wave when the centre frequency and transducer bandwidth (-6 dB) were 15 MHz and 8.6 MHz, respectively. In this simulation, attenuation was applied. (A) The photoacoustic wave from the epidermis (First photoacoustic wave) and blood vessel layers (Second photoacoustic wave). (B) The photoacoustic wave from the blood vessel.

2. PULSE LASER DIODES TO GENERATE PHOTOACOUSTIC EMISSIONS
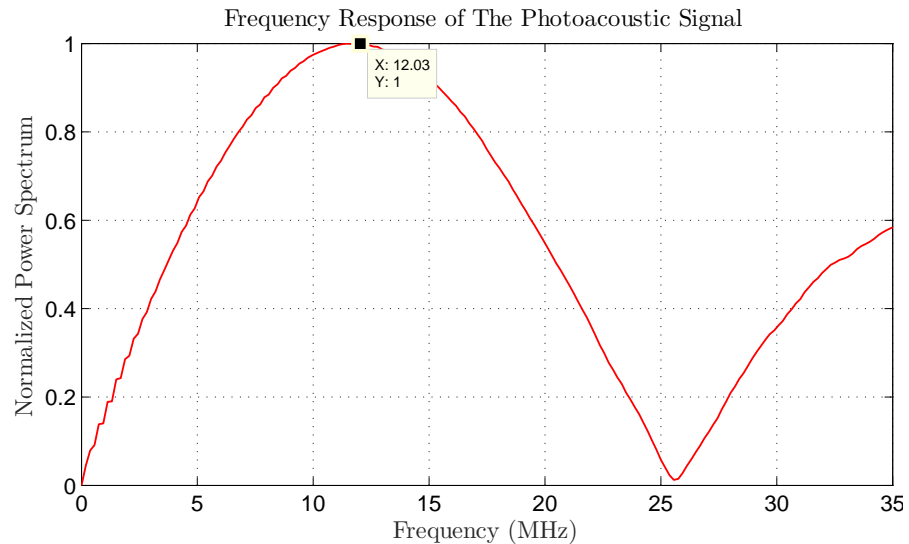
Figure 2.6: Power spectrum of the ideal photoacoustic emission. The peak of the normalized power spectrum was at 12.03 MHz.

2.2.3 The Required Number of PLDs for A Specific SNR

The block diagram of the simulation is shown in figure 2.7. The Monte Carlo simulation was used to calculate the distribution of the laser pulse energy in tissue. Then, the velocity potential was calculated based on the absorbed energy (Jacques, 2014). The amplitude of the velocity potential was scaled based on the output energy of the PLDs. Then, the photoacoustic wave was generated from the velocity potential (Jacques, 2014). Following this, attenuation was applied to the photoacoustic wave whose value depends on the frequency of the photoacoustic wave and the tissue type. The amplitude and the shape of the photoacoustic wave was affected by the sensitivity and bandwidth of the ultrasound transducer. Then, noise was added followed by calculating the SNR of the photoacoustic signal. If the SNR was not acceptable, the number of PLDs was increased and the beam width of the laser source was scaled to not exceed the limitation for fluence. This process was applied until meeting the acceptable SNR. The relevant Matlab code is given in Appendix (1). In this simulation, the 3.5 MHz transducer was used. In addition, the source of noise was taken from the photoacoustic

signal generated in our laboratory, as shown in figure 2.8 (experiment performed by Dr James McLaughlan). This signal, as shown in figure 2.8, was amplified by 40 dB and averaged 100 times. Therefore, this signal was attenuated by 40 dB before used for calculating for the SNR.
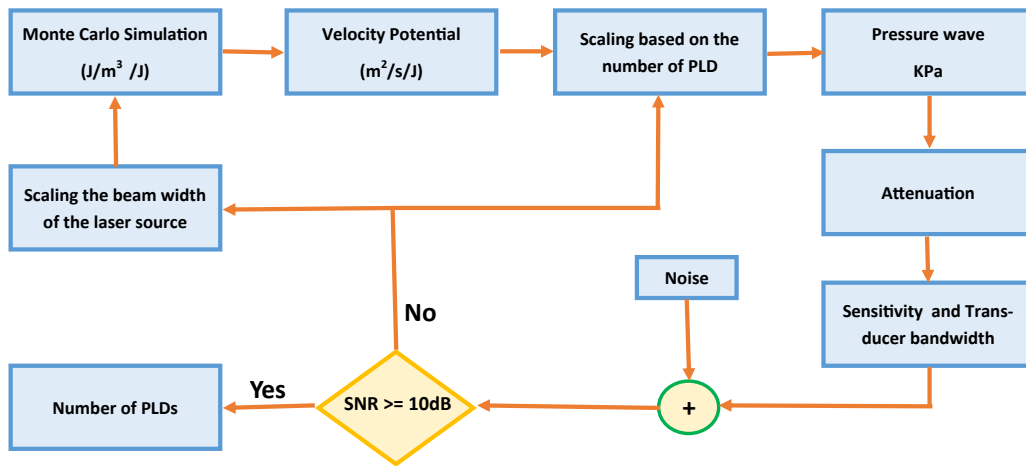
Figure 2.7: Block diagram showing the procedure to calculate the required number of PLDs to generate photoacoustic emissions with a specific SNR. Acoustic attenuation, the sensitivity and bandwidth of the transducer were considered in this simulation.
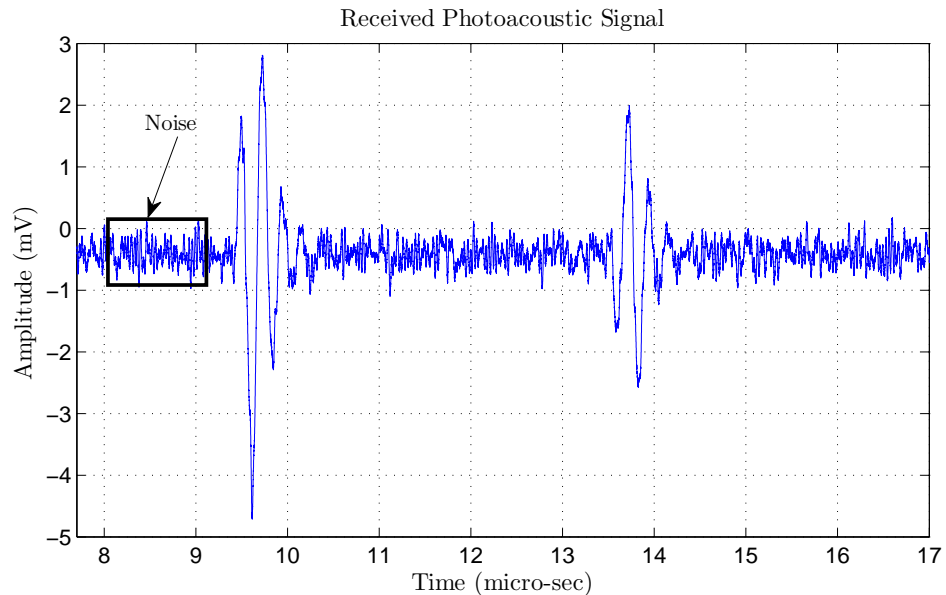
Figure 2.8: Experimental photoacoustic emission. Noise in the solid rectangular was
used to calculate the required number of PLDs to achieve a specific SNR.

The SNR (SNR_{dB}) was calculated by using equation 2.1 (Heinz *et al.*, 2015):

$$\text{SNR}_{\text{dB}} = 20 \log_{10} \frac{\text{RMS}_{\text{signal}}}{\text{RMS}_{\text{noise}}}, \tag{2.1}$$

where $\text{RMS}_{\text{signal}}$ is the root mean square of the acoustic signal and $\text{RMS}_{\text{noise}}$ is the root
mean square of noise. The relationship between the number of the PLDs and SNR of
the photoacoustic emission is shown in Table 2.5 and figure 2.9.

Number of PLDs	Mean SNR (Linear)	Standard Deviation (Linear)
10	0.1771	1.2062
20	0.3587	1.1914
30	0.5254	1.1956
40	0.6970	1.2111
50	0.8622	1.1751
60	1.0400	1.1759
70	1.1638	1.2257
80	1.3110	1.1882
90	1.5632	1.1859
100	1.6939	1.2314
110	1.8637	1.1612
120	2.1201	1.2000
130	2.1841	1.2303
140	2.2312	1.1800
150	2.4648	1.1929
160	2.6056	1.1935
170	2.7175	1.2108
180	2.8867	1.1603
190	3.1722	1.2005

Table 2.5: Relationship between the number of PLDs and SNR of the photoacoustic emission. The standard deviation was calculated based on 100 measurements.
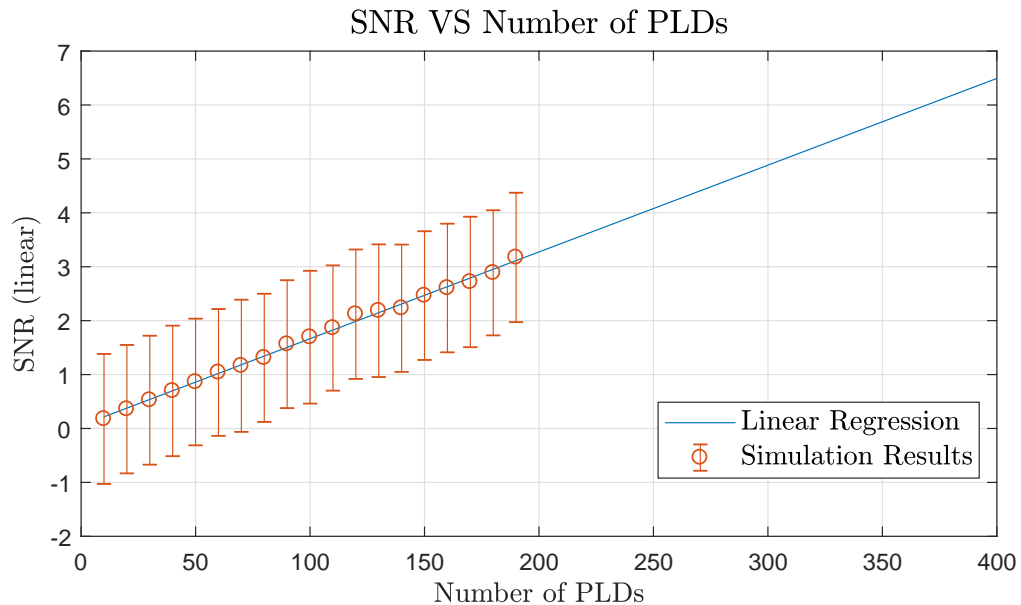
Figure 2.9: Relationship between the number of PLDs and SNR of the photoacoustic emission. The standard deviation was calculated from 100 measurements.

From Table 2.5 and figure 2.9, it can be seen that to obtain a SNR of 3.1722 (10.02 dB) for imaging blood vessel, 190 PLDs are needed. In this calculation, 100 noise samples were used to calculate the standard deviation of SNR. The standard deviation of the SNR when using 190 PLDs is 1.2005 (1.58 dB). By calculating the linear regression, it can be expected the required number of PLDs to achieve specific SNR. This linear regression was calculated by using the least squares criterion (Brase & Brase, 2013). The required number of PLDs (NP) to achieve specific SNR can be expected by using equation 2.2:

$$SNR = 0.0558 + 0.0161NP. \tag{2.2}$$

For example, when the number of PLDs is 300, the expected SNR is 4.885 (13.77 dB). However, when the Nd-YAG Laser (Continuum SLI-10) with OPO(SLIII-10) is used, the output peak energy with a wavelength of 905 nm is almost 100 mJ, achieving a SNR of 29.24 dB±1.65 dB. To achieve this SNR when using 190 PLDs, the generated photoacoustic wave should be averaged by almost 84 times. By increasing the number of PLDs, the number of averaging photoacoustic signals to achieve 29.24 dB SNR is

reduced. For instance, if 300 PLDs were to be used, the number of averaging would be almost 35 times to achieve this SNR.

2.3   Experiment Setup

In the experiment, the peak optical energy of PLDs was compared with the peak optical energy of the Nd:YAG laser in term of SNR of the generated photoacoustic emission. A gelatine phantom with an ink inclusion (PARKER-BLACK INK) as shown in figure 2.10 was used. The inclusion was placed at a depth of 1 cm. The inclusion had a same optical absorption coefficient of the blood used in the Monte Carlo simulation using a 905 nm wavelength ($\mu_a = 5$ cm^{-1}). The recipe of this phantom is given in Appendix (2). The tunable Nd:YAG laser was used to generate photoacoustic emissions from the inclusion. The laser pulses were guided using an optical fibre, as shown in figure 2.11. The wavelength of the laser pulses was 905 nm. The peak optical energy from the laser was changed based on the assumption of the number of PLDs that were used. The generated photoacoustic emissions were recorded by using a 3.5 MHz single element transducer (OLYMPUS-V384). These received photoacoustic emissions were then amplified by 30 dB using a preamplifier (SPA Pre-Amplifier SPECTRUM) and captured by an oscilloscope (LeCroy waveSurfer 104Xs 1GHz Oscilloscope) with 100-times averaging. The optical energy of the laser pulse was controlled by using a computer that sent control signals to the pulse generator (Quantum 9520 series pulse generator).

Figure 2.10: Gelatine phantom with an inclusion. The inclusion had an optical absorption coefficient of 5 cm^{-1} which is same to the value used in Monte Carlo simulation.

Figure 2.11: Experimental setup used to compare the PLDs with the Nd:YAG laser in team of SNR of the generated photoacoustic emissions. The generated photoacoustic emissions were amplified 1000 times and averaged 100 times. The wavelength of the laser pulse was 905 nm.

2.4 Experimental Results and Discussion

The relation between the number of PLDs and the SNR of generated photoacoustic emissions is shown in figure 2.12. The mean SNR was less than 1.122 (1 dB) when the peak optical energy of the laser was equivalent to the peak output optical energy of the 50 PLDs or less. However, the SNR of the photoacoustic emission reached 2.38 (7.5 dB) if the peak output optical energy was equivalent to the peak output optical energy of 190 PLDs. This number of PLDs was large to generate this amount of SNR, however, by using the Nd:YAG laser, it can achieve a higher SNR. For example, if the peak output optical energy of the Nd:YAG laser was 4.3 mJ, the SNR of the generated photoacoustic emission was 9.6 dB $\pm$ 0.128 dB. The SNR improved by almost 2.1 dB when compared with using 190 PLDs. In addition, when the number of PLDs increased,

these PLDs will be difficult to assemble. For example, the dimension of a single driver
module for pulsed lasers (LDP-V 50-100 V3 & LDP-V BOB) was 7.5 × 4.4 × 3.7 cm
= 122.1 cm^3. As a result, the size produced by combining 190 driver modules is 122.1
cm^3. This size is still smaller than the size of the Nd-YAG Laser with OPO (77.5
× 17.8 × 19 cm = 26210.5 cm^3) (Upputuri & Pramanik, 2015). However, the PLD
(905D3s3J09S) used in this calculation was not coupled with the optical fibre. This
optical fibre is needed to combine the output optical energy from the PLDs. As a result,
assembling multiple PLDs with optical fibre bundle that its diameter is 3 mm will be
more complex (Allen & Beard, 2006; Laser-Components, 2015). The price of a single
PLD with a driver module is £ 945. As a result, the price of 190 PLDs with driver
modules is around £ 179k. This price is expensive when compared with the price of
a Nd-YAG laser, which is around £ 110k (Upputuri & Pramanik, 2015). These limit
PLDs for superficial imaging applications. However, the PRF of PLD (10 KHz) is much
higher than that of a Nd-YAG laser (10 Hz). This high PRF makes PLD suitable for
real-time imaging (Daoudi et al., 2014).
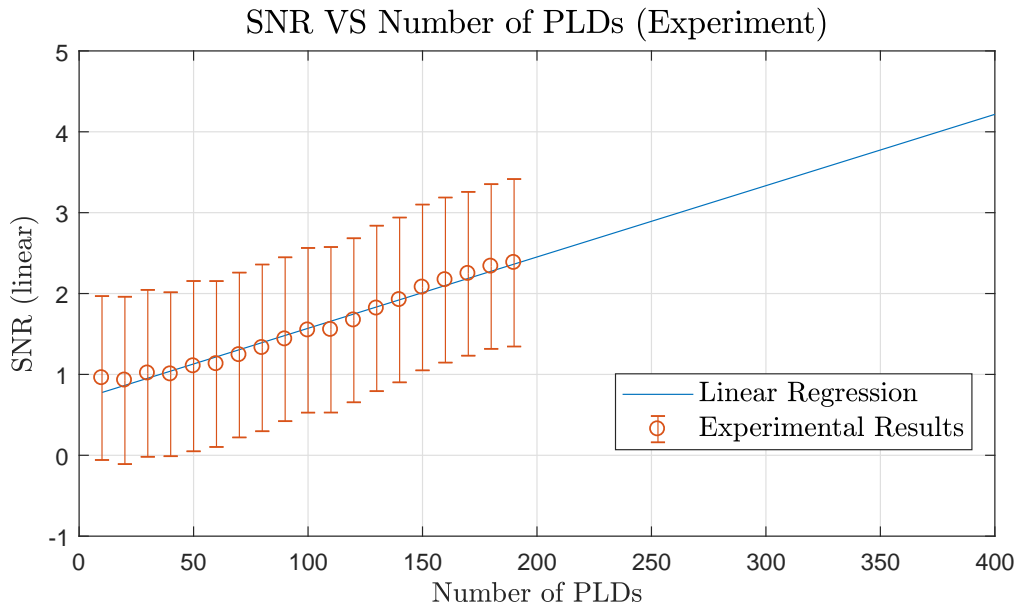
Figure 2.12: Relationship between the number of PLDs and SNR of the experimental
photoacoustic emission. The standard deviation was calculated with 10 samples.

A 2.5 dB SNR difference was found when comparing simulations and experiments, with a smaller SNR in experiments. This could be explained by a few reasons. In the simulation, the laser beam was assumed vertical to the imaging target, while in the experiment the angle of incidence was approximately 35°. Then, the beam width of the incidence laser was wider than that in the simulation. In addition, the characteristics of the phantom used in the experiment were different from those in the simulation. The simulation and experiment results showed the limitation of using PLDs, however, the higher PRF afforded by PLDs can be investigated to increase the imaging frame rate and reduce the noise level by averaging multiple acquisitions and coded excitation techniques.

In this study, the effect of the pulse length on the generated photoacoustic was not taken into account. The pulse length of PLDs was assumed to be very short (7ns). However, in the reality the pulse length is 150 ns. This pulse length will affect the shape of the generated photoacoustic emission. For example, the high frequency components of the photoacoustic emissions are reduced as the pulse length of the laser source is increased. As a result, the spatial resolution of the target will be reduced. This is because the impulse response of the generated photoacoustic emission is affected by the time profile of the laser pulse (Allen *et al.*, 2005; Gao *et al.*, 2017). In addition, the value of the stress confinement coefficient will be reduced as the pulse length of the laser source becomes close to the size of the imaging target (Equation 1.8). As a result, the increase in the amplitude of the photoacoustic emission will be reduced (Equation 1.10) (Allen *et al.*, 2005; Jacques, 2004). In this calculation, the diameter of the blood vessel was 0.5 mm. This means that the value of the stress confinement coefficient (A = 0.8) will not significantly affect the amplitude of the generated photoacoustic emission.

Recently, there is another portable light source in photoacoustic imaging, namely light emitted diode (LED). There are some advantages and disadvantages of LED compared with PLD. For instance, LED is cheaper and more resistant to electrical static than PLD. In addition, the LEDs chip can combine multiple wavelengths that can support photoacoustic spectroscopic applications. However, the wavelength of the output light from the LED is more affected by the heat than that of PLD. The output optical energy from LED is very low compared with that of PLD. As a result, the output optical energy from LED will be significantly reduced if it is connected to optical fibre

(Zhong *et al.*, 2018). This LED has been applied in some photoacoustic applications such as tracking needle (Xia *et al.*, 2018) and spectroscopic (Allen & Beard, 2016).

2.5 Conclusion

In this chapter, the number of PLDs needed for a specific SNR was first calculated based on a Monte Carlo simulation. In addition, the output optical energy of the PLDs was compared with that from a Nd:YAG laser in terms of SNR of the experimental photoacoustic emission. By using 190 PLDs, a mean SNR of 10.02 and 7.5 dB were obtained in the simulation and experiment, respectively. This large number of PLDs make it only suitable for superficial applications. This is because the optical energy that reaches the shallow imaging target is less attenuated than that of the deep imaging target. For example, in photoacoustic microscopy, one PLD is used to achieve micrometre scale imaging depth (Zeng *et al.*, 2013). In photoacoustic tomography, an array of PLDs is used to achieve millimetre scale imaging depth for real-time imaging (Daoudi *et al.*, 2014).

Chapter 3

Improved Unipolar Golay Code for Photoacoustic imaging

Abstract

In photoacoustic imaging, coded excitations are used to increase the frame rate and improve the image SNR. Some coded excitation techniques, such as pulse position modulation (PPM) and the Legendre code sequence, generate coded artefacts in the photoacoustic image, while unipolar golay codes do not. In the unipolar golay codes, four sequences of pulses should be transmitted to generate the photoacoustic emissions. In this chapter, this unipolar golay code was developed to reduce the number of transmitted sequences to two. This reduced the time for acquiring photoacoustic waves compared with that when using the original unipolar golay code. However, this developed unipolar golay code generated artefact signals. This type of code was simulated and compared with some coded excitations. From the simulation results, it can be noticed that the coded gain and SNR of the photoacoustic wave that was generated by using the developed unipolar golay code was better than those generated by the original unipolar golay code when the noise level was high. In addition, the acquisition time of the developed unipolar golay code was less than that of the original unipolar golay code by 78 μsec.

3. IMPROVED UNIPOLAR GOLAY CODE FOR PHOTOACOUSTIC IMAGING

3.1 Introduction

In photoacoustic imaging, averaging multiple acquisitions of the photoacoustic signals is used to improve the SNR (Mienkina *et al.*, 2010) at the cost of reduced frame rate (Mienkina *et al.*, 2010; Wei *et al.*, 2015). Coded excitations provide an alternative to increase the image SNR instead of solely averaging multiple acquisitions (Beckmann & Schmitz, 2013; Beckmann *et al.*, 2010; Mienkina *et al.*, 2010; Zhang *et al.*, 2012). This effectively enables high-frame-rate photoacoustic imaging. The unipolar golay code does not generate coded artefacts in the photoacoustic emission, which differs from other coded excitation techniques such as pulse position modulation (PPM) (Beckmann & Schmitz, 2013) and the Legendre code sequence (Beckmann *et al.*, 2010). In this type of coded excitation four sequences of pulses should be transmitted to generate the photoacoustic emissions (Mienkina *et al.*, 2010).

In this chapter, the unipolar golay code was developed to reduce the number of transmitted sequences to two. In addition, it was compared with the original unipolar golay code, Legendre code sequence and PPM, in terms of SNR and code gain for the generated photoacoustic emission. This chapter is organised as follows: first, the theoretical analysis of a number of coded excitations. Second, the theoretical analysis of the developed unipolar golay code. Third, simulation setup. Fourth, simulation results and discussion and, finally, conclusion.

3.2 Coded Excitation

3.2.1 Unipolar Golay Code

In 2010, the unipolar golay code was used to improve the SNR of photoacoustic images when a laser diode was used (Mienkina *et al.*, 2010). In this type of coded excitation, a PRF should be higher than the inversed time of flight that the photoacoustic wave travels from the deepest source of the photoacoustic signal to obtain positive gain when compared with averaging technique. Two sequences of bits are used in this technique which are complementary to each other. To utilise the unipolar golay code in photoacoustic imaging, four pulse sequences will be transmitted. Figure 3.1 shows the distribution of these transmitted sequences when four pulses per sequence are used (Mienkina *et al.*, 2010).
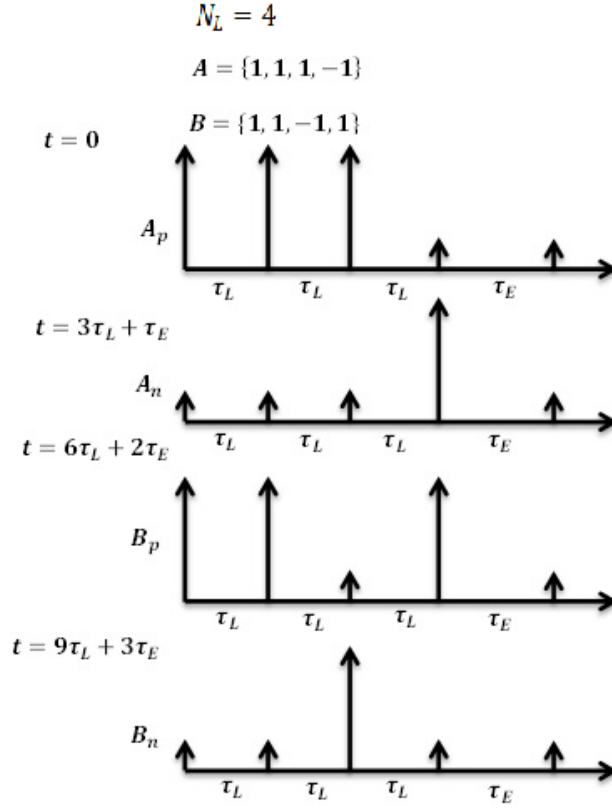
Figure 3.1: Transmitted pulse sequences when using the original unipolar golay code. Four pulse sequences are transmitted. Two of them consist of positive pulses while others consist of negative pulses (Mienkina *et al.*, 2010).

In figure 3.1, τ_L is the pulse repetition interval and τ_E is the time of flight of the photoacoustic wave from the deepest target. It can be noticed that in each transmitted sequence, the positive pulses and negative pulses are transmitted separately due to the laser system is unable to transmit a negative pulse. After transmitting these sequences, sequences of photoacoustic signals with noise will be received. Then, the received photoacoustic waves from negative laser pulses will be swapped and added to those from the positive laser pulses. These are explained by equations 3.1 and 3.2 (Mienkina

3. IMPROVED UNIPOLAR GOLAY CODE FOR PHOTOACOUSTIC IMAGING

et al., 2010):

$$A_r(k) = (A_p(k) * h_{PA}(k) + n_1(k)) - (A_n(k) * h_{PA}(k) + n_2(k)), \qquad (3.1)$$

$$B_r(k) = (B_p(k) * h_{PA}(k) + n_3(k)) - (B_n(k) * h_{PA}(k) + n_4(k)), \qquad (3.2)$$

where $A_r(k)$ is the received sequence of photoacoustic waves due to the transmitted pulse sequence A; $B_r(k)$ is the received sequence of photoacoustic waves due to the transmitted pulse sequence B; $h_{PA}(k)$ is the impulse response of the system and $n(k)$ is noise.

To decode the photoacoustic emissions when using the unipolar golay coded excitation, the received signals will be cross correlated with the transmitted pulse sequences, and then summed together as explained in equations 3.3 and 3.4 (Mienkina *et al.*, 2010):

$$y_{UGC}(k) = (A_r(k) * A(-k)) + (B_r(k) * B(-k)), \qquad (3.3)$$

$$y_{UGC}(k) = 2N_L h_{PA}(k) + R(k), \qquad (3.4)$$

where $y_{UGC}(k)$ is the decoded photoacoustic signal when using the original unipolar golay code; $A(k)$ is the transmitted pulse sequence A; $B(k)$ is the transmitted pulse sequence B; N_L is the code length and $R(k)$ is noise. As a result, the decoded photoacoustic signal will be generated with noise. However, the amplitude of the photoacoustic signal will be amplified by twice the code length as given in equation 3.4 (Mienkina *et al.*, 2010). The relationship between the code length and the time that is needed to receive sequences of photoacoustic signals is given in equation 3.5 (Mienkina *et al.*, 2010):

$$T_{UGC} = 4((N_L - 1)\tau_L + \tau_E), \qquad (3.5)$$

where T_{UGC} is the time needed to receive sequences of the photoacoustic waves when using the unipolar golay coded excitation. To compare the original unipolar golay coded

excitation technique with the averaging technique, the code gain will be calculated as given in equation 3.6 (Mienkina *et al.*, 2010):

$$G_{UGC} = 10 \log_{10}(\frac{N_L}{4((N_L - 1)\tau_L \frac{c}{z_a} + 1)}), \tag{3.6}$$

where G_{UGC} is the code gain of the unipolar golay code and z_a is the maximum depth for photoacoustic imaging. M. Mienkina and his colleagues have experimentally applied a unipolar golay code in photoacoustic imaging by using a laser diode (Mienkina *et al.*, 2010). The PRF and the wavelength of laser pulses from the laser diode were 1 MHz and 808 nm, respectively. The output energy of the laser diode was within Maximum Permissible Exposure (MPE) of the laser safety. In this experiment, the code length was 512 bit. The distance between a transducer and object was 50 mm. With the equal time used by the averaging technique and the unipolar golay code, it was found that the SNR of the photoacoustic signal was higher for the coded excitation. The gain of this experiment was 8.75 dB. This gain is reduced as the distance between the deepest target and the transducer is decreased. This is because the time flight of the photoacoustic wave from the deepest target to the transducer is reduced. As a result, the improvement of the SNR that results from averaging becomes close to the improvement of SNR that results from the unipolar golay code. In addition, this gain is reduced if the PRF of the laser diode is decreased. This is because the number of transmitted bits within the time of flight of the photoacoustic wave from the deepest target is reduced. Moreover, in each transmitted pulse sequence, it will be wait for the time flight of the photoacoustic wave from the deepest target to the transducer before transmitting the second sequence (Mienkina *et al.*, 2010). This is time consuming when compared to certain coded excitations, such as the legendre code sequence (Beckmann *et al.*, 2010). This is because four sequence of pulses are needed to transmit in the unipolar golay code.

3.2.2   Legendre code sequence

The Legendre code sequence has been used to improve the SNR of the photoacoustic emission in 2010 (Beckmann *et al.*, 2010). This type of code depends on primitive roots

3. IMPROVED UNIPOLAR GOLAY CODE FOR PHOTOACOUSTIC IMAGING

as explained in equation 3.7 (Beckmann *et al.*, 2010; Fan & Darnell, 1996):

$$a_k = \{ {}^{1 \, or \, -1, k=0}_{(-1)^t, k \equiv a^t K}, \tag{3.7}$$

where a_k is the value of the pulse at k and α is the primitive root of K. In this type of coding technique, two sequences of laser pulses are transmitted; one for positive pulses and the other for negative pulses. The received sequences of photoacoustic waves from negative laser pulses will be converted and added to those from the positive laser pulses. Then, the received sequence of photoacoustic waves will be decoded being cross correlated with the transmitted laser pulse sequence as given in equations 3.8 and 3.9 (Beckmann *et al.*, 2010):

$$y_{LS}(k) = [(A_p(k) * h_{PA}(k) + n_1(k)) - (A_n(k) * h_{PA}(k) + n_2(k))] * A(-k), \tag{3.8}$$

$$y_{LS}(k) \approx N_L h_{PA}(k) + R(k), \tag{3.9}$$

where $y_{LS}(k)$ is the decoded photoacoustic signal when using the Legendre code sequence. From equation 3.9, it can be noticed that the amplitude of the decoded photoacoustic signal will be amplified by the code length of the transmitted laser pulses. In addition, the resultant photoacoustic signal will be affected by noise and some coded artefacts. The relationship between the code length and time for the received sequences of photoacoustic signals is given in equation 3.10 (Beckmann *et al.*, 2010):

$$T_{LS} = 2((N_L - 1)\tau_L + \tau_E), \tag{3.10}$$

where T_{LS} is the time needed to receive all sequences of photoacoustic waves when using the Legendre code sequence. The code gain can be calculated by using equation 3.11 (Beckmann *et al.*, 2010):

$$G_{LS} = 10 \log_{10}(\frac{N_L}{4((N_L - 1)\tau_L \frac{c}{z_a} + 1)}), \tag{3.11}$$

where G_{LS} is the code gain of the Legendre code sequence. In the experiment that M. Beckmann and his colleagues have performed to apply Legendre code sequence in photoacoustic imaging, using a PRF of 500 KHz and pulses with a wavelength of 652 nm (Beckmann *et al.*, 2010). The output energy of the PLD was 1.53 μJ. The code length varied between 11 and 547 bits. The distance between the transducer and the object was 45 mm. It was found that when the code length was 547 bits, the code gain was 6 dB (Beckmann *et al.*, 2010). Moreover, the coded artefacts, when using this coding technique, were reduced with a longer code length (Beckmann *et al.*, 2010). When comparing the experiment result of the legendre code sequence with the experiment result of the unipolar golay code, the code gain of the unipolar golay code is higher than the code gain of the legendre code sequence by 2.75 dB. However, this comparison is not accurate because the specifications of each experiment were different from each other. For example, the PRF in the unipolar golay code experiment was 1 MHz while the PRF in the legendre code sequence experiment was 500 KHz. In addition, the depth of the imaging target of the unipolar golay code was 50 mm while the depth of the target in the legendre code sequence was 45 mm. The wavelength of the laser source (808 nm) in the unipolar golay code was also different from the wavelength of the laser source (652nm) in the legendre code sequence (Beckmann *et al.*, 2010; Mienkina *et al.*, 2010). Therefore, these coded excitations will be compared and studied when their simulation specifications are the same to produce an accurate comparison.

3.2.3 Pulse Position Modulation (PPM)

PPM relies on the arrangement of temporal positions of the laser pulse, as shown in figure 3.2 (Beckmann & Schmitz, 2013). It can be seen that the time delay between each transmitted laser pulse is gradually increased. The increment step is τ_s. This increment makes the length of the code limited to have a positive gain compared with the averaging technique (Beckmann & Schmitz, 2013).
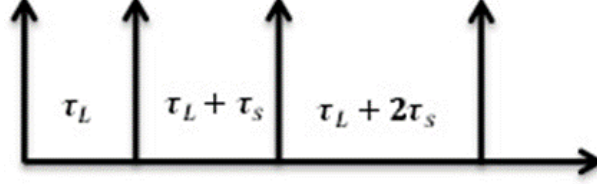
Figure 3.2: Schematic of transmitted laser pulses when using PPM. The increment of the time delay between every two pulses is τ_s.

The maximum code length (N_{Lmax}) with the highest code gain can be calculated by using equation 3.12 (Beckmann & Schmitz, 2013):

$$N_{Lmax} = \sqrt{2\frac{\tau_E - \tau_L + 2\tau_s}{\tau_s}}, \tag{3.12}$$

In this coding technique, one sequence will be transmitted. The sequence of photoacoustic signals received by the ultrasound transducer will be decoded, being cross correlated with the transmitted laser pulse sequence, as formulated by equation 3.13 (Beckmann & Schmitz, 2013):

$$y_{PPM}(k) = (A_p(k) * h_{PA}(k) + n(k)) * A(-k), \tag{3.13}$$

where $y_{PPM}(k)$ is the decoded photoacoustic signal when using the PPM technique. The relationship between the PPM code length and the time for the received sequence of photoacoustic signals is described by equation 3.14 (Beckmann & Schmitz, 2013):

$$T_{PPM} = \tau_E + (N_L - 1)\tau_L + \frac{(N_L - 1)(N_L - 2)}{2}\tau_s, \tag{3.14}$$

where T_{PPM} is the time needed to receive the sequence of photoacoustic waves when using PPM coded excitation. The code gain (G_{PPM}) of using PPM can be calculated

by equation 3.15 (Beckmann & Schmitz, 2013):

$$G_{PPM} = 10 \log_{10}\left(\frac{N_L}{1 + (N_L - 1)\frac{\tau_L}{\tau_E} + \frac{1}{2}(N_L - 2)(N_L - 1)\frac{\tau_S}{\tau_E}}\right) \qquad (3.15)$$

In the experiment that M. Beckmann and his colleagues have performed to detect the photoacoustic signal by using PPM, a PRF of 500 KHz and a laser pulse wavelength of 808 nm were used (Beckmann & Schmitz, 2013). The output energy of the laser diode was 0.55μJ. The code length was 63 bits. The increment of the time delay between pulses was 25 ns. As a result, the PPM achieved a high code gain ($\sim$ 9 dB) with a short code length. A drawback of this type of coding technique was the coded artefact in the decoded photoacoustic signal (Beckmann & Schmitz, 2013). PPM has advantage over the unipolar golay code and legendre code sequence in term of acquisition time. However, the different specifications of each experiment setup, such as depth of target, PRF and wavelength of laser source, mean that the comparison between these coded excitations is not accurate. These coded excitations will be compared with the same simulation specifications in this study.

3.3 Reducing the Acquisition Time When Using Unipolar Golay Code

When the unipolar golay code is used for photoacoustic imaging, four sequences of pulses are transmitted, as shown in figure 3.1 (Mienkina *et al.*, 2010). Two of them for positive laser pulses, while the others for negative ones (Mienkina *et al.*, 2010). This results in the increased time for coding. To reduce this time, a method of transmitting two pulse sequences is proposed. These two sequences are selected based on the highest number of positive or negative pulses in each main sequence, as shown in figure 3.3. It can be noticed that in sequence A and sequence B, the positive bits are transmitted due to the number of positive bits is higher than that of the negative bits in both A and B sequences.
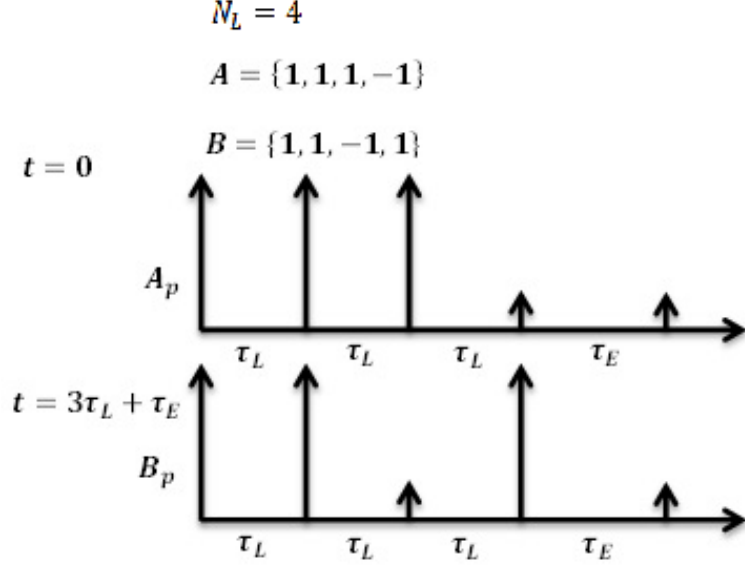
Figure 3.3: Transmitted sequences for the developed unipolar golay coding technique with four pulses in each sequence. Two sequences of pulses out of the original four sequences are transmitted. These two sequences are selected based on the highest number of positive or negative pulses in each main sequence.

To decode the photoacoustic signal, the received two sequences of photoacoustic signals will be cross correlated, one of them with sequence A while the other with sequence B. Then the results of cross correlation are summed together, as given in equation 3.16:

$$y_{dUGC}(k) = ((A_{max}(k)*h_{PA}(k)+n_1(k))*A(-k))+((B_{max}(k)*h_{PA}(k)+n_2(k))*B(-k)), \quad (3.16)$$

where $y_{dUGC}(k)$ is the decoded photoacoustic signal, $A_{max}(k)$ is the received sequence of photoacoustic signals from the highest pulse number of positive or negative sequence A, and $B_{max}(k)$ is the received sequence of photoacoustic signals from the highest pulse number of positive or negative sequence B. This technique of decoding has been utilised by M. Azuma and his colleagues using unipolar and bipolar m-sequences in photoacoustic computer tomography (Azuma *et al.*, 2015). In this photoacoustic com-

puter tomography, unipolar m-sequences achieved 19 dB coded gain when transmitted a 511-bit sequence (Azuma *et al.*, 2015).

The relationship between the code length and the time for receiving all sequences of photoacoustic signals is described by equation 3.17:

$$T_{dUGC} = 2((N_L - 1)\tau_L + \tau_E),\tag{3.17}$$

where T_{dUGC} is the time needed to receive all sequences of photoacoustic waves when using the developed unipolar golay code. The code gain (G_{dUGC}) can be calculated using equation 3.18:

$$G_{dUGC} \approx 10 \log_{10}\left(\frac{N_L}{4((N_L - 1)\tau_L \frac{c}{z_a} + 1)}\right).\tag{3.18}$$

3.4 Simulation Setup

The Monte Carlo simulation (Jacques *et al.*, 2014) was first used with details as shown in figure 3.4 (A). The specifications of the simulation are shown in Table 3.1, and the specifications of the medium and targets are shown in Table 3.2 (Jacques *et al.*, 2014; Jacques, 2014). Light propagation in the medium is shown in figure 3.4 (B) (Jacques *et al.*, 2014).
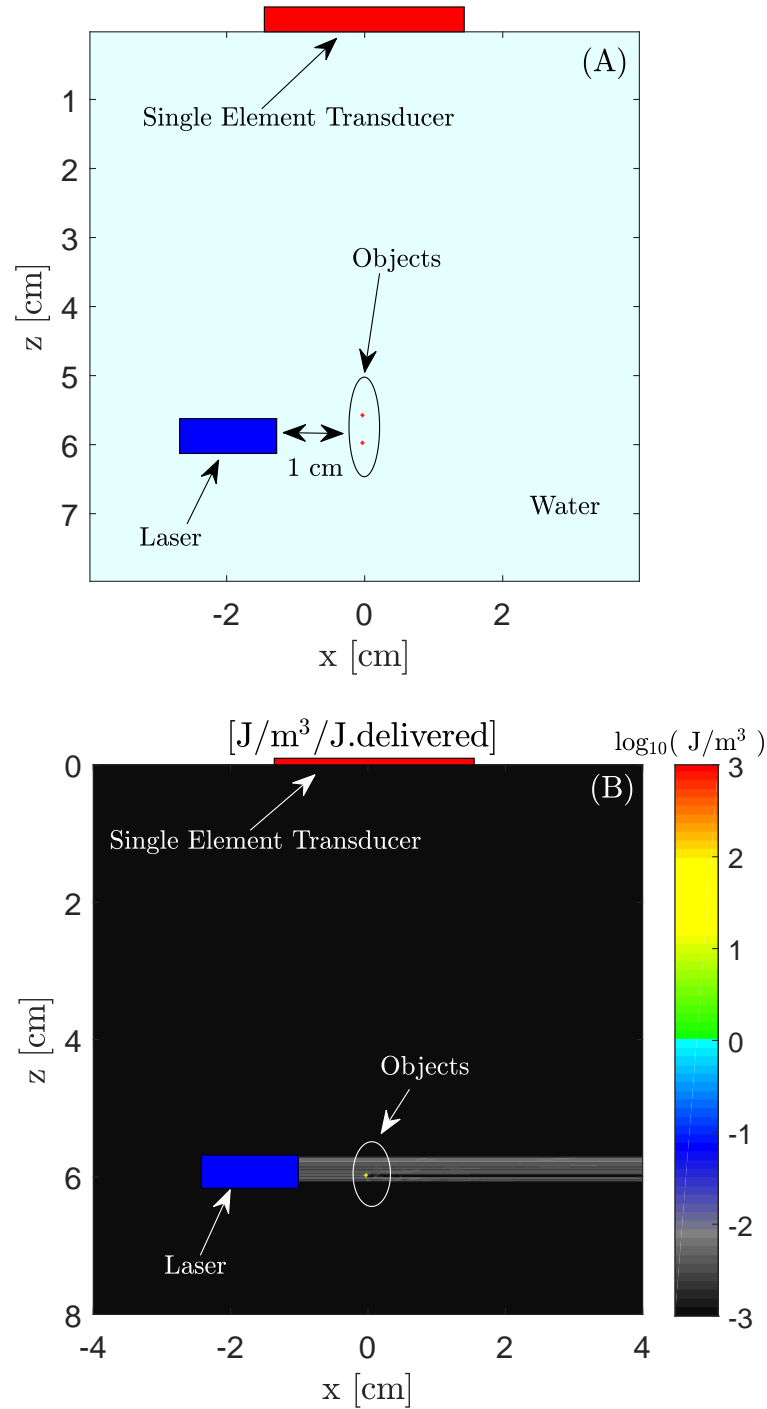
Figure 3.4: (A) Simulation setup for the photoacoustic coded excitation and (B) Absorbed optical energy inside the simulated medium.

Specifications	
Wavelength	905 nm
Diameter of the laser beam	Based on the maximum transmitted energy
Number of bins	400
Bin size	0.02 cm
Simulation time	10 min
Speed of sound (Jacques, 2014)	1500 m/s
Thermal expansion (Jacques, 2004)	$2.29 X 10^{-4} \text{c}^{-1}$
Specific heat capacity (Jacques, 2004)	4184 J/Kg
Density of the target (Jacques, 2004)	1000 Kg/m^3

Table 3.1: Specifications of simulation the propagation of the laser light in the simulated medium.

Water	
Absorption coefficient	0.0004 cm^{-1}
Scattering coefficient	100 cm^{-1}
Anisotropy	1
Tubes	
Radius	200 μm
Absorption coefficient	5.9458 cm^{-1}
Scattering coefficient	55.2 cm^{-1}
Anisotropy	0.9

Table 3.2: Specifications of the simulated medium and targets (Jacques *et al.*, 2014; Jacques, 2014).

The transmitted pulse energy of the laser source should be within the limit of MPE for safety (Laser-Safety, 2014). The wavelength of the laser source was 905 nm. In addition, the pulse duration was 100 ns. The PRF was also 1 MHz and the MPE of the laser source was 0.5 μJ/cm^2. This fluence was calculated when the diameter of the laser spot was 3.5 mm. This resulted in the maximum output energy of 48 nJ per pulse

3. IMPROVED UNIPOLAR GOLAY CODE FOR PHOTOACOUSTIC IMAGING

(Laser-Safety, 2014).

In this simulation, the photoacoustic emission was generated by using the velocity potential technique (Jacques, 2004, 2014; Paltauf *et al.*, 2002). When the distance between the two objects in the Z axis was 0.4 cm, the ideal photoacoustic signal is shown in figure 3.5 (A). There was a large difference between the amplitude of the two photoacoustic signals. This was because the target object that was at a depth of 6 cm absorbed optical light higher than that of the target object, which was at a depth of 5.6 cm. This was due to the size of the laser beam (Diameter = 3.5 mm) used in this simulation, as shown in figure 3.4 (A) and (B). For figure 3.5 (A), the sampling frequency was 7.5 MHz which increased by ten times (75 MHz) as shown in figure 3.5 (B). This increase in sampling frequency improved the accuracy of applying the transducer bandwidth on the signal (Nyquist rate). The ultrasound transducer had a centre frequency of 5 MHz and a bandwidth of 65.29%. Furthermore, the sensitivity of the transducer was 600 mV/MPa. The received photoacoustic signal was amplified by 40 dB as shown in figure 3.5 (C).
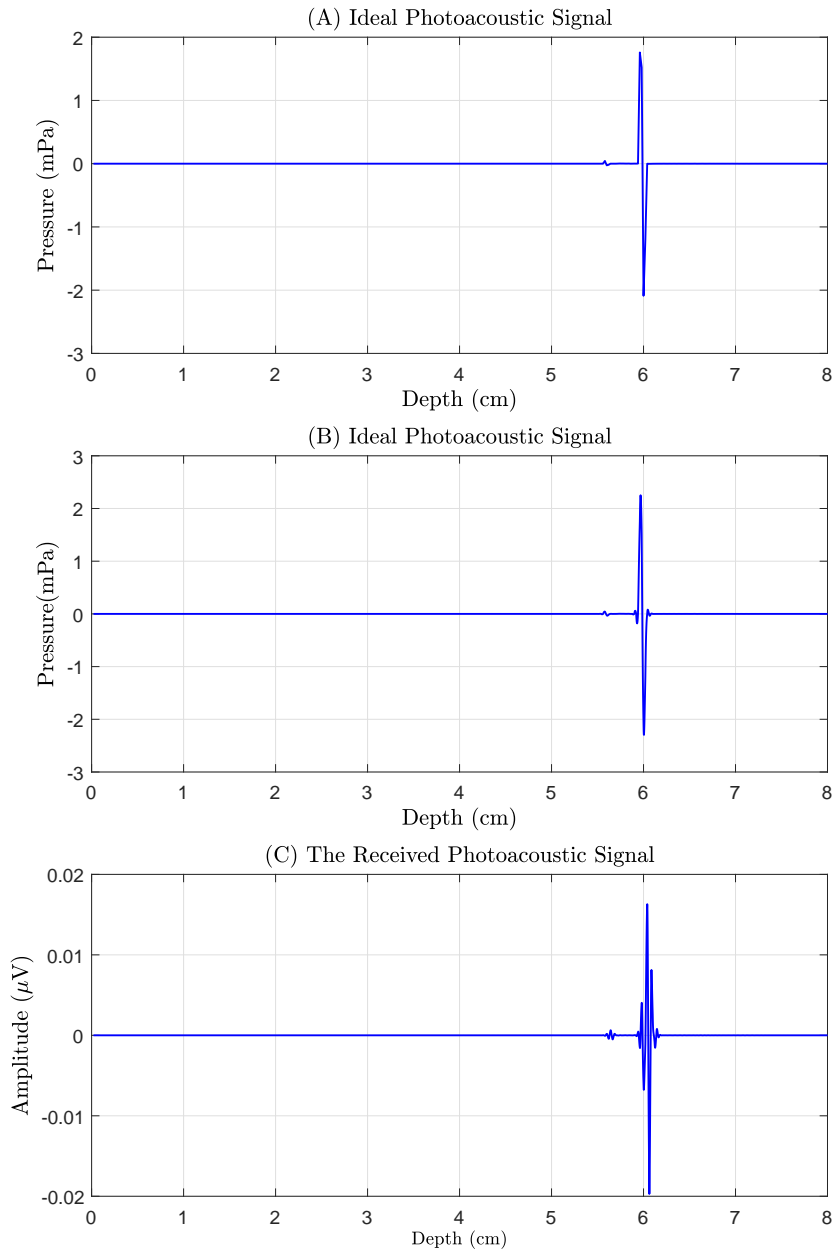
Figure 3.5: (A) Ideal photoacoustic signal when using a sampling frequency of 7.5 MHz, (B) Ideal photoacoustic signal when using a sampling frequency of 75 MHz and (C) Photoacoustic signal amplified by 40 dB and received by a 5 MHz transducer.

3.5 Results and Discussion

The SNR of the received single laser pulse photoacoustic signal from the target at 6 cm depth was assumed to be -10 dB (RMS) as shown in figure 3.6. This assumption was because the optical energy for a single laser pulse should be reduced as the PRF of the laser source is increased. This was for safety purposes (Laser-Safety, 2014). As a result, the photoacoustic signal generated by a single laser pulse was very weak when compared with background noise.
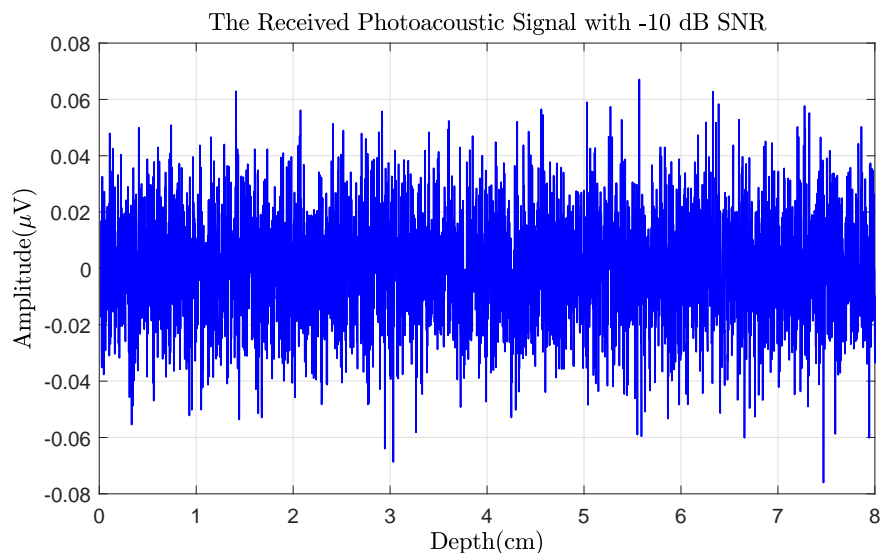
Figure 3.6: Received single laser pulse photoacoustic signal from the target at 6 cm depth with a SNR of -10 dB (RMS).

When using the unipolar golay code with a 512 bit code length, the decoded photoacoustic signal and the equivalent time averaging (Number of averaging is 55) photoacoustic signal are shown in figure 3.7 (A) and (B) respectively. The SNR of these signals were calculated using the root mean square value (RMS) (equation 2.1 (Heinz et al., 2015)). It was found that the unipolar golay code achieved an improved SNR (17.08 dB) when compared to the averaging technique (8.35 dB). These SNRs were calculated for the absorbent which was located at a depth of 6 cm. When the Legendre code sequence with a code length of 639 bits was used, the decoded photoacoustic signal is shown in figure 3.7 (C), with the result of the averaging technique (Number

of averaging is 34) for comparisons (Figure 3.7 (D)). From figure 3.7 (A) and figure 3.7 (C), the unipolar golay code provided the photoacoustic signal with an improved SNR compared against the Legendre code sequence. This is because the unipolar golay code sends two sequences A and B, while the Legendre code sequence transmits one sequence. In addition, the Legendre code sequence produced coded artefacts when compared with the unipolar golay code. These artefacts were within the noise level. The shape of these artefacts is shown in appendix 3. When PPM was used with a code length of 54 bits and $\tau_s = 26.66$ ns, the decoded photoacoustic signals for the coding and averaging techniques (Number of averaging is 3) are shown in figure 3.7 (E) and (F) respectively. PPM achieved a higher SNR with a short code length. For example, when the code length of 54 bits that was the maximum code length to obtain the highest code gain was used, the SNR was 7.4 dB. However, the code length of PPM is limited to obtain a positive code gain due to the time delay.
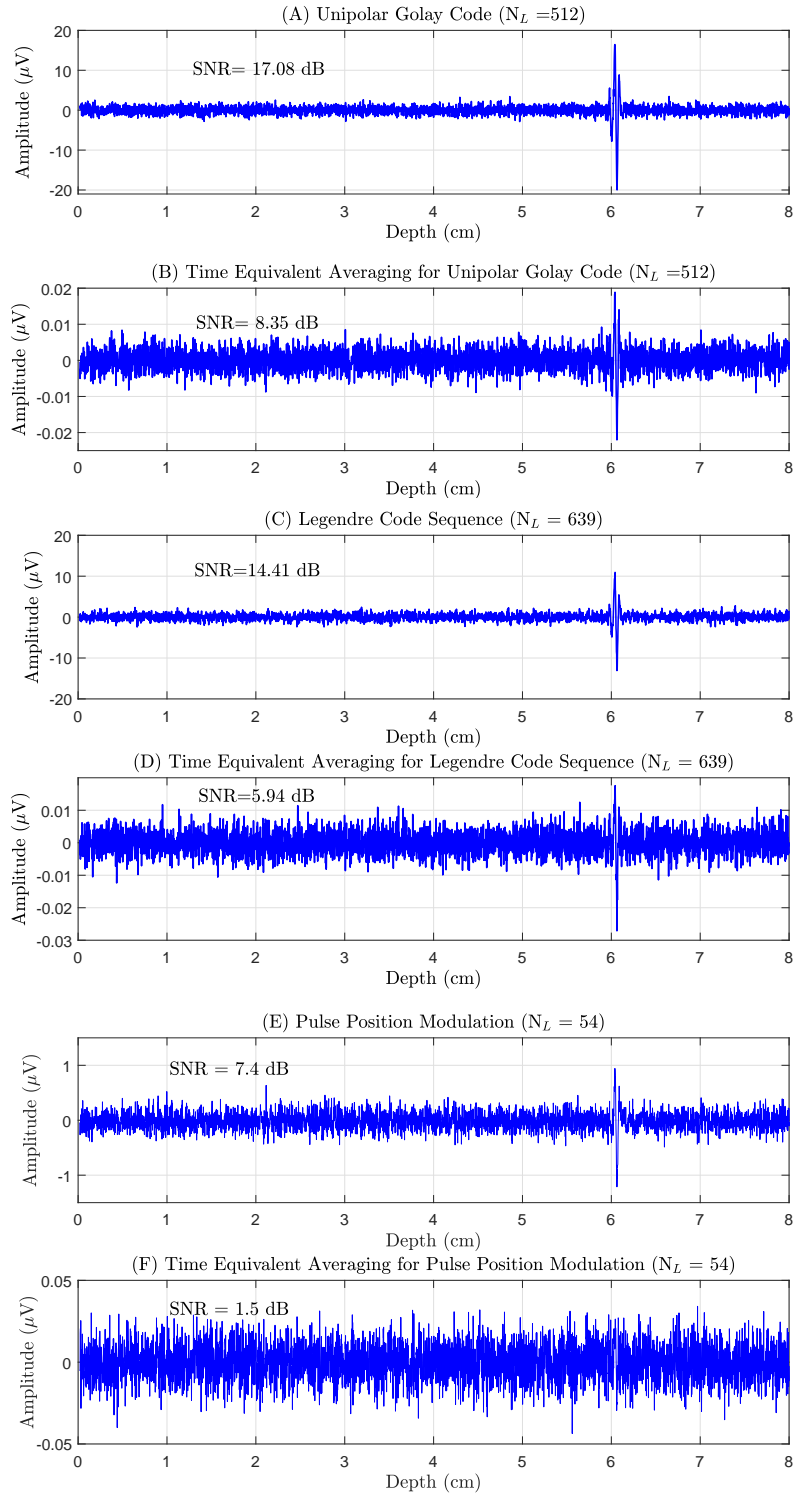
Figure 3.7: Photoacoustic signals that result of coded excitations and time equivalent averaging.

When the developed unipolar golay code was used with a code length of 1024 bits, which is equivalent to the code length of the original unipolar golay code used above, the decoded photoacoustic signals using the coding and averaging techniques (Number of averaging is 53) are shown in figure 3.8. Compared against the original unipolar golay code, it was found that the developed unipolar golay code provided photoacoustic signals with a comparable SNR (17.12 dB). This was due to the coded artefacts that were generated by using the developed unipolar golay code. The coding artefacts were generated due to the cross correlation of two received sequences of photoacoustic signals with four sequences of laser pulses. This cross correlation also enhanced the amplitude of the decoded photoacoustic signal when compared with the original unipolar golay code.
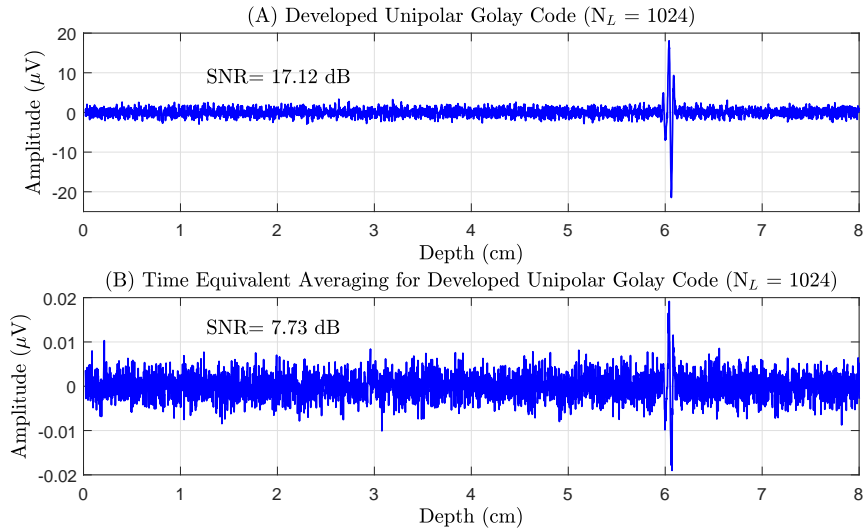
Figure 3.8: The developed unipolar golay code improved the SNR of the photoacoustic signal by 9.39 dB when compared with the averaging technique.

Figure 3.9 shows comparisons between these coded excitation techniques in terms of the code gain and time of receiving all sequences of photoacoustic signals when the SNR (RMS) of the single laser pulse photoacoustic signal was -10 dB. In addition, figure 3.10 illustrates the comparisons between these coded excitation techniques in terms of SNR of the decoded photoacoustic signal and time of receiving all sequences of photoacoustic signals when the SNR (RMS) of the single laser pulse photoacoustic signal was -10

3. IMPROVED UNIPOLAR GOLAY CODE FOR PHOTOACOUSTIC IMAGING

dB. PPM (Simulation) achieved a high code gain (code gain = 6.7 dB) with short consumption time (T = 0.13 msec) compared with other coded excitations, however, the code length in PPM was limited to get a positive code gain. In the simulation results, when the time to receive sequences of photoacoustic waves from these coded excitations was less than 2 msec, the developed unipolar golay code improved the code gain and SNR of the photoacoustic signal relative to the Legendre code sequence and the original unipolar golay code. However, when the time was longer than 2 msec, the original unipolar golay code achieved a slightly higher SNR relative to the developed unipolar golay code. This difference in SNR was due to the artefacts that were produced in the developed unipolar golay code. The code gain and SNR of the photoacoustic signal were still higher for the developed unipolar golay code, if the noise level is higher than the artefact signals produced by using the developed unipolar golay code. The developed unipolar golay code had less acquisition time than the original unipolar golay code. This was because the developed unipolar golay code transmitted only two sequences of pulses. Therefore, the time of flight acoustic signal from the deepest imaging target is needed two times to acquire sequences of the photoacoustic emissions generated by the deepest imaging target. However, in the original unipolar golay code, four sequences of pulses were transmitted. As a result, the time of flight acoustic signal from the deepest imaging target is needed four times to acquire sequences of the photoacoustic emissions generated by the deepest imaging target. By comparing these coded excitations, the developed unipolar golay code reduced the acquisition time by twice the time of the flight acoustic signal from the deepest imaging target (78 μsec) when compared with the original unipolar golay code. This reduction depends on the deepest imaging target.

In the figure 3.9, the theoretical gains were higher than the numerical gains (simulation) for all types of coded excitations. For instance, when the consumption time for receiving sequences of photoacoustic waves from PPM was 0.13 msec, the theoretical gain of PPM was higher than the numerical gain by almost 5.5 dB. This was because, in the theoretical calculation, the effect of the generated artefacts for each coded excitation on the coded gain was not taken into account. This is unlike in the numerical calculation (simulation), which took the effect of artefacts into account. In addition, the fraction number of averaging was rounded up in the numerical calculation (simulation), unlike in the theoretical calculation (Beckmann & Schmitz, 2013). However,

the theoretical calculation provided the first prediction for the coded gain of the coded excitations.
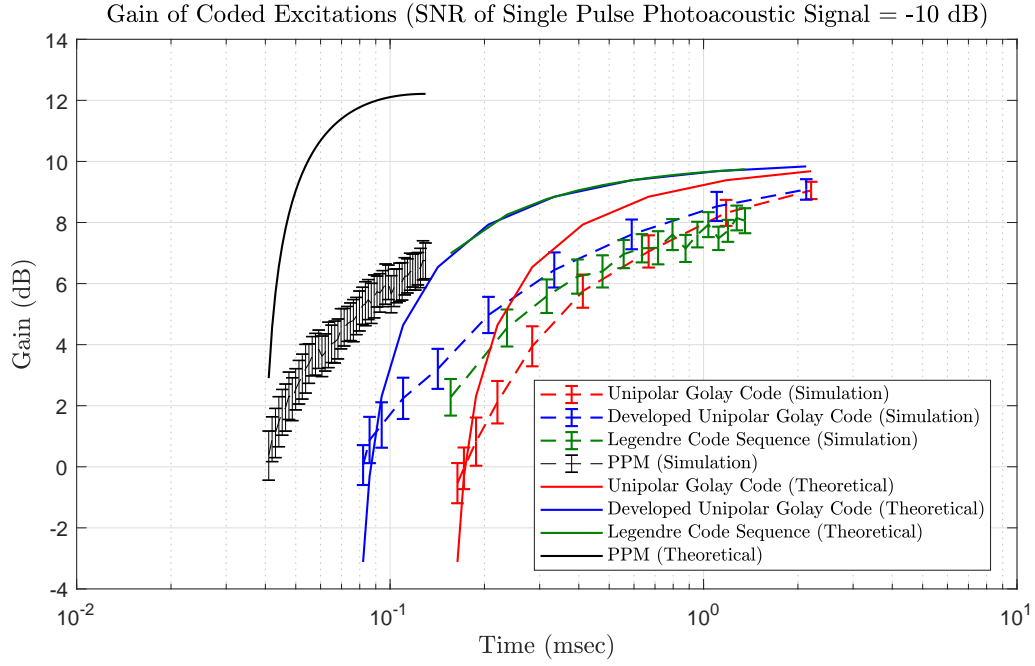
Figure 3.9: Relationship between the time of receiving all sequences of photoacoustic signals and code gain for different coded excitation schemes when the SNR (RMS) of the received single laser pulse photoacoustic signal was -10 dB.
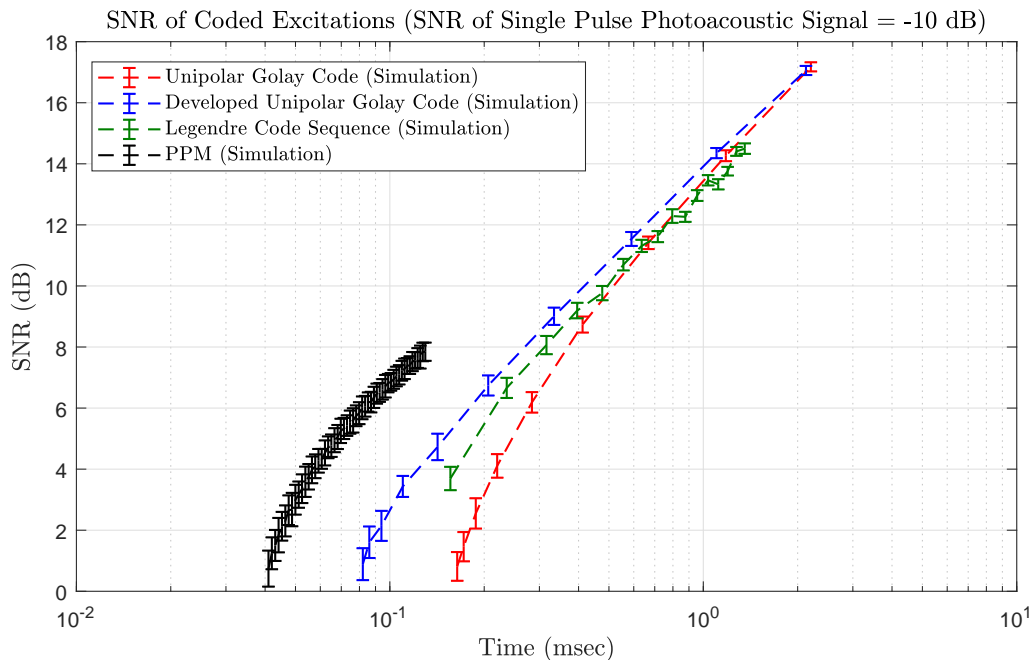
Figure 3.10: Relationship between the time of receiving all sequences of photoacoustic signals and SNR for different coded excitation schemes when the SNR (RMS) of the received single laser pulse photoacoustic signal was -10 dB.

Figure 3.11 shows comparisons between these coding schemes in terms of the code gain and time of receiving all sequences of photoacoustic signals when the SNR (RMS) of the received single laser pulse photoacoustic signal was -15 dB. Figure 3.12 shows comparisons between these coding schemes in terms of the SNR and time of receiving all sequences of photoacoustic signals when the received single laser pulse photoacoustic signal had an original SNR (RMS) of -15 dB. When the consumption time for receiving all sequences of photoacoustic waves from these types of coding schemes was higher than 2 msec, the developed unipolar golay code achieved a higher code gain and SNR compared with the original unipolar golay code with less consumption time. This is because the noise level was higher than the coded artefact signals when using the developed unipolar golay code. In addition, two sequences of laser pulses were only transmitted in the developed unipolar golay code when compared with the original one which reduced the acquisition time by 78 μsec. This reduction depends on the deepest

imaging target.
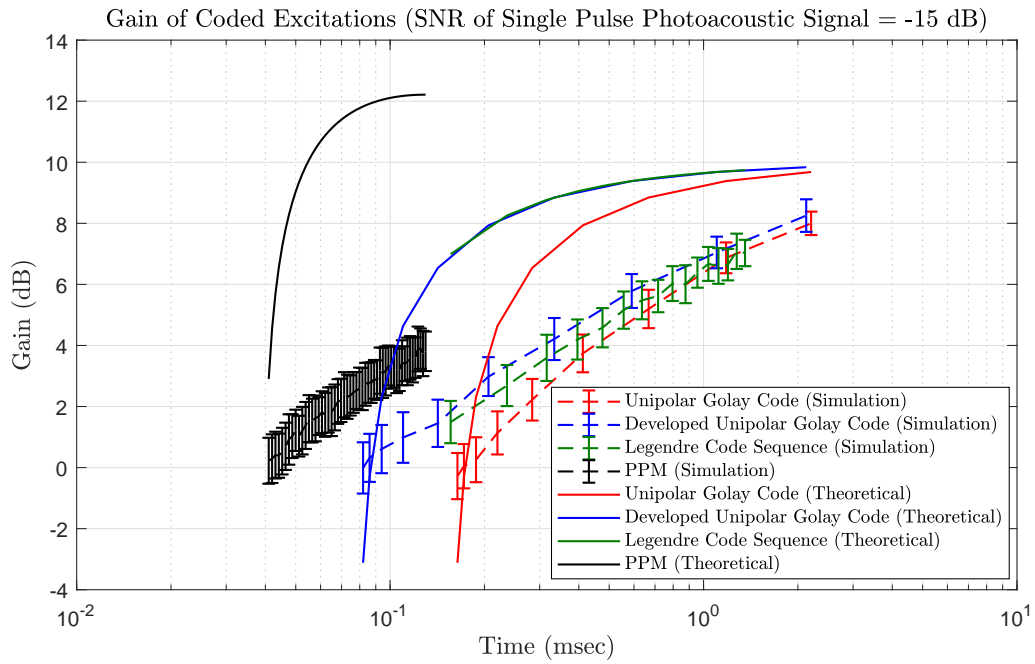
Figure 3.11: Relationship between the time of receiving all sequences of photoacoustic signals and code gain for different coded excitation schemes when the SNR (RMS) of the received single laser pulse photoacoustic signal was -15 dB.
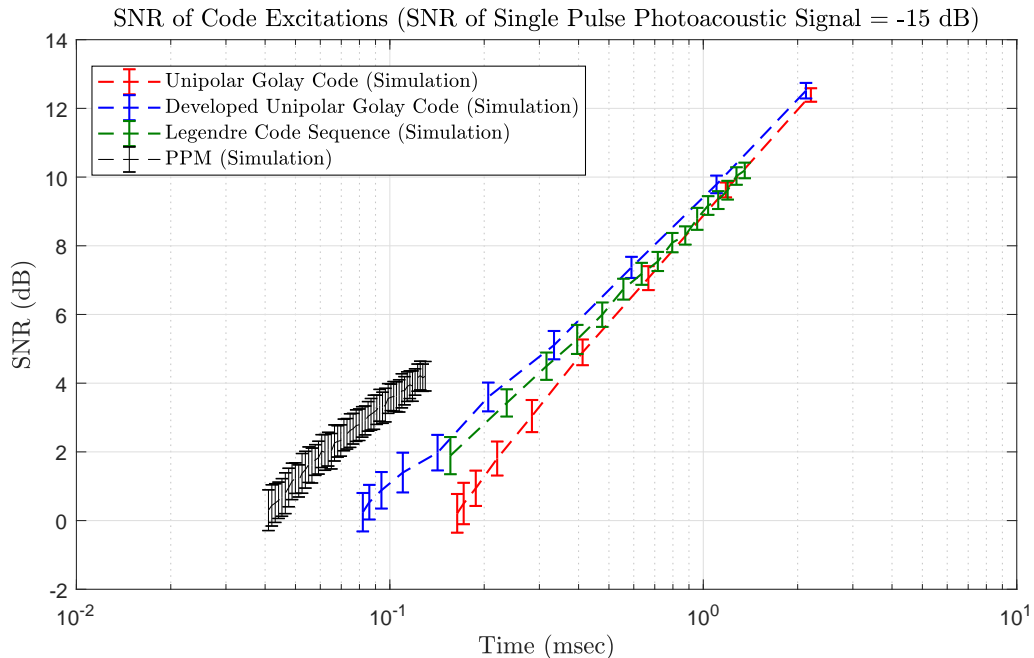
Figure 3.12: Relationship between the time of receiving all sequences of photoacoustic signals and SNR for different coded excitation schemes when the SNR (RMS) of the received single laser pulse photoacoustic signal was -15 dB.

From figure 3.9 and figure 3.11, the difference between the theoretical gains and the numerical gains (Simulation) was increased when the noise level was increased. This was because the theoretical calculation was the ratio between the mean squared error of averaging technique to the mean squared error of coded excitation (Mienkina *et al.*, 2010). Therefore, the noise level did not affect the theoretical calculation (equations 3.6, 3.11, 3.15 and 3.18). However, the output of the cross correlation operation in the coded excitations was more affected by the noise level than the output of avenging technique. As a result, the numerical gains (simulation) were reduced when the noise level was increased.

3.6 Conclusion

In this chapter, unipolar golay code, Legendre code sequence and PPM photoacoustic coded excitation schemes were explained. In addition, the unipolar golay coded exci-

tation was developed to reduce its acquisitions time and produce photoacoustic signals with higher SNR. These coding techniques were simulated and compared. It was found that the code gain and SNR of the developed unipolar golay code was slightly higher than those of the original unipolar golay code when the noise level was high. In addition, the consumption time of the developed unipolar golay code was less than that of the original unipolar golay code by 78 μsec. This reduction of consumption time depends on the deepest imaging target.

Chapter 4

Supporting Photoacoustic Emissions with Ultrasound Signals

Abstract

The shape of the photoacoustic wave is affected by the transducer bandwidth. The optical and ultrasound attenuations limit the imaging depth. To extract a weak photoacoustic emission and recover a large part of the photoacoustic emission, this photoacoustic emission was modulated with ultrasound signals using a linear array transducer in this chapter. Then, the photoacoustic emission was extracted from this modulated signal. This micro-Doppler technique was originally developed for photoacoustic imaging using a dual-element Doppler transducer, and was investigated in this chapter for the first time using a 1-D array ultrasound transducer. The processing was performed based on simulations and experimental measurements. In the simulation, the micro-Doppler technique improved the SNR of the photoacoustic image by 16.18 dB compared with a passive technique. In addition, the low frequency part of the photoacoustic image was recovered using this technique. In the experiment, the micro-Doppler technique enhanced the SNR of the photoacoustic image by 15 dB compared with the passive technique.

4. SUPPORTING PHOTOACOUSTIC EMISSIONS WITH ULTRASOUND SIGNALS

4.1 Introduction

Photoacoustic imaging is used to generate functional and structural information of the biological tissue (Taruttis & Ntziachristos, 2015). It is used to detect cancers, such as breast cancer (Manohar *et al.*, 2007), lymphoma (Kim *et al.*, 2011) and melanoma (Oh *et al.*, 2006), at an early stage. The response of the cancer after treatment and the process of drug delivery can be also monitored using this type of imaging modality (Lao *et al.*, 2008; Rajian *et al.*, 2011) as the generated ultrasound signal, due to the photoacoustic effect, is much less scattered inside the biological tissue when compared with light.

The photoacoustic effect is generated due to thermoelastic expansion of the medium which absorbs optical energy of nanoscale laser pulses (Beard, 2011; Yao & Wang, 2011). The generated photoacoustic emissions that are broadband signals are received by an ultrasound transducer. Then, these received RF signals will be beamformed to generate photoacoustic images. However, some parts of the photoacoustic signals which have frequency components out of the transducer bandwidth will be lost (Chen *et al.*, 2009). In addition, these photoacoustic emissions will be highly attenuated as the depth of the target is increased (Hu & Wang, 2010). The imaging depth is also limited by the transmitted optical energy. All of these will affect the SNR and spatial resolution of the beamformed photoacoustic image. This effect will be increased if the generated photoacoustic emission is weak. Researchers have tried to improve the SNR of the photoacoustic signal by using advanced techniques, for instance, the dual optical pulses technique which has been proposed (Tian *et al.*, 2015). In this method, the first optical pulse is used to change the thermal properties of the medium, whilst the second is used to generate the photoacoustic emission with a higher SNR. Instead, the SNR can be improved by repeatedly retransmitting the reflected laser light from the skin layer by using a reflective surface (Wang *et al.*, 2012). The accumulated optical energy reaching the imaging target will be finally increased, improving the SNR and imaging depth. Gao *el al.* have investigated the Doppler effect to increase the SNR of the photoacoustic emission (Gao *et al.*, 2016). In this technique, a dual-element Doppler transducer is used to detect the micro-Doppler frequency shift due to the vibration of the target as a result of thermoelastic expansion. Then, the photoacoustic emission is extracted by using frequency demodulation. McLaughlan *el al.* have carried the photoacoustic

emission with ultrasound signals to activate the nanorods with a lower laser fluence that can create bubbles (McLaughlan *et al.*, 2014). As a result, the SNR of the photoacoustic image was enhanced by overlapping ultrasound signals and photoacoustic emissions.

In this chapter, the lost parts of the photoacoustic signal as a result of the finite transducer bandwidth are recovered using the micro-Doppler technique. Here, a linear array transducer was used instead of a dual-element Doppler transducer that was used in the original micro-Doppler technique (Gao *et al.*, 2016). In addition, the effect of the micro-Doppler technique in photoacoustic image will be presented, unlike the original micro-Doppler technique that was only studied on a photoacoustic signal. This chapter is organised as follows: first, the theoretical analysis of micro-Doppler technique. Second, a comparison between passive technique and micro-Doppler technique based on simulation software in terms of SNR and recover the lost parts of photoacoustic image. Third, a comparison between passive technique and micro-Doppler technique based on experiments in terms of SNR and recover the lost parts of photoacoustic image. Finally, a discussion and conclusion.

4.2 Methods

4.2.1 Ultrasound Doppler Shift

The Doppler shift technique is used to measure the speed and direction of blood flow inside the blood vessel (Wells *et al.*, 1977). In this technique, continuous ultrasound waves can be transmitted with a certain angle relative to the blood vessel. The ultrasound wave is reflected back when it reaches the blood cells and detected by a separate transducer. Based on the frequency shift (f_d) of the received ultrasound signal, when compared with the centre frequency of the transmitted one (f_t), the direction and the speed (V) of the blood cell motion can be determined using equation 4.1 (Hoskins *et al.*, 2010):

$$f_d = \frac{2 f_t V \cos \theta}{C}, \tag{4.1}$$

where θ is the angle between propagation direction of the ultrasound beam and blood vessel and C is the speed of sound inside the biological tissue.

4.2.2 Supporting Photoacoustic Emissions with Ultrasound Signals

The photoacoustic emission can be modulated by ultrasound signals for an improved
SNR and enhanced imaging depth (Gao *et al.*, 2016). In this technique, a linear array
transducer is used to generate the micro-Doppler shift. This transducer transmits
ultrasound signals during the generation of photoacoustic emissions. As a result, the
frequency of the transmitted ultrasound signal will be shifted based on the vibration
of the blood vessel wall due to thermoelastic expansion, as shown in figure 4.1 (Gao
et al., 2016).
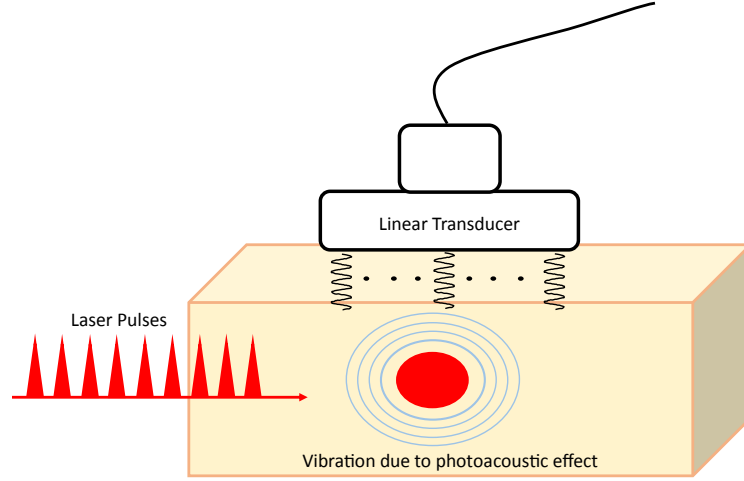
Figure 4.1: Supporting photoacoustic emissions with ultrasound signals. The ultra-
sound signals are kept transmitted when generating the photoacoustic emissions.

The vibration of the blood vessel is related to the derivative of the photoacoustic wave
with time as given in equation 4.2 (Gao *et al.*, 2016):

$$V_{PH} = k_s R_d \frac{\partial P(t)}{\partial t},\tag{4.2}$$

where V_{PH} is the vibration of the blood vessel due to thermoelastic expansion, k_s
is adiabatic compressibility, R_d is the diameter of the blood vessel and $P(t)$ is the
generated photoacoustic signal with time.

The frequency shift of the carrier signal (supporting ultrasound signal) depends on the change of the amplitude of the carried signal (photoacoustic emission). As shown in figure 4.2, the photoacoustic emission will be generated when the supporting signal (ultrasound signal) reaches the target object. As a result, the generated photoacoustic emission will be modulated with the ultrasound signal. This modulated signal, which has micro-Doppler components, is received by an ultrasound transducer with noise (from the electronic components). The relationship between the micro-Doppler signal and the photoacoustic emission is described by equation 4.3 (Gao *et al.*, 2016):

$$f_{mic-d} = \frac{2f_o k_s R_d}{C} \frac{\partial P(t)}{\partial t} \cos\theta, \tag{4.3}$$

where f_{mic-d} is the frequency shift of the micro-Doppler signal, and f_o is the frequency of the carrier signal. To extract the photoacoustic emission from the modulated signal, the received signal is multiplied by the carrier signal with a 90-degree phase shift as explained in equation 4.4 (Gao *et al.*, 2016):

$$M_{mic-d} = A_{mic-d} A_R \sin(2\pi(f_o + f_{mic-d})t) \cos(2\pi f_o t), \tag{4.4}$$

where A_R is the amplitude of the carrier signal with a 90-degree phase shift, and A_{mic-d} is the amplitude of the modulated signal. This multiplication down converts the micro-Doppler signal, as shown in Appendix (4). To extract the photoacoustic signal, a low-pass filter and small angle approximation are employed (Gao *et al.*, 2016). This technique reduces the effect of the limited transducer bandwidth as the generated photoacoustic signal is modulated by an ultrasound signal before being received by the ultrasound transducer. In addition, the effect of ultrasound attenuation on the generated photoacoustic signal is reduced. This is because the amplitude of the photoacoustic signal (Vibration of the target image) is modulated by the ultrasound signal (Carrier signal) (Gao *et al.*, 2016). This differs from the photoacoustic emission that is directly received by an ultrasound transducer (passive technique) as shown in figure 4.3.
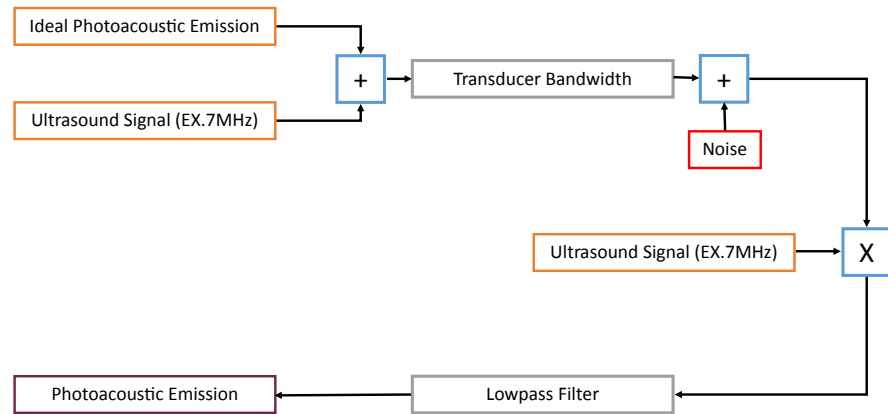
Figure 4.2: Extracted photoacoustic emission from the modulated signal.
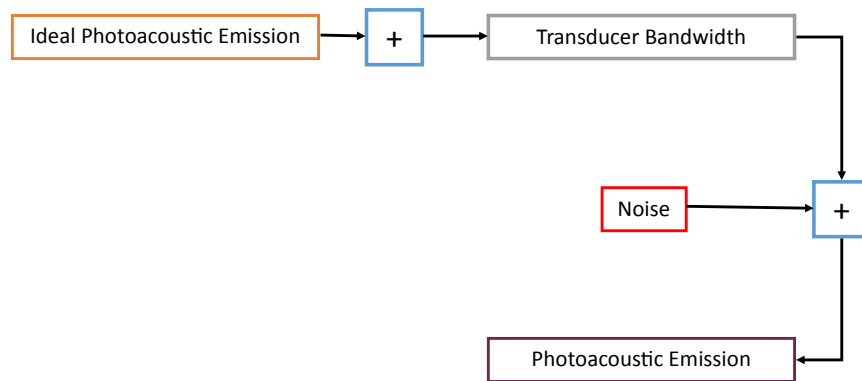
Figure 4.3: Received photoacoustic emission by using the passive technique.

4.3 Simulation Setup

The K-wave toolbox was used to simulate the photoacoustic emissions from a single
point with a diameter of 1 mm at depth of 30 mm from the linear array transducer, as
shown in figure 4.4 (Treeby & Cox, 2010; Treeby *et al.*, 2016). The specifications of the

transducer were the same to those of a Verasonics L11-4v transducer as shown in Table 4.1. The frequency of the carrier signal was 7 MHz. The speed of sound was set to be 1520 m/s. In this simulation, after the photoacoustic emissions were extracted from modulated signals, the photoacoustic image was reconstructed using the DAS beamforming technique. The image was then compared with the passive technique in terms of SNR and the structure of the target. The analysis and beamforming were done using MATLAB (R2014a, MathWorks).
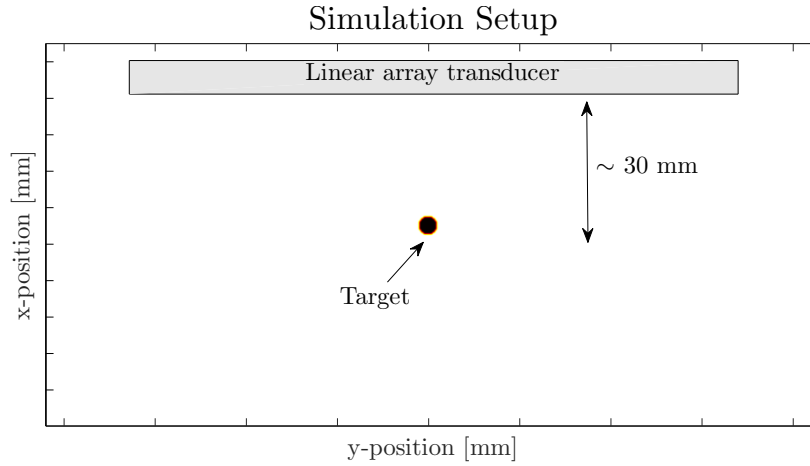
Figure 4.4: Simulation setup. The ultrasound signals were generated to reach the point target when the photoacoustic emissions were produced from. The depth of the target was 30 mm from the linear array transducer.

Verasonics L11-4V	
Center Frequency	7.5 MHz
Bandwidth (-6 dB)	90.8 %
Pitch Size	0.3 mm

Table 4.1: Specifications of the linear array transducer.

4.4 Simulation Results

In this simulation, continuous ultrasound waves were transmitted when the photoacoustic emissions were generated. The transmitted ultrasound waveform is shown in

4. SUPPORTING PHOTOACOUSTIC EMISSIONS WITH ULTRASOUND SIGNALS

figure 4.5 (A). When the photoacoustic emission was generated, as shown in figure 4.5 (B), the micro-vibration of the point target created the micro-Doppler effect on the continuous ultrasound wave based on equation 4.3, as shown in figure 4.5 (C). The solid black rectangle highlights the location of the micro-Doppler signal. This micro-Doppler technique changed the frequency of the carrier signal based on the amplitude of the generated photoacoustic emission (Gao *et al.*, 2016). Figure 4.5 (D) shows the down conversion of the micro-Doppler signal by multiplying the modulated signal (sine wave) with the reference signal whose phase was shifted by 90 degrees (cosine wave). The solid black rectangle shows the location of the micro-Doppler signal in the down conversion signal. The frequency-domain representation of the down conversion signal is shown in figure 4.6 (A). The carrier signal was up converted to 14 MHz. This carrier signal will be removed using low-pass filtering (Cutoff frequency : 10 MHz). After the low-pass filter and small angle approximation were applied to the modulated signal, the photoacoustic emission is shown in figure 4.5 (E). It was established that some frequency components of the photoacoustic emission that were out of the transducer bandwidth were detected using the micro-Doppler technique. This is because the generated photoacoustic emission was modulated with ultrasound signals before being received by the ultrasound transducer. This received modulated signal, that carries large parts of photoacoustic emissions, is not significantly affected by the transducer bandwidth. Figure 4.5 (F) shows the photoacoustic emission that was received using the passive technique. By using the passive technique, the low-frequency parts of the signal were missing due to the finite transducer bandwidth as shown in figure 4.6 (C). In the frequency domain, figure 4.6 (B) and (D) show the photoacoustic emission obtained with the micro-Doppler technique and the ideal photoacoustic emission respectively. From these figures, most parts of the photoacoustic emission were recovered when using the micro-Doppler technique, however, the high-frequency part was lost due to low-pass filtering. This is because the photoacoustic signal was a broadband signal. In addition, this low-pass filter had high attenuation at 10 MHz frequency to remove the effect of the up conversion carrier signal on the extracted photoacoustic signal. The frequency response of the low-pass filter is shown in figure4.7. The attenuation at the cut-off frequency (Normalized Frequency = 0.25 π rad/sample) was -3 dB. The attenuation at 14 MHz (Normalized Frequency = 0.35 π rad/sample) was -82 dB. In addition, the

attenuation before the cut-off frequency (Normalized Frequency = 0.2 π rad/sample) was almost 0 dB.
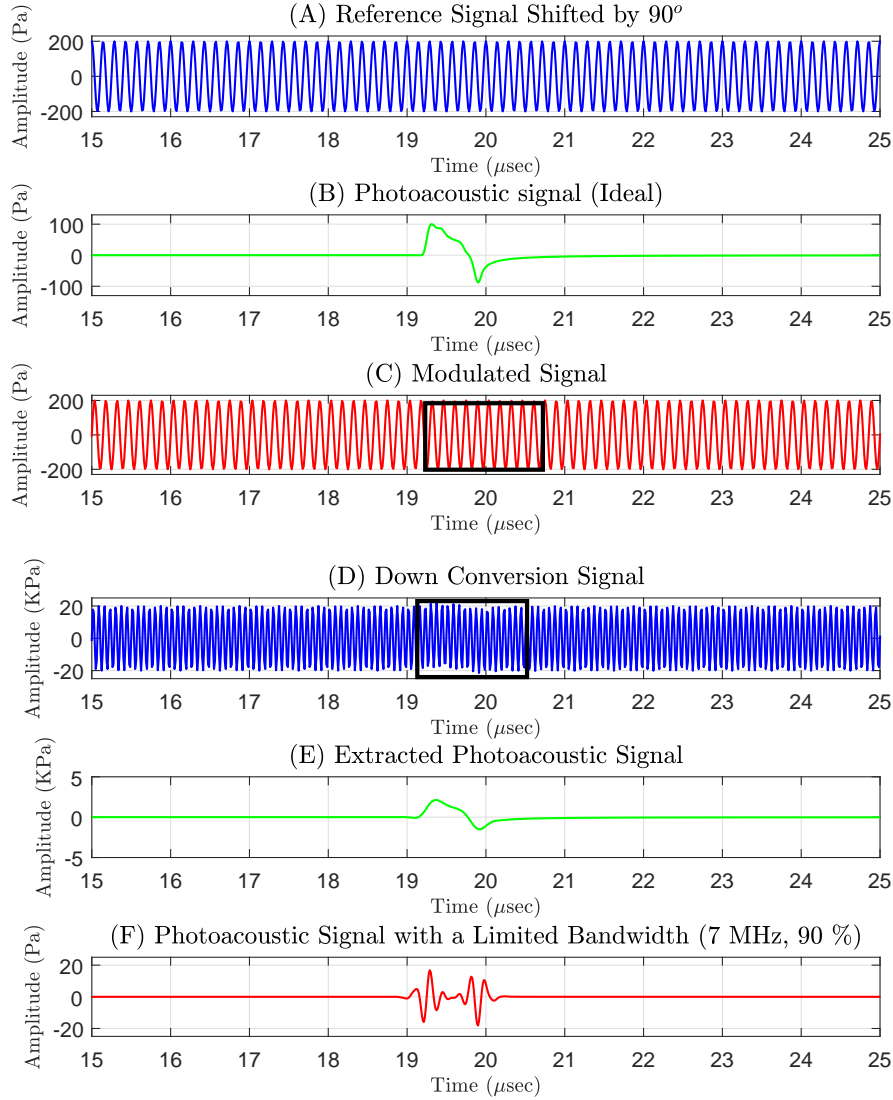
Figure 4.5: (A) Signal achieved by shifting the reference (carrier) signal with a 90-degree phase difference. The frequency of this signal was 7 MHz. (B) Ideal photoacoustic signal. (C) The modulated signal for the photoacoustic emission that was shown in the solid black rectangle.(D) The down conversion signal by multiplying the modulated signal with the reference signal shifted with a 90-degree phase difference. (E) Extracted photoacoustic emission. (F) Received photoacoustic emission with a finite bandwidth (7 MHz, 90%) by using the passive technique.
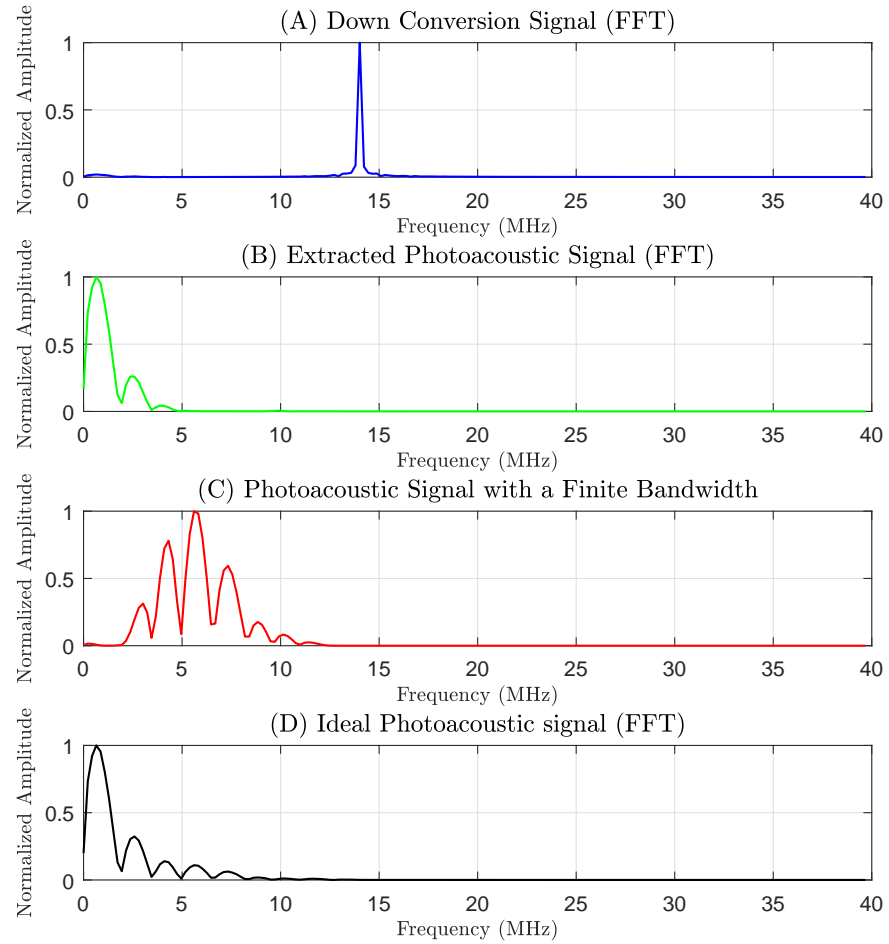
Figure 4.6: (A) Down conversion signal, (B) extracted photoacoustic emission, and (C) ideal photoacoustic emission in the frequency domain.
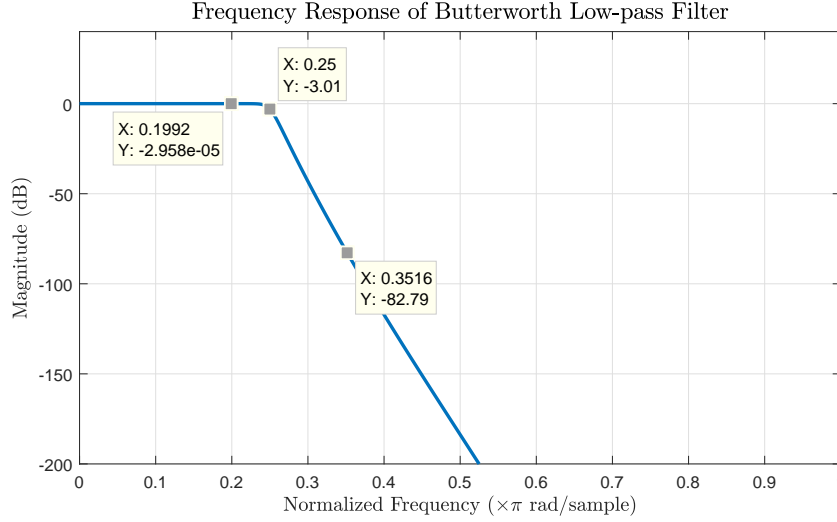
Figure 4.7: Frequency response of Butterworth low-pass filter.

The ideal photoacoustic image of the absorption point is shown in figure 4.8 (A). The transducer bandwidth was assumed infinite, which results in beamforming all parts of the image. This differs from the case with a finite bandwidth (figure 4.8 (B)). In this figure, the image target consists of two parts as the low frequency part of the signal was out of the transducer bandwidth. Figure 4.8 (C) illustrates the photoacoustic image resulting from the micro-Doppler technique. Most parts of the photoacoustic emissions were recovered and beamformed. By comparing figure 4.8 (A) with figure 4.8 (C), the photoacoustic image from the micro-Doppler technique is comparable with the ideal photoacoustic image. This was because the frequency parts of the generated photoacoustic signal were saved by modulating the amplitude of the generated photoacoustic signal by ultrasound signal. However, some high frequency parts were lost due to the down conversion filter when extracting photoacoustic emissions.
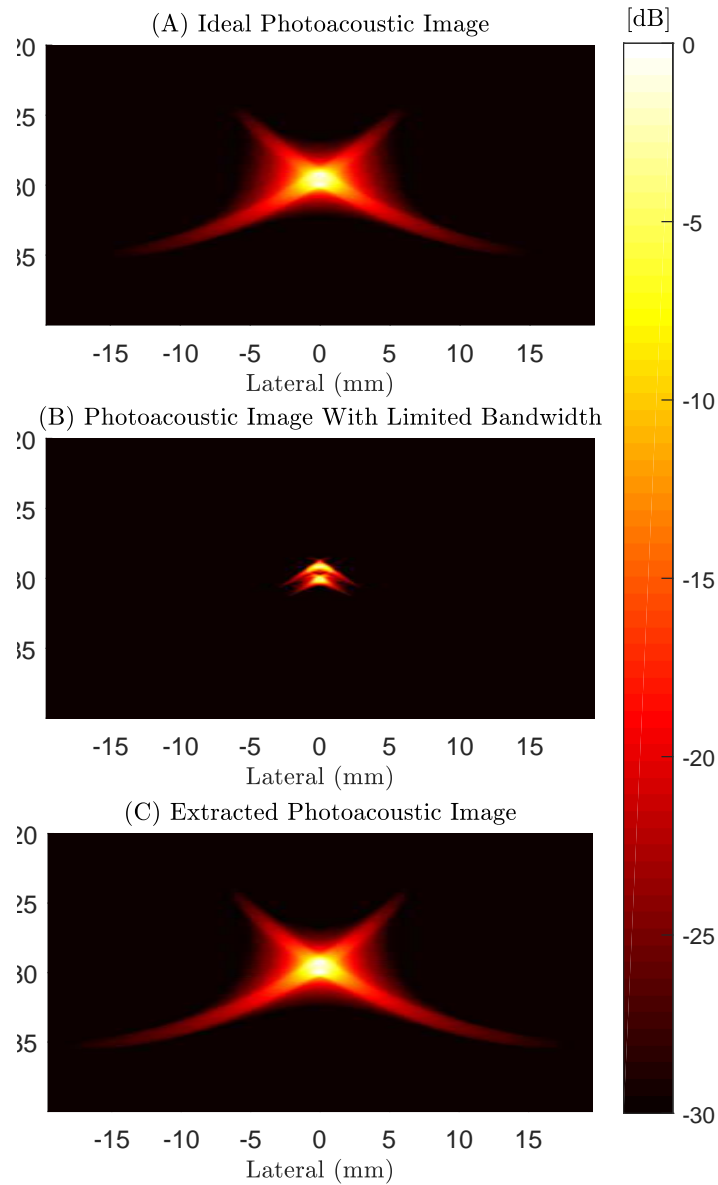
Figure 4.8: (A) Ideal photoacoustic image beamformed using the broadband transducer. (B) Photoacoustic image when using the transducer with a finite bandwidth (Centre frequency: 7.5 MHz. -6 dB Bandwidth: 90.8 %). (C) Photoacoustic image beamformed from the demodulated signals when using the transducer with a finite bandwidth (Centre frequency: 7.5 MHz. -6 dB Bandwidth: 90.8 %). Dynamic range: 30 dB.

In this simulation, noise was added to the photoacoustic emissions with a SNR

(Peak) of 0 dB using a K-wave toolbox (Treeby & Cox, 2010; Treeby *et al.*, 2016) to study the benefit of the micro-Doppler technique for photoacoustic imaging. Figure 4.9 (A) shows the photoacoustic image when having a finite transducer bandwidth. The background noise was significantly high but was reduced when the micro-Doppler technique was used (Figure 4.9 (B)). The SNR of these images were calculated using equation 4.5 (Wang *et al.*, 2017):

$$SNR_{dB} = 20\log_{10}(\frac{\mu_{Signal}}{\sigma_{background}}), \tag{4.5}$$

where μ_{Signal} is the mean of the signal and $\sigma_{background}$ is the standard deviation of the background noise. In figure 4.9 (A), the dashed rectangle number 1 and number 2 show the signal and the background noise areas used for the SNR calculation, respectively. The SNR when having a finite transducer bandwidth was 11.74 dB, while by using the micro-Doppler technique, this SNR was improved by 16.18 dB (SNR = 27.92).
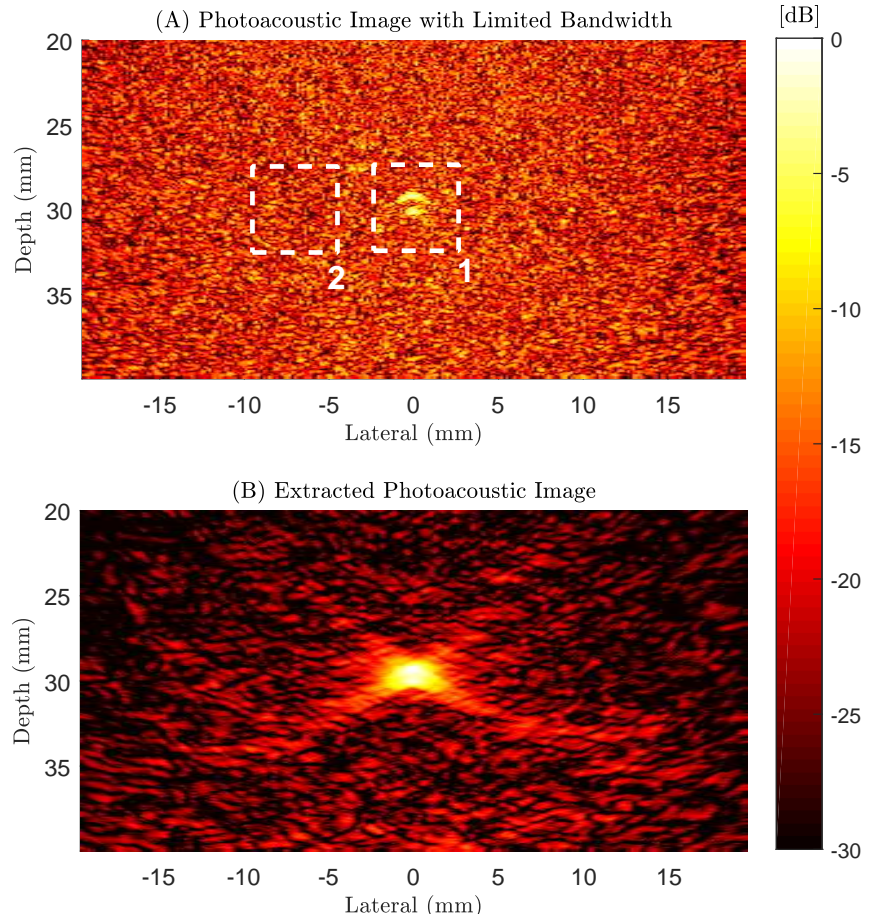
Figure 4.9: (A) Photoacoustic image when having a finite transducer bandwidth. (B) Photoacoustic image beamformed from the demodulated signals. Centre frequency: 7.5 MHz. -6dB Bandwidth: 90.8 %. SNR (Peak) of the RF signals: 0 dB. Dynamic range: 30 dB.

4.5 Experimental Setup

In the experiment, a tube (Cole.parmer 06422.02) made from pharmaceutical-grade thermoplastic materials was filled with black Indian ink (brianclegg, Drawing Ink) as shown in figure 4.10. The internal and outer diameters of this tube were 1.6 and 3.2 mm, respectively. The absorption coefficient of the ink was 5 cm^{-1} at the wavelength of 905 nm. The Nd:YAG laser was used to generate laser pulses with OPO to tune the wavelength of the laser pulse. The laser output was guided to the tube phantom through

a fibre optic (Ceram Optec, 03592-REV.A). The wavelength and fluence of the laser pulse were 905 nm and 0.8 mJ/cm^2, respectively. For the micro-Doppler technique, 25-cycle sinusoidal waves with a centre frequency of 7 MHz were transmitted to the tube. The peak amplitude of the sinusoidal waves was 1V. The pressure that these waves generated was almost 10 KPa. These waves reached the target when the photoacoustic emissions were generated. The RF signals were detected by 128 elements linear array transducer (L11-4v) and acquired simultaneously using the Ultrasound Array Research Platform II (UARP II) (Cowell *et al.*, 2013; Harput *et al.*, 2013; Smith *et al.*, 2012, 2013). The sampling frequency was set to 80 MHz. These RF signals were then transferred to a local PC and processed using MATLAB (R2014a, MathWorks). To improve the SNR of RF signals, they were averaged by 100 times.
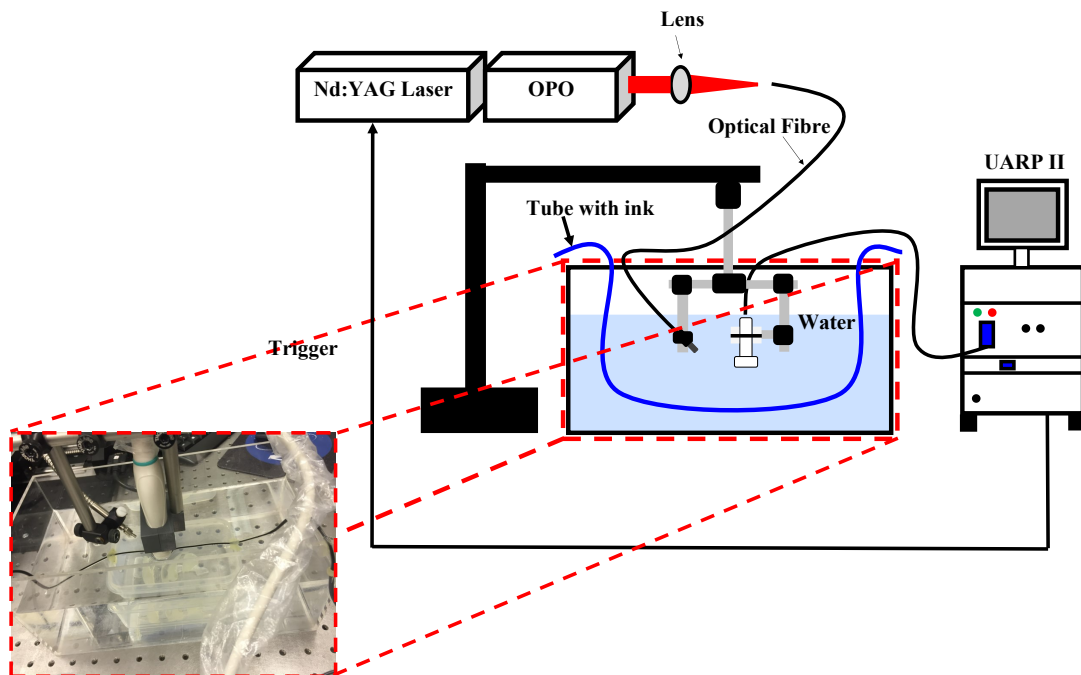
Figure 4.10: Experiment setup for investigating the micro-Doppler technique.

4.6 Experimental Results

The photoacoustic image was generated by using the passive technique together with DAS beamforming, as shown in figure 4.11 (A). Before beamforming, the RF signals

were bandpass filtered (4 MHz - 11 MHz) to reduce noise. In this image, the background noise was high as the fluence of the firing laser was relatively low (0.8 mJ/cm^2). This low fluence was used to study the effect of the micro-Doppler technique on the SNR of the photoacoustic image, especially when a low optical energy source, such as PLD, is used. There was a specific pattern for the background noise in this image. This was because there was a coherent noise between each group of 16 channels. The main source of this noise was the hardware of time gain compensation (TGC). The SNR of this image was 9 dB. In this calculation, the dashed rectangle number 1 and number 2 represented the signal and background noise regions, respectively.

To experimentally apply the micro-Doppler technique by using a linear array transducer, some modifications are needed to extract the micro-Doppler signals. First, the carrier signal was a 25-cycle sinusoid wave in this experiment. To down convert the micro-Doppler signal, the modulated signal should be multiplied with the carrier signal shifted with a 90-degree phase difference (cosine wave). However, a cosine wave cannot be experimentally generated due to the finite transducer bandwidth. This was because that by using finite transducer bandwidth, the generated signal cannot start with a peak amplitude. This was unlike the sine wave, which starts with zero amplitude. Therefore, to down convert the micro-Doppler signal, the modulated signal was multiplied with the carrier signal without shifting (sine wave). The carrier signal was the echo from the target without firing the laser. The mathematical analysis for extracting the photoacoustic emission is shown in Appendix (5).

By experimentally using a linear array transducer in the micro-Doppler technique, the number of transmitted cycles of the sinusoidal wave was limited. The number of transmitted cycles in this experiment was 25 and, as a result, the frequency spectrum of the carrier signal will be broad. To remove the effect of this broad signal in the extracted photoacoustic emission, this carrier signal was multiplied with itself (down converting the broadband spectrum). Then, this signal was demodulated with the steps as given in Appendix (5). By subtracting the extracted broadband signal of the carrier from the extracted photoacoustic emission, the artefact in the photoacoustic image was reduced, as shown in figure 4.11 (B). By using this technique, the SNR improved by 15 dB when compared with that from the passive technique. This SNR was calculated using the same steps used when calculating the SNR with the passive technique. This

improvement in SNR was due to the generated photoacoustic emissions being modulated by ultrasound signals before being received by the ultrasound transducer. These modulating signals saved the photoacoustic emissions from attenuation. As a result, the photoacoustic emissions were higher than the noise level after being extracted from the modulated signals (Gao *et al.*, 2016). In figure 4.11 (B), there are artefacts due to the reflection of the photoacoustic emission from the tube wall. For example, there was an artefact at a depth of around 26 mm. This was because the reflection of the photoacoustic signal from the outer diameter of the tube that was 3.2 mm. As a result, this artefact was presented at around 6 mm depth from the target signal. In addition, there were reflected signals every ~1 mm between 21 mm and 26 mm depth. This was a result of the mismatching acoustic impedance and ultrasound speed between the target (Ink) and the wall of the tube, whose thickness was 1.6 mm. When the laser pulse was not fired, there was no photoacoustic information extracted, as shown in figure 4.11 (C).
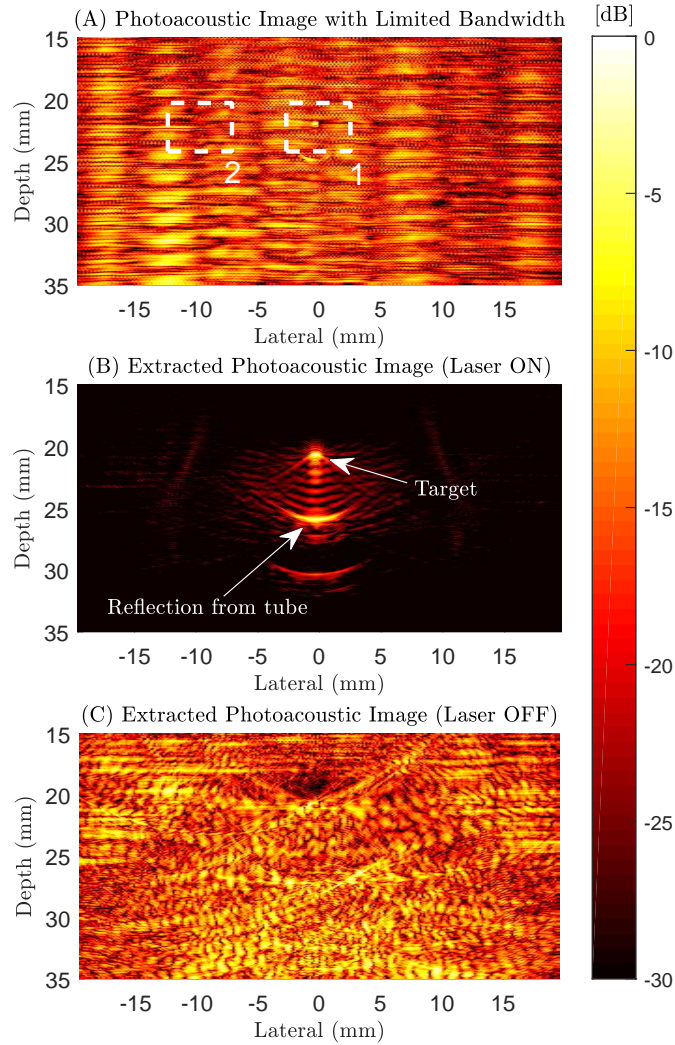
Figure 4.11: Photoacoustic image of the tube filled with ink using (A) the passive technique (Laser ON), (B) the micro-Doppler technique (Laser ON) and (C) the micro-Doppler technique (Laser OFF). Dynamic range: 30 dB.

4.7 Discussion

In the simulation, the lost parts of the photoacoustic emissions were recovered and the background noise was significantly reduced by using the micro-Doppler technique. This was because the micro-Doppler technique converted the amplitude of the generated photoacoustic signal to a frequency shift in the carrier signal. This means that the photoacoustic signal was less affected by transducer bandwidth and ultrasound at-

tenuation (Gao *et al.*, 2016). There were some assumptions in simulation that cannot be experimentally applied using a linear array transducer. For example, the carrier signal was assumed a continuous wave (CW), which cannot be experimentally generated using a linear array transducer. This was because the linear array transducer is not designed to transmit CW that can damage the transducer. In the experiment, the duration of the transmitted ultrasound wave was 3.57 μsec. The performance of the micro-Doppler technique will be improved as much as when increasing the number of transmitted cycles. This results in reducing the width of the frequency spectrum of the carrier signal. In addition, the micro-Doppler signal was down converted by multiplying the modulated signal with the carrier signal shifted with a 90-degree phase difference. This cannot be experimentally achieved due to the finite transducer bandwidth. This was because that when the carrier signal was a sine wave that starts with zero amplitude, the carrier signal with 90-degree phase difference was a cosine wave. This cosine wave cannot be generated by using a finite bandwidth linear array transducer. This was because the cosine wave started with a peak amplitude. Instead, the micro-Doppler technique was experimentally investigated with some modifications in extracting signals (Appendix (5)). The experimental results show that weak photoacoustic signals (Figure 4.11 (A)) can be enhanced by using this technique, as shown in figure 4.11 (B). This technique enhanced the SNR of the image by 15 dB compared with the passive technique. This was because that, with the micro-Doppler technique, the amplitude of the generated photoacoustic signal was converted to a frequency shift in the carrier signal. As a result, the photoacoustic signal was less effected by ultrasound attenuation. This was unlike the photoacoustic signal which was received by using the passive technique (Gao *et al.*, 2016). However, the low-frequency part was not significantly recovered by using experimentally micro-Doppler technique. This is because the bandpass filter that was used to extract the DC part of small angle approximations affected the low frequency part of the extracted photoacoustic emission. This imaging technique could increase the imaging depth especially when the output optical energy of the laser source is low, such as PLD. In future work, the effect of the DC part of the small angle approximation will be reduced by applying windows to the carrier signals rather than applying a bandpass filter. In this technique, to generate the carrier signal with 90-degree phase shift, the cycle number of the carrier signal will be increased and the time of the transmitted carrier signal will be delayed to create 90-degree phase

difference. In addition, the effect of the increasing number of cycles on the extracted micro-Doppler signal will be reduced by applying windows to the carrier signals with 90-degree phase difference to attenuate the extra number of cycles.

4.8 Conclusion

In this chapter, the micro-Doppler technique was applied to photoacoustic imaging by using a linear array transducer. In the simulation, most frequency parts of photoacoustic emissions were recovered. In addition, the background noise was noticeably reduced. In the experiment, the SNR of the photoacoustic image was improved by 15 dB when the micro-Doppler technique was used. The low-frequency part was not recovered in the experiment due to the bandpass filter that was used to remove the DC part of the small angle approximation. In future work, the effect of the DC part of small angle approximation will be reduced by applying windows on the carrier signals rather than applying a bandpass filter.

Chapter 5

Photoacoustic Imaging with Filter Delay Multiply and Sum Beamforming Technique

Abstract

Photoacoustic imaging is used to differentiate tissue types based on varied ratios of light absorption. Different structures, such as vascular capillaries, can be analysed by using photoacoustic imaging, providing diagnostic information to detect early-stage breast cancer. DAS beamforming is the traditional method to reconstruct photoacoustic images. However, for structures located deep in tissue, the SNR of the photoacoustic signal drops significantly. The filter delay multiply and sum (FDMAS) beamforming technique was applied in this chapter to increase the SNR and improve the image quality. Experimental results showed that the FDMAS beamformer improved the SNR by 6.9 dB when compared to the DAS beamformer. Based on simulation results, the FDMAS beamformer improved the lateral resolution by 34% compared to the DAS beamformer. Moreover, the effect of the aperture size on the proposed method was presented as the sub-group FDMAS, opening avenues to further improve the image quality.

5. PHOTOACOUSTIC IMAGING WITH FILTER DELAY MULTIPLY AND SUM BEAMFORMING TECHNIQUE

5.1 Introduction

Photoacoustic imaging is a type of medical imaging modality that combines ultrasound resolution and optical contrast (Treeby *et al.*, 2010; Xu & Wang, 2006). Photoacoustic signals are used to reconstruct photoacoustic images by using one of photoacoustic beamforming techniques, such as time reversal, Fourier transform and DAS (Cox & Treeby, 2010; Kornel *et al.*, 2001; Treeby *et al.*, 2010; Yoon *et al.*, 2012). Photoacoustic imaging holds promise in detecting breast cancer at an early stage (Oraevsky *et al.*, 2002). However, the SNR of photoacoustic emissions will drop when the penetration depth of the target object is increased or the optical energy of the laser pulse is reduced. This is mainly because the increased absorption and scattering of the laser light in tissue before it reaches the target object. In addition, the generated acoustic signals, due to the photoacoustic effect, will be more attenuated before being received by an ultrasound transducer when the objects are deep. Moreover, the speed of sound is assumed to be constant inside tissue during the beamforming operation. As a result, the quality of the photoacoustic image will be degraded in terms of SNR and spatial resolution due to phase aberrations (Cong *et al.*, 2014). In photoacoustic imaging, a linear array transducer is preferable, by providing the capability of combing ultrasound imaging to depict anatomical structures (Daoudi *et al.*, 2014; Kolkman *et al.*, 2008; Montilla *et al.*, 2012). Whereas, by using this transducer, the photoacoustic image will suffer from clutter noise arising from the out-of-imaging plane (Alles *et al.*, 2014).

The effects of the clutter noise and phase aberrations on the photoacoustic image were reduced by using some adaptive beamforming technique. For example, in 2008, Park and his colleagues (Park *et al.*, 2008a) applied coherence factor (CF) and minimum variance (MV) adaptive weighting to a photoacoustic image to reduce the effect of the clutter noise and the phase aberrations on the SNR and lateral resolution of the image. CF weight improved the lateral resolution by 20 to 30 % when compared with the DAS beamformer. In addition, CF with MV weight enhanced the lateral resolution by 40 to 50 % when compared with the DAS beamformer. CF weight improved the contrast by almost 8 dB when compared with the DAS beamformer. Moreover, CF with MV weight increased the contrast by 9.69 dB when compared with the DAS beamformer. In 2013, Pourebrahimi and his colleagues (Pourebrahimi *et al.*, 2013) applied the short-lag spatial coherence beamforming technique to the photoacoustic

imaging. This beamformer decreased the sidelobes by 5 to 15 dB and enhanced SNR of the photoacoustic image by almost 15.5 dB when compared with the DAS beamformer.

In this study, the filter delay multiply and sum (FDMAS) beamforming technique was proposed to improve SNR and resolution of a photoacoustic image. The FDMAS beamforming technique depends on cross correlation between the delayed RF data received by individual elements of an ultrasound probe (Matrone *et al.*, 2015). The idea of this beamforming technique is taken from the delay multiply and sum (DMAS) beamforming technique applied to radar microwave imaging to detect early-stage breast cancer (Lim *et al.*, 2008). In addition, this technique has been introduced into ultrasound imaging showing improvement in image resolution (Matrone *et al.*, 2015). The FDMAS was used to construct photoacoustic images for three static absorbents embedded in an ultrasound phantom by using an ultrasound system and a PLD. The photoacoustic images were constructed using the FDMAS and DAS beamforming techniques, respectively, and compared with each other in terms of SNR and spatial resolution. This chapter is organised as follows: first, the theoretical analysis of DAS and FDMAS beamforming techniques. Second, a comparison between FDMAS and DAS beamformers based on simulation software in terms of the artefact level. Third, a comparison between FDMAS and DAS beamformers based on experiment setup in terms of SNR and spatial resolution and, finally, a discussion and conclusion.

5.2 Methods

5.2.1 DAS Beamforming Technique

In DAS beamformer, the received RF signal from each transducer element is delayed to focus the photoacoustic signal at the imaging points. This time delay is calculated by using equation 5.1 (Cong *et al.*, 2015; Yoon *et al.*, 2012):

$$T_i = \frac{\sqrt{(x - x_i)^2 + (z - z_i)^2 - F_d}}{C}, \tag{5.1}$$

where T_i is time delay for focusing photoacoustic signal at the imaging point (x, z) with the transducer element located at (x_i, z_i). F_d is the depth of the focal point. After

delaying the RF signals, these signals are summed as given in equation 5.2 (Liao *et al.*,
2004):

$$y_{\text{DAS}} = \sum_{i=1}^{N} RF_i(t, T_i), \tag{5.2}$$

where N is the number of transducer elements and $RF_i(t, T_i)$ is the delayed RF signal
for the ith element.

5.2.2 FDMAS Beamforming Technique

The FDMAS beamforming technique depends on cross correlation between delayed RF
data (Matrone *et al.*, 2015). This cross correlation operation will reduce the artefacts
and improve SNR by reducing the uncorrelated signal (Noise) as given in equation 5.3
(Matrone *et al.*, 2015):

$$y_{\text{FDMAS}} = \left\{ \sum_{i=1}^{N-1} \sum_{j=i+1}^{N} \text{sgn}(S_i(t)S_j(t)) . \sqrt{|S_i(t)S_j(t)|} \right\} * f, \tag{5.3}$$

where y_{FDMAS} is the output of the FDMAS beamforming technique and $S_i(t)S_j(t)$
are the delayed RF signals for the ith element and jth element, respectively. In this
equation, the sgn operation is used to maintain the sign of the delayed RF signals
after the multiplication operation (Matrone *et al.*, 2015). In addition, the square root
operation is applied to the multiplied delayed RF signals to remove the effect of the
multiplication operation on the unit of delayed RF signals (Matrone *et al.*, 2015). Fur-
thermore, a bandpass filter (f) is applied before generating the output of the FDMAS
beamformer (Matrone *et al.*, 2015). This is because the multiplication operation be-
tween signals in the FDMAS beamformer generates two frequency bands. One of them
is the summing frequency bands of the two multiplied signals, and the other is the sub-
tracting frequency bands (low frequency part). The low frequency part creates blurring
in the photoacoustic image. Therefore, the bandpass filter is used to extract the high
frequency band of the generated photoacoustic signal (Matrone *et al.*, 2015).

In the FDMAS beamforming technique, all delayed RF signals will be multiplied with each other and summed. There could be one drawback if the generated photoacoustic emission is not received by all elements of the linear ultrasound transducer. This is because the generated photoacoustic signals will be multiplied with noise, reducing the signal amplitude and hence the SNR of the photoacoustic image. To deal with this problem, a sub-group of delayed RF signals will be multiplied with each other as shown in equation 5.4:

$$y_{\text{Sub-FDMAS}} = \left\{ \sum_{i=1}^{N-1} \sum_{j=i+1}^{m} \text{sgn}(S_i(t)S_j(t)).\sqrt{|S_i(t)S_j(t)|} \right\} * f, \qquad (5.4)$$

where:

$$m = \{^{i+g_s,g_s<N-i}_{N,\text{else}},$$

g_s is the group size of delayed RF signals. This size is selected based on the position of the absorbent relative to the ultrasound transducer. For example, when the absorbent is close to the transducer, the group size of the multiplication operation will be small. This is because the number of transducer elements that receive the photoacoustic emission will be reduced when a target become close to the transducer. Otherwise, the group size will be increased when the distance between the absorbent and transducer is increased. When comparing the computation time of FDMAS and Sub-FDMAS beamforming techniques, the Sub-FDMAS beamforming technique is faster. This is because the Sub-FDMAS beamforming technique has fewer number of multiplication operations compared with the FDMAS beamforming technique. The number of multiplication operations for FDMAS and Sub-FDMAS beamforming techniques can be calculated by using equation 5.5 (Matrone *et al.*, 2015) and equation 5.6, respectively:

$$M_{\text{FDMAS}} = \frac{N^2 - N}{2}, \qquad (5.5)$$

$$M_{\text{Sub-FDMAS}} = g_s(N - (g_s + 1)) + \frac{(g_s + 1)^2 - (g_s + 1)}{2}. \qquad (5.6)$$

For example, if the number of transducer elements was 128, the number of multiplications for the FDMAS beamformer would be 8,128. However, the number of multiplications for the Sub-FDMAS beamformer depends on the group size of the delayed RF-signals. If the group size was 64 elements, the number of multiplications would be 6,112. As a result, the Sub-FDMAS beamformer with 64-element group size (64-FDMAS) would reduce the number of multiplications by 2,016 multiplications. This reduction would be increased as the group size is reduced.

5.3 Simulation

FDMAS and DAS beamforming techniques were compared in team of artefact level by using the K-Wave simulation toolbox (Treeby & Cox, 2010). In this simulation, the RF signals were generated from a single absorbent point, as shown in figure 5.1. The specifications of this simulation are shown in Table 5.1. Figure 5.2 (A) shows the photoacoustic image for the single absorbent point when the DAS beamformer was used. The amplitude of artefact is high when compared with the amplitude of the target signal. For example, the highest amplitudes of the artefact at line (1) and line (2) in figure 5.2 (A) were -32.18 dB and -26.34 dB respectively when compared with the amplitude of the target signal as shown in figure 5.2 (B) and (C). Figure 5.3 (A) shows the photoacoustic image for the single absorbent point when the FDMAS beamformer was used. The highest amplitudes of the artefact at line (1) and line (2) were -50.43 dB and -50.29 dB respectively as shown in figures 5.3 (B) and (C). When these artefact amplitudes were compared with the artefact amplitudes that were generated from the DAS beamformer (Figure 5.2), it is clear that the FDMAS beamformer reduced the highest artefact amplitudes at line (1) and line (2) by 18.25 dB and 23.95 dB, respectively. This was due to the correlation operation.
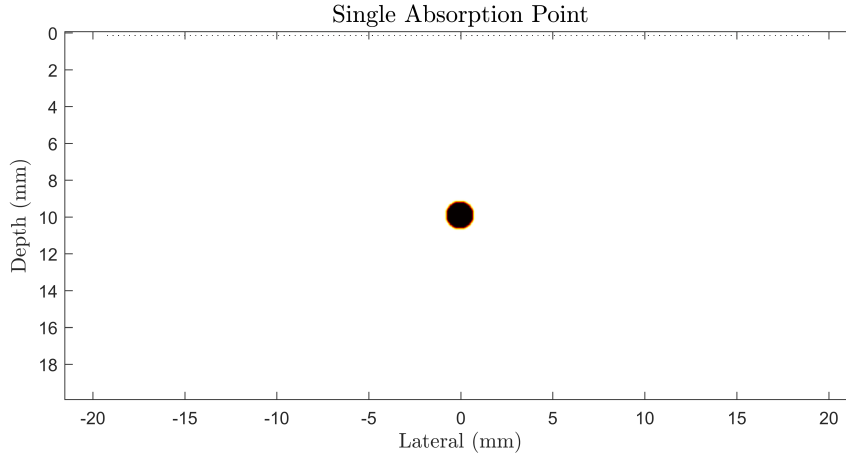
Figure 5.1: Single absorbent point in the K-wave simulation to compare the FDMAS and DAS beamforming techniques.

Specifications of the Simulation	
Grid Size (mm)	0.05
Element Number	128
Pitch Size (mm)	0.3
Centre frequency (MHz)	5
Fractional Bandwidth	60 %
Radius of the absorption target (mm)	0.75
Depth of the absorption target (mm)	10
Speed of sound in the medium (m/sec)	1500
Sampling frequency (MHz)	100

Table 5.1: Specifications of the simulation to compare DAS and FDMAS beamforming techniques.
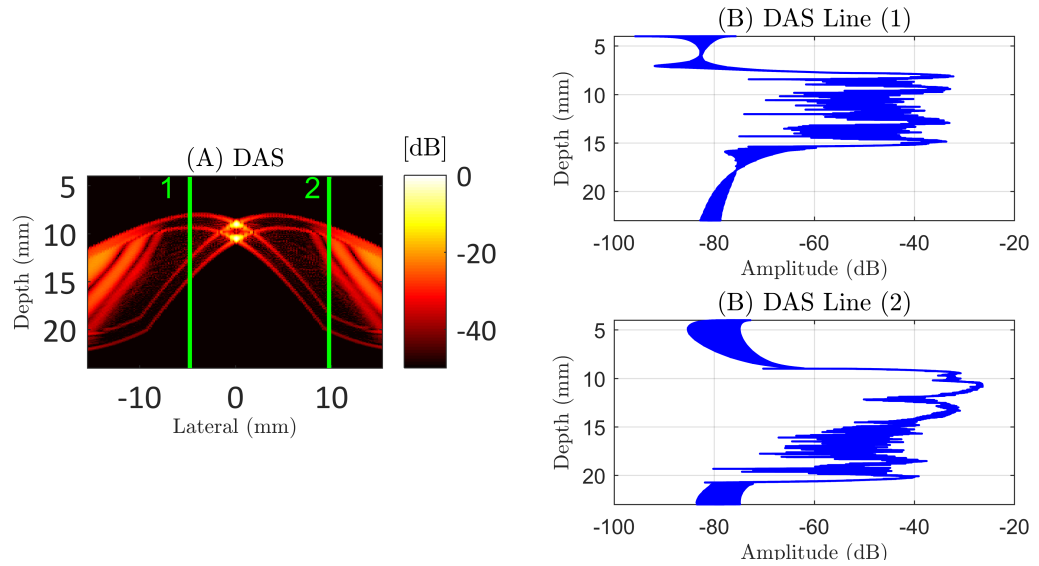
Figure 5.2: (A) Photoacoustic image of the single absorbent point when beamformed by using the DAS beamformer (Dynamic range: 50 dB). (B) The beamforming artefact when using the DAS beamformer at line (1) in figure (A). (C) The beamforming artefact when using the DAS beamformer at line (2) in figure (A).
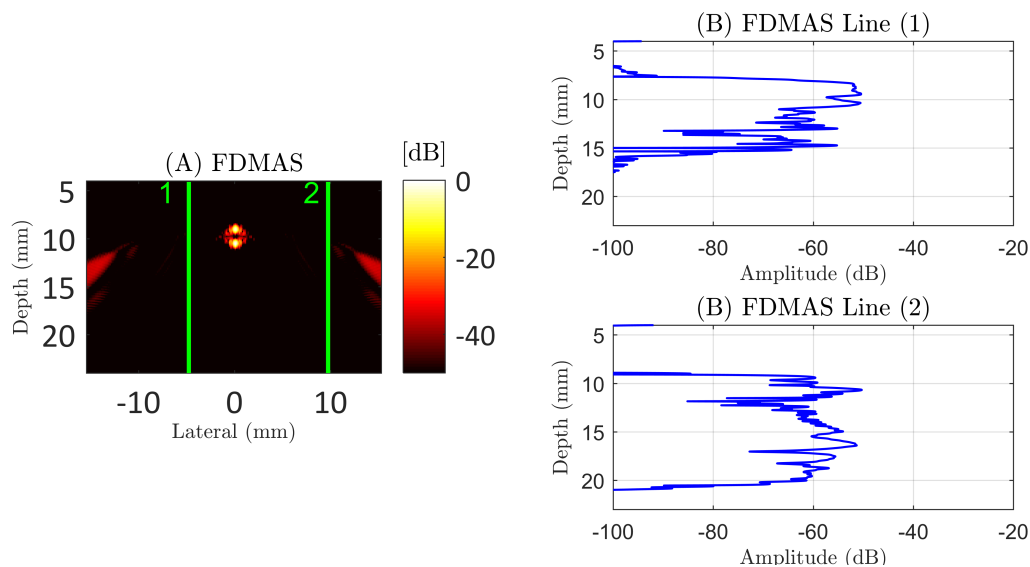
Figure 5.3: (A) Photoacoustic image of the single absorbent point when beamformed by using the FDMAS beamformer (Dynamic range: 50 dB). (B) The beamforming artefact when using the FDMAS beamformer at line (1) in figure (A). (C) The beamforming artefact when using the FDMAS beamformer at line (2) in figure (A).

5.4 Experimental Measurements

5.4.1 Experimental Setup

In the experiment, measurements were performed on a polyacrylamide hydrogel phantom with carbon fibre rods, as shown in figure 5.4. The recipe of this phantom was taken from (Choi *et al.*, 2013), however, no scattering material was used in this phantom due to the weak optical energy of the laser source used in this experiment. In this phantom, a thin layer of gel with 1 % ink was used to mimic an epidermis layer that generates clutter signals. The setup of this experiment is shown in figure 5.5. The photoacoustic emissions were generated from the phantom by using a 905 nm PLD (905D3s3J09S). The pulse length and the output optical energy from this PLD were 100 ns and 10 μJ/pulse, respectively. The pulse length and the optical energy were controlled using a driver module (LDP-V 50-100 v3). This module was triggered by using a function generator (Agilent, 33600A series). The duration and voltage of this trigger were 100

ns and 5 V respectively. The output current of this module was 30 A. The generated photoacoustic emissions were acquired using the UARP II with a 128-element linear 3-8 MHz transducer (Prosonic L3-8/40EP). The received photoacoustic emissions were averaged 100 times before being beamformed using the DAS and FDMAS beamforming techniques. In this process, MATLAB (R2014a, MathWorks) was used. In the experiment setup (Figure 5.5), the laser source was on the opposite side of the linear array transducer. The generated photoacoustic signals from this setup were different from those produced when the laser source and the ultrasound transducer were on the same side. For example, if the laser source and ultrasound transducer were on the same side, the amplitude of clutter signals from the thin layer (Gel with 1 % ink) was high. This is because this thin layer is close to the ultrasound transducer. This is unlike when the laser source was on the opposite side of the ultrasound transducer. In addition, the amplitude of the generated photoacoustic signals from the targets for each setup was different. This is because the distance between the target and the transducer when the laser source is on the opposite side of the ultrasound transducer is different from that when the laser source and ultrasound transducer are on the same side. As a result, the ultrasound attenuation is different for each setup.
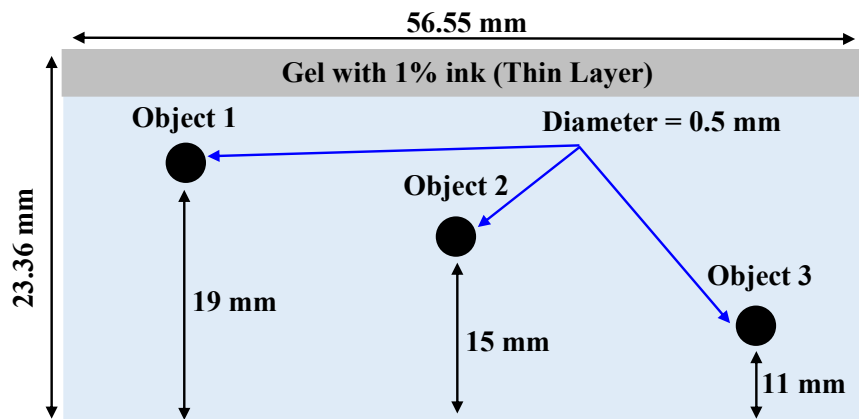
Figure 5.4: Polyacrylamide hydrogel phantom with carbon fibre rods. In this phantom, a thin layer of gel with 1 % ink was used to mimic an epidermis layer that generates clutter signals.
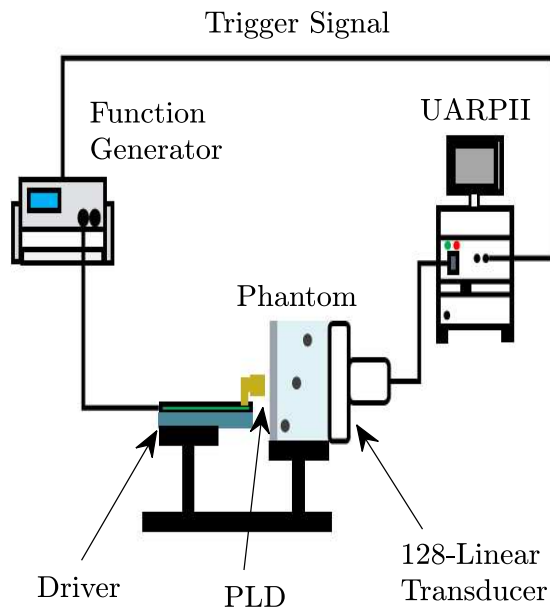
Figure 5.5: Experimental setup for generating photoacoustic emissions by using a PLD. The schematic of triggering PLD and detecting the generated photoacoustic emissions by using a linear array transducer.

5.4.2   Experimental Results

SNR Measurements

Figure 5.6 illustrates photoacoustic images for object 2 when using the DAS and FD-MAS beamforming techniques. The SNR of these images was calculated which was the ratio between the RMS of the target signal and the RMS of the background noise as shown in equation 2.1 (Heinz *et al.*, 2015). The FDMAS beamformer achieved an improved SNR of 6.9 dB over the DAS beamformer. This is because the effect of phase aberrations and noise were reduced due to the correlation operation that FDMAS employed. The improvement of SNR was almost 12 dB when the photoacoustic emissions that travel to the laser source are used in the image reconstruction. This is because the part of the object near the laser source will absorb more optical energy. However, the improvement in image quality in term of SNR that the FDMAS beamformer achieved is affected by the group size of the delayed RF signals, as shown in figure 5.7. The highest gain of SNR for object 3 was achieved when the group size was 19 elements.

5. PHOTOACOUSTIC IMAGING WITH FILTER DELAY MULTIPLY AND SUM BEAMFORMING TECHNIQUE

This is because that the place of the absorbent object was at the corner of the linear transducer and close to it. As a result, not all the transducer elements received photoacoustic emissions. In addition, this object absorbed the lowest optical energy when compared with other objects. Therefore, the image quality was better when the group size was close to a number of elements, making sure that unwanted noise was minimised. In addition, the largest SNR gains for object 1 and object 2 were achieved when the group size was 64 elements and 32 elements respectively. This is because the linear transducer has a large field of view (FOV) for object 1 and object 2. Furthermore, the optical energy that reached object 3 was lower than that for object 1 and object 2, due to its deeper location.
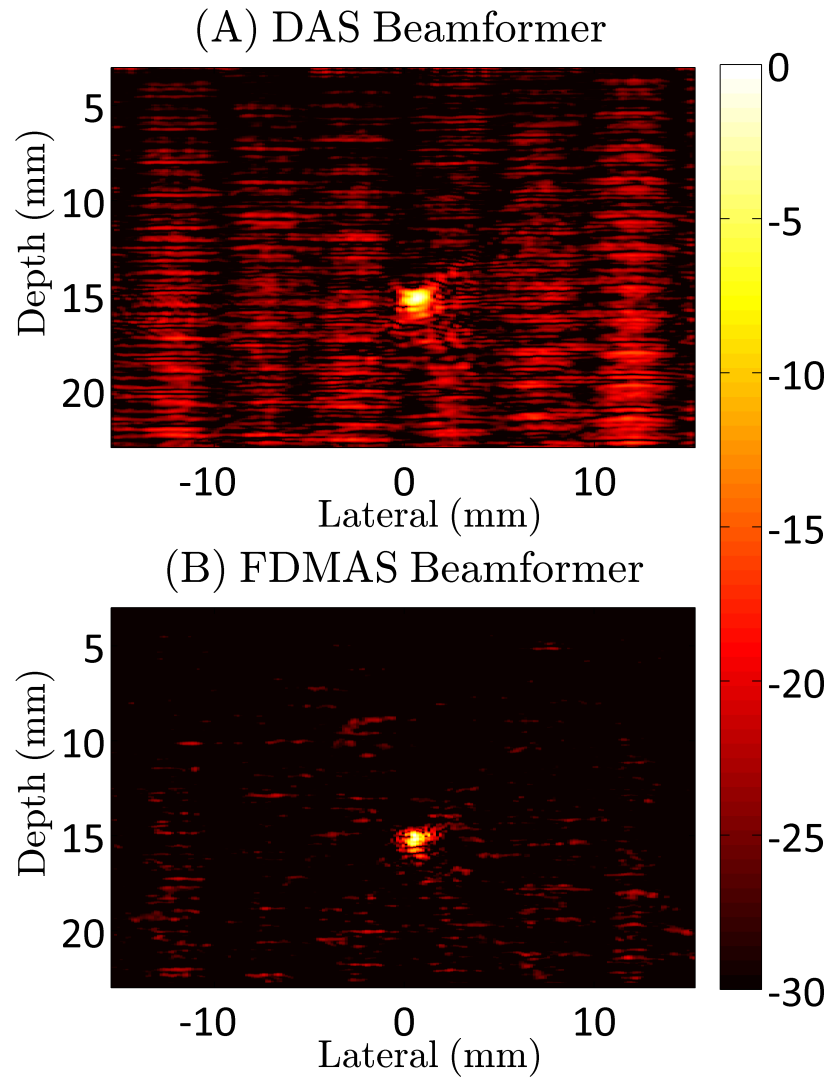
Figure 5.6: Photoacoustic images of the single carbon fibre rod. When (A) the DAS beamformer was used, the background noise was high and the resolution of the target was poor. When (B) the FDMAS beamformer was used, the background noise was noticeably reduced and the Lateral resolution was extremely improved. Dynamic range: 30 dB.
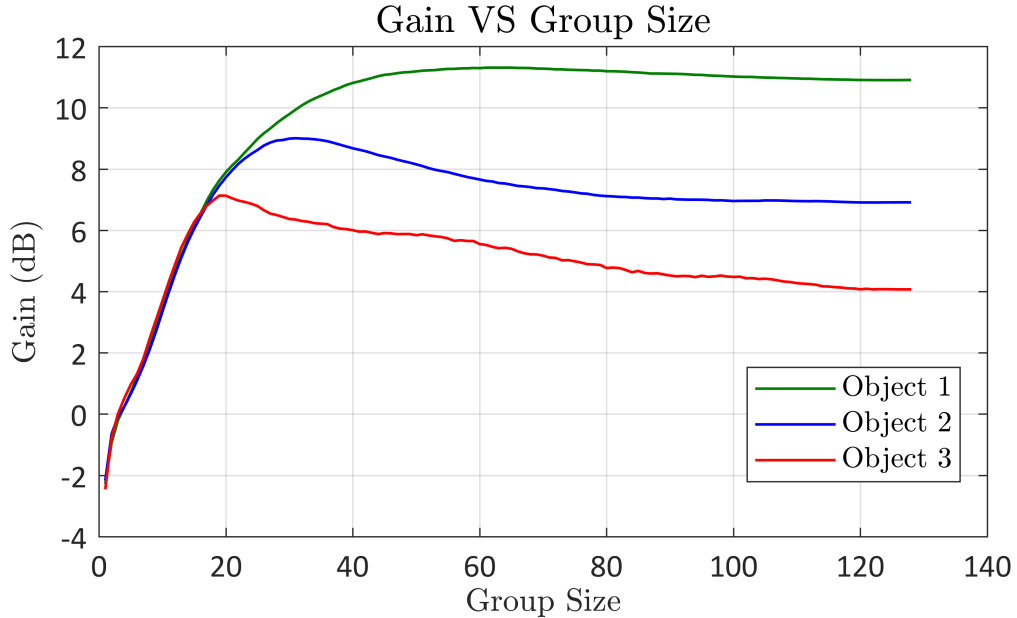
Figure 5.7: Gain of SNR when using the Sub-FDMAS beamforming technique compared
with DAS beamforming technique versus the group size of correlation points.

Spatial resolution (-6 dB) Measurements

The diameter of the carbon fibres that were used in this experiment was 0.5 mm. This
diameter was larger than the wavelength of the centre frequency of the transducer (0.3
mm). As a result, these targets were not suitable for studying the effect of FDMAS and
Sub-FDMAS beamformers on the spatial resolutions (- 6 dB). The spatial resolutions
were measured based on simulation measurement. The depths and positions of the
targets relative to the transducer in the simulation were the same as in the experiment
setup (Figure 5.4). However, the diameter of the target was 0.1 mm. The RF-signals
were generated by using the K-Wave simulation toolbox (Treeby & Cox, 2010). Ap-
pendix (6) shows the specifications of this simulation and the resulting images. From
this simulation, the point spread function of a single absorbent located at the 15 mm
depth (Object 2) allowed the axial and lateral resolutions to be compared, as shown
in figures 5.8 (A) and (B), respectively. The -6 dB axial resolution was comparable in
both cases, where FDMAS performed 10 % better than DAS. This small improvement
in axial resolution was because the correlation operation was applied to the lateral
direction. As a result, the effect of FDMAS beamforming on the axial resolution was

weak. However, the -6 dB resolution in the lateral direction was improved by 34%. Furthermore, by using FDMAS the side lobes were reduced. Table.5.2 shows the axial and lateral resolutions for object 2.
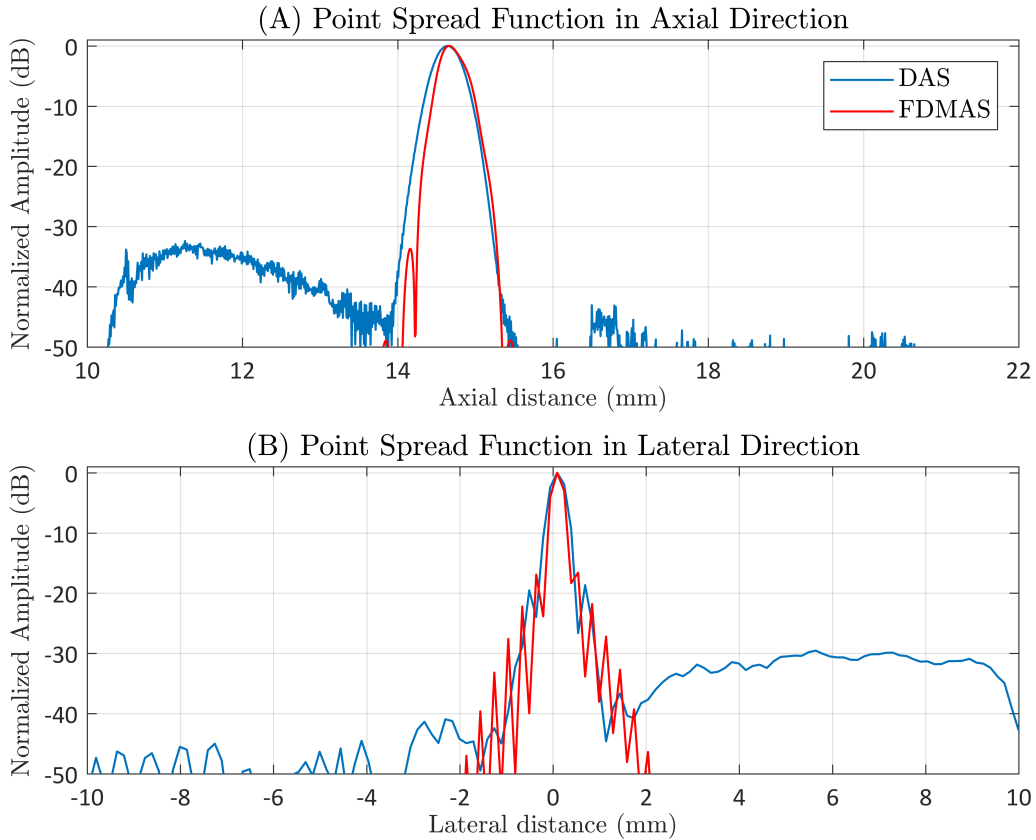
Figure 5.8: Point spread function of the single absorbent point based on simulation setup. (A) Axial resolution of the signal absorbent point when using the DAS (Blue) and FDMAS (Red) beamformers. There was almost 10 % improvement in the axial resolution by using the FDMAS beamformer. (B) Lateral resolution of the single absorbent point when using the DAS (Blue) and FDMAS (Red) beamformers. The FDMAS beamformer led to the improvement of 34 % in lateral resolution.

Beamforming	Axial Resolution (mm)	Lateral Resolution(mm)
DAS	0.5	0.5
FDMAS	0.45	0.33

Table 5.2: Axial and lateral resolutions for target 2 (diameter = 0.1 mm) when using the DAS and FDMAS beamformers.

Figure 5.9 shows the relation between the image resolution and the group size. The lateral resolutions of object 1 and object 3 were reduced when the group size of elements exceeded a certain number of elements. For example, when the group size was 20 elements, the lateral resolutions of object 1 and object 3 were 0.3 mm and 0.25 mm, respectively. These lateral resolutions of object 1 and object 2 were reduced to 0.39 mm and 0.3 mm when the group size was 60 elements. This reduction of the lateral resolution was because the FOV of the transducer to object 1 and object 3 was not large. The lateral resolution of object 2 was changed slightly when group size was changed. The lateral resolution of object 2 was 0.32 mm when the group size was 20 elements. This lateral resolution of object 2 was changed by 0.01 mm when the group size was 60 elements. This slight change in lateral resolution was because the linear transducer had a large FOV for object 2. The axial resolution was slightly improved when increasing the group size of elements. For example, the axial resolution of object 2 was 0.5 mm when the group size was 20 elements. This axial resolution was improved to 0.45 mm when the group size was 128 elements.
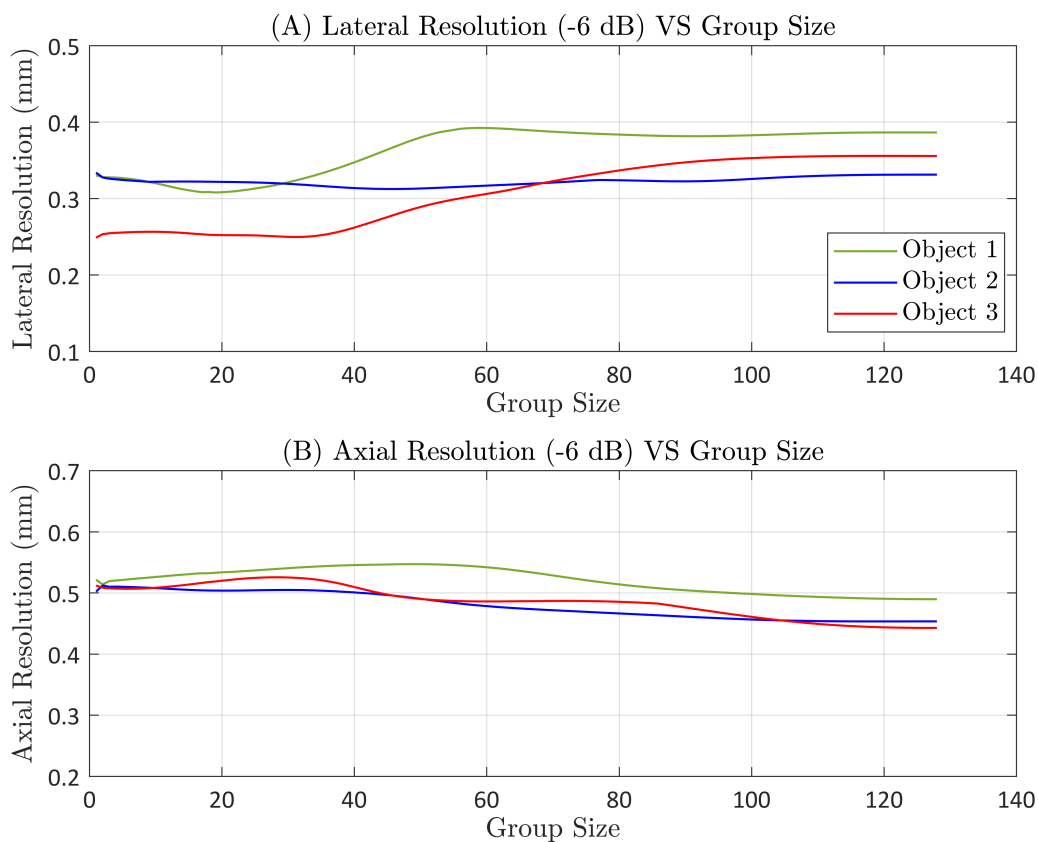
Figure 5.9: Axial and lateral resolutions for object 2 versus the group size.

From figure 5.7 and figure 5.9, it can be noticed that the optimum value of the group size was 32 elements. By using this group size, object 2 achieved the highest SNR (9 dB). In addition, SNR of object 3 increased by 2 dB when compared with using all transducer elements as group size (FDMAS beamformer). However, SNR of object 1 slightly reduced (0.83 dB) when compared with that of the FDMAS beamformer.

Three absorbed objects at different depths were experimentally imaged using the UARP II and processed with DAS, FDMAS and Sub-FDMAS with a 32-element group size (32-FDMAS) beamformers as shown in figure 5.10. The intensity of object 2 and object 3 when using the 32-FDMAS beamformer was higher than that when using the FDMAS beamformer (group size = 128 elements). In addition, the processing time for the 32-FDMAS beamformer was less than that for the FDMAS beamformer due to the number of multiplications for 32-FDMAS was smaller. As can be seen in equation 5.5

and equation 5.6, the number of multiplications for the 32-FDMAS beamformer was 3,568, while this number for the FDMAS beamformer was 8,128.
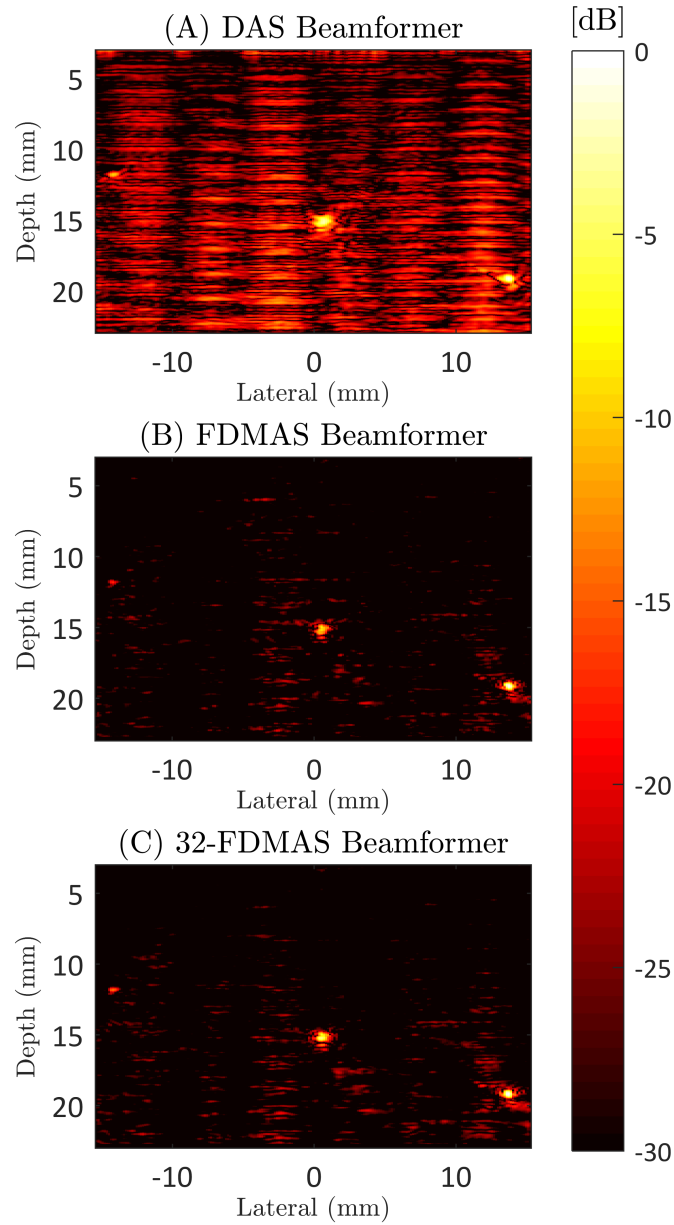
Figure 5.10: Photoacoustic images of the three absorbents when using (A) DAS, (B) FDMAS and (C) 32-FDMAS beamformers. The 32-FDMAS beamformer increased the intensity of object 2 and object 3 when compared with the FDMAS beamformer. Dynamic range: 30 dB.

The FDMAS and 32-FDMAS beamformers were affected by the lateral beamforming

step. This effect was experimentally studied as shown in figure 5.11. This is because that increasing the lateral beamforming step enhances the correlated signals in the correlation operation. For instance, in figure 5.11 (B) and (C), when the lateral step was increased from $\lambda/2$ to $\lambda/4$ and $\lambda/6$, the sidelobe levels decreased. In addition, the width of the main lobe became thinner at -13 dB. For the DAS beamformer, as shown in figure 5.11 (A), the side lobes and main lobe were almost unaffected when changing the lateral beamforming step. The reduction in the lateral beamforming step increased the processing time for all beamformers. This was because the number of points that participated in each beamformer was increased. However, the increasing of the processing time of FDMAS was the highest due to its number of multiplications. For example, when using an i5-3337U CPU 1.80 GHz processor, 8 GB RAM and MATLAB R2017a, the processing time of the DAS beamformer increased from 4.11 sec to 8.13 sec when the lateral step changed from $\lambda/2$ to $\lambda/4$. In addition, the processing time of the FDMAS beamformer increased from 54.91 sec to 110.38 sec when the lateral step changed from $\lambda/2$ to $\lambda/4$. The increasing of the processing time of the 32-FDMAS beamformer (27.64 sec for $\lambda/2$ lateral step and 55.17 sec for $\lambda/4$ lateral step) was less than that of the FDMAS beamformer. This was because the multiplication number of the 32-FDMAS beamformer was less than that of the FDMAS beamformer.
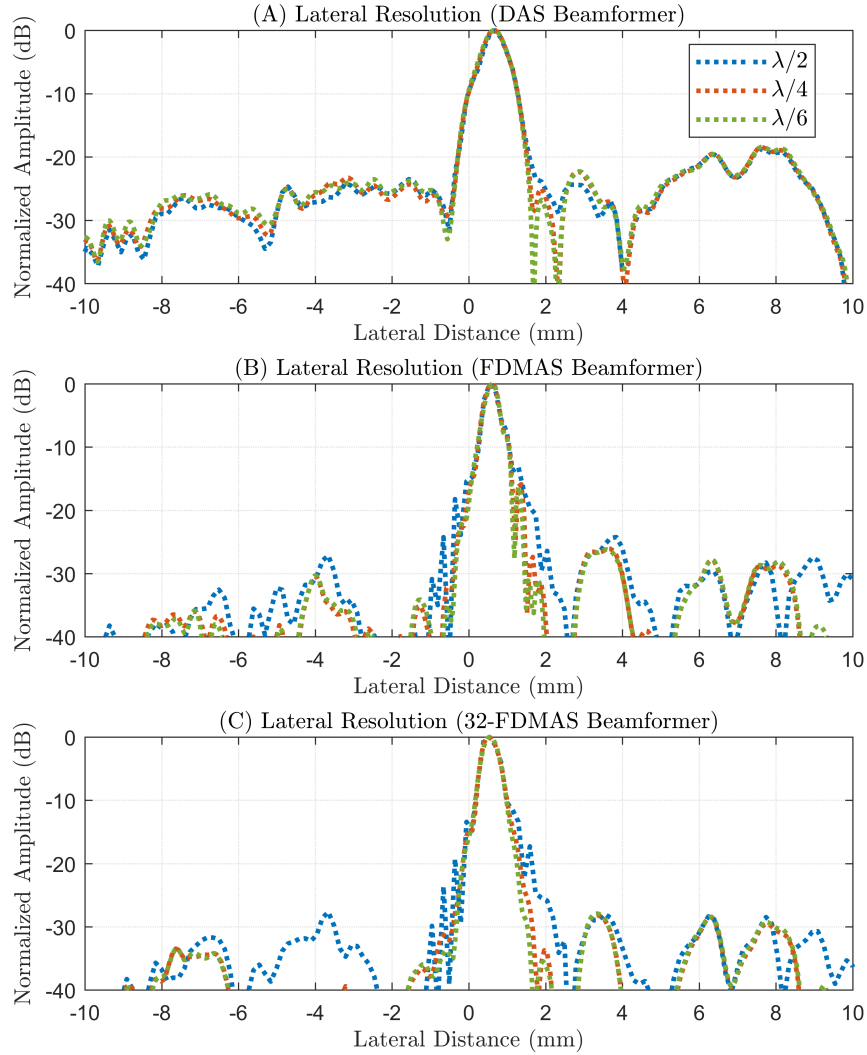
Figure 5.11: Point spread functions of object 2 for different lateral beamforming steps when (A) DAS, (B) FDMAS and (C) 32-FDMAS beamforming techniques were used.

5.5 Discussion

The phase aberration and clutter cause artefacts on the photoacoustic image when the DAS beamformer is used. The FDMAS beamformer reduces these artefacts significantly as the correlation operation enhances the highly correlated signals and attenuates uncorrelated noise. However, the correlation operation in the FDMAS beamformer will

affect the image quality if the background noise is high when compared with the pho-
toacoustic emissions. This effect will be increased if the target is not in the middle of
the linear transducer. To reduce background noise and the effect of the correlation op-
eration on image quality, the correlation operation in the FDMAS beamformer should
be performed with a sub-group of elements. The use of sub-group elements results in
the reduced number of multiplications between the target signals and unwanted signals
(noise). As a result, the SNR of the photoacoustic image will be increased as shown in
figure 5.7 and figure 5.10. The highest gain of the point absorbent (Object 3) with a
depth of 11 mm relative to the transducer is 7.13 dB, when the sub-group size was 19
elements. This gain is reduced as the sub-group element is increased. The group size
of the Sub-FDMAS beamformer is selected based on the level of background noise, the
position and depth of the target relative to the transducer. However, in vivo applica-
tions, the position of the target relative to the transducer can be controlled by moving
the ultrasound transducer. Therefore, with in vivo applications, the group size is se-
lected based on the level of the background noise. For example, if the laser source has
low output optical energy, as is the case with the PLD, the amplitude of the generated
photoacoustic emissions will be low when compared with noise level. As a result, the
group size of elements should be small to reduce the number of multiplications between
target signals and noise signals. This is unlike when the laser source has high output
optical energy, such as with the Nd:YAG laser, which generates photoacoustic emissions
with high SNR. As a result, the group size of elements will be relatively large.

By decreasing the lateral beamforming step with the FDMAS beamformer and 32-
FDMAS beamformer, the side lobes are reduced, as shown in figure 5.11 (B) and (C).
This is because the number of signals that participates in the correlation operation
is increased as the number of lateral beamforming steps is increased. This does not
happen for the DAS beamformer as shown in figure 5.11 (A).

The FDMAS beamforming technique will be beneficial for imaging targets with
a deeper penetration depth, holding promise for diagnosing early-stage breast cancer
and localising the sentinel lymph node (SLN). (Kim et al., 2010a; Xi et al., 2014). In
addition, when a portable PLD that has a high PRF is used, the penetration depth
of the photoacoustic image is shallow (Upputuri & Pramanik, 2015). This is because
of the low output optical energy of a PLD, generating a weak photoacoustic emission
in the deep tissue. The FDMAS beamformer will increase the imaging depth when a

PLD is used as the correlation operation will emphasise the correlated photoacoustic signal rather than the uncorrelated background noise.

5.6   Conclusion

In this study, the effect of the time delay estimation of image reconstruction in imaging resolution was reduced by using the FDMAS beamforming technique. In addition, the FDMAS beamformer showed the improvement of 6.9 dB in SNR over the DAS beamformer. From the point spread functions of a single absorbent point (Simulation), the -6 dB axial and lateral resolutions were improved by 10% and 34%, respectively, with the FDMAS beamformer. In addition, the Sub-FDMAS beamformer was explained. This Sub-FDMAS beamformer showed improvement in image equality over FDMAS and DAS beamformers, however, this improvement in image quality depends on the group size which should be reduced when the target object is close to the transducer surface.

Chapter 6

Elevation Resolution Enhancement in 3D Photoacoustic Imaging

Abstract

Photoacoustic imaging is used to identify the abnormal tissue based on the generated photoacoustic emissions from absorbed laser energy with different wavelengths. To have a better visualisation of the imaging target, three-dimensional (3D) imaging is normally used. In this type of imaging protocol, a 1D linear array transducer is not preferred due to its poor elevation resolution. However, this type of transducer is cheap, commercially available and widely used compared with other types of 3D ultrasound transducers. In this study, the 3D filter delay multiply and sum beamforming technique (FDMAS (3D)) was used to improve the spatial resolution and enhance the SNR of the 3D photoacoustic image created by mechanically moving a 1D linear array transducer. This beamforming technique showed improvement in the elevation and lateral resolution of 35% and 17.5%, respectively, when compared with the 3D delay and sum beamforming technique (DAS (3D)). In addition, it enhanced the SNR of the photoacoustic image by almost 11 dB when compared with DAS (3D).

6. ELEVATION RESOLUTION ENHANCEMENT IN 3D PHOTOACOUSTIC IMAGING

6.1 Introduction

Photoacoustic imaging is used to visualise different structures of the biological tissue based on the wavelength of the absorbed light (Hu & Wang, 2010; Ntziachristos, 2010; Wang & Hu, 2012). As a result, this type of imaging modality is used to measure the oxygen saturation in blood and detect breast cancer at an early stage (Chen *et al.*, 2012; Mallidi *et al.*, 2015). The resolution of the photoacoustic imaging depends on the bandwidth of the ultrasound transducer (Chen *et al.*, 2009) as the photoacoustic emissions are broadband signals. In addition, photoacoustic imaging is affected by the field of view (FOV) of the ultrasound transducer (Piras *et al.*, 2012). To get better visualisation of the imaging target, three dimensional (3D) photoacoustic imaging is used. In 3D photoacoustic imaging, different ultrasound transducers, such as the circular view transducer, matrix transducer and linear array transducer, are used (Xia & Wang, 2014). The 1D linear array transducer has advantages over other types of ultrasound transducers in terms of price and commercial use. In addition, by using a linear array transducer, it is easy to combine ultrasound images with photoacoustic images (Wei *et al.*, 2015). However, the 1D linear array transducer has poor resolution in the elevation direction and suffers from clutter noise during beamforming.

A number of methods have been proposed to improve the elevation resolution of the photoacoustic image when a 1D linear array transducer is used. For instance, Wang *et.al* (Wang *et al.*, 2016b) inserted a metal slice at the focal point in the elevation direction between the transducer and imaging target. This slice will lead to diffraction of the photoacoustic signals in the elevation direction, thereby increasing the aperture size in the elevation direction and improving the elevation resolution. Schwarz *et.al* (Schwarz *et al.*, 2015) have applied a bi-directional scan by using a 1D linear array transducer. The RF data for each scanning direction was beamformed and then combined with each other. This technique has shown improved elevation resolution, however, in this technique, two scans are needed, therefore, increasing the scanning time. Gateau *et.al* (Gateau *et al.*, 2015) have improved the FOV in the elevation direction by investigating translation and rotation of the 1D array transducer in the elevation direction. However, the improvement in the elevation direction depends on the translation and rotation region. Wang *et.al* (Wang *et al.*, 2016a) have combined the coherent factor (CF) with

a focal line (FL) technique to improve the elevation resolution with a 1D linear array transducer. This technique showed improvement in the SNR and elevation resolution.

In this study, the elevation resolution of the 3D photoacoustic image is improved with a 1D linear array transducer by using the FDMAS beamforming technique. This beamforming technique has been applied to ultrasound and photoacoustic imaging. It depends on the correlation between the delayed RF data from each channel (Al-shaya *et al.*, 2016; Matrone *et al.*, 2015; Moubark *et al.*, 2016). In this study, both the FDMAS (3D) and DAS beamforming techniques are compared in terms of spatial resolution and SNR for 3D photoacoustic imaging consisting of 2D stacked planes (Fournelle *et al.*, 2009; Xia *et al.*, 2011). In addition, it is compared with the 3D DAS beamforming technique when a 3D image is beamformed by focusing the received RF data in both lateral and elevation directions (Xia *et al.*, 2011; Xu & Wang, 2005). This chapter is organised as follows: first, the theoretical analysis of DAS (3D) and FDMAS (3D) beamforming techniques. Second, a comparison between DAS (3D) and FDMAS (3D) beamformers for three different phantoms in terms of SNR and spatial resolution. Finally, a discussion and conclusion.

6.2 Method

6.2.1 3D DAS Beamforming Technique

When a 1D linear transducer array is used in 3D photoacoustic imaging, each scanning plane is normally beamformed by using DAS (2D). Then, these scanning planes are stacked together to form a 3D photoacoustic image (Xia *et al.*, 2011). This 3D photoacoustic image suffers from poor elevation resolution out of the focal point because most 1D linear array transducers have a fixed focal depth in the elevation direction. To reduce the effect of the poor elevation resolution, the received RF data has been beamformed in both the lateral and elevation directions by using the DAS (3D) beamforming technique (Wang *et al.*, 2016a). In this beamforming technique, the FOV of each transducer element in the lateral and elevation directions will be taken into account. This technique is explained by equation 6.1 (Wang *et al.*, 2016a):

$$R(t) = \sum_{j=1}^{M} \sum_{i=1}^{N} SS_{ji}(t), \tag{6.1}$$

113

where N is the number of transducer elements, M is the number of scanning planes in the elevation direction, and $SS_{ji}(t)$ is the delayed RF signals that is received by the ith element in the jth scanning plane.

6.2.2 3D FDMAS Beamforming Technique

FDMAS depends on the correlation between delayed RF signals. The 2D-FDMAS beamforming technique can be calculated by using equation 6.2 (Moubark *et al.*, 2016):

$$y_{\text{FDMAS}} = \left\{ \sum_{i=1}^{N-1} \sum_{j=i+1}^{N} \text{sgn}(S_i(t)S_j(t)).\sqrt{|S_i(t)S_j(t)|} \right\} * f, \tag{6.2}$$

where $S_i(t)$ and $S_j(t)$ are the delayed RF signals for the transducer element i and j, respectively. The sgn and square root operations are used to remove the effect of the multiplication operation on the sign and the unit of the beamformed data. Due to the multiplication operation, two frequency bands are generated. One of these is within the base band, therefore, a bandpass filter (f) will be used to extract the high frequency band.

The FDMAS beamforming technique cannot be applied directly to 3D photoacoustic imaging as the FDMAS depends on the cross correlation operation (Matrone *et al.*, 2015). To deal with this issue, it should be used to beamform the RF signals in the lateral and elevation directions, separately, before combining them together with the steps as follows. In the first step, the RF signals will be beamformed in the lateral direction by using FDMAS. Then, the resultant data will be beamformed again in the elevation direction by using DAS. This step improves the lateral resolution and focuses the beamformed data in the elevation direction. In the second step, the RF signals will be beamformed in the lateral direction using DAS. After that, the resultant data will be beamformed again in the elevation direction by using FDMAS. This step enhances the elevation resolution of the photoacoustic image which is out of the focal point of the acoustic lens and focuses the beamformed data in the lateral direction. The results of these two steps are then combined by two techniques. For the first technique the

result of each step will be summed as given in equation 6.3:

$$y_{\text{S-FDMAS(3D)}} = Y_1 + Y_2, \tag{6.3}$$

where Y_1 is the beamformed data of the first step, and Y_2 is the beamformed data of the second step. For the second technique, the result of each step will be multiplied with each other, as given in equation 6.4:

$$y_{\text{M-FDMAS(3D)}} = \text{sgn}(Y_1 Y_2)\sqrt{|Y_1 Y_2|}. \tag{6.4}$$

The square root operation is used to retain the unit of the beamformed data and the sgn operation is used to retain the sign of the signals. By combining the results of these two steps, both lateral and elevation resolutions will be improved. Figure 6.1 illustrates the diagram of the FDMAS(3D) beamforming technique.
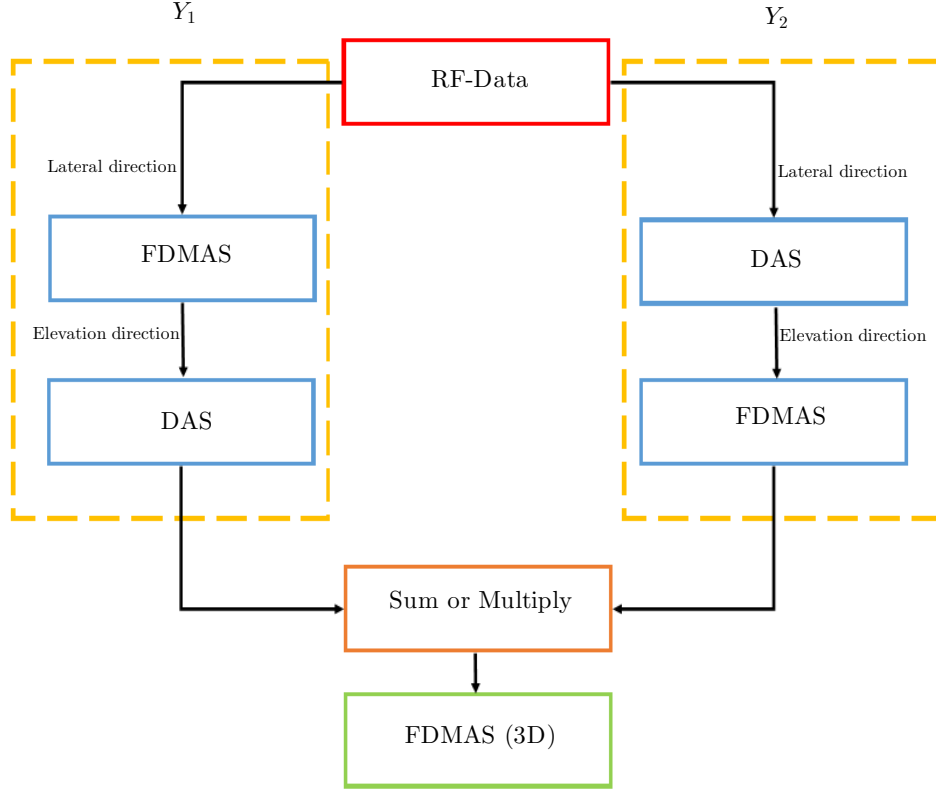
Figure 6.1: Diagram of applying the FDMAS beamforming technique to 3D photoacoustic imaging. FDMAS was applied to the lateral and elevation directions separately. The results of the two steps were combined by sum or multiplication operations.

6.3 Experiments

6.3.1 Phantoms

In this study, three phantoms were used. The first was a turbid polyacrylamide hydrogel phantom with carbon fibre rods as shown in figure 6.2 (B). The recipe of this gel phantom was taken from (Choi *et al.*, 2013) without adding ultrasound scattering materials. The diameter of the carbon fibre rods was 2.5 λ. Latex beads (1.1μm) were added to this phantom to achieve a 0.3 mm^{-1} optical scattering coefficient. The Mie scattering calculator was used to calculate the required amount of optical scattering materials (Prahl, 2017). This phantom was used to evaluate the spatial resolution and SNR of
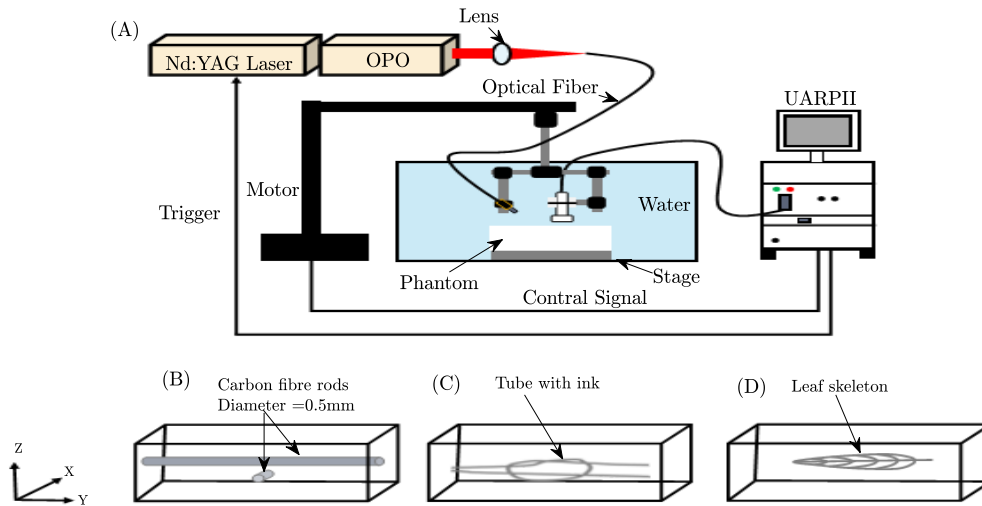
Figure 6.2: (A) Experimental setup for 3D photoacoustic imaging. The photoacoustic emissions were generated using a Nd:YAG laser and recorded by the UARP II in conjunction with a linear array transducer. (B) Carbon fibre rods phantom used to study the effect of FDMAS beamformer on the spatial resolution. (C) Tube phantom filled with ink. (D) Leaf skeleton phantom.

the photoacoustic image when the FDMAS(3D) beamformer was used. The second phantom was a transparent tube (cole.parmer 06422.02) made from pharmaceutical-grade thermoplastic materials and filled with Indian ink. The concentration of the ink was 16%. This tube with a complex structure, as shown in figure 6.2 (C), was then submerged into water for measurements. This phantom was used to study the FDMAS (3D) beamformer on the complex structure. The third phantom was a leaf skeleton which was painted with a black colour (brand was Pilot) and submerged into water as shown in figure 6.2 (D). This phantom was used to present the effect of the FDMAS (3D) beamformer on the complex and micro scale target.

6.3.2   Experimental Setup

The setup of these experiments is shown in figure 6.2(A). The photoacoustic emissions were generated using a tuneable Nd:YAG laser. The pulse length and pulse repetition frequency (PRF) of this laser were 7 ns and 10 Hz, respectively. The wavelength and the optical energy of the firing laser were 850 nm and 3.7 mJ, respectively. This

firing laser was directed at the phantoms through a single optical fibre with an output diameter of 2 mm (NA = 0.22). The generated photoacoustic emissions were recorded using the UARP II (Cowell *et al.*, 2013; Harput *et al.*, 2013; Smith *et al.*, 2012, 2013) through a linear array transducer (Verasonics L11-4v). This transducer consisted of 128 elements with a centre frequency of 7.5 MHz and a -6 dB bandwidth of 90 %. In this experiment, the linear array transducer was moved in the elevation direction by using a stepper motor (Zolix, PSA 100-11-X) with a step size of 0.1 mm. All transducer elements received the photoacoustic signals simultaneously which were digitised with a sampling rate of 80 MS/s. In this experiment, the received signals were averaged 100 times before being beamformed.

6.4 Experimental Results

The FDMAS (3D) beamforming technique was compared with DAS (2D) and DAS (3D) beamforming techniques with photoacoustic images of carbon fibre rods, as shown in figure 6.3. These images were reconstructed based on maximum intensity projection (MIP). The SNR of these images was calculated using equation 6.5 (Deng *et al.*, 2011):

$$SNR = 20\log(\frac{S_{\text{peak}}}{N_{\text{Average}}}), \tag{6.5}$$

where S_{peak} is the maximum intensity of the target signal and N_{Average} is averaged background noise. The region of the target signal and the background noise are defined with a dashed rectangular region number 1 and number 2, respectively, in figure 6.3 (D). Form these images, It can be seen that when the photoacoustic image was beamformed using DAS (2D) (Figure 6.3 (A)), the background noise of the photoacoustic image was high (SNR = 16 dB). This is due to the weakness of the generated photoacoustic signals and electrical noise. In addition, the elevation resolution of this image was poor due to clutter. This is due to the FOV of the linear array transducer was assumed fixed and narrow in the elevation direction when this image was beamformed. When the photoacoustic image was beamformed using DAS (3D) (Figure 6.3 (B)), the background noise was reduced (SNR = 23 dB) as the RF signals were beamformed in the lateral and elevation directions. In addition, the elevation resolution of the photoacoustic image was mostly improved as the elevation FOV of the transducer was taken into account

during beamforming. The size of the focus (f_{se}) point in the elevation direction is calculated using equation 6.6 (Nikolov & Jensen, 2000):

$$f_{se} \approx 0.82 \lambda k_d \frac{f_{de}}{h}, \tag{6.6}$$

where λ is the wavelength at the centre frequency of the transducer and k_d is a constant value that depends on the type of apodization. k_d is 1 if the apodization is rectangular, f_{de} is the elevation focus depth and h is the height of transducer element. The divergence angle in the elevation ($\frac{\theta}{2}$) after the focal point is calculated using equation 6.7 (Nikolov & Jensen, 2000):

$$\frac{\theta}{2} \approx \tan^{-1} \frac{h}{2f_{de}}. \tag{6.7}$$

In this calculation, the wavelength (λ) was calculated for the centre frequency of the transducer that was 7.5 MHz. The height of the transducer element (h) is 8 mm. The depth of the focal point (f_{de}) is 20 mm. k_d is 1 (The apodization is rectangular). The windowing size (Number of scanning planes) in the elevation direction was selected based on the divergence angle of the lens in the elevation direction after the focal point. For instance, when the depth of the imaging point from the focal point in the elevation direction was increased, the windowing size was increased. This increased the number of scanning planes that participated in the beamforming. As a result, the elevation resolution out of focal point was improved.

When the FDMAS (3D) beamformer with sum combination (S-FDMAS (3D)) was used, background noise was significantly reduced (SNR = 35 dB), as shown in figure 6.3 (C). In addition, the elevation resolution was noticeably improved. If the FDMAS (3D) beamformer with multiplication combination (M-FDMAS(3D)) was used, as shown in figure 6.3 (D), the highly correlated signals will be more enhanced. The SNR of the photoacoustic images beamformed by using S-FDMAS(3D) and M-FDMAS(3D) and their computation times have be compared with that by using DAS (2D) and DAS (3D) as given in Table 6.1. The S-FDMAS (3D) beamformer improved the SNR by 19 dB when compared with the DAS (2D) beamformer, and by 12 dB when compared with the DAS (3D) beamformer. In addition, M-FDMAS (3D) improved the SNR by 18 and 11

dB compared with DAS (2D) and DAS (3D) beamformers, respectively. However, the S-FDMAS (3D) and M-FDMAS (3D) beamformers had high computation times when compared with the computation time of the DAS (2D) and DAS (3D) beamformers. As can be seen in Table 6.1, the computation time of the S-FDMAS (3D) beamformer was higher than that of the DAS (3D) beamformer by 8.87 times.
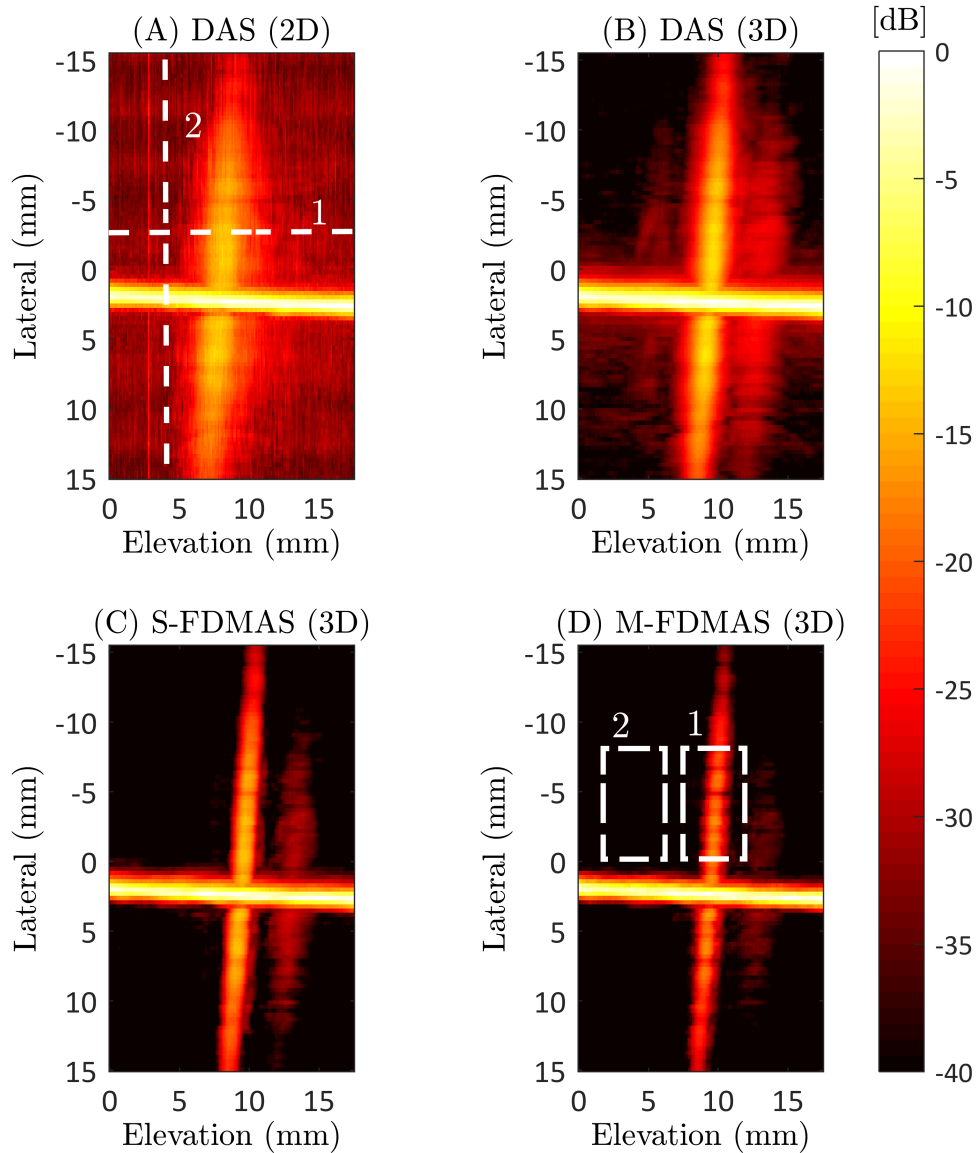
Figure 6.3: Photoacoustic images of carbon fibre rods beamformed using (A) DAS (2D), (B) DAS (3D), (C) S-FDMAS (3D), and (D) M-FDMAS (3D). Dynamic range: 40 dB.

Figure 6.4 shows a 3D visualisation of the carbon fibre rods for DAS (2D), DAS (3D), S-FDMAS (3D) and M-FDMAS (3D) beamforming techniques (The surfaces were extracted with an isosurface value of 30 dB). When the DAS (2D) and DAS (3D) beamformers were used, the structural information of the carbon fibre rod that was

Beamformer	SNR (dB)	Computation time (Hours:Minutes:Seconds)
DAS (2D)	16	00:02:10
DAS (3D)	23	00:17:56
S-FDMAS (3D)	35	02:39:10
M-FDMAS (3D)	34	02:40:07

Table 6.1: SNR of carbon fibre rod photoacoustic images and computation time of beamforming techniques.

along the lateral direction was hard to interpret, as shown in figure 6.4 (A) and (B), due to noise and clutter. This was different from the case when the S-FDMAS (3D) beamformer was used as shown in figure 6.4 (C). The S-FDMAS (3D) beamforming technique reduced noise and clutter. When M-FDMAS (3D) beamforming was used, the correlated signals between the two parts of FDMAS (3D) was emphasised, as shown in figure 6.4 (D).
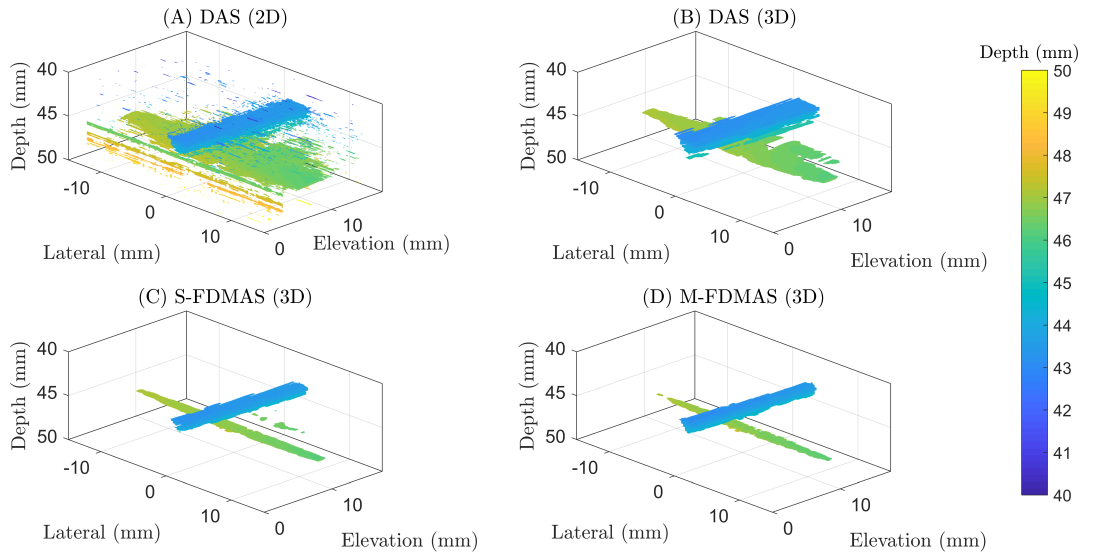
Figure 6.4: 3D photoacoustic images of the carbon fibre rods beamformed using (A) DAS (2D), (B) DAS (3D), (C) S-FDMAS (3D), and (D) M-FDMAS (3D). The surfaces were extracted with an isosurface value of 30 dB.

The point spread function was measured for the carbon fibre rod in the elevation and lateral directions. This point spread function was calculated from a line of the

beamformed data based on MIP (Figure 6.3) in the elevation and lateral directions. Based on the point spread function, -6 dB resolution was measured. Figure 6.5 (A) shows the point spread function for the carbon fibre rod in the elevation direction (dashed line number 1 in figure 6.3 (A)). From figure 6.5 (A), it can be seen that the peak of DAS(2D) was misaligned with the peak of DAS (3D), S-FDMAS (3D) and M-FDMAS (3D). This was because, when using DAS (2D), the RF-data was not beamformed in the elevation direction that, unlike with other beamformers. In addition, in DAS (2D), the 3D image was created by stacking the 2D scanning planes together. As a result, the location of the peak signal in the elevation direction was affected by the clutter noise. The clutter noise was created due to the direction of the firing laser to the target. When the S-FDMAS (3D) beamformer was used, the elevation resolution (-6 dB) was improved by 59% and 28% when compared with DAS (2D) and DAS (3D) beamformers, respectively. In addition, the M-FDMAS (3D) beamformer improved the elevation resolution (-6 dB) by 63% and 35% when compared with DAS(2D) and DAS (3D) beamformers, respectively, as given in figure 6.6. Figure 6.5 (B) shows the point spread function of the carbon fibre rod (dashed line number 2 in figure 6.3 (A)) in the lateral direction. The S-FDMAS (3D) beamformer improved the lateral resolution (-6 dB) by 14% and 20% when compared with DAS (2D) and DAS (3D) beamformers, respectively, as the beamformed data using both the DAS beamformer and FDMAS beamformer were added together. This affected the lateral resolution of the image. M-FDMAS (3D) improved the lateral resolution (-6 dB) by 12% and 17.5% when compared with DAS (2D) and DAS (3D) beamformers, respectively, as shown in figure 6.6. In addition, the sidelobes were extremely reduced when S-FDMAS (3D) and M-FDMAS (3D) were used. The improvement in the spatial resolution depends on the FOV of the transducer to the target. For example, if the target is close to the focal point in the elevation direction, the improvement in the elevation resolution achieved by using the S-FDMAS (3D) and M-FDMAS (3D) beamformers will be low. This is because the windowing size will be small close to the focal point. As a result, the number of scanning planes that participate in the beamformer is small. However, when the target is far from the focal point in the elevation direction, the number of scanning planes that participate in the beamformer will be large. As a result, the improvement in the elevation resolution will be high. This improvement in the resolution brings with it high computation costs. As can be seen in figure 6.6, the S-FDMAS beamformer increased

the computation time by 8.87 times and 73.46 times when compared with the DAS (3D) and DAS (2D) beamformers, respectively. In addition, the M-FDMAS beamformer increased the computation time by 8.92 times and 73.9 times when compared with the DAS (3D) and DAS (2D) beamformers, respectively.
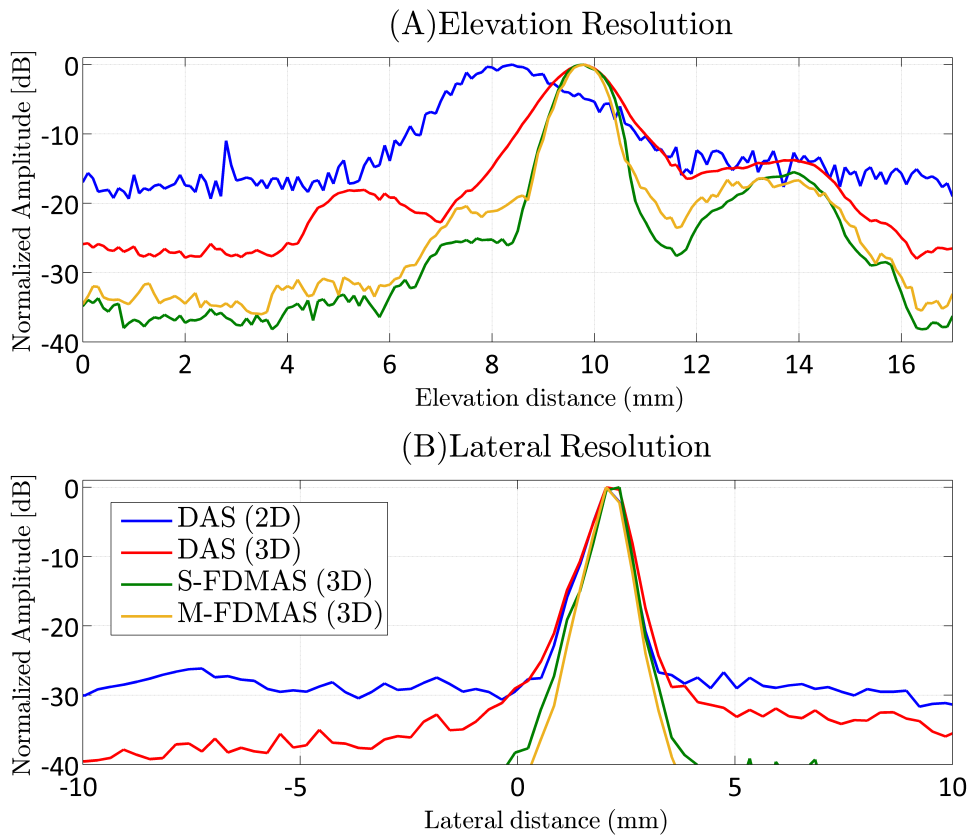
Figure 6.5: Point spread function of the carbon fibre rod (A) in the elevation direction, and (B) in the lateral direction of the linear array transducer.
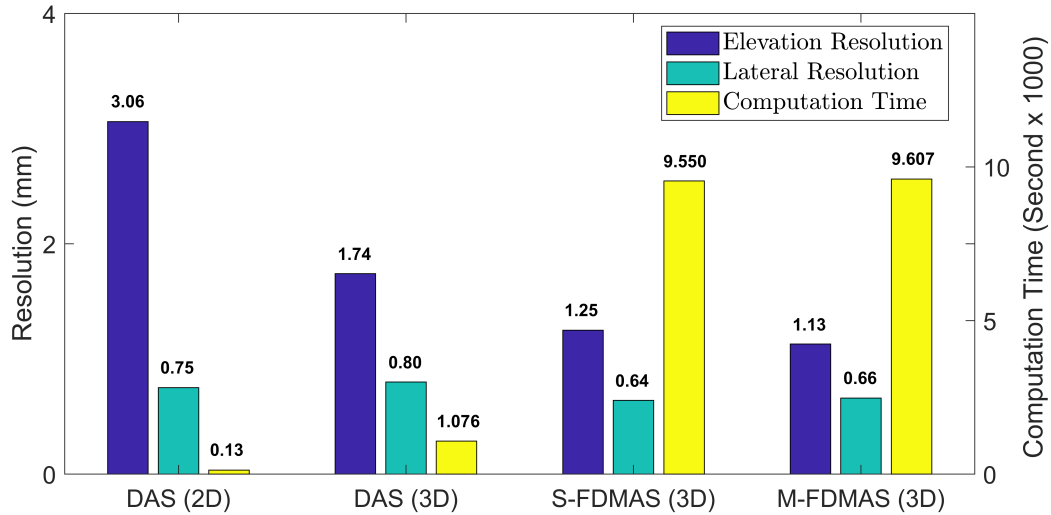
Figure 6.6: Elevation and lateral resolutions (-6 dB) of carbon fibre rod virus computation time for the DAS (2D), DAS (3D), S-FDMAS (3D), M-FDMAS (3D) beamformers.

These beamforming techniques were then compared when beamforming the tube that had a complex structure, as shown in figure 6.7 (A). The S-FDMAS (3D) beamformer significantly reduced the clutter and background noise when compared with DAS (2D) and DAS (3D) beamformers. The S-FDMAS (3D) beamformer also improved the elevation resolution of the tube, as shown in figure 6.7 (D). M-FDMAS (3D) provided the same quality of photoacoustic image when compared to the S-FDMAS (3D) beamformer. However, the M-FDMAS (3D) beamformer had more emphasis on the correlated signals. Figure 6.8 shows the 3D visualisation of the tube phantom filled with ink for the DAS (2D), DAS (3D), S-FDMAS (3D) and M-FDMAS (3D) beamforming techniques (The surfaces were extracted with an isosurface value of 30 dB). The noise and clutter created difficulties to differentiate between tube parts when DAS (2D) (Figure 6.8 (A)) and DAS (3D) (Figure 6.8 (B)) were used. The S-FDMAS (3D) and M-FDMAS (3D) beamformers provided a better 3D view of tube parts as shown in figure 6.8 (C) and (D), respectively. This was due to reducing the noise and clutter.
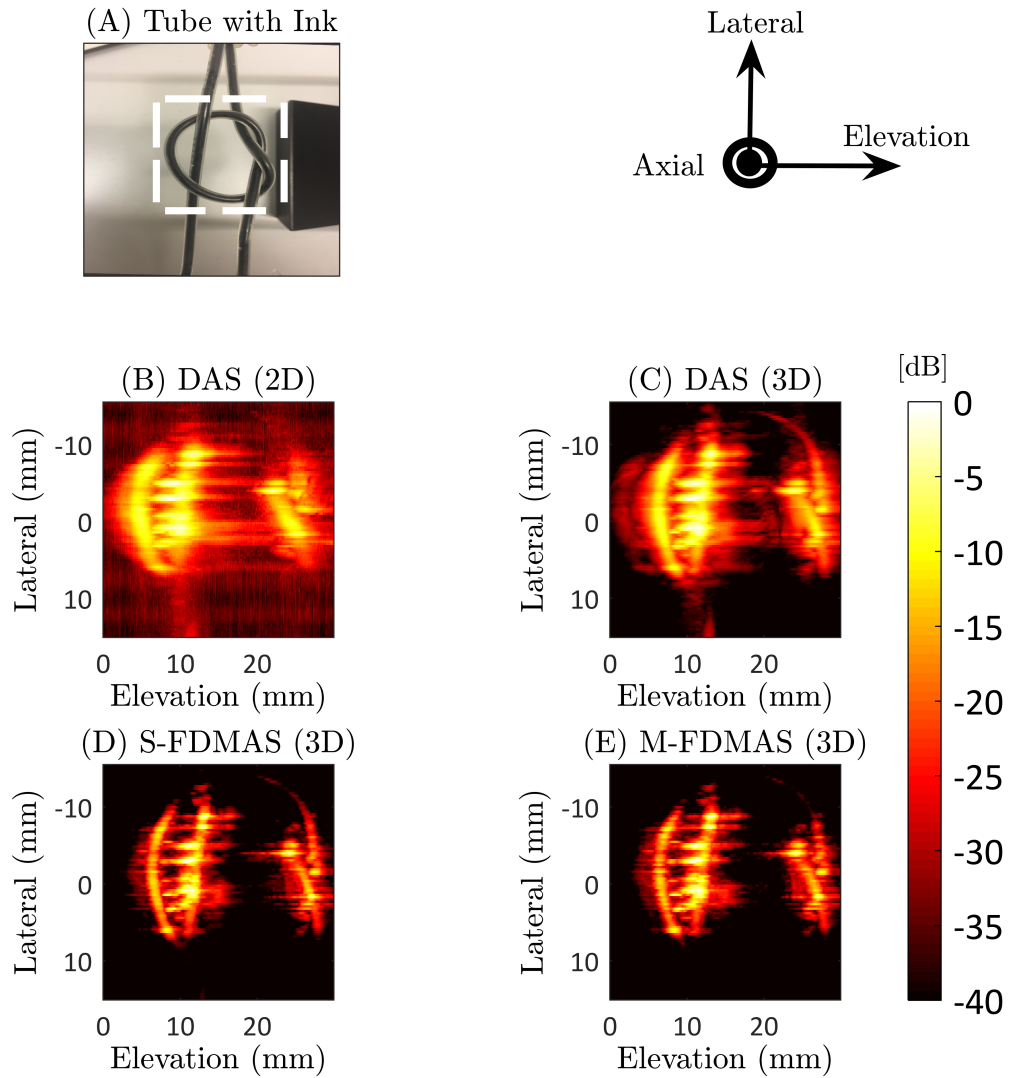
Figure 6.7: (A) Tube phantom filled with ink. Photoacoustic image of the tube using (B) DAS (2D), (C) DAS (3D), (D) S-FDMAS (3D), and (E) M-FDMAS (3D). Dynamic range: 40 dB.
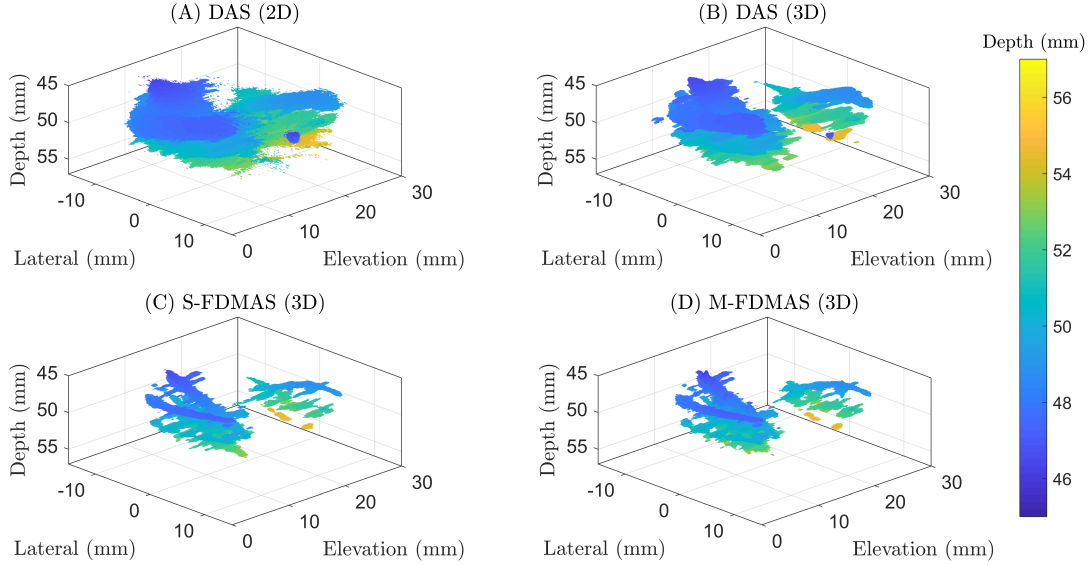
Figure 6.8: 3D photoacoustic images of the tube phantom filled with ink beamformed using (A) DAS (2D), (B) DAS (3D), (C) S-FDMAS (3D) and (D) M-FDMAS (3D). The surfaces were extracted with an isosurface value of 30 dB.

These beamforming techniques were then compared with the leaf skeleton as shown in figure 6.9. The region of interest is delineated with the rectangular dashed region in figure 6.9 (A). The photoacoustic image beamformed by using DAS (2D) had poor lateral and elevation resolutions as shown in figure 6.9 (B). In addition, the small skeleton branches cannot be recognised. When DAS (3D) was used, as shown in figure 6.9 (C), the spatial resolution was slightly improved as indicated in the main branch (arrow number 1 in figure 6.9(A)). The small branches were also still difficult to be differentiated from each other. When S-FDMAS (3D) was employed, the lateral and elevation resolutions were extremely improved, as shown in figure 6.9 (D). It was challenging to image the small branches of the leaf skeleton (microscale size) with a low-frequency transducer. In addition, to image these small branches, the step size of scanning should be reduced to increase the resolution. However, some small skeleton branches can be clearly recognised when comparing figure 6.9 (A) and (D) (arrow number 2 and number 3). This is because the S-FDMAS (3D) beamforming technique emphasised the correlated delayed RF signals. When M-FDMAS (3D) was used, the sharpness of the leaf skeleton increased, as shown in figure 6.9 (E). The quality of this photoacoustic image would be better if the scanning step was reduced. In these experiments, the

scanning step was not reduced. This was because a stepper motor with very small step size (<0.1 mm) is needed. In addition, the scanning time will be increased if the step size of scanning is reduced.
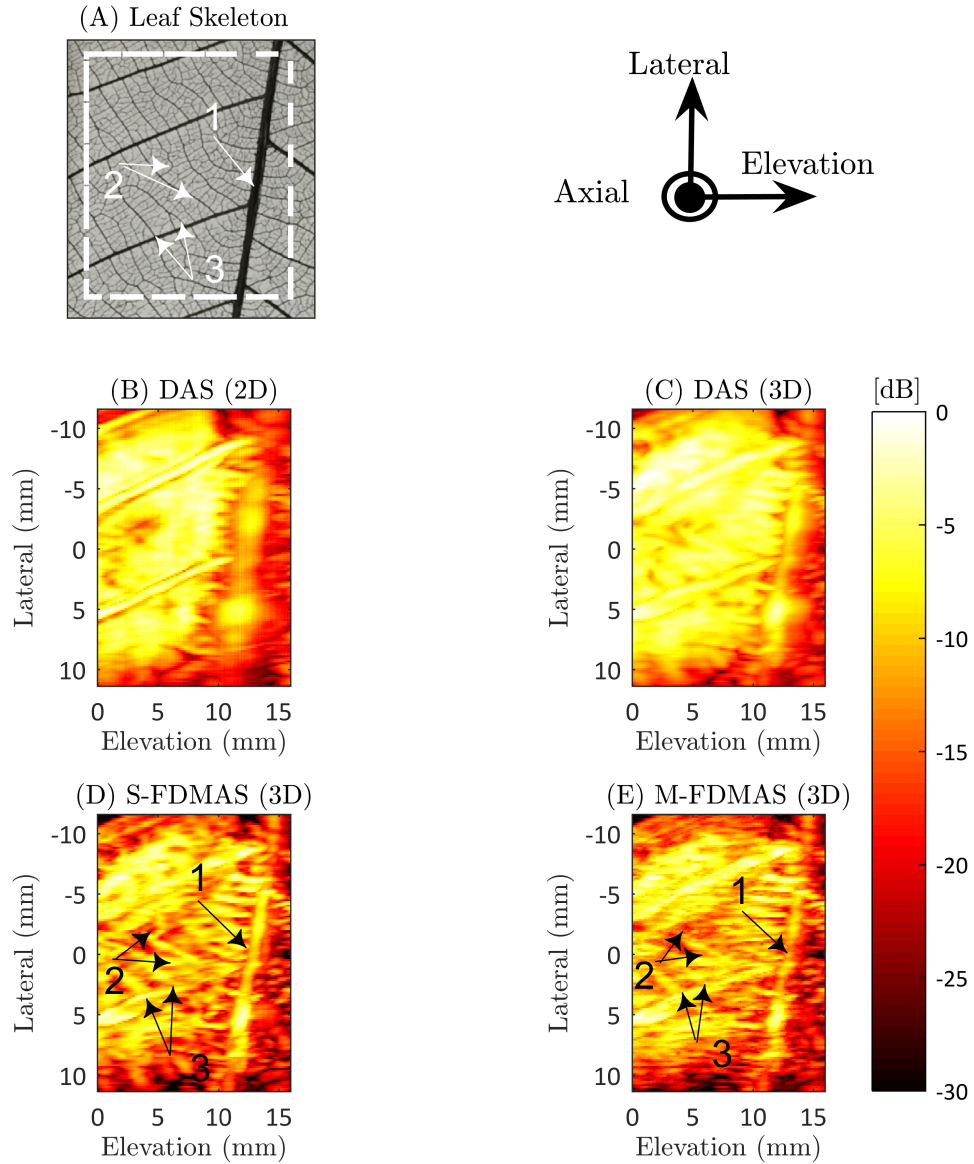
Figure 6.9: (A) Region of interest on the leaf skeleton. Photoacoustic images of the leaf skeleton using (B) DAS (2D), (C) DAS (3D), (D) S-FDMAS (3D), and (E) M-FDMAS (3D) beamformers. Dynamic range: 30 dB.

6.5 Discussion

The FDMAS (3D) beamformer showed improvement in SNR and spatial resolution over the DAS (2D) and DAS (3D) beamformers. In FDMAS (3D), the RF signals were beamformed in two steps as shown in figure 6.1. This is because the propagation of photoacoustic emissions has different shapes based on the FOV of the linear transducer. For instance, for the phantom of the carbon fibre rods (Figure 6.3), the received photoacoustic emissions of the carbon fibre rod along the elevation direction owned a circular shape, while the received photoacoustic emissions of carbon fibre rod along the lateral direction had a linear shape. As a result, the correlation operation of the FDMAS beamformer will produce high contrast difference between imaging targets. To reduce this effect, the FDMAS beamformer was applied to the lateral and elevation directions separately at the cost of increased processing time. The FDMAS (3D) beamformer significantly reduced the artefact and clutter for the tube with ink phantom (Figure 6.7 (D) and Figure 6.7 (E)). The elevation resolution will be improved and the clutter will be reduced if the size of the scanning step in the elevation direction is reduced. This will increase the number of lines participating in the correlation operations of the FDMAS beamformer. For the leaf skeleton phantom, the microscale branches were difficult to image using a low frequency transducer. This is because the high frequency part of the generated photoacoustic emissions was lost due to the transducer bandwidth. As a result, the resolution of the microscale branches will be very low, however, by using the FDMAS (3D) beamformer, the resolution of the small branches was improved. In addition, some microscale branches can be noticed clearly by using FDMAS(3D) when compared with DAS (2D) and DAS (3D) beamformers. This resolution will be better if a high frequency transducer is used. Whereas, the imaging depth will be reduced. By using the FDMAS (3D) beamformer, the resolution at the deep imaging depth can be improved.

In vivo applications, the scanning process for creating a 3D photoacoustic image by using a 1D linear array transducer cannot be achieved by using freehand scanning. This is because the step size of scanning should be known and fixed in order to beamform the 3D images. In addition, by using freehand, the step size of scanning cannot be controlled. Therefore, with in vivo applications, the scanning part, such as the breast, will be fixed on a holder and scanned by using a stepper motor with a fixed step size.

6.6 Conclusion

In this study, the FDMAS beamforming technique was applied to 3D photoacoustic imaging by using a linear array transducer. This beamforming technique improved the elevation resolution out of the elevation focal area. In addition, the correlation operation of this beamformer reduced clutter and background noise in the photoacoustic image. M-FDMAS (3D) showed improvement in the elevation resolution of 63% and 35% when compared with the DAS (2D) and DAS (3D) beamformers, respectively. It also enhanced the SNR of the photoacoustic image by 18 and 11 dB when compared with the DAS (2D) and DAS (3D) beamformers, respectively. This beamforming technique also improved the spatial resolution and SNR when it was used for imaging a tube with a complex structure and a leaf skeleton. In addition, the small branches of the leaf skeleton were enhanced with FDMAS (3D).

Chapter 7

Performance of the FDMAS Beamformer by Using Dynamic Elements

Abstract

Photoacoustic imaging is used to localise the sentinel lymph node (SLN) and track the needle to take a sample (biopsy) from it. Photoacoustic imaging is affected by artefacts, especially from the needle, when the DAS beamformer is used. The FDMAS beamformer has been used to reduce background noise and artefacts in photoacoustic imaging, however, the FDMAS beamformer amplifies the contrast difference between imaging targets. Therefore, in this chapter, the dynamic filter delay multiply and sum (D-FDMAS) beamformer was proposed and a sub-array averaging filter delay multiply and sum (SA-FDMAS) beamformer was applied to photoacoustic imaging to reduce the artefacts and contrast difference. In the needle experiment, the D-FDMAS with 16 sub-group of elements (16 D-FDMAS) beamformer reduced the contrast difference between the needle and inclusion by almost 12 dB when compared with the FDMAS beamformer. In addition, the 16 D-FDMAS beamformer improved the SNR of inclusion and needle regions by almost 5 and 8 dB, respectively, compared with the DAS beamformer.

7. PERFORMANCE OF THE FDMAS BEAMFORMER BY USING DYNAMIC ELEMENTS

7.1 Introduction

Breast cancer is one of the common forms of cancer that women suffer from. It is the cause of death more than 0.5 million women in 2012 (Heijblom *et al.*, 2015; Nounou *et al.*, 2015). An early detection of breast cancer will lead to an increase in the percentage of the survival rate (Mehrmohammadi *et al.*, 2013; Zackrisson *et al.*, 2014). Usually, surgery is needed to test if the lymph node that drains the breast is affected by malignant cells or not. In this surgery, a sample from the lymph node is taken to examine the presence of cancer cells (Garcia-Uribe *et al.*, 2015). There are different ways to perform this surgery (Garcia-Uribe *et al.*, 2015; Sivasubramanian *et al.*, 2018; Zackrisson *et al.*, 2014). For example, it could be too invasive to take a sample from most of the axillary lymph nodes (ALN). The drawback of this technique is the surgical side effects. The patient could face arm numbness, upper extremity lymphedema and impaired shoulder mobility (Sivasubramanian *et al.*, 2018). There is another technique which is less invasive. In this surgery, the sample is taken from the SLN which is the nearest lymph node to the cancer (Garcia-Uribe *et al.*, 2015). In this technique, first the location of the SLN will be defined by injecting some dyes, such as the methylene Blue (MB), near the tumour. As a result, the dye will spread through the lymphatic system to the SLN where a sample will then be taken for examination (Garcia-Uribe *et al.*, 2015). This technique also has some side effects such as lymphedema and seroma formation (Sivasubramanian *et al.*, 2018).

Some researchers have investigated photoacoustic imaging to localise the SLN and provide the guidance for taking a sample from it (Kim *et al.*, 2010b,c; Sivasubramanian *et al.*, 2018). In this technique, some dyes which have narrow absorption spectrums, such as MB and indocyanine green (ICG), will be injected near the tumour. This dye will spread through the lymphatic system to the SLN, then be identified to localise the SLN by firing a nano-scale laser pulse near the tumour. The wavelength of this laser pulse matches the peak absorption spectrum of the dye. As a result, photoacoustic emissions will be generated due to thermoelastic expansion. This photoacoustic emission will be detected using an ultrasound transducer and beamformed to create a photoacoustic image. By using the photoacoustic image, the SLN will be localised, then a needle will take a sample minimal-invasively (Kim *et al.*, 2010b,c; Sivasubramanian *et al.*, 2018).

In photoacoustic imaging, when a linear array transducer is used for recording the photoacoustic emissions, the image will be affected by clutter and phase aberration (Jaeger *et al.*, 2013; Park *et al.*, 2008a; Preisser *et al.*, 2016). As a result, the contrast and spatial resolution of photoacoustic imaging will be degraded when DAS is used (Park *et al.*, 2007, 2008a). There are some adaptive beamforming techniques used to reduce the effect of clutter and phase aberration in photoacoustic imaging, such as short-lag spatial coherence weight (Alles *et al.*, 2014), minimum variance (MV) (Park *et al.*, 2008a) and FDMAS (Alshaya *et al.*, 2016). The FDMAS beamformer enhances the correlated delayed RF signals. This beamformer could affect the contrast difference between the imaging targets having different RF signal shapes. For instance, the contrast difference between the needle and the SLN will be affected. In addition, the contrast of the imaging structure along the lateral direction will be affected by the imaging structure along the elevation direction.

In this chapter, the dynamic filter delay multiply and sum (D-FDMAS) beamformer is proposed. This beamformer depends on the correlation operation between sub-group transducer elements to reduce the contrast difference between imaging targets that have different propagation shapes and decrease the effect of clutter and phase aberration on photoacoustic imaging. In this chapter, the sub-array averaging filter delay multiply and sum (SA-FDMAS) used in ultrasound imaging (Su *et al.*, 2018) is also applied to photoacoustic imaging and compared with the D-FDMAS beamformer in terms of SNR, contrast ratio (CR), spatial resolution and computation time. This chapter is organised as follows: first, the theoretical analysis of SA-FDMAS and D-FDMAS is provided. Second, SA-FDMAS and D-FDMAS are compared with some beamforming techniques in teams of SNR and spatial resolution based on simulations. Third, these beamforming techniques are compared in terms of SNR, CR and spatial resolution with different experimental measurements. A discussions and conclusion finalise the chapter.

7.2   Methods

7.2.1   SA-FDMAS Beamformer

The FDMAS beamforming technique depends on the correlation between the delayed RF signals from each transducer element as shown in equation 7.1 (Matrone *et al.*,

7. PERFORMANCE OF THE FDMAS BEAMFORMER BY USING DYNAMIC ELEMENTS

2015):

$$y_{\text{FDMAS}} = \left\{ \sum_{i=1}^{N-1} \sum_{j=i+1}^{N} \text{sgn}(S_i(t)S_j(t)).\sqrt{|S_i(t)S_j(t)|} \right\} * f, \qquad (7.1)$$

where N is the number of transducer elements, $S_i(t)$ and $S_j(t)$ are the delayed RF signals for transducer element i and j, respectively. The sgn and square root operations are used to remove the effect of the multiplication operation on the sign and the unit of the beamformed data. f is the band pass filter to remove the DC and low frequencies. T. Su *et al.* (Su *et al.*, 2018) improved the energy of the beamforming data when using the FDMAS beamforming technique. This improvement was achieved by multiplying the delayed RF signals with themselves. In addition, the covariance matrix was investigated to perform sub-array averaging for the FDMAS beamformer (SA-FDMAS). The equation of the covariance matrix is shown in equation 7.2 (Su *et al.*, 2018):

$$R_{\text{out}} = \frac{1}{N-L+1} \sum_{l=1}^{N-L+1} X_l(t)X_l^H(t), \qquad (7.2)$$

where R_{out} is the output of the covariance matrix, L is the size of sub-group transducer elements, $X_l(t)$ is a sub-group of transducer elements ($X_l(t) = [x_l(t), x_{l+1}(t), ..., x_{l+L-1}(t)]^{T_{tp}}$) (Su *et al.*, 2018). T_{tp} means transpose of the vector. H is the complex conjugate. If the size of the sub-group is equal to the whole number of transducer elements (N), the covariance matrix is given in equation 7.3 (Su *et al.*, 2018):

$$R_{L=N} = \begin{bmatrix} x_{11}(t) & x_{12}(t) & ... & x_{1N}(t) \\ x_{21}(t) & x_{22}(t) & ... & x_{2N}(t) \\ . & . & ... & . \\ . & . & ... & . \\ x_{N1}(t) & x_{N2}(t) & ... & x_{NN}(t) \end{bmatrix}, \qquad (7.3)$$

To apply the covariance matrix to the FDMAS beamformer, the sign and square root

operations will be applied as explained in equation 7.4 (Su *et al.*, 2018):

$$m_{ij} = \text{sgn}(x_{ij})\sqrt{\mid x_{ij} \mid},$$

$$M_{(L=N)} = \begin{bmatrix} m_{11}(t) & m_{12}(t) & ... & m_{1N}(t) \\ m_{21}(t) & m_{22}(t) & ... & m_{2N}(t) \\ . & . & ... & . \\ . & . & ... & . \\ m_{N1}(t) & m_{N2}(t) & ... & m_{NN}(t) \end{bmatrix}, \tag{7.4}$$

To extract the FDMAS beamformer from equation 7.4, equation 7.5 will be used (Su *et al.*, 2018):

$$y_{\text{FDMAS}} = 0.5[sum(M_{(L=N)}) - trace(M_{(L=N)})] * f, \tag{7.5}$$

However, in the SA-FDMAS beamformer, the trace is not subtracted to emphasise the energy of the beamformed signal, as shown in equation 7.6 (Su *et al.*, 2018):

$$y_{\text{SA-FDMAS}} = 0.5[sum(M_{(L=N)}) + trace(M_{(L=N)})] * f, \tag{7.6}$$

The size of sub-group elements will affect the resolution, CR, and SNR of the image. Moreover, the SA-FDMAS beamformer has high computation time due to the number of multiplications that can be calculated using equation 7.7:

$$NU_{\text{SA-FDMAS}} = \left(\frac{L^2 - L}{2} + L\right) \times \left(N - L + 1\right). \tag{7.7}$$

7.2.2 D-FDMAS Beamformer

For the D-FDMAS beamformer, a group of delayed RF signals for transducer elements will be correlated with each other. The idea of the D-FDMAS beamformer is taken from the Sub-FDMAS beamformer (Chapter 5). However, in the D-FDMAS beamformer, the delayed RF signal for each transducer element is correlated with itself to emphasise

the energy of the beamformed data, as given in equation 7.8:

$$
y_{\text{D-FDMAS}} = \left\{ \sum_{i=1}^{N} \sum_{j=i}^{m} \operatorname{sgn}(S_i(t)S_j(t)).\sqrt{|S_i(t)S_j(t)|} \right\} * f,
$$

(7.8)

$$
m = \begin{cases} i + L - 1 & L \leq N - i \\ N & \text{else} \end{cases},
$$

where L is the size of the sub-group elements. In this beamformer, not all transducer elements correlate with each other to avoid making correlation operation between the delayed RF signals for the transducer elements that receive weak photoacoustic emission with others. This reduces the contrast difference between imaging targets. In this beamforming technique, each delayed RF signal will be also correlated with itself to emphasise the energy of the beamformed data as have done in SA-FDMAS (Su *et al.*, 2018). The multiplication number of D-FDMAS can be calculated using equation 7.9:

$$
NU_{\text{D-FDMAS}} = LN - \left(\frac{L^2 - L}{2} \right).
$$

(7.9)

From equation 7.7 and equation 7.9, the computation time of the D-FDMAS beamformer is much lower than that of the SA-FDMAS beamformer. For example, if the number of transducer elements was 128 and the size of the sub-group was 32 elements, the number of multiplications for the D-FDMAS beamformer would be 3,600. However, the number of multiplications for the SA-FDMAS beamformer is 51,216. As a result, the number of multiplications of the D-FDMAS beamformer is less than that of SA-FDMAS beamformer by 47,616 multiplications.

7.3 Simulation Setup

In the simulation, the K-wave toolbox (Treeby & Cox, 2010) was used to generate the photoacoustic emissions from the absorbers. These emissions were received by a linear array transducer that had 128 elements. Its central frequency and -6 dB bandwidth were 7 MHz and 90 %, respectively. Ten absorption points with a diameter of 0.1 mm were simulated. These absorption points were separated by 5 mm in the axial direction. The distance between the first absorption point and the ultrasound transducer surface

was 5 mm. The speed of sound and the ultrasound attenuation coefficient in the medium were set to 1520 m/s and 0.9 dB/MHz/cm, respectively. The sampling frequency was 80 MHz. After the RF signals were generated, they were used to study the effect of the group size of elements on photoacoustic images by using SA-FDMAS and D-FDMAS beamformers in terms of spatial resolution and SNR. In addition, they were used to make comparisons between DAS, FDMAS, MV, SA-FDMAS and D-FMDAS in terms of resolution and SNR.

7.4 Simulation Results

7.4.1 SA-FDMAS Beamformer

Figure 7.1 shows the photoacoustic images beamformed by using SA-FDMAS with different sub-groups of elements. The artefacts were reduced when the size of sub-group elements was increased until the sub-group size exceeded 64 elements. The highest amplitude of artefacts was obtained when there were 4 elements in each sub-group. The amplitude of these artefacts was significantly reduced when the sub-group had 64 elements. Figure 7.2 shows the point spread function in the lateral direction for the absorption points located at 5 and 30 mm, respectively. For the absorption point with a depth of 5 mm (figure 7.2 (A)), its side lobes were reduced as the sub-group size was increased as shown in Table 7.1. For instance, the peak amplitude of the side lobes was -25.92 dB when the sub-group had 4 elements. This peak amplitude of the side lobes was decreased to -37.77 dB when the sub-group had 64 elements. However, the -6 dB lateral resolution was slightly reduced when the sub-group size was increased, as shown in Table 7.2. This is because the FOV of the transducer element was narrow at a location close to the transducer surface. This differs from the case for the absorption point with a depth of 30 mm as shown in Figure 7.2 (B) and Table 7.2. The -6 dB lateral resolution was improved when the size of the sub-group was increased. For example, the lateral resolution was 1.86 mm when the sub-group had 4 elements. It was improved to be 1.52 mm with a sub-group of 64 elements. In addition, by using 128 elements, the lateral resolution of the absorption point located at the depth of 30 mm was 1.64 mm, which was worse than using 64 elements. This is because by using 128 elements, the beamformed signal was not enhanced by the covariance matrix.
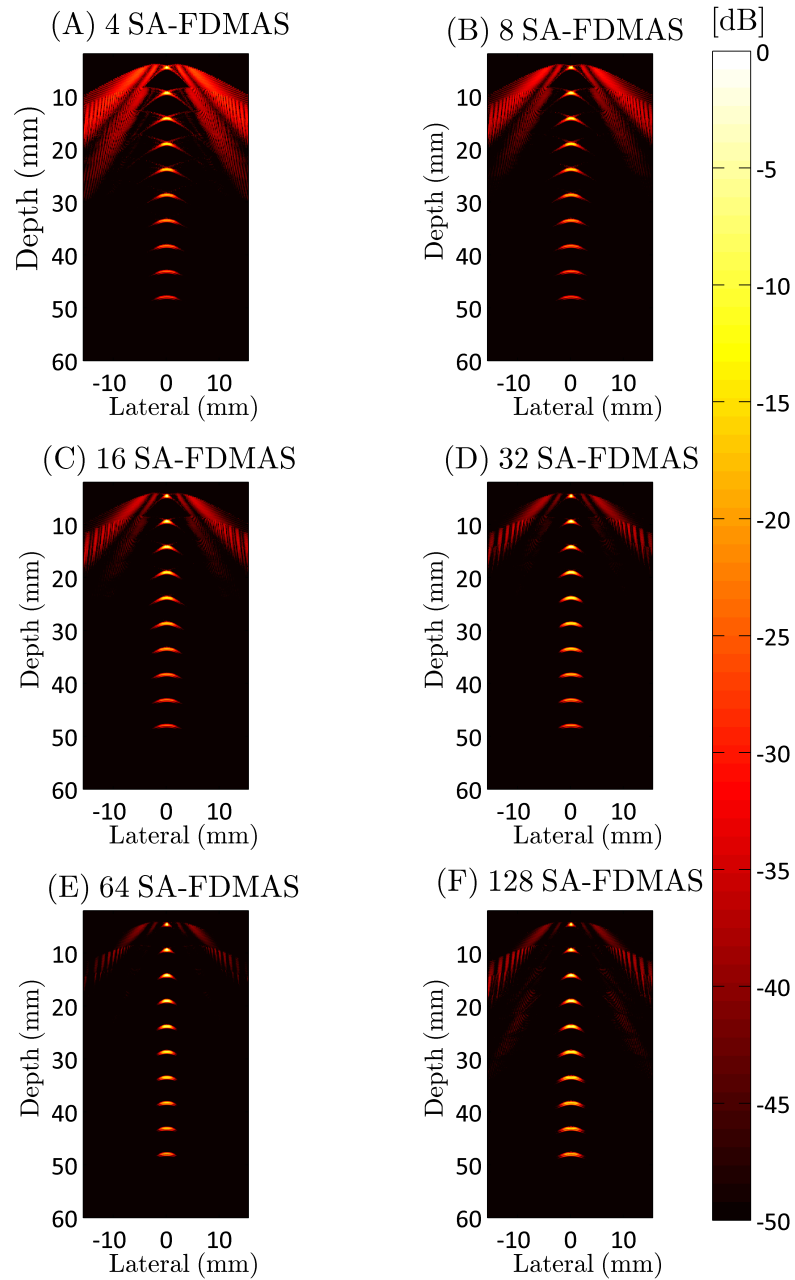
Figure 7.1: Photoacoustic images beamformed by using SA-FDMAS with different sub-groups of elements. (A) Sub-group of 4 elements. (B) Sub-group of 8 elements, (C) Sub-group of 16 elements. (D) Sub-group of 32 elements. (E) Sub-group of 64 elements. (F) Sub-group of 128 elements. Dynamic range: 50 dB.
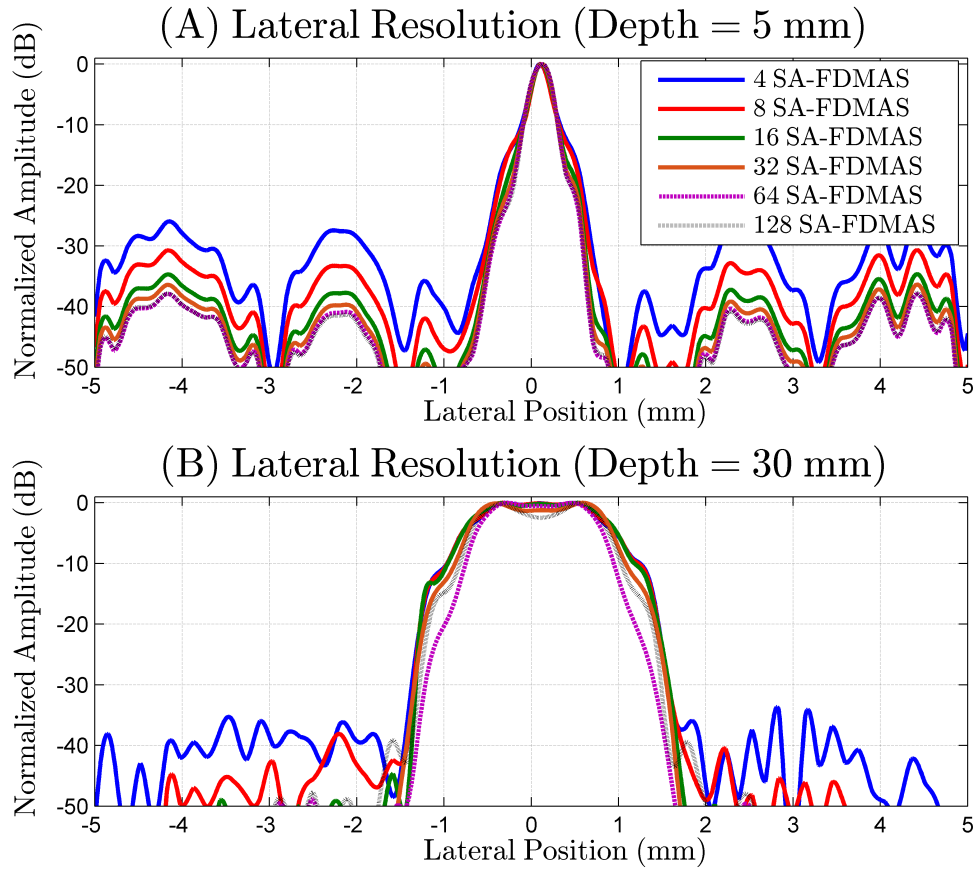
Figure 7.2: Lateral resolution of the absorption points at the depth of (A) 5 mm and (B) 30 mm depth when the SA-FDMAS beamformer was used.

SA-FDMAS	Depth (5 mm)	Depth (30 mm)
Sub-group	Peak Sidelobe level (dB)	
4	-25.92	-33.76
8	-30.70	-38.11
16	-34.65	-44.65
32	-36.37	-51.87
64	-37.77	-48.91
128	-37.77	-39.12

Table 7.1: Peak sidelobe level of the absorption points beamformed by using the SA-FDMAS beamformer.

SA-FDMAS	Depth (5 mm)	Depth (30 mm)
Sub-group	- 6 dB Lateral Resolution (mm)	
4	0.29	1.86
8	0.26	1.86
16	0.29	1.85
32	0.30	1.72
64	0.31	1.52
128	0.31	1.64

Table 7.2: -6 dB lateral resolution of the absorption points beamformed by using the SA-FDMAS beamformer.

7.4.2 D-FDMAS Beamformer

Figure 7.3 shows the photoacoustic images beamformed by D-FDMAS with different sub-groups of elements. The lowest artefact amplitude was obtained when the sub-group had 16 and 32 elements. The effect of the sub-group size when using D-FDMAS on lateral resolution (-6 dB) is shown in figure 7.4 and Table 7.3. For the 5 mm deep absorption point, the lowest side lobes were obtained when 16 or more elements were used in a sub-group as shown in Table 7.4. In addition, the lateral resolution (-6 dB) was decreased when the sub-group had 16 or more elements, as shown in Table 7.3. This is due to the limited FOV of the transducer elements. For the absorption point

at the depth of 30 mm, the lowest side lobes were obtained when the sub-group had 16 elements (Peak sidelobe level = -45.31 dB) and 32 elements (Peak sidelobe level = -50 dB). In addition, the -6 dB lateral resolution of this absorption point was improved as the sub-group size increased due to the FOV of the transducer elements became broader when the depth was increased. As a result, most transducer elements received photoacoustic emissions and this emphasised the correlation operation.
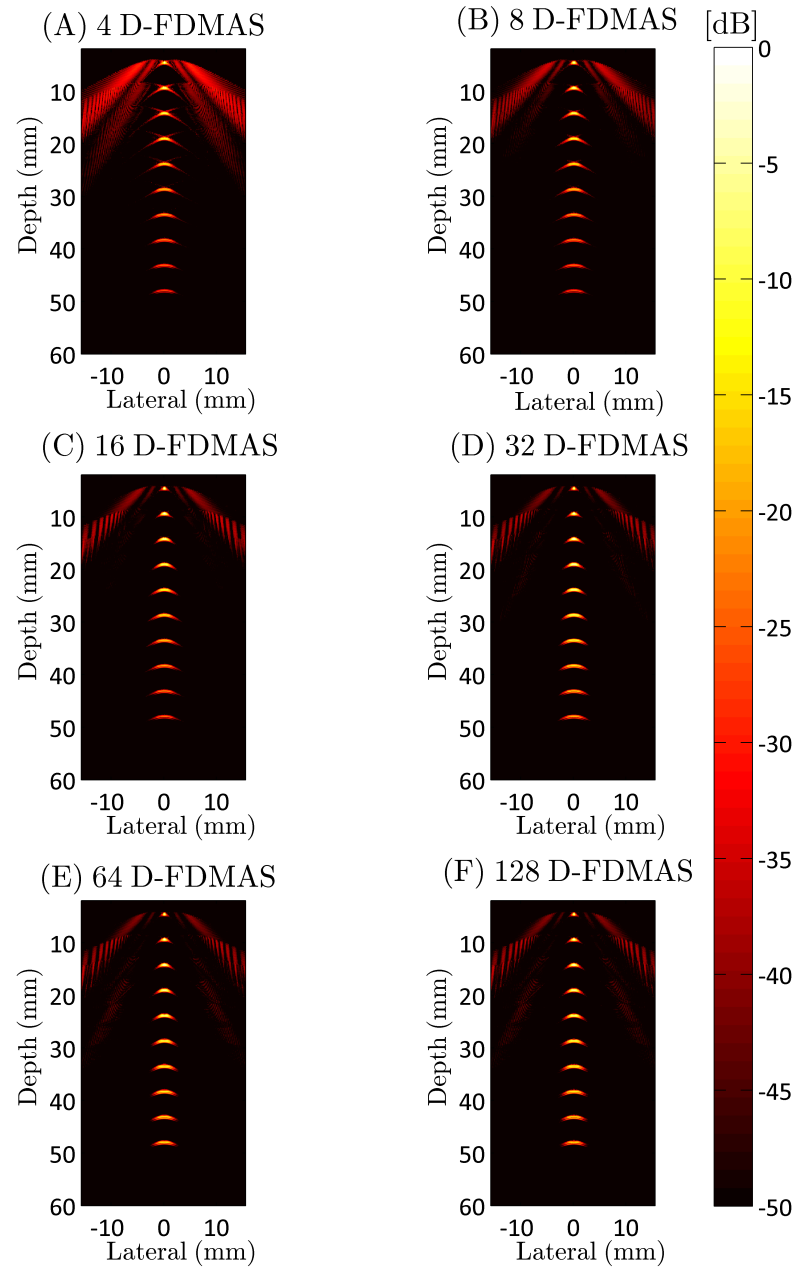
Figure 7.3: Photoacoustic images beamformed by using D-FDMAS with different subgroups of elements. (A) Sub-group of 4 elements. (B) Sub-group of 8 elements. (C) Sub-group of 16 elements. (D) Sub-group of 32 elements. (E) Sub-group of 64 elements. (F) Sub-group of 128 elements. Dynamic range: 50 dB.
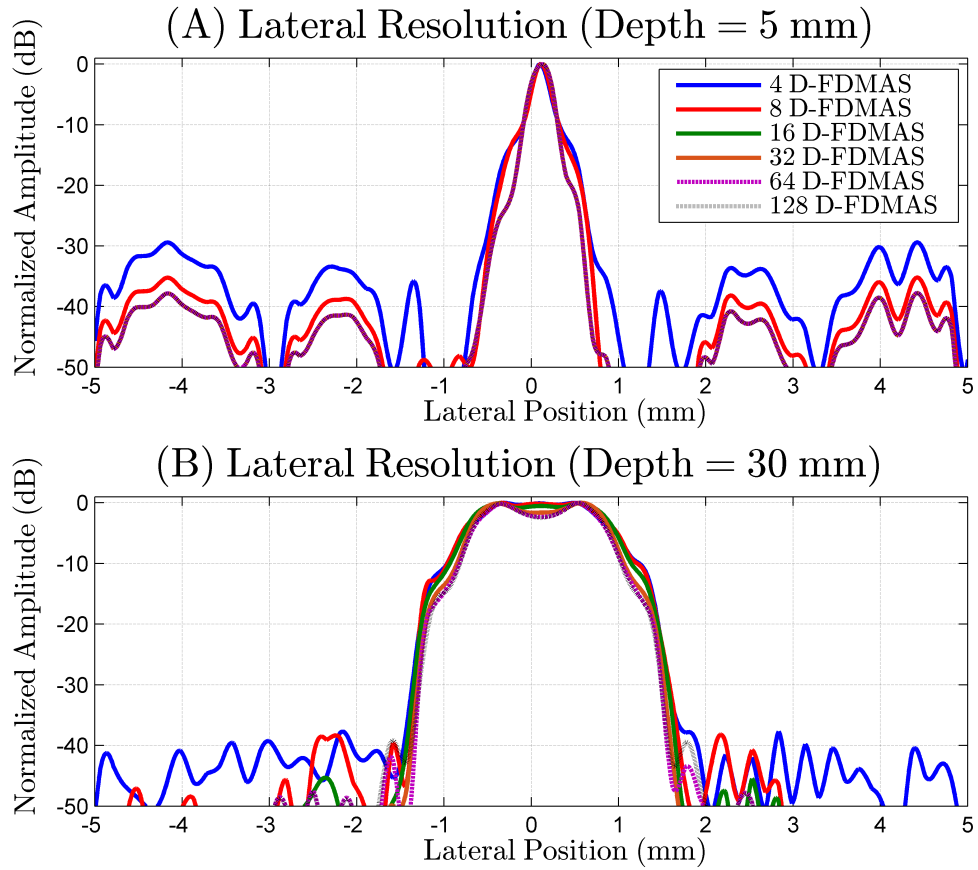
Figure 7.4: Lateral resolution of the absorption points at the depth of (A) 5 mm and (B) 30 mm depth when the D-FDMAS was used.

D-FDMAS	Depth (5 mm)	Depth (30 mm)
Sub-group	- 6 dB Lateral Resolution (mm)	
4	0.27	1.86
8	0.27	1.86
16	0.31	1.81
32	0.31	1.70
64	0.31	1.64
128	0.31	1.64

Table 7.3: -6 dB lateral resolution of the absorption points beamformed by using the D-FDMAS beamformer.

D-FDMAS	Depth (5 mm)	Depth (30 mm)
Sub-group	Peak Sidelobe level (dB)	
4	-29.41	-37.71
8	-35.20	-38.11
16	-37.77	-45.31
32	-37.77	-50
64	-37.77	-41.86
128	-37.77	-39.12

Table 7.4: Peak sidelobe level of the absorption points beamformed by using the D-FDMAS beamformer.

7.4.3 Comparison Different Beamforming Techniques

The 32 D-FDMAS beamforming technique was compared with DAS, MV with the sub-group of 42 elements (42 MV), FDMAS and 64 SA-FDMAS beamforming techniques in terms of the photoacoustic images (Figure 7.5) and point spread function (Figure 7.6). For figure 7.5, the photoacoustic image beamformed by DAS (Figure 7.5 (A)) had high-level artefacts, which were slightly reduced by using 42 MV (Figure 7.5 (B)). The reduction of artefacts depends on the sub-array size where 42 elements were employed in this case. The FDMAS beamformer decreased significantly the artefacts as shown in figure 7.5 (C). The computation time was calculated for each beamforming technique

by using an i5-4460 CPU 3.2 GHz processor, 16 GB RAM and MATLAB R2014a as shown in figure 7.7. In this calculation, the range of the image depth was 2 mm to 60 mm. In addition, the lateral step size was $\lambda/2$. The sampling frequency was also 80 MHz. The FDMAS beamformer (Computation time = 252 second) has high computation time when compared with the DAS beamformer (Computation time = 5 second). This made the FDMAS beamforming technique unsuitable for applications that need a high frame rate such as real time monitoring. By using the 64 SA-FDMAS beamformer (Figure 7.5 (D)), the contrast of the image was emphasised compared with that of using the FDMAS beamformer. The drawback of 64 SA-FDMAS is that its computation time is much higher than when using FDMAS as shown in figure 7.7. The 32 D-FDMAS beamformer (Figure 7.5 (E)), reduced more artefacts when compared with other beamformers, except 64 SA-FDMAS. The advantage of the 32 D-FDMAS beamformers over the 64 SA-FDMAS beamformer is the computation time which is much less than that of using the FDMAS beamformer. The 32 D-FDMAS beamformer also reduced the side lobes compared with DAS and 42 MV beamformers as shown in figure 7.6 and Table 7.5. From figure 7.6, it can be seen that the point spread functions which were the result of the DAS beamformer and the 42 MV beamformer for the absorption point with a depth of 5 mm overlapped. In addition, the point spread functions that were created by using the 64 SA-FDMAS beamformer and the 32 D-FDMAS beamformer for the same absorption point also overlapped. In term of -6 dB lateral resolution, the 32 D-FDMAS beamformer provided improved results than DAS and 42 MV beamformers for the point that was close to the ultrasound transducer surface as shown in figure 7.7. However, 32 D-FDMAS did not improve the lateral resolution of the point at the depth of 30 mm as shown in figure 7.7. This issue can be addressed by increasing the size of the sub-group.
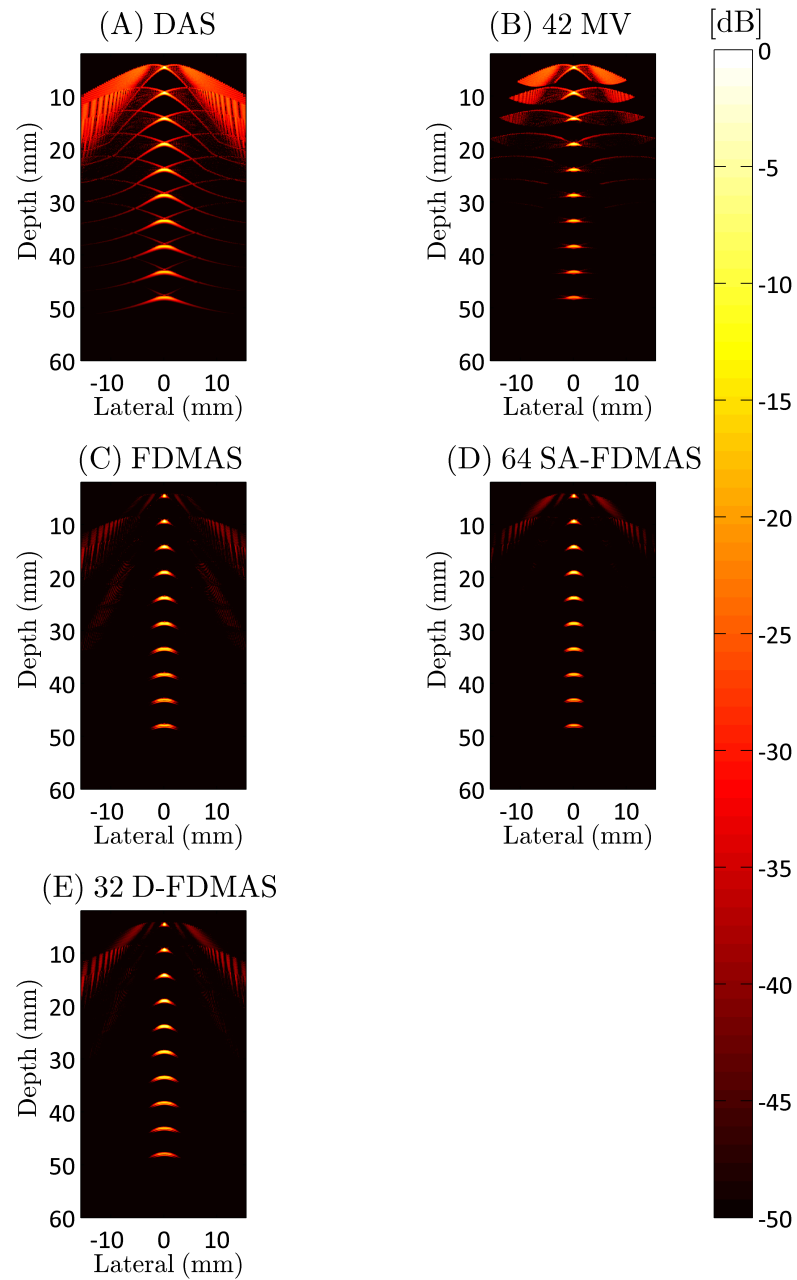
Figure 7.5: Photoacoustic images beamformed by using (A) DAS, (B) 42 MV, (C) FDMAS, (D) 64 SA-FDMAS, and (E) 32 D-FDMAS. Dynamic range : 50 dB.
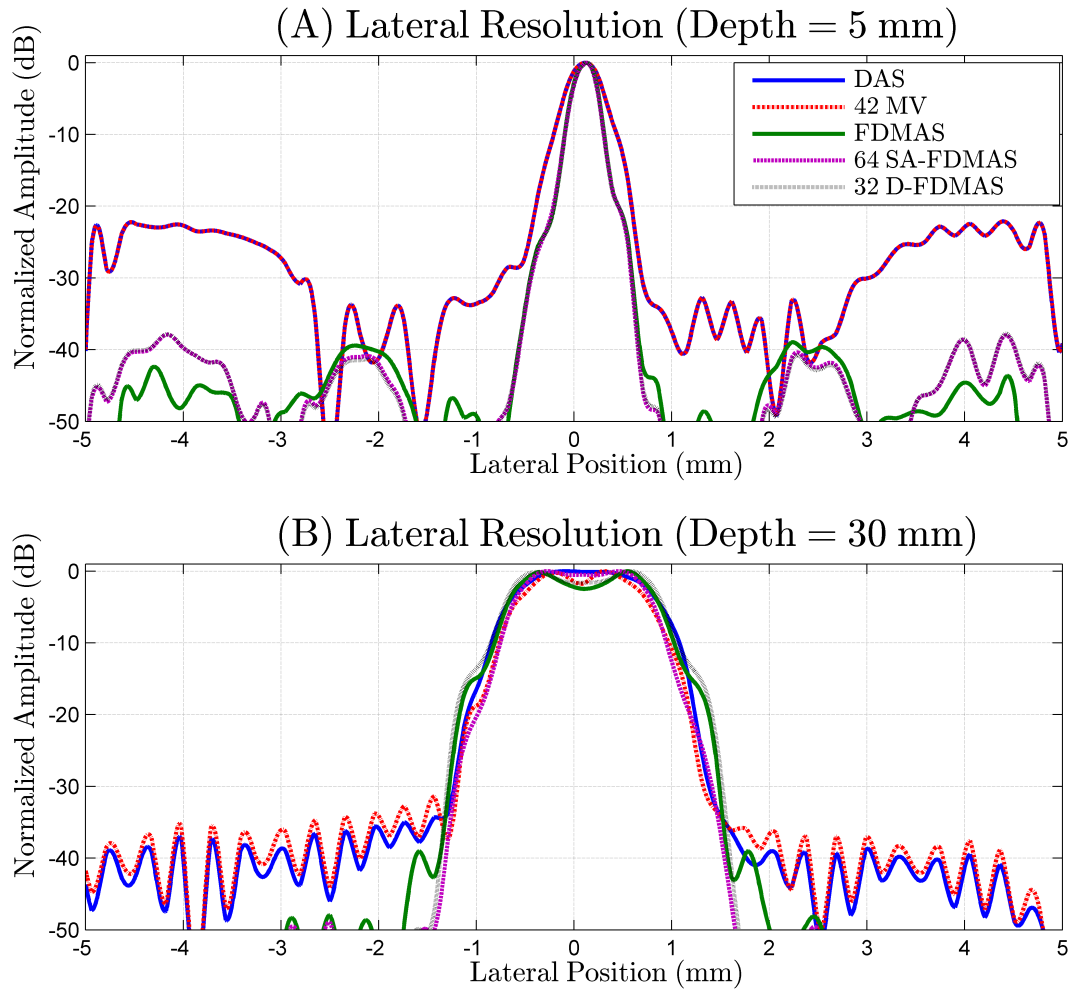
Figure 7.6: Lateral resolutions of the point targets located at the depth of (A) 5 mm and (B) 30 mm, respectively, when using DAS, 42MV, FDMAS, 64 SA-FDMAS, and 32 D-FDMAS beamforming techniques.
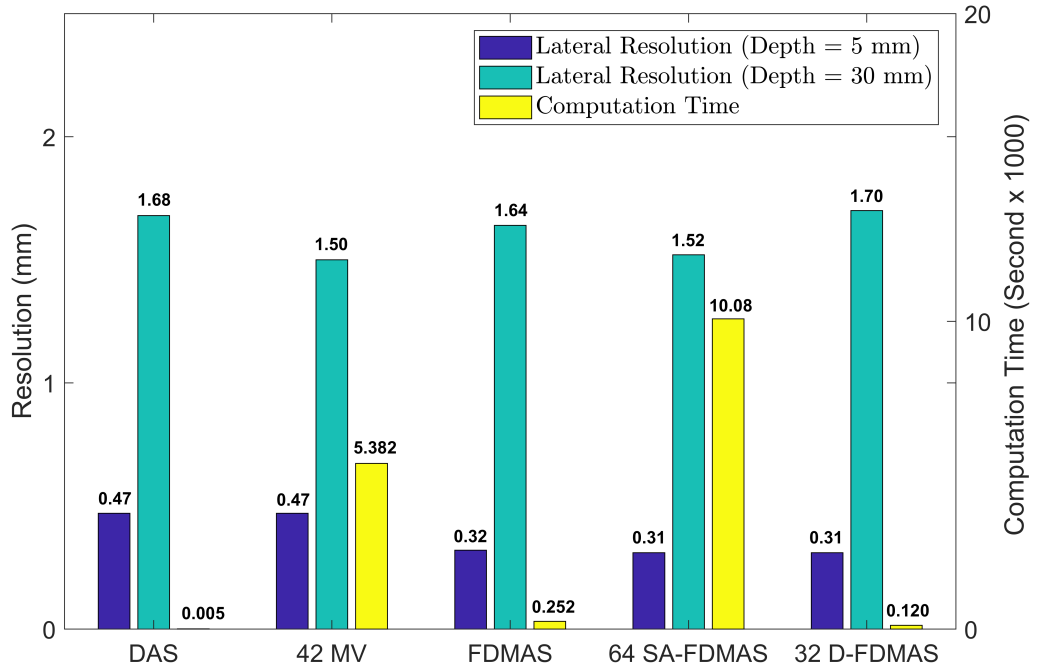
Figure 7.7: Lateral resolutions (-6 dB) and computation time for the DAS, 42 MV, FDMAS, 64 SA-FDMAS and 32 D-FDMAS beamformers.

	Depth (5 mm)	Depth (30 mm)
Beamforming Technique	**Peak Sidelobe Level (dB)**	
DAS	-22.24	-34.99
42 MV	-22.24	-31.37
FDMAS	-39.46	-39.04
64 SA-FDMAS	-37.77	-48.91
32 D-FDMAS	-37.77	-41.86

Table 7.5: Peak sidelobe level using different beamforming techniques for the points with a 5 and 30 mm depth.

In this simulation, noise was added to the RF signals to investigate the effect of the beamforming techniques on reducing background noise. Noise was added by using the K-wave toolbox (Treeby & Cox, 2010) to have a SNR (RMS) of 0 dB. Figure 7.8

shows the photoacoustic images beamformed by using DAS, 42 MV, FDMAS, 64 SA-FDMAS, and 32 D-FDMAS beamforming techniques. The background noise was high when the photoacoustic image was beamformed by using DAS and 42 MV beamformers (Figure 7.8 (A) and (B)). The SNR of the point targets that was the ratio between the mean of the signal and the standard deviation of background noise (Wang *et al.*, 2017), was calculated as shown in figure 7.9. The average SNRs of the absorption points beamformed by DAS and 42 MV were 12.34 dB and 11.40 dB, respectively. The FDMAS beamformer (Figure 7.8 (C)) significantly reduced noise, achieving an average SNR of 15.03 dB. The 64 SA-FDMAS beamformer (Figure 7.8 (D)) provided an average SNR of 16.52 dB, which was better than the FDMAS beamformer. For the 32 D-FDMAS beamformer (Figure 7.8 (E)), the average SNR of 16.10 dB was achieved which was comparable when using 64 SA-FDMAS but with much less computation time as shown in figure 7.9. As a result, the 32 D-FDMAS beamformer balances the SNR and computation time of beamforming, which could be beneficial for real-time applications such as image-guided sample taking from the SLN (Kim *et al.*, 2010b).
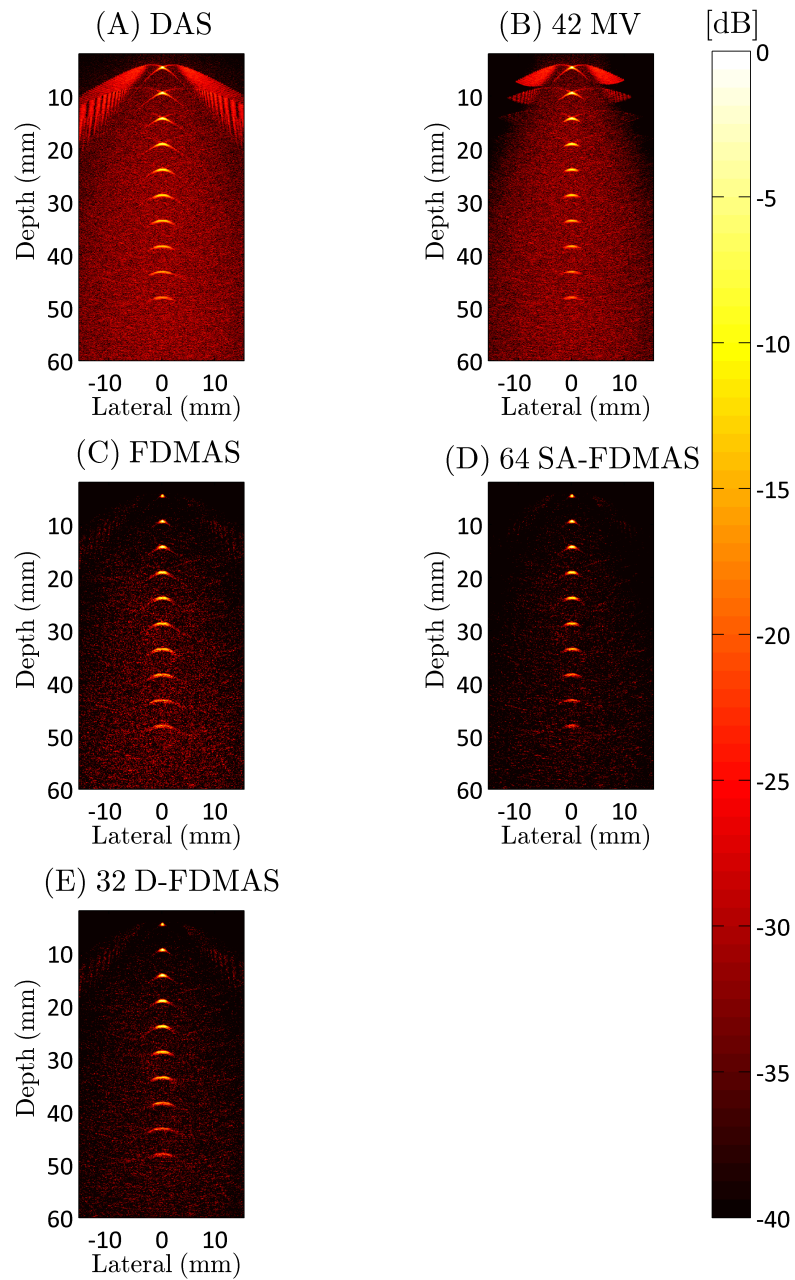
Figure 7.8: Photoacoustic images beamformed by (A) DAS, (B) 42 MV (C) FDMAS, (D) 64 SA-FDMAS, and (E) 32 D-FDMAS beamforming techniques. The SNR (RMS) of the RF signals was 0 dB after noise addition and the dynamic range was 40 dB.
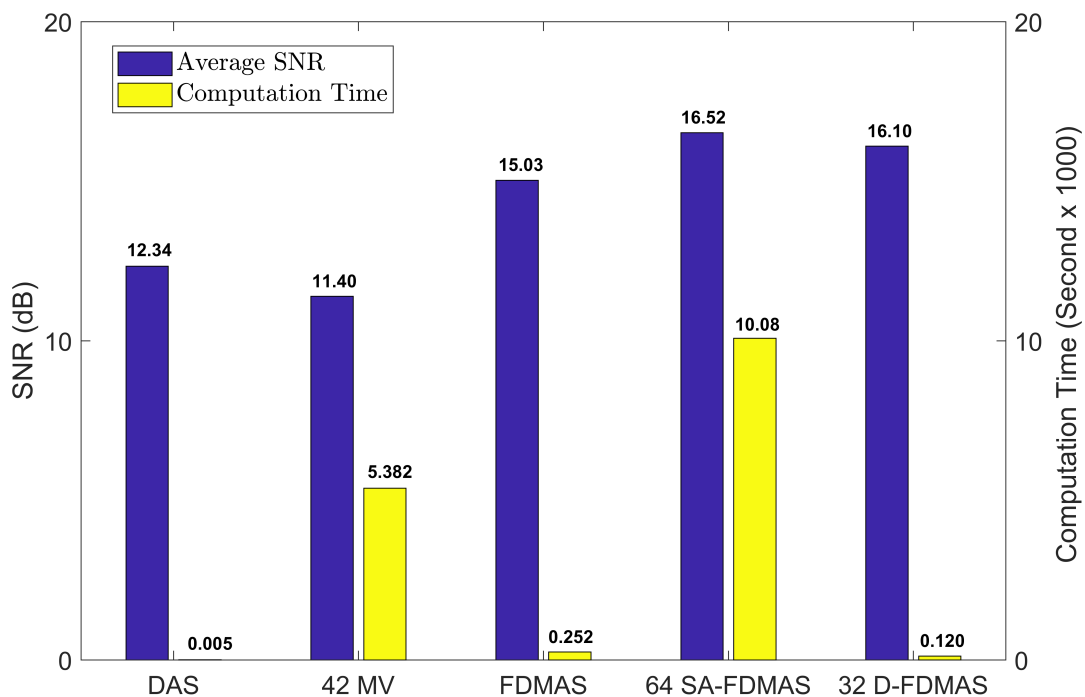
Figure 7.9: Average SNRs of point targets at different depths and computation time for the DAS, 42 MV, FDMAS, 64 SA-FDMAS and 32 D-FDMAS beamformers.

7.5 Experiments

7.5.1 Phantoms

Three experiments were performed as illustrated in figure 7.10. In the first experiment (Figure 7.10 (B)), two carbon fibre rods were used. One rod was along the lateral direction of the linear array transducer and the other was placed along the elevation direction. These carbon fibre rods were inserted inside the turbid polyacrylamide hydrogel. The recipe of this phantom was taken from (Choi *et al.*, 2013). The optical scattering coefficient was 3 cm^{-1} by adding 1.1 μm latex beads. The optical scattering was calculated using the Mie Scattering calculator (Prahl, 2017). This phantom was used to study the effect of SA-FDMAS and D-FDMAS beamformers on the contrast difference and the lateral resolution.

In the second experiment, an agar phantom with an inclusion was used (Figure

7.10 (C)). The phantom (Browne *et al.*, 2003; Nie *et al.*, 2018) consisted of 4% of agar powder (Acros, Organics), 6% of gelatin (Sigma, G2500-1KG), 2% of germall (Gracefruit, Germall Plus), and 88% of degassed and de-ionised water. The inclusion was created with the same steps that were used to create the agar phantom although the agar powder was not used. In addition, 20% of the materials were black India ink (Dr.Ph.Martins, Black Star). Subsequently, this mixture was injected inside a hole that was created inside the agar phantom, as shown in figure 7.10 (C). The inclusion located at a depth of 12 mm was used to mimic a SLN. A needle was guided to the inclusion to study the effects of different beamforming techniques on the SNR and contrast difference between the needle and the inclusion.

In the third experiment, D-FDMAS and SA-FDMAS beamformers were applied to in-vivo investigations. These two beamformers were used to image cross sections of blood vessels of a healthy human hand (dotted line in figure 7.10 (D)). In this experiment, the effects of these beamformers on the contrast difference and lateral resolution of the blood vessel were investigated.

7.5.2 Experimental Setup

The experimental setup is shown in figure 7.10 (A). The Nd:YAG laser was used to generate photoacoustic emissions from the phantom. The PRF of the laser source was 10 Hz, and the pulse length was 7 ns. The laser pulses were guided to the phantom through an optical fibre (BF76LS01, Thorlabs). This optical fibre has one input and seven outputs which were arranged on one side of the linear array transducer. The diameter of each optical fibre output was 0.6 mm with a 0.39 NA number. The wavelength and the output energy per pulse in this experiment were 850 nm and 3.7 mJ, respectively. The generated photoacoustic emissions were detected using a linear array transducer (Verasonics L11-4v) with 128 elements. The centre frequency of this transducer was 7.5 MHz, and its -6 dB bandwidth was 90 %. The RF signals were detected via the UARP II with a sampling rate of 80 MS/s. The RF signals were averaged 100 times before beamforming with MATLAB (R2014a, MathWorks).
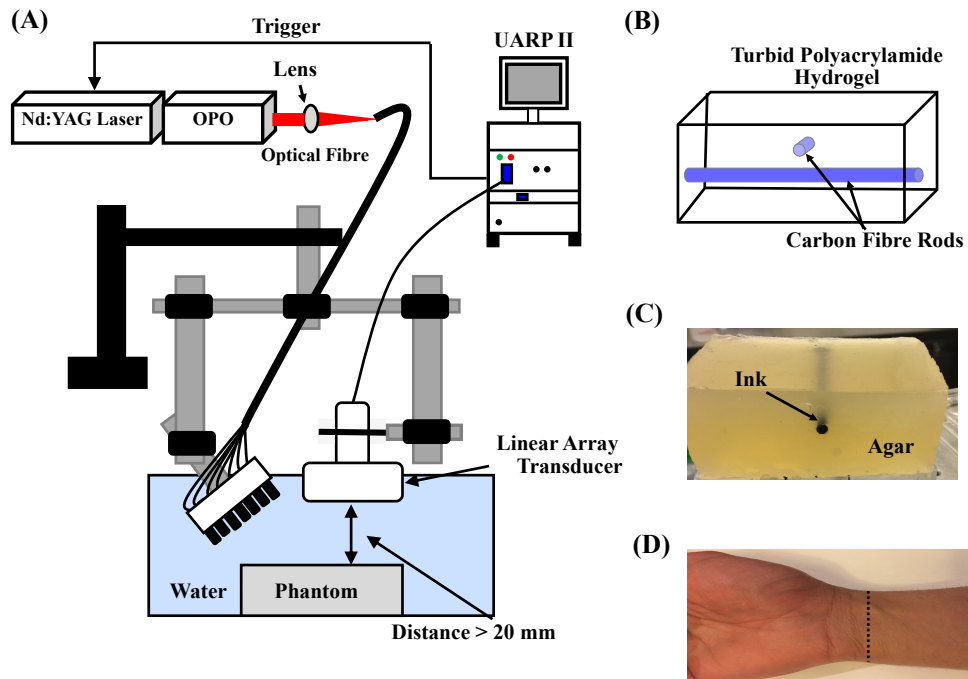
Figure 7.10: (A) Experimental setup by using a Nd-YAG laser and the UARP II. (B) Turbid polyacrylamide hydrogel with two carbon fibre rods. (C) Agar phantom with an ink inclusion. (D) A healthy human hand.

7.5.3   Experimental Results

Carbon Fibre Rods Phantom

The experimental results of the carbon fibre rods phantom using SA-FDMAS and D-FDMAS with different sub-groups of elements are shown in figures 7.11 and 7.12, respectively. The artefacts and noise were reduced when the sub-group size was increased for both SA-FDMAS and D-FDMAS beamformers. However, the contrast of the carbon fibre rod along the lateral direction was significantly reduced with respect to that along the elevation direction for a sub-group having more than 32 elements. This is because the propagation shape RF signals of the carbon fibre rod along the lateral direction of the transducer was not circular, as shown in figure 7.13. As a result, the contrast of the carbon fibre rod along the lateral direction was affected by the size of the sub-group. This effect was calculated for SA-FDMAS and D-FDMAS as given in

Table 7.6 and Table 7.7. The calculation of the contrast ratio is based on equation 7.10 (Hverven *et al.*, 2017):

$$CR = 20\log_{10}\left(\frac{\mu_{\text{Signal}}}{\mu_{\text{Background}}}\right), \tag{7.10}$$

where CR is the contrast ratio, μ_{Signal} is the mean of the target signal, and $\mu_{\text{Background}}$ is the mean of the background. Figure 7.11 (A) shows the areas that were used to calculate the contrast ratio of the photoacoustic images. The solid rectangle number 1 and number 2 show the signal regions of carbon fibre rods along the elevation and lateral directions, respectively, and the dashed rectangle shows the background region. From Table 7.6 and Table 7.7, the contrast difference was increased as the sub-group size was increased. In addition, the contrast difference of the photoacoustic images when using the D-FDMAS beamformer was largely affected by the sub-group size compared with that when using the SA-FDMAS beamformer. For instance, the contrast difference increased from 5.32 to 9.46 dB when the sub-group size was changed from 16 to 32 elements for the SA-FDMAS beamformer. However, the contrast difference increased from 7.6 to 14.32 dB when the sub-group size was changed from 16 to 32 elements for the D-FDMAS beamformer. In addition, the computation time of the SA-FDMAS beamformer significantly increased with increasing sub-group size. This differs from the D-FDMAS beamformer whose computation time slightly increased with the increased sub-group size. Therefore, the size of sub-group elements should be selected to improve the image quality and meet the application. For example, for real-time monitoring applications such as monitoring a needle biopsy of the SLN, the group size of elements for the D-FDMAS beamformer should be small (32 elements). This small group size is used to reduce the contrast difference between targets (Needle biopsy and SLN). As a result, the artefact and clutter will be reduced and the shape of targets will not be affected. In addition, by using a small group size, the multiplication numbers of this beamformer will be reduced. As a result, the computation time will be reduced. However, for measuring the size of target applications, such as measuring the size of a tumour, a large group size for the D-FDMAS beamformer will be needed. This is because, by using a large group size, the lateral resolution will be improved. In addition, one target will be imaged in the application. As a result, the contrast of the target will not be affected by another target.
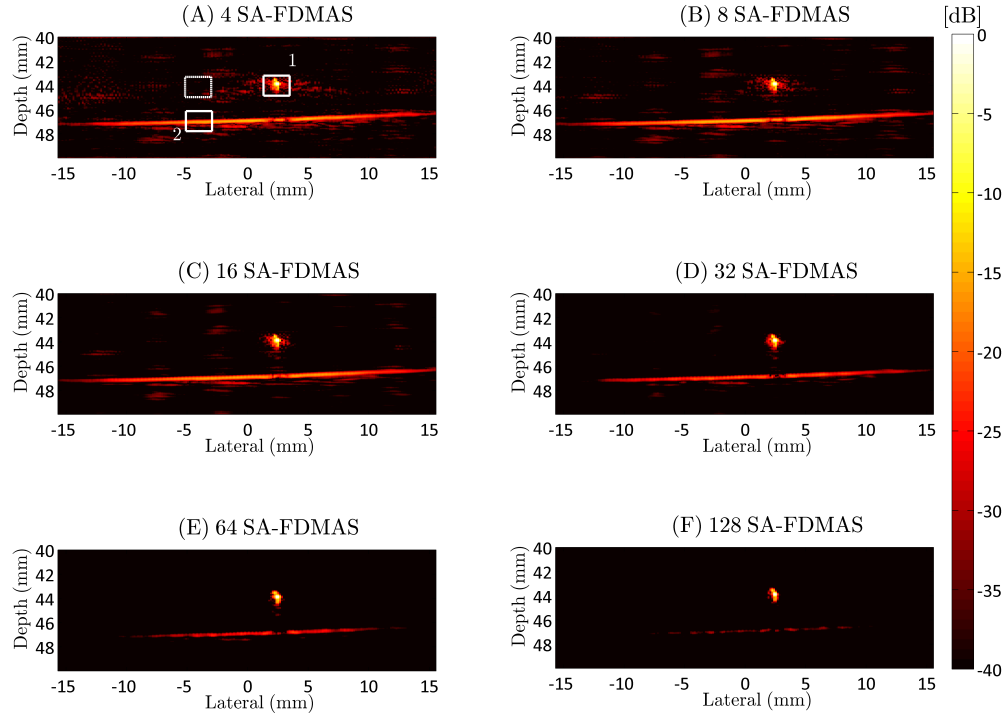
Figure 7.11: Photoacoustic images of carbon fibre rods beamformed by using SA-FDMAS with different sub-group sizes. (A) 4 elements, (B) 8 elements, (C) 16 elements, (D) 32 elements, (E) 64 elements, and (F) 128 elements. Dynamic range: 40 dB.
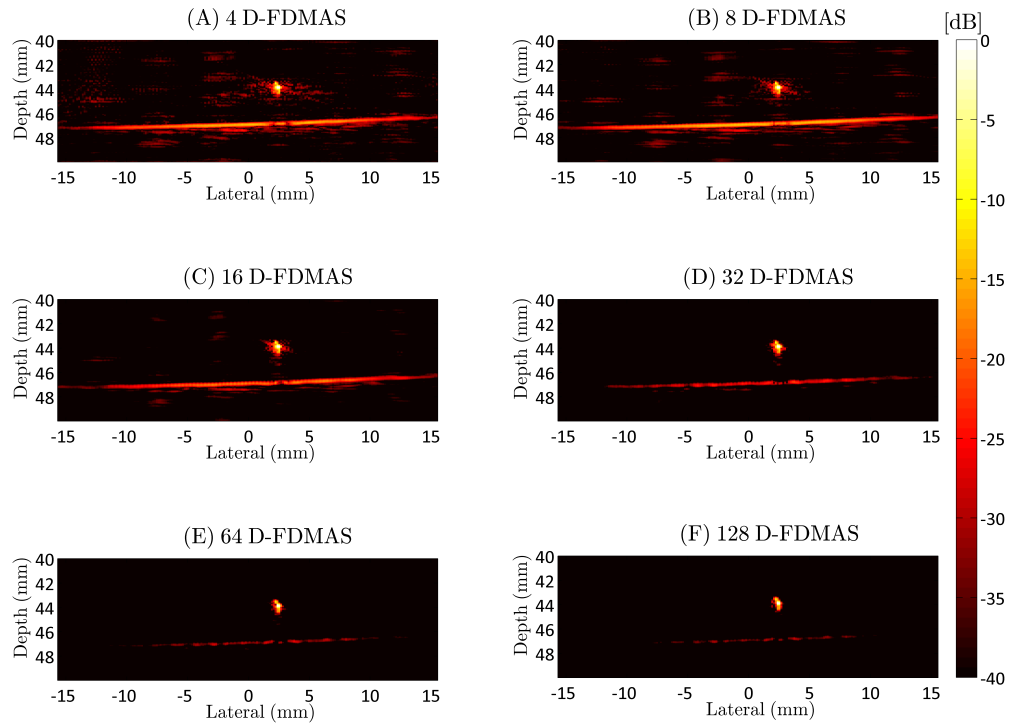
Figure 7.12: Photoacoustic images of carbon fibre rods beamformed by using D-FDMAS with different sub-group sizes. (A) 4 elements, (B) 8 elements, (C) 16 elements, (D) 32 elements, (E) 64 elements, and (F) 128 elements. Dynamic range: 40 dB.
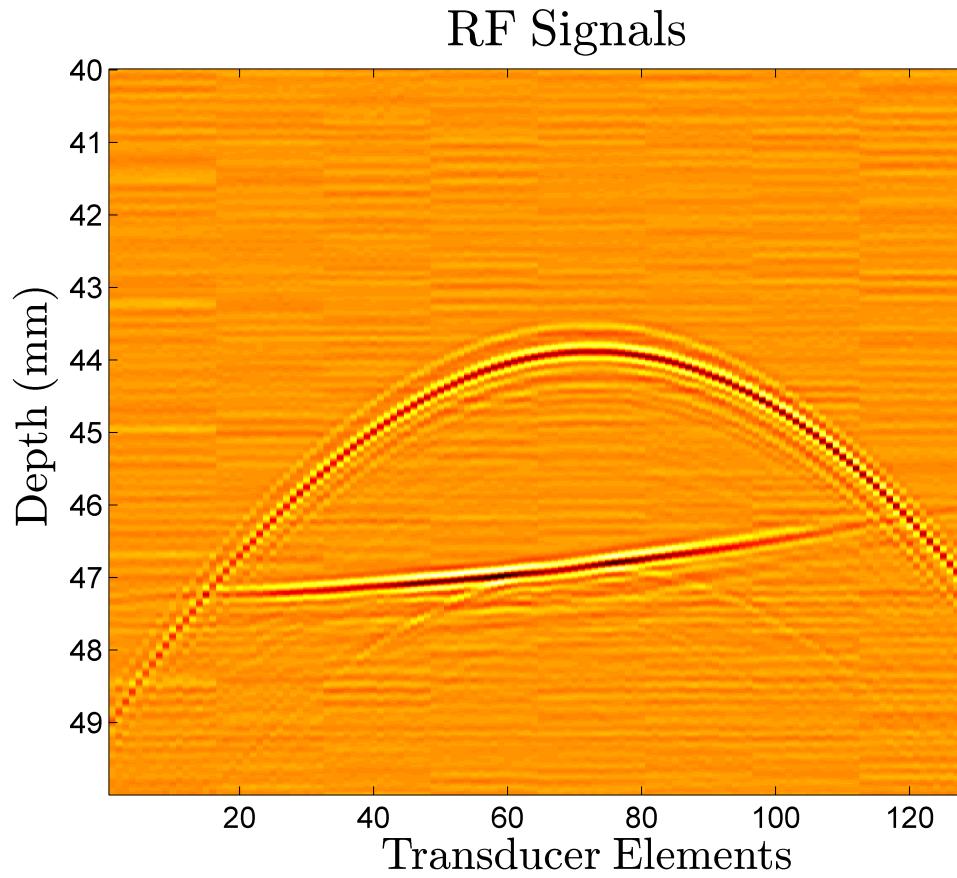
Figure 7.13: RF signals for two carbon fibre rods. One of them along the lateral direction (Linear propagation) of the transducer while the other along the elevation direction (Circular propagation).

Sub-group	Contrast Ratio (dB)		
	SA-FDMAS (AL)	SA-FDMAS (AE)	SA-FDMAS Difference
4	19.2	23.83	4.63
8	23.23	27.55	4.32
16	25.74	31.06	5.32
32	25.33	34.79	9.46
64	23.89	39.30	15.41
128	23.42	44.09	20.67

Table 7.6: Effects of the sub-group size on contrast ratio of the carbon fibre rods along lateral (AL) and along elevation (AE) directions when using the SA-FDMAS beamformer.

Sub-group	Contrast Ratio (dB)		
	D-FDMAS (AL)	D-FDMAS (AE)	D-FDMAS Difference
4	20.85	25.51	4.66
8	24.43	28.20	3.77
16	24.74	32.34	7.6
32	22.45	36.77	14.32
64	22.87	41.25	18.38
128	23.42	44.09	20.67

Table 7.7: Effects of the sub-group size on contrast ratio of the carbon fibre rods along lateral (AL) and along elevation (AE) directions when using the D-FDMAS beamformer.

32 SA-FDMAS and 32 D-FSMAS beamformers were compared with DAS, 42 MV and FDMAS beamformers, as shown in figure 7.14. When the DAS (Figure 7.14 (A)) and 42 MV (Figure 7.14 (B)) beamformers were used, the contrast of the carbon fibre rod along the lateral direction was high. Whereas, the photoacoustic images suffered from high-level artefacts and background noise for both beamformers. These artefacts and background noise were significantly reduced when the FDMAS beamformer (Figure 7.14 (C)) was used. The drawback of the FDMAS beamformer was that the contrast

difference between the carbon fibre rods was significantly large (Contrast difference = 21 dB). As a result, a large part of the carbon fibre rod along the lateral direction was lost. The 32 SA-FDMAS and 32 D-FDMAS beamformers (Figure 7.14 (D) and (E)) reduced the background noise when compared with DAS and 42 MV beamformers and emphasised the contrast of both carbon fibre rods compared with the FDMAS beamformer. Figure 7.15 compared the -6 dB lateral resolution when using these beamforming techniques for the carbon fibre along the elevation direction of the ultrasound transducer. From this figure, 32 D-FDMAS improved the lateral resolution (-6 dB) by 25% compared with the DAS beamformer. 42 MV beamformer generated high side lobes that was more than - 25 dB. These side lobes were significantly reduced using the 32 D-FDMAS beamformer. However, FDMAS and 32 SA-FDMAS beamformers improved lateral resolution (-6 dB) over the 32 D-FDMAS beamformer by 33% and 10%, respectively.
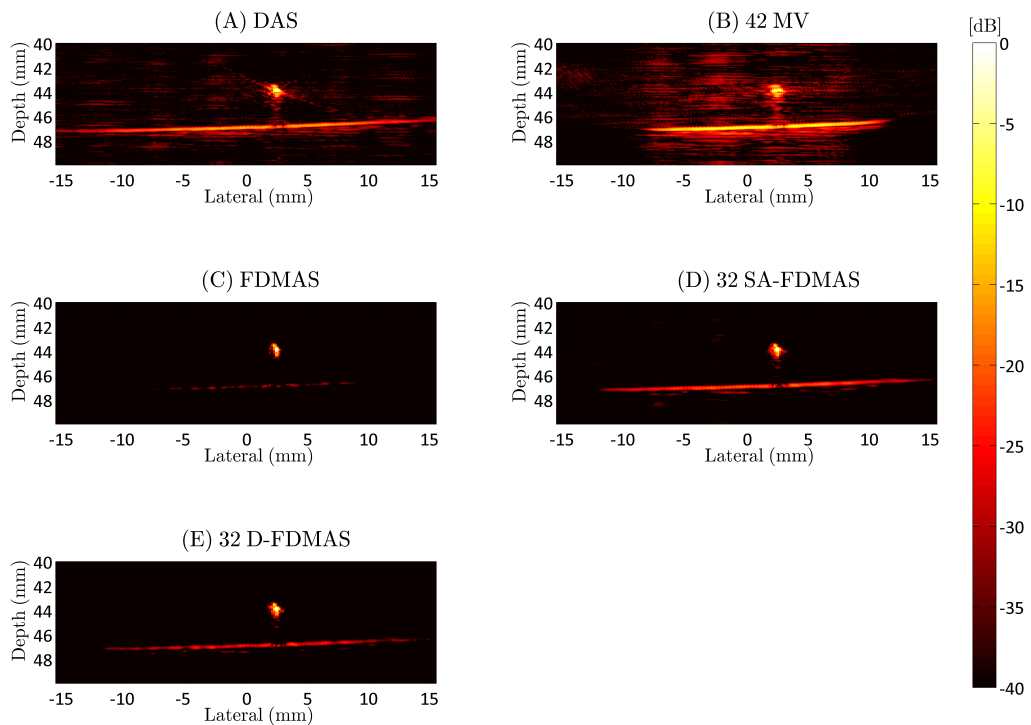
Figure 7.14: Photoacoustic images of carbon fibre rods beamformed using (A) DAS, (B) 42 MV, (C) FDMAS, (D) 32 SA-FDMAS, and (E) 32 D-FDMAS. Dynamic range: 40 dB.
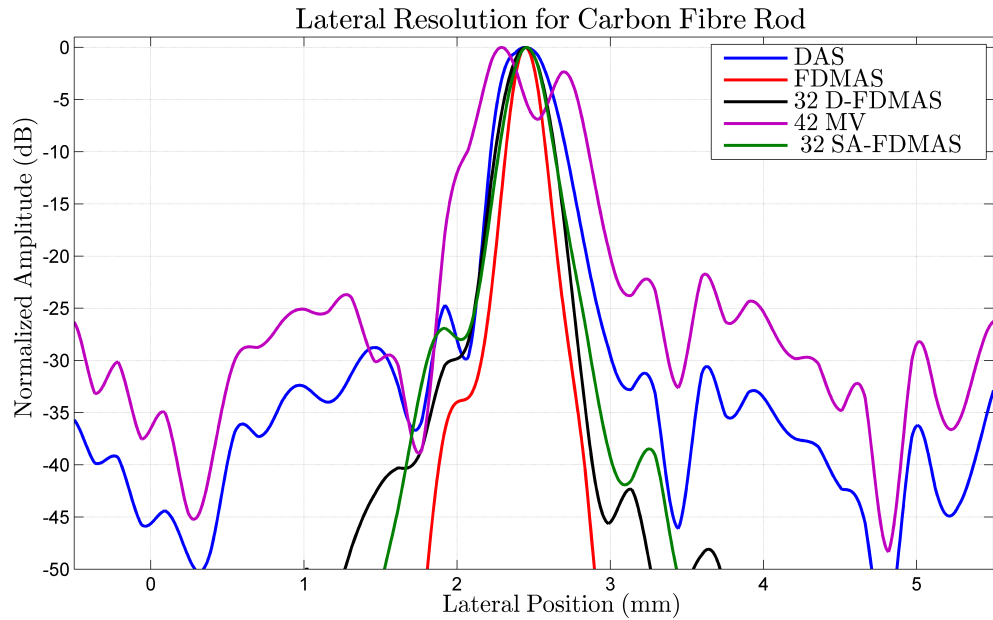
Figure 7.15: Lateral resolution of the carbon fibre rod along the elevation direction with DAS, 42 MV, FDMAS, 32 SA-FDMAS, and 32 D-FDMAS beamformers.

Agar Phantom with Inclusion

In the second experiment, an agar phantom with one inclusion, as shown in figure 7.16 (A), was used. The ultrasound image was combined with the photoacoustic one. Figure 7.16 (B) illustrates the ultrasound image of the cross section of the inclusion beamformed by using DAS. The RF signals were generated by transmitting a single plane wave of two-cycle 7.5 MHz sinusoids. Figure 7.16 (C) shows the photoacoustic image of the inclusion beamformed by using DAS. In this image, only the boundary of the inclusion was imaged. This was because the finite transducer bandwidth resulted in the loss of the low frequency components. By combining ultrasound and photoacoustic images as shown in figure 7.16 (D), more structural details of the agar phantom can be seen.
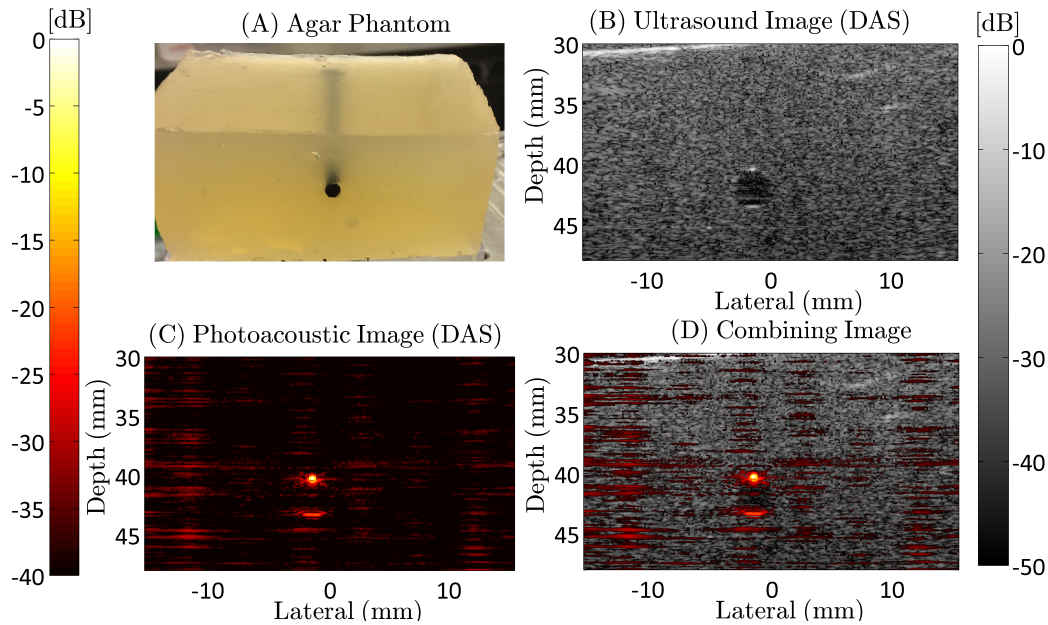
Figure 7.16: Ultrasound and photoacoustic images of the agar phantom. (A) Structure of the agar phantom. (B) Ultrasound image. (C) Photoacoustic image. (D) Combined image. Dynamic range of the ultrasound image: 50 dB. Dynamic range of the photoacoustic image: 40 dB.

In this experiment, a needle (Blunt Fill Needle, 18G) was inserted inside the phantom to study the effect of beamforming techniques on the image contrast and SNR. Figure 7.17 shows the photoacoustic image of the agar phantom with a needle when the SA-FDMAS beamformer with different sub-group sizes was used. When 4 elements was used in a sub-group (Figure 7.17 (A)), artefacts, especially those generated from the needle, and noise were high. These artefacts and noise were reduced as the sub-group size was increased. However, the contrast of the needle was noticeably reduced when 64 or more elements were used in a sub-group. The contrast difference between the inclusion and the needle was calculated for different sub-group sizes as shown in Table 7.8. In this calculation, the solid rectangle number 1 and the dashed rectangle number 1 in the figure 7.17 (A) represented the signal from the needle and inclusion,

respectively. In addition, the solid rectangle number 2 in the same figure represented the background signal. From this table, the contrast difference was increased as the sub-group size was increased. To improve image quality, the contrast difference should be the lowest and the SNR for the inclusion and the needle should be the highest. The SNR for the inclusion and needle was calculated as given in Table 7.9. The SNR of this calculation was a ratio of the mean of the signal to the standard deviation of noise (Wang *et al.*, 2017). The solid rectangle number 1 and number 2 in figure 7.17 (A) represented the signal and the noise of the needle, respectively. The dashed rectangle number 1 and number 2 in the same figure represented the signal and the noise of inclusion, respectively. From Table 7.8 and Table 7.9, the highest SNR and the lowest contrast difference between the inclusion and needle were obtained when 16 elements were utilised in a sub-group. For this sub-group size, the contrast difference was 0.22 dB and the SNR for the inclusion and needle were 29.14 and 25.73 dB, respectively. However, the SNR for the inclusion was improved by almost 4 dB when the sub-group size was 32 elements. This improvement provided better localisation of the inclusion. In addition, the SNR for the needle did not change (SNR = 25.54 dB). However, the contrast difference between the inclusion and needle was increased to be 3.69 dB. This increase in contrast difference is because the number of transducer elements that participated in beamforming the inclusion (SLN) was high. This was due to the FOV of the transducer, which was large and the shape of the propagation RF signals from the inclusion (SLN), which had a circular shape. However, the number of transducer elements that participated in beamforming the needle was relatively low. This was because the shape of the propagation RF signals from the needle had a linear shape. As a result, the contrast of inclusion was significantly increased as the sub-group size was increased (Table 7.8). This was unlike the contrast of the needle, which was slightly increased as the sub-group size was increased a certain amount.
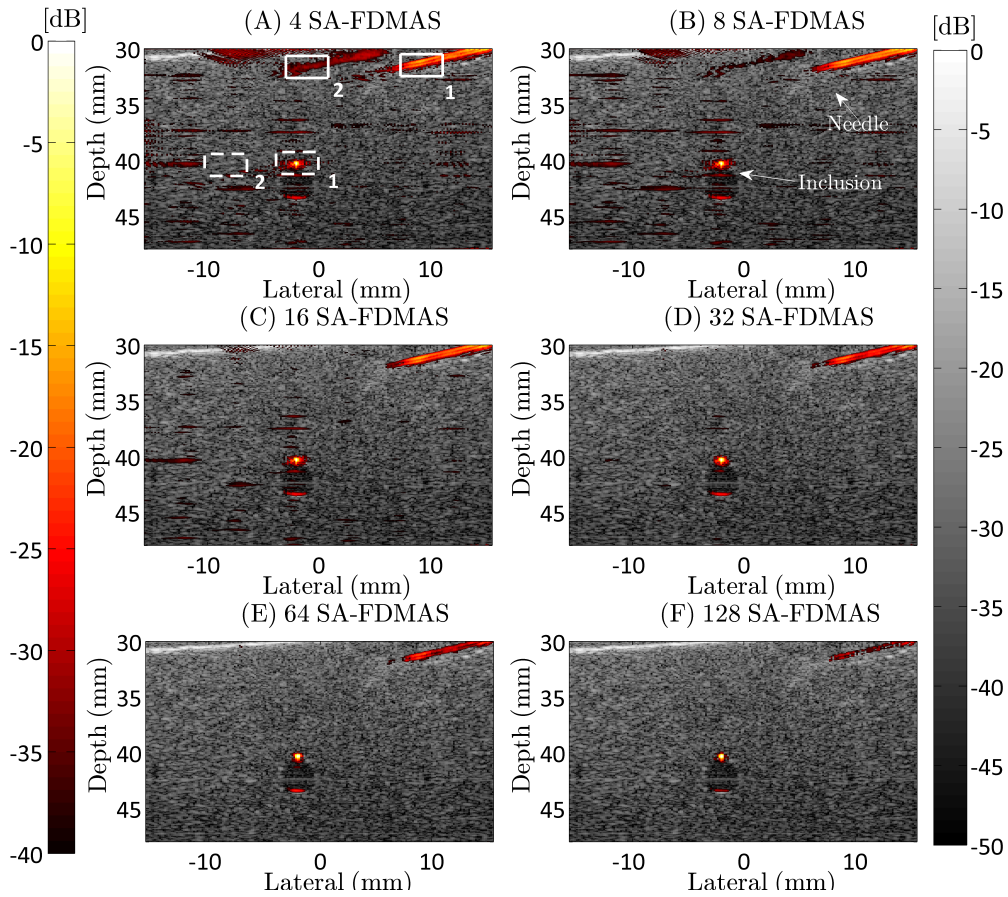
Figure 7.17: Combined ultrasound and photoacoustic images of the agar phantom with a needle. The photoacoustic images were beamformed using SA-FDMAS with different sub-groups of elements. (A) 4 elements, (B) 8 elements, (C) 16 elements, (D) 32 elements, (E) 64 elements, and (F) 128 elements. Dynamic range of the ultrasound image: 50 dB. Dynamic range of the photoacoustic image: 40 dB.

Sub-group	Contrast Ratio (dB)		
	SA-FDMAS (Inclusion)	SA-FDMAS (Needle)	SA-FDMAS Difference
4	14.93	15.33	0.39
8	16.88	17.59	0.71
16	19.55	19.34	0.22
32	23.41	19.72	3.69
64	27.18	20.39	6.80
128	31.52	17.74	13.78

Table 7.8: Effects of the sub-group size on the contrast of the inclusion and needle when using the SA-FDMAS beamformer.

Sub-group	SNR (dB)	
	SA-FDMAS (Inclusion)	SA-FDMAS (Needle)
4	25.11	20.86
8	28.2	23.99
16	29.14	25.73
32	33.03	25.54
64	39.1	23.83
128	43.47	21.13

Table 7.9: Effects of the sub-group size on the SNR of the inclusion and needle when using the SA-FDMAS beamformer.

Figure 7.18 shows the photoacoustic images of the agar phantom with the needle beamformed by using D-FDMAS with different sub-group sizes. The artefacts and noise were high when the sub-group had less than 16 elements, as shown in figure 7.18 (A) and (B). The contrast difference between the inclusion and needle significantly increased when the sub-group had 64 or more elements, as shown in figures 7.18 (E) and (F). The contrast difference between the inclusion and needle and the SNR were calculated using the same steps as those used for the SA-FDMAS beamformer, and the results are given in Table 7.10 and Table 7.11, respectively. When the sub-group was composed of 64 elements, the contrast difference was 12.52 dB. This difference created difficulties in recognising the needle from the inclusion. This difference was increased

as the sub-group size was increased. However, the highest SNR for the inclusion and needle was achieved when the sub-group consisted of 16 elements. By using this sub-group size, the contrast difference between the inclusion and needle was 2.23 dB. The image quality was not affected by this contrast difference, as shown in figure 7.18 (C).
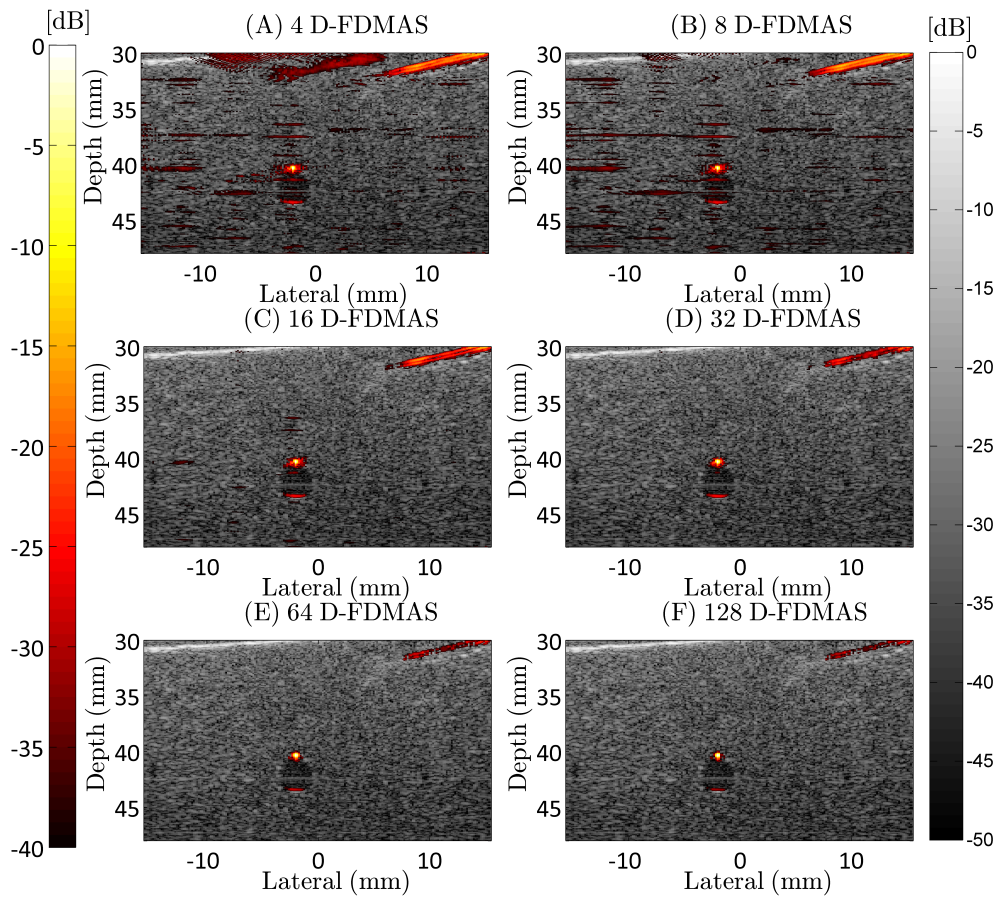
Figure 7.18: Combined ultrasound and photoacoustic images of the agar phantom with a needle. The photoacoustic images were beamformed by using D-FDMAS with different sub-groups of elements. (A) 4 elements, (B) 8 elements, (C) 16 elements, (D) 32 elements, (E) 64 elements, and (F) 128 elements. Dynamic range of the ultrasound image: 50 dB. Dynamic range of the photoacoustic image: 40 dB.

Sub-group	Contrast Ratio (dB)		
	D-FDMAS (Inclusion)	D-FDMAS (Needle)	D-FDMAS Difference
4	15.01	15.53	0.52
8	17.79	18.79	1.00
16	22.41	20.18	2.23
32	26.11	18.23	7.89
64	30.27	17.74	12.52
128	31.52	17.74	13.78

Table 7.10: Effects of the sub-group size on the contrast of the inclusion and needle when using the D-FDMAS beamformer.

Sub-group	SNR (dB)	
	D-FDMAS (Inclusion)	D-FDMAS (Needle)
4	25.86	21.14
8	27.52	25.4
16	32.17	26.29
32	36.03	21.71
64	42.04	21.05
128	43.47	21.13

Table 7.11: Effects of the sub-group size on the SNR of the inclusion and needle when using the D-FDMAS beamformer.

The 32 SA-FDMAS and 16 D-FDMAS beamformers were compared with DAS, 42 MV and FDMAS beamformers for the inclusion with the needle images as shown in figure 7.19. Figure 7.19 (A) shows only the ultrasound image of the agar phantom with the needle, and the contrast of the needle here was low which was different from the case in the photoacoustic image. By using photoacoustic imaging and the DAS beamformer, the contrast of the needle was emphasised, as shown in figure 7.19 (B). However, the photoacoustic image had high-level background noise and artefacts, especially from the needle. The photoacoustic image with the 42 MV beamformer also suffered from background noise and artefacts from the needle, as shown in figure 7.19 (C). The FDMAS beamformer significantly reduced background noise and artefacts. Whereas,

the contrast difference between the inclusion and needle was high, as shown in figure
7.19 (D) and Table 7.12. This created difficulties in guiding the needle. By using the
32 SA-FDMAS beamformer, the inclusion and needle were clearly defined, as shown
in figure 7.19 (E). The contrast difference between the inclusion and needle was 3.69
dB which was very low compared with 14.12 dB from the FDMAS beamformer. In
addition, the SNRs of the inclusion and needle when using 32 SA-FDMAS were higher
than that when using DAS by 6.28 and 7.63 dB, respectively as shown in Table 7.13. By
using the 16 D-FDMAS beamformer, the photoacoustic image has comparable quality
compared with that when using the 32 SA-FDMAS beamformer, as shown in figure
7.19 (F). From Table 7.12 and Table 7.13, the contrast difference from the 16 D-
FDMAS beamformer is 2.23 dB. This difference was slightly smaller than that from
the 32 SA-FDMAS beamformer (3.69 dB). The SNRs of the inclusion and needle in
the image when utilising the 16 D-FDMAS beamformer were 32.17, and 26.29 dB,
respectively. However, for the 32 SA-FDMAS beamformer, they became 33.03 and
25.54 dB, respectively.
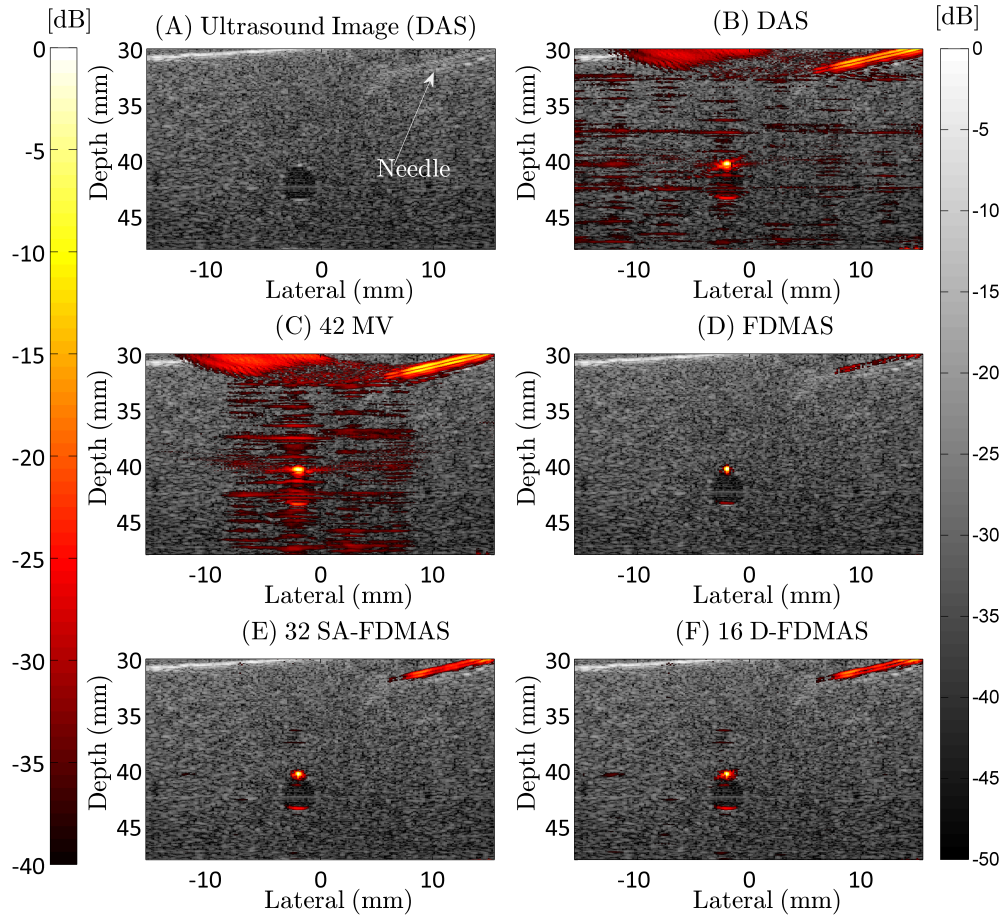
Figure 7.19: Ultrasound image for inclusion and needle when using (A) the DAS beamformer. Photoacoustic images for the inclusion and needle when using (B) DAS, (C) 42 MV, (D) FDMAS, (E) 32 SA-FDMAS, and (F) 16 D-FDMAS beamforming techniques. The background of all photoacoustic images is its corresponding ultrasound image. Dynamic range of the ultrasound image: 50 dB. Dynamic range of the photoacoustic image: 40 dB.

	Contrast Ratio (dB)		
Beamforming Technique	Inclusion	Needle	Difference
DAS	10.82	9.85	0.97
42-MV	7.74	9.82	2.09
FDMAS	31.53	17.41	14.12
32 SA-FDMAS	23.41	19.72	3.69
16 D-FDMAS	22.41	20.18	2.23

Table 7.12: Effect of DAS , 42 MV, FDMAS, 32 SA-FDMAS and 16 D-FDMAS beamforming techniques on contrast ratio for the inclusion and needle.

	SNR (dB)	
Beamforming Technique	Inclusion	Needle
DAS	26.75	17.91
42-MV	24.66	18.01
FDMAS	44.19	20.95
32 SA-FDMAS	33.03	25.54
16 D-FDMAS	32.17	26.29

Table 7.13: Effects of DAS, 42 MV, FDMAS, 32 SA-FDMAS and 16 D-FDMAS beamforming techniques on SNR for the inclusion and needle.

Healthy Human Hand

For the in-vivo investigations with a healthy human hand, the black dashed line in figure 7.10 (D) shows the place of scanning. Figure 7.20 (A) shows the corresponding ultrasound image by using the DAS beamformer. This image shows the boundary of the hand. Figure 7.20 (B) shows the photoacoustic image (hot colormap) of the blood vessels by using the DAS beamformer with a high-level background noise. SNR was calculated using the same steps used to calculate the SNR for the inclusion and needle experiment. The solid green rectangle number 1 in figure 7.20 (D) presents the signal region while the solid green rectangle number 2 shows the background region. When DAS was used, the SNR was 21 dB. In addition, the blood vessels within dashed ellipse number 1 overlap with each other. When the 42 MV beamformer was used (Figure 7.20 (C)), some blood vessels were lost due to the generated photoacoustic emissions having

a high-level of noise. Therefore, the sub-group size should be reduced to increase the robustness of the MV beamformer at the cost of resolution (Synnevag *et al.*, 2007). In addition, the MV beamformer will provide improved results if it is combined with another adaptive beamformer (Park *et al.*, 2008a). When FDMAS, 32 SA-FDMAS and 16 D-FDMAS beamformers were used, as shown in figures 7.20 (D), (E), and (F), the background noise was significantly reduced and the SNR was improved by almost 3 dB. The blood vessels within dashed ellipse number 1 in figure 7.20 (B) can now be clearly identified. However, the shape of blood vessels was smooth when the 16 D-FDMAS beamformer was used, which was different from the case using FDMAS and 32 SA-FDMAS beamformers. In addition, the 16 D-FDMAS beamformer has an advantage over FDMAS and 32 SA-FDMAS in terms of computation time.
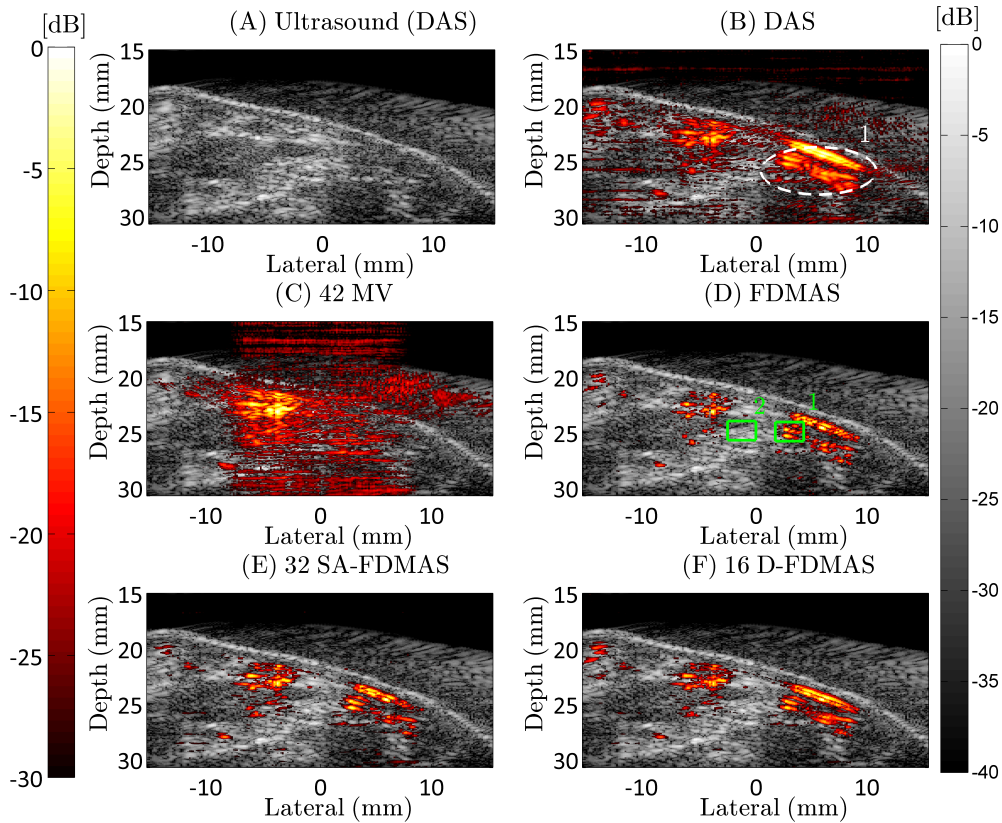
Figure 7.20: Ultrasound image of a healthy human hand when using (A) the DAS beamformer. Photoacoustic images of a healthy human hand when using (B) DAS, (C) 42 MV, (D) FDMAS, (E) 32 SA-FDMAS, and (F) 16 D-FDMAS beamforming techniques. The background of all photoacoustic images is its corresponding ultrasound image. Dynamic range of the ultrasound image: 40 dB. Dynamic range of the photoacoustic image: 30 dB.

7.6 Discussion

The D-FDMAS and SA-FDMAS beamformers show improvement in SNR for photoacoustic imaging when compared with the DAS and MV beamformers. These beamformers provided better localisation of the target, such as a needle in the image. The

7. PERFORMANCE OF THE FDMAS BEAMFORMER BY USING DYNAMIC ELEMENTS

FDMAS beamformer also improved the SNR of the photoacoustic image. However, it affected the contrast difference between imaging targets, such as the inclusion and needle. This contrast difference was reduced by using the D-FDMAS and SA-FDMAS beamformers, preserving detailed structures of the imaging target.

The D-FDMAS beamformer has advantages over the SA-FDMAS beamformer in terms of computation time and complexity. Figure 7.21 shows the relation between the sub-group size in D-FDMAS and SA-FDMAS beamformers and the number of multiplications. The number of multiplications in D-FDMAS is much less than that in SA-FDMAS for all sub-group sizes. The optimum sub-group for SA-FDMAS should have 32 to 64 elements, while the optimum sub-group for D-FDMAS has 16 to 32 elements. SA-FDMAS needs 40000 more multiplications to achieve the comparable image quality when compared against D-FDMAS. The D-FDMAS beamformer reduces the multiplication required of FDMAS from 8128 multiplications for 128 elements to 3600 multiplications or fewer. These multiplication numbers affect the computation time of each beamforming technique. For example, the computation times for the 32 SA-FDMAS, 32 D-FDMAS and FDMAS beamformers were calculated when the range of the image depth was 2 mm to 60 mm. In addition, the lateral step size was $\lambda/2$. The sampling frequency was also 80 MHz. In this calculation, i5-4460 CPU 3.2 GHz, 16 GB RAM and MATLAB R2014a were used. The computation time of the 32 D-FDMAS beamformer was 120 sec. This computation time was increased to 252 and 9622.4 sec when the FDMAS and 32 SA-FDMAS beamformers were used, respectively. These computation times were increased as the lateral step size and sampling frequency were increased. When the lateral step size increased from $\lambda/2$ to $\lambda/4$, the computation time of the 32 D-FDMAS and 32 SA-FDMAS beamformers increased to 236.4 and 18829 sec, respectively. These computation times could be significantly reduced when implanting it on a GPU.
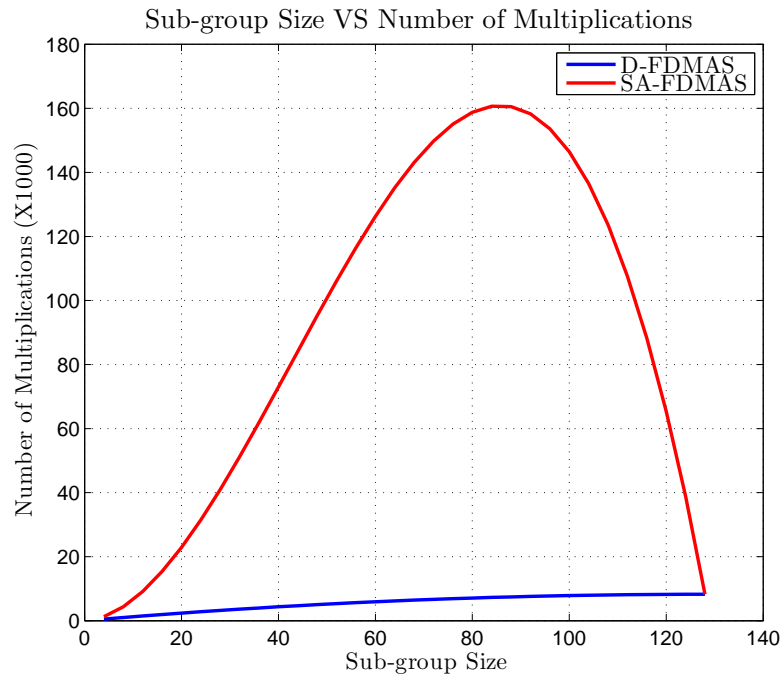
Figure 7.21: Relationships between the sub-group size and the number of multiplications for D-FDMAS and SA-FDMAS beamformers.

The D-FDMAS beamformer improves the lateral resolution (-6 dB) compared with DAS and MV beamformers. However, this improvement is not better than when using FDMAS and SA-FDMAS beamformers as the FDMAS beamformer depends on the correlation between all transducer elements. In addition, the repetition of covariance matrix in the SA-FDMAS beamformer emphasises the lateral resolution at the cost of computation time. Whereas, the D-FDMAS beamformer depends on the correlation of a sub-group of elements.

7.7   Conclusion

In this study, the D-FDMAS and SA-FDMAS beamformers were applied to photoacoustic imaging. These beamformers reduced background noise and artefacts of the

photoacoustic image when compared with the DAS beamformer. In addition, they had less of an effect on the contrast difference between imaging targets compared with the FDMAS beamformer. Based on the experiments, the optimum sub-group in the D-FDMAS beamformer should have 16 to 32 elements, and for SA-FDMAS, 32 to 64 elements should be used in a sub-group. In-vivo experiment, the D-FDMAS beamformer identified the close blood vessels clearly compared with DAS and MV beamformers. The D-FDMAS beamformer has advantages over the SA-FDMAS beamformer in terms of complexity and computation time.

Chapter 8

Multispectral Photoacoustic Imaging by Using Dynamic Multiply and Sum Beamforming Technique

Abstract

Multispectral photoacoustic imaging (MPI) provides information on different types of tissue. The DAS beamformer is one of the most common beamformers used in MPI due to its high computational efficiency and simplicity. However, DAS suffers from artefacts and sidelobes. In this chapter, the dynamic filter delay multiply and sum (D-FDMAS) beamformer was investigated in MPI. The D-FDMAS beamformer was also linearised and termed dynamic sign delay and multiply and sum (D-sDMAS). The effect of linearizing this beamformer on MPI was studied. For in-vivo experiments, there was no significant difference in the measurement accuracy using D-FDMAS and D-sFDMAS beamformers. For the measurement of oxygen saturation in a vein, D-FDMAS ($O_2 = 68 \pm 9$ %) and D-sDMAS ($O_2 = 71 \pm 9$ %) beamformers provided more accurate results than the DAS ($O_2 = 79 \pm 17$ %) beamforming technique.

8. MULTISPECTRAL PHOTOACOUSTIC IMAGING BY USING DYNAMIC MULTIPLY AND SUM BEAMFORMING TECHNIQUE

8.1 Introduction

Multispectral photoacoustic imaging (MPI) has been used to differentiate types of tissue. MPI depends on the different optical absorption spectra of biological tissues, such as oxy-hemoglobin, deoxy-hemoglobin and melanin dye. Photoacoustic images are generated for the imaging target by applying laser pulses with different wavelengths, then, these images are analysed based on the optical absorption spectra to differentiate tissue types (Taruttis & Ntziachristos, 2015). MPI has been investigated for a lot of applications, such as oxygen saturation measurement (Chen *et al.*, 2012; Deng & Li, 2016), melanoma depth measurement(Oh *et al.*, 2006), nerve separation from other biological tissue (Mari *et al.*, 2015) and breast cancer diagnosis (Oraevsky *et al.*, 2002).

In MPI, linear beamforming techniques, such as the DAS beamformer, is normally used. This beamformer is simple, linear and fast. These make it suitable for real time applications (Kirchner *et al.*, 2018). However, this beamformer suffers from high-level artefacts and sidelobes (Moein Mozaffarzadeh, 2018). Kirchner *el al.* have applied the FDMAS beamformer to MPI to reduce imaging artefacts and side lobes. This beamformer has been linearised and called signed delay multiply and sum (sDMAS) before applying it to MPI (Kirchner *et al.*, 2018). The sDMAS beamformer needs more computation power (Kirchner *et al.*, 2018). In this chapter, the dynamic filter delay multiply and sum (D-FDMAS) beamformer is applied to MPI with a low-level computation burden than the FDMAS beamformer. In addition, the D-FDMAS beamformer is linearised and the effect of the linearity on the MPI will be studied. This chapter is organised as follows: first, the theoretical analysis for linearised DAS and linearised D-FDMAS beamformers. Second, a comparison between linearised D-FDMAS, DAS and non-linearised D-FDMAS beamformers based on simulation. Third, a comparison between linearised D-FDMAS, DAS and non-linearised D-FDMAS beamformers in terms of MPI based on experiment setup. Finally, a discussion and conclusion.

8.2 Method

8.2.1 Linearity of Beamforming Techniques

Linearity of the DAS Beamforming Technique

For DAS beamformer, there is a linear relationship between the amplitude of the beamformed image and the initial photoacoustic pressure. For example, if the initial photoacoustic pressure is $P_o(X, Y, \lambda)$, the amplitude of photoacoustic image is given by equation 8.1 (Kirchner *et al.*, 2018):

$$Y_{\text{DAS}}(X, Y, \lambda) = \sum_{i=1}^{N}(A(X, i)e^{-\alpha_t C \tau_{\text{delay}}(X, Y, i)})P_o(X, Y, \lambda), \qquad (8.1)$$

where $Y_{\text{DAS}}(X, Y, \lambda)$ is the output of the DAS beamformer, N is the number of transducer elements, $A(X, i)$ is the apodization coefficient for transducer element number i and position X, α_t is the ultrasound attenuation coefficient, C is the speed of sound in the medium and τ_{delay} is the time delay. It can be seen the amplitude of the beamformed data is linear to the initial photoacoustic pressure, however, the beamformed data will be affected with apodization and attenuation, which can be written as a constant as shown in equation 8.2 (Kirchner *et al.*, 2018):

$$Y_{\text{DAS}}(X, Y, \lambda) = K_{\text{DAS}}(X, Y)P_o(X, Y, \lambda). \qquad (8.2)$$

Linearty of D-FDMAS Beamforming Technique

The D-FDMAS beamformer is linearised by the same steps that Kirchner *el al.* have used to linearise the FDMAS beamforming technique (Kirchner *et al.*, 2018). In the D-FDMAS beamforming technique, the delayed RF signal from each transducer element

will be multiplied with a sub-group of elements as given in equation 8.3:

$$S_{ij} = S_i(X, Y, \lambda)S_j(X, Y, \lambda),$$

$$Y_{\text{D-FDMAS}}(X, Y, \lambda) = \left\{ \sum_{i=1}^{N} \sum_{j=i}^{m} \text{sgn}(S_{ij}).\sqrt{|S_{ij}|} \right\} * f, \tag{8.3}$$

$$m = \begin{cases} i + L - 1 & L \leq N - i \\ N & \text{else} \end{cases},$$

where S_{ij} is the result of the multiplication between the delayed RF signals from transducer element i and j, L is the sub-group size. The sign operation ($\text{sgn}(S_{ij})$) keeps the beamformed data always positive. In addition, the bandpass filter (f) leads to the loss of some parts of the signal. This makes a nonlinear relationship between the beamformed data and the initial photoacoustic pressure (Kirchner *et al.*, 2018). The delayed RF signal from the single element can be written in terms of the apodization coefficient ($A(X, i)$) and ultrasound attenuation (α_t) as given in equation 8.4 (Kirchner *et al.*, 2018):

$$S_i(X, Y, \lambda) = A(X, i)e^{-0.5\alpha_t C\tau_{\text{delay}}(X,Y,i)}P_o(X, Y, \lambda). \tag{8.4}$$

By applying equation 8.4 to equation 8.3, The D-FDMAS beamformer is given in equation 8.5:

$$S_{ij} = A(X, i)e^{-0.5\alpha_t C\tau_{\text{delay}}(X,Y,i)}P_o(X, Y, \lambda)A(X, j)e^{-0.5\alpha_t C\tau_{\text{delay}}(X,Y,j)}P_o(X, Y, \lambda),$$

$$Y_{\text{D-FDMAS}}(X, Y, \lambda) = \left\{ \sum_{i=1}^{N} \sum_{j=i}^{m} \text{sgn}(S_{ij}).\sqrt{|S_{ij}|} \right\} * f,$$

$$m = \begin{cases} i + L - 1 & L \leq N - i \\ N & \text{else} \end{cases}. \tag{8.5}$$

Equation 8.5 can be rewritten as shown in equation 8.6:

$$Y_{\text{D-FDMAS}}(X, Y, \lambda) = \left\{ \sum_{i=1}^{N} \sum_{j=i}^{m} a(i,j).|P_o(X, Y, \lambda)| \right\} * f,$$

(8.6)

$$a(i,j) = \sqrt{A(X,i)A(X,j)}e^{-0.5\alpha_t C(\tau_{\text{delay}}(X,Y,i)+\tau_{\text{delay}}(X,Y,j))}.$$

To make that relationship linear in equation 8.6, the bandpass filter (f) should be removed and the phase of the initial photoacoustic wave should be retained. The absolute operation leads to loss the phase of the photoacoustic wave. The phase can be maintained by multiplying the beamformed data with the sign of the DAS beamformed data (Kirchner *et al.*, 2018). The resultant beamforming technique termed dynamic sign delay multiply and sum (D-sDMAS) is given in equation 8.7:

$$Y_{\text{D-sDMAS}}(X, Y, \lambda) = \text{sgn}(Y_{\text{DAS}}(X, Y)) \left\{ \sum_{i=1}^{N} \sum_{j=i}^{m} a(i,j).|P_o(X, Y, \lambda)| \right\},$$

(8.7)

$$a(i,j) = \sqrt{A(X,i)A(X,j)}e^{-0.5\alpha_t C(\tau_{\text{delay}}(X,Y,i)+\tau_{\text{delay}}(X,Y,j))}.$$

Equation 8.7 can be simplified to equation 8.8:

$$Y_{\text{D-sDMAS}}(X, Y, \lambda) = \text{sgn}(Y_{\text{DAS}}(X, Y))K_{\text{D-DMAS}}(X, Y)|P_o(X, Y, \lambda)|,$$

(8.8)

where $K_{\text{D-DMAS}}(X, Y)$ is the apodization and ultrasound attenuation that result from the multiplication of D-FDMAS beamforming without applying a bandpass filter.

8.2.2 Quantitative Photoacoustic Imaging

There is a linear relationship between the amplitude of the photoacoustic pressure and the absorption coefficient of the target as given in equation 8.9 (Brochu *et al.*, 2016; Li *et al.*, 2018):

$$P(X, Y, \lambda_i) = \alpha_s \Gamma F(X, Y, \lambda_i)\mu_a(X, Y, \lambda_i),$$

(8.9)

where $P(X, Y, \lambda_i)$ is the received photoacoustic pressure, α_s is the specification of the receiving system, Γ is the Gruneisen parameter, $F(X, Y, \lambda_i)$ is the local fluence, and $\mu_a(X, Y, \lambda_i)$ is the local absorption coefficient. The local fluence depends on the wavelength of the laser pulse and optical attenuation through the tissue layers. Therefore, the quantitative area should be normalized by the laser fluence to reduce the percentage of measurement errors (Brochu *et al.*, 2016; Deng & Li, 2016). One of the most common techniques for quantitative measurements is the least squares method (Li *et al.*, 2018; Zhang *et al.*, 2007). For example, to measure the oxygen saturation in blood, the concentration of oxy-hemoglobin and deoxy-hemoglobin will be quantified. The absorption coefficient of blood can be written in terms of the concentration of oxy-hemoglobin and deoxy-hemoglobin as shown in equation 8.10 (Zhang *et al.*, 2007):

$$\mu_a(X, Y, \lambda_i) = \epsilon_{\text{HbR}}(\lambda_i)C_{\text{HbR}}(X, Y) + \epsilon_{\text{HbO}_2}(\lambda_i)C_{\text{HbO}_2}(X, Y), \qquad (8.10)$$

where $\epsilon_{\text{HbR}}(\lambda_i)$ is the molar extinction coefficient of deoxy-hemoglobin at the wavelength λ_i, $\epsilon_{\text{HbO}_2}(\lambda_i)$ is the molar extinction coefficient of oxy-hemoglobin at wavelength λ_i, $C_{\text{HbR}}(X, Y)$ is the molar concentration of deoxy-hemoglobin and $C_{\text{HbO}_2}(X, Y)$ is the molar concentration of oxy-hemoglobin. As a result, the equation of the photoacoustic pressure (Equation 8.9) can be written as equation 8.11 (Brochu *et al.*, 2016; Li *et al.*, 2018):

$$P(X, Y, \lambda_i) = \alpha_s \Gamma F(X, Y, \lambda_i)(\epsilon_{\text{HbR}}(\lambda_i)C_{\text{HbR}}(X, Y) + \epsilon_{\text{HbO}_2}(\lambda_i)C_{\text{HbO}_2}(X, Y)). \quad (8.11)$$

If the specification of the receiving system (α_s) and the Gruneisen parameter (Γ) are assumed constant, and the local fluence is accurately normalised, the concentration of the oxy-hemoglobin and deoxy-hemoglobin can be calculated by using the least squares

method as given in equation 8.12 (Li *et al.*, 2018; Zhang *et al.*, 2007):

$$\begin{bmatrix} C_{\text{HbR}}(X,Y) \\ C_{\text{HbO}_2}(X,Y) \end{bmatrix} = (E^T E)^{-1} E^T P,$$

$$P = \begin{bmatrix} P(X,Y,\lambda_1) \\ . \\ . \\ . \\ P(X,Y,\lambda_i) \end{bmatrix} E = \begin{bmatrix} \epsilon_{\text{HbR}}(\lambda_1) & \epsilon_{\text{HbO}_2}(\lambda_1) \\ . \\ . \\ . \\ \epsilon_{\text{HbR}}(\lambda_i) & \epsilon_{\text{HbO}_2}(\lambda_i) \end{bmatrix}. \tag{8.12}$$

The oxygen saturation $(\text{sO}_2(X,Y))$ is calculated by using equation 8.13 (Li *et al.*, 2018; Zhang *et al.*, 2007):

$$\text{sO}_2(X,Y) = \left(\frac{C_{\text{HbO}_2}(X,Y)}{C_{\text{HbO}_2}(X,Y) + C_{\text{HbR}}(X,Y)} \right) \times 100. \tag{8.13}$$

8.2.3 Estimation of Local Fluence

The local fluence was estimated by using one-dimension fluence attenuation as given in equation 8.14 (An & Cox, 2018):

$$F = F_o e^{-\mu_{eff}(\lambda)z}, \tag{8.14}$$

where F is the optical fluence at depth z, F_o is the optical fluence on the surface of the medium and $\mu_{eff}(\lambda)$ is the optical attenuation coefficient inside of the medium for the laser wavelength λ. The optical attenuation coefficient can be calculated by using equation 8.15 (An & Cox, 2018):

$$\mu_{eff} = \sqrt{3\mu_a(\mu_a + \mu_s')}, \tag{8.15}$$

where μ_a is the absorption coefficient and μ_s' is the reduced scattering coefficient. In this estimation, the beam width of the laser was assumed to be wide (An & Cox, 2018). In addition, the absorption and scattering coefficients were taken from the database of Monte Carlo simulation (Jacques *et al.*, 2014; Jacques, 2014).

8.3 Simulation

8.3.1 Simulation Setup

A Monte Carlo simulation (Jacques *et al.*, 2014; Jacques, 2014) was used to simulate laser light propagation and absorption inside the biological tissue. The biological structure that was used in this simulation is shown in figure 8.1 with the absorption and scattering coefficients of the biological tissue given in chapter 2. Figure 8.2 shows the absorbed laser light inside the biological tissue when the wavelength of the laser pulse was 760 nm. From this absorbed optical energy, photoacoustic emissions were generated using the K-wave toolbox (Treeby & Cox, 2010; Treeby *et al.*, 2016). In the K-wave simulation, the generated photoacoustic emissions were received using a linear array transducer (Verasonics L11-4v) whose specifications are shown in Table 4.1. The sampling frequency was 80 MS/sec.
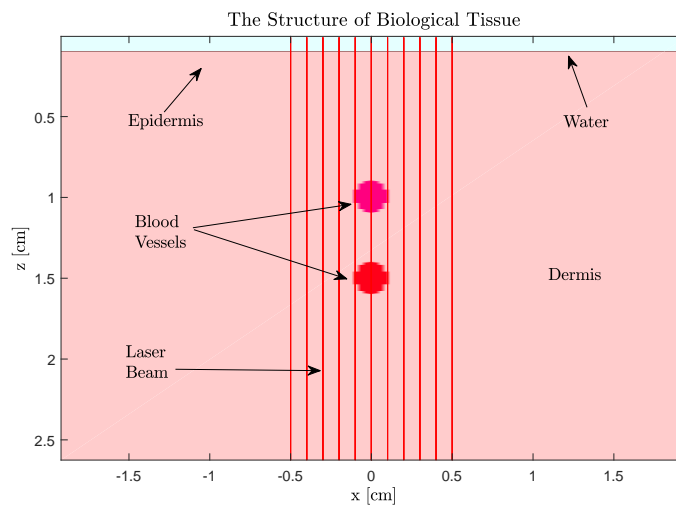
Figure 8.1: Simulated tissue consisting of two blood vessels.
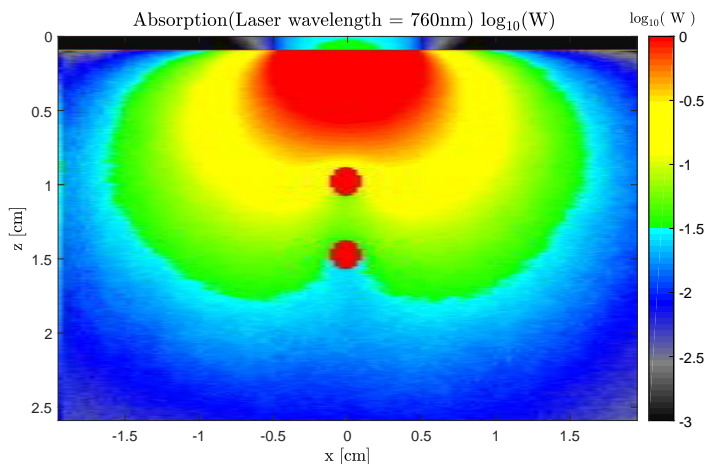
Figure 8.2: Absorbed laser light inside tissue.

8.3.2 Simulation Results

After generating the photoacoustic emissions, noise was added to achieve a 5 dB SNR (rms) by using the K-wave toolbox (Treeby & Cox, 2010; Treeby et al., 2016). These photoacoustic emissions were used to study the effect of the linearity on the D-FDMAS beamforming technique. In this study, 32 elements were employed in a sub-group. This is because these 32 elements in a sub-group provided the improved performance when using the D-FDMAS beamformer as demonstrated in chapter 7. Figure 8.3 shows the beamformed images and the frequency response when using DAS, 32 D-DMAS, 32 D-FDMAS, and 32 D-sDMAS beamforming techniques. Figure 8.3 (A) shows the photoacoustic image created by using DAS. This beamformer is linear and the frequency response of the beamformed line located at Lateral distance = 0 mm is shown in figure 8.3 (B). This frequency response is within the transducer bandwidth. When the 32 D-DMAS beamformer was used, the generated photoacoustic image had high-level sidelobes, as shown in figure 8.3(C). The corresponding frequency response of the beamformed line is shown in figure 8.3 (D). This response had two frequency bands. One of them was the low-frequency part, while the other was the high-frequency due to the multiplication operation. As a result, the 32 D-DMAS beamformer is non-linear. To remove the sidelobes when using the 32 D-DMAS beamformer, the 32 D-FDMAS beamformer was used, as shown in figure 8.3 (E). In this beamformer, a bandpass

filter was used to remove the low-frequency part, as shown in figure 8.3 (F). This beamforming technique led to the loss of some parts of the photoacoustic signal. To reduce the sidelobes resultant from the multiplication operation without losing some parts of the signal, the 32 D-sDMAS beamformer was used, as shown in figure 8.3 (G). In this beamformer, the bandpass filter was not used. In addition, the beamformed data was multiplied with the sign of the beamformed data using the DAS beamformer. This keeps the linearity of the beamformed data, as shown in figure 8.3 (B) and figure 8.3(H). However, some high-frequency parts will be emphasised due to the correlation operation.

The computation times of these beamformers were measured by using an i5-4460 CPU 3.2 GHz processor, 16 GB RAM and MATLAB R2014a. In this measurement, the range of the image depth was 2 mm to 26 mm. In addition, the sampling frequency and lateral step size were 80 MHz and $\lambda/4$, respectively. The computation time of the DAS beamformer (Computation time = 4.4 sec) was much lower than that of the 32D-DMAS (Computation time = 100.5 sec), the 32D-FDMAS (Computation time = 100 sec) and the 32D-sDMAS (Computation time = 99.7 sec) beamformers. In contrast, the computation times of the 32D-DMAS, 32D-FDMAS and 32D-sDMAS beamformers were comparable with each another.
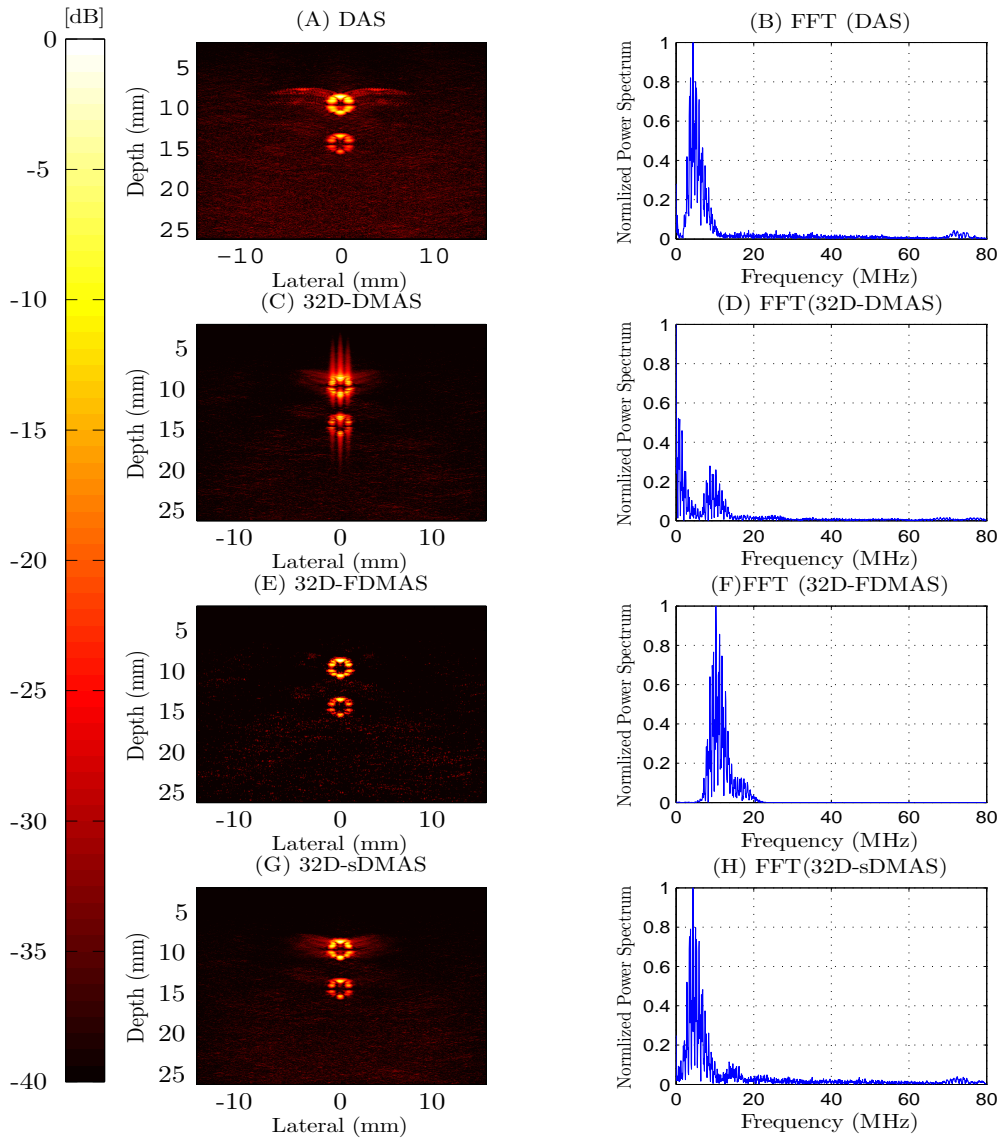
Figure 8.3: Photoacoustic images beamformed using different beamforming techniques and the frequency response of images line at Lateral = 0 mm after each beamformer: (A) DAS beamfomer (Photoacoustic image). (B) Normalised frequency response of the DAS beamformer. (C) 32D-DMAS beamformer (Photoacoustic image). (D) Normalised frequency response of the 32D-DMAS beamformer. (E) 32D-FDMAS beamformer (Photoacoustic image). (F) Normalised frequency response of the 32D-FDMAS beamformer. (G) 32D-sDMAS beamformer (Photoacoustic image). (H) Normalised frequency response of the 32D-sDMAS beamformer. Dynamic range: 40 dB.

8.4 Experiments

Two experiments were performed applying the D-FDMAS beamformer to the MPI and studying the effect of its linearity on the quantitative measurements.

Comparisons Between the Optical Spectrum and Photoacoustic Spectrum

In this experiment, the optical absorption spectrum of black Parker ink was compared with the photoacoustic spectrum of it when DAS, 32D-FDMAS and 32D-sDMAS beamformers were used. The structure of the phantom is shown in figure 8.4. In this phantom, a tube (TUBING SILICONE RUBBER with an inner diameter of 2 mm and wall thickness of 1 mm) was filled with black Parker ink. The absorption coefficient of this ink is shown in figure 8.5. This tube was submerged into water with 1% whole milk as the optical scattering material ($\mu'_s \approx 0.22$ cm^{-1} at 800 nm) (Aernouts *et al.*, 2015). In this experiment, the cross sections of the tubes that created three point targets at different depths were imaged. In the photoacoustic measurement, the laser wavelength was varied between 700 nm and 800 nm with a 20 nm step. The transmitted optical energy was 1.2 mJ through 4 optical fibre outputs.
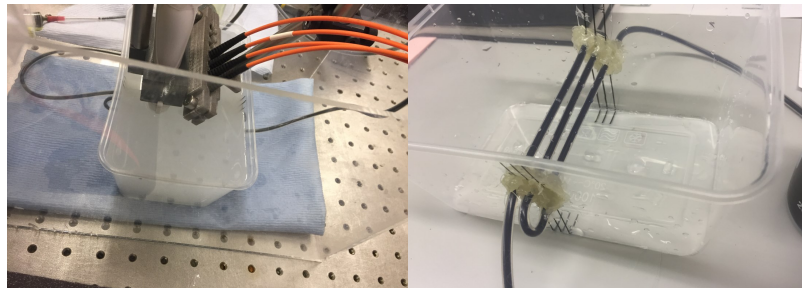
Figure 8.4: Structure of the phantom used to measure the photoacoustic spectrum of Parker black ink.
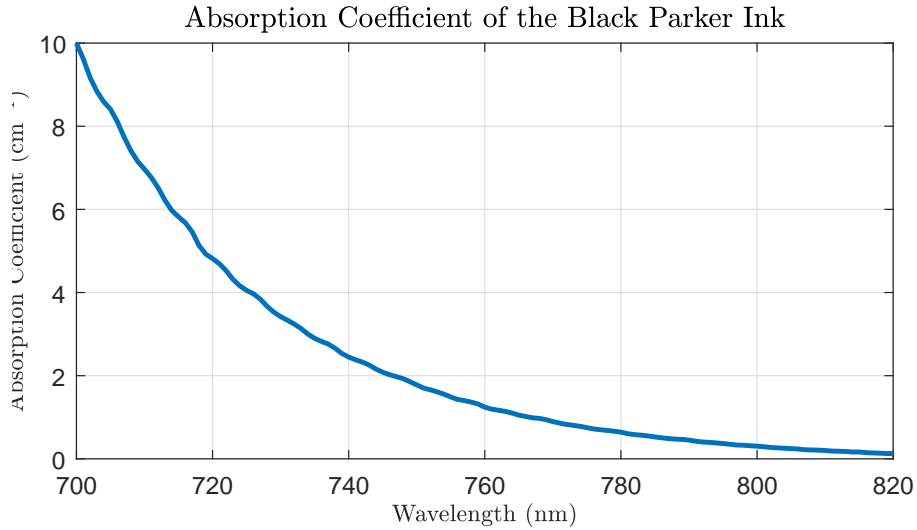
Figure 8.5: Absorption coefficient of black parker ink for different optical wavelength.

In-Vivo MPI Investigations

In this experiment, the multispectral photoacoustic images were created in-vivo by using DAS, 32 D-FDMAS and 32 D-sDMAS beamformers. These multispectral photoacoustic images were compared in terms of measurement accuracy. In this experiment, photoacoustic emissions were generated from the back hand of a healthy human, as shown in figure 8.6. The wavelengths that were used in this experiment were 741, 773, 805, 840, 876 and 913 nm. These wavelengths were measured by using a spectrometer (Ocean Optics). In addition, the optical fluence on the surface of the back hand was maintained within the limit of the maximum permissible exposure (MPE) (Laser-Safety, 2014). The generated photoacoustic emissions were also averaged 100 times before creating photoacoustic images.
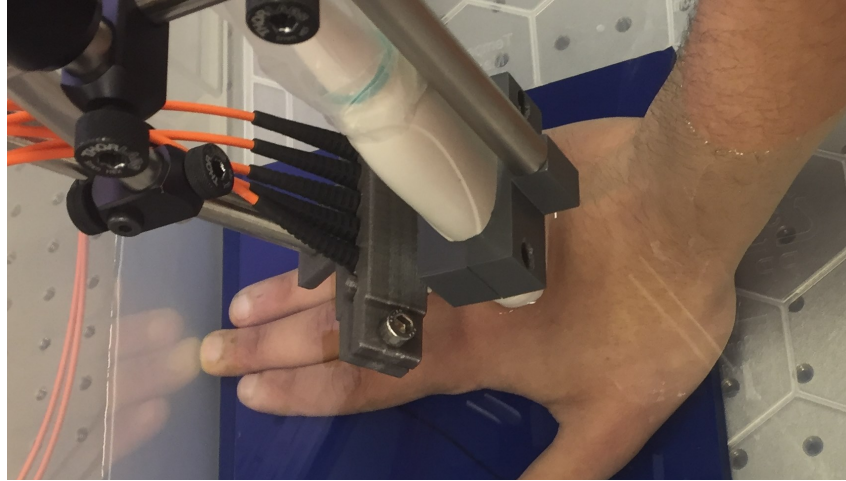
Figure 8.6: The part of the hand that the MPI was generated from.

8.4.1 Experimental Setup

The experimental setup is shown in figure 8.7. A Nd:YAG laser with OPO was used to fire laser pulses. The PRF of the laser was 10 Hz and the pulse length was 7 ns. These laser pulses were guided to the target through an optical fibre (BF76LS01, Thorlabs). This optical fibre had one input and seven outputs. Two outputs of this optical fibre were fed to the optical energy meter (THORLABS, ES120C) to measure the energy fluctuation of laser pulses. Other outputs were guided to the target. The generated photoacoustic emissions were detected using a linear array transducer (Verasonics L11-4) with 128 elements. The centre frequency of this transducer was 7.5 MHz and its -6 dB bandwidth was 90%. The received photoacoustic emissions were processed via the UARP II. The RF signals were digitalised by 80 MS/s. In these experiments, the received photoacoustic emissions were divided by the optical energy that was recorded by the optical energy meter before averaging them for 100 times. MATLAB (R2014a, Mathworks) was used to process the RF signals and create multispectral photoacoustic images.
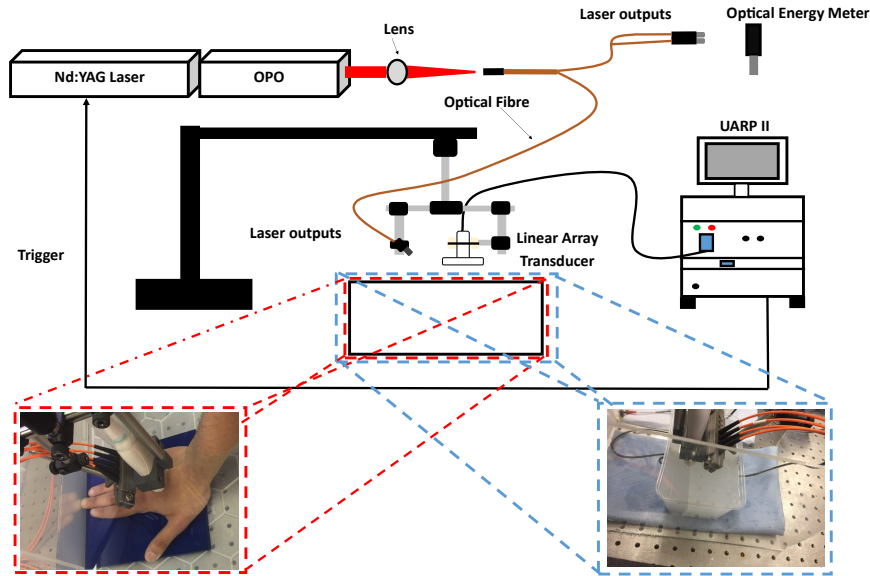
Figure 8.7: Experimental setups for comparisons between the optical spectrum and photoacoustic spectrum and generating MPI.

8.4.2 Experiments results

Comparisons Between the Optical Spectrum and Photoacoustic Spectrum

In this experiment, the tube walls absorbed optical energy and had a large mismatch acoustic impedance with water. As a result, acoustic signals were generated from the tube walls. These acoustic signals affected the measurements of the ink absorption. This effect does not happen in vivo measurements. This is because the acoustic impedances of soft tissues are close to each other (Hoskins *et al.*, 2010). In addition, the absorption coefficients of biological materials are known (Jacques *et al.*, 2014). To reduce the effect of tube walls on the experimental results, this tube was filled with water and photoacoustic emissions were generated from it at all wavelengths used in this experiment. After that, these photoacoustic emissions were subtracted from the photoacoustic emissions generated from the tube when it was filled with ink. Photoacoustic images were created using DAS, 32 D-FDMAS and 32 D-sDMAS beamformers as shown in figures 8.8, 8.9 and 8.10, respectively. By using the DAS beamformer (figure 8.8), the contrast of the image is high when the wavelength of the firing laser

was 700 nm. This is because the optical absorption coefficient of the ink was high at 700 nm. This optical absorption was significantly reduced as the wavelength of the firing laser was increased. As a result, the contrast of the photoacoustic image was noticeably reduced when the wavelength of laser pulse was 800 nm (figure 8.8 (F)). However, the photoacoustic images resultant from the DAS beamformer suffered from background noise. This noise was significantly reduced when the 32 D-FDMAS beamformer was used, as shown in figure 8.9. In this beamforming technique, some parts of photoacoustic signals were lost due to the use of a bandpass filter. By using the 32D-sDMAS beamformer as shown in figure 8.10, all parts of the signals were preserved. However, the noise level of the photoacoustic images was higher than that by using the 32D-FDMAS beamformer.
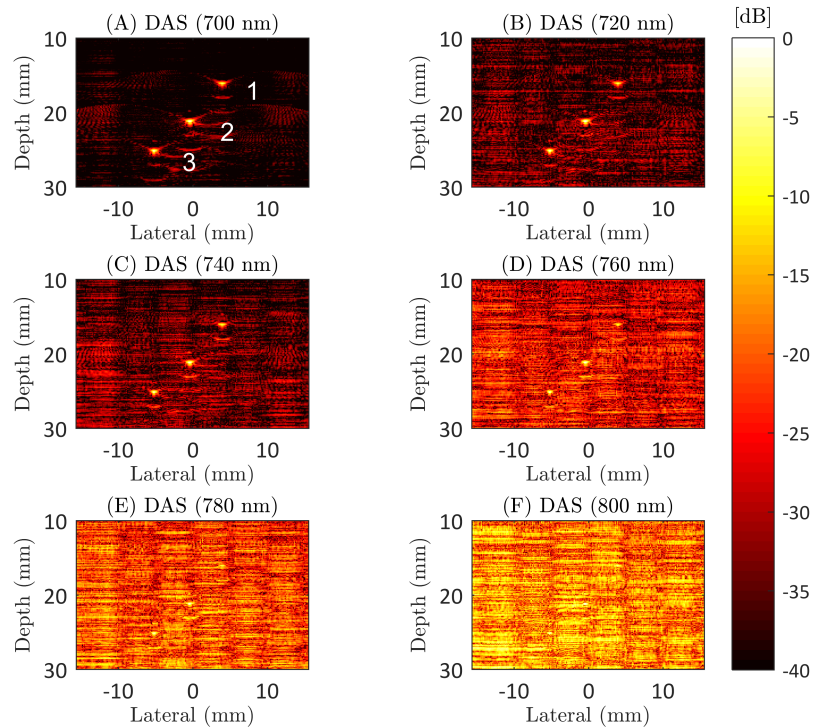
Figure 8.8: Photoacoustic images of the tube phantom filled with ink. These images show the effect of the wavelength of firing lasers on the generated photoacoustic images when DAS beamformer was used. Dynamic range: 40 dB.
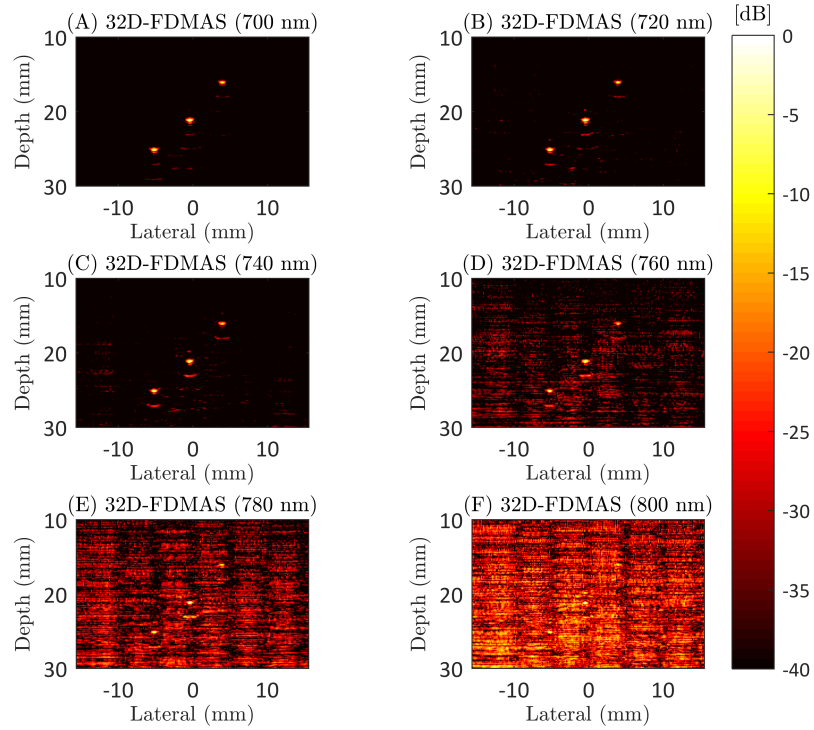
Figure 8.9: Photoacoustic images of the tube phantom filled with ink. These images show the effect of the wavelength of firing lasers on the generated photoacoustic images when 32D-FDMAS beamformer was used. Dynamic range: 40 dB.
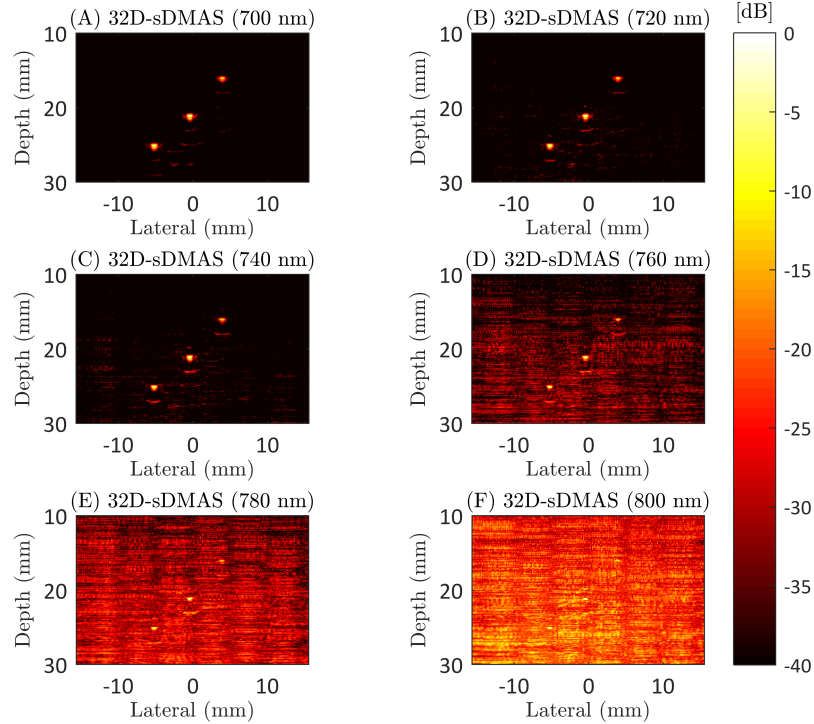
Figure 8.10: Photoacoustic images of the tube phantom filled with ink. These images show the effect of the wavelength of firing lasers on the generated photoacoustic images when 32D-sDMAS beamformer was used. Dynamic range: 40 dB.

Figure 8.11 shows comparisons between the normalised optical spectrum and normalised photoacoustic spectrum of the black Parker ink for different beamforming techniques. These measurements were based on six samples. The photoacoustic spectrum was calculated based on the peak amplitude of each target in the image. As it can be seen the normalised photoacoustic spectrum meets the normalised optical spectrum of the ink for all beamforming techniques.
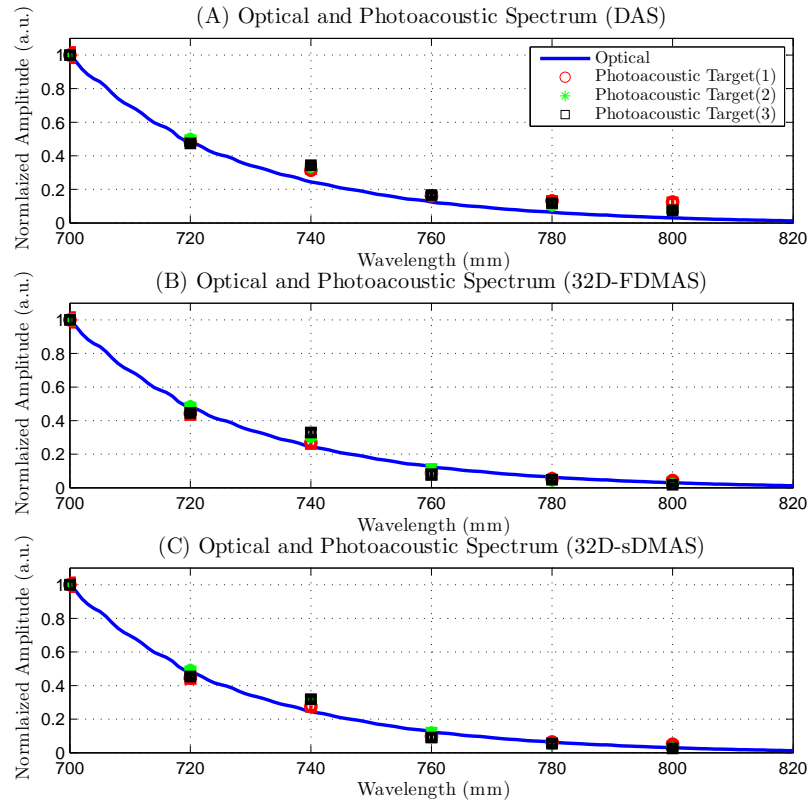
Figure 8.11: The optical and photoacoustic spectrums of the Parker ink for three point targets when DAS, 32 D-FDMAS, and 32 D-sDMAS beamformers were used.

Results of In-Vivo MPI Measurements

The ultrasound and photoacoustic images of the back hand are shown in figure 8.12. The wavelength of the laser pulses that were used to generate photoacoustic images was 840 nm. Figure 8.12 (A) shows the ultrasound image of this back hand generated from a single plane wave. In this ultrasound image, the contrast of the blood vessels was low. This contrast will be emphasised by using photoacoustic imaging. Figure 8.12 (B) shows the photoacoustic image (hot colormap) of the back hand when the DAS beamformer was used. The contrast of the blood vessels increased when compared with using ultrasound imaging. However, this photoacoustic image suffered from high-level clutter. The clutter was significantly reduced when the 32 D-FDMAS beamformer was used, as shown in figure 8.12 (C). This beamformer is non-linear, and a bandpass filter was used to remove the low-frequency component. Figure 8.12 (D) shows the

photoacoustic image that was created by using the 32 D-sDMAS beamformer. The 32 D-sDMAS beamformer is the linear form of 32 D-FDMAS. This beamformer reduced clutter compared with the DAS beamformer (Figure 8.12 (B)). However, this reduction in clutter was not as significant as that obtained using the 32 D-FDMAS beamformer. SNRs of the photoacoustic images were calculated which were the ratio between the mean of the signal and the standard deviation of background noise (Wang *et al.*, 2017). The dashed rectangle number 1 and number 2 in figure 8.12 (B) show the regions of signal and background, respectively. The 32 D-sDMAS beamformer improved SNR by 4 dB compared with the DAS beamformer. However, the 32 D-FDMAS beamformer enhanced the SNR by 5 dB compared with the 32 D-sDMAS beamformer.
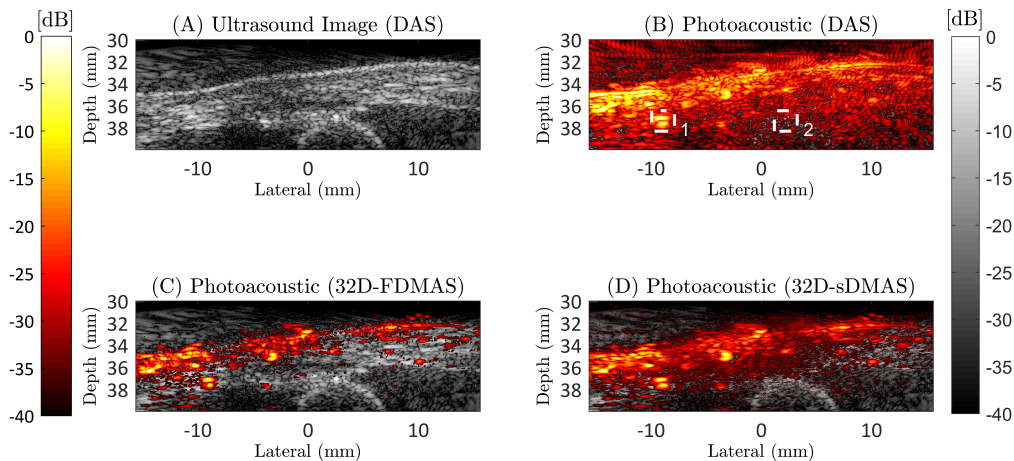
Figure 8.12: Ultrasound and photoacoustic images of the back hand. (A) Ultrasound image. (B) Photoacoustic image by using the DAS beamformer. (C) Photoacoustic image by using the 32 D-FDMAS beamformer. (D) Photoacoustic image by using the 32 D-sDMAS beamformer. In all photoacoustic images, ultrasound images were combined with them. Dynamic range of ultrasound images (gray): 40 dB. Dynamic range of photoacoustic images (hot): 40 dB.

In MPI, the absorbed laser fluence depends on its wavelength. As a result, the fluence should be corrected to reduce the measurement error (Li *et al.*, 2018). Figure 8.13 shows the oxygen saturation of the blood vessels of the back hand by using different

beamforming techniques. Before the oxygen saturation was calculated, the fluence was corrected by assuming one dimensional fluence attenuation (An & Cox, 2018). The absorption and reduced scattering coefficients of the biological tissue were calculated based on (Jacques, 2013). The photoacoustic image was divided by the fluence correction to reduce the measurement error. The multiple wavelength images of the back hand are shown in Appendix (7). Figure 8.13 (A) shows the measurement of oxygen saturation with the DAS beamformer where the clutter affected MPI. This effect was significantly reduced when 32 D-FDMAS and 32 D-sDMAS beamformers were used, as shown in figure 8.13 (B) and (C), respectively. The oxygen saturation measurement of the blood vessel in the green box was 79 ± 17 % (mean ± standard deviation of pixel values) with the DAS beamformer. This measurement had high fluctuations due to noise and clutter. By using the 32 D-FDMAS and 32 D-sDMAS beamformers, the oxygen saturations were 68 ± 9 % and 71 ± 9 %, respectively. These measurements had fewer fluctuations than when using the DAS beamformer. In addition, It was close to the value of oxygen saturation in veins as shown in (Sacks, 2004).
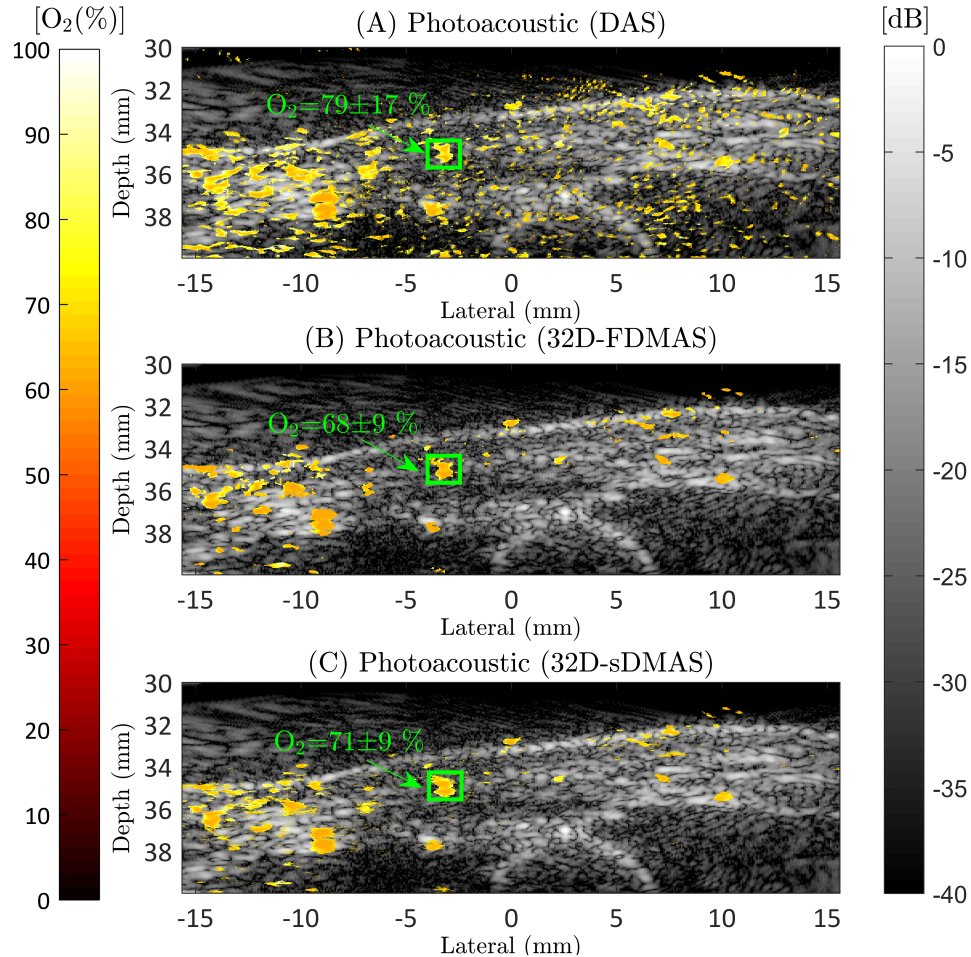
Figure 8.13: Oxygen saturation of blood vessels in the back hand by using (A) DAS, (B) 32 D-FDMAS, and (C) 32 D-sDMAS beamformers. This oxygen saturation was measured for veins (The normal values are between 70 % and 75 % (Sacks, 2004)) which were close to the hand surface. The oxygen saturation measurements were superimposed on the corresponding ultrasound image with a dynamic range: 40 dB.

8.5 Discussion

The results of blood vessel simulations (Figure 8.3) show that the 32 D-sDMAS beamformer generated sidelobes in photoacoustic images. This is different from the 32D-FDMAS beamformer. These sidelobes were due to the phase of signals that were the result of DAS beamformer. However, the level of sidelobes was lower than when using

the DAS beamformer. This is because the correlation operation in the 32 D-sDMAS beamformer enhances the correlated signals. For MPI of the back hand (Figure 8.13), the values of oxygen saturation when using the 32 D-FDMAS and 32 D-sDMAS beamformers were more comparable to each other. This means that the linearity of D-FDMAS beamformer does not significantly affect the MPI. In addition, these values were close to the normal value of oxygen saturation in veins (70 % - 75 %) (Sacks, 2004). These were different from the oxygen saturation from the DAS beamformer. This oxygen saturation suffered from high fluctuations. However, the accuracy of MPI using 32 D-sDMAS and 32 D-FDMAS beamformer will be reduced as the noise level is increased due to the correlation operation. The noise level can be reduced if the effect of optical attenuation on the generating photoacoustic emissions is reduced by delivering laser pulses to the target through a needle (Xia *et al.*, 2016). To produce more accurate measurements for oxygen saturation, the number of wavelength measurements should be increased. Moreover, one of the accurate fluence correction models should be used (Brochu *et al.*, 2016; Cox *et al.*, 2006). However, the accurate fluence correction models increased the computation times. This is because these models had many iterations for fluence correction. Therefore, D-sDMAS and D-FDMAS beamformers are preferred to be used in applications of MPI that do not need a high accuracy. For example, molecular tracking and tumour monitoring by using a contrast agent such as single walled carbon nanotubes conjugated with cyclic Arg-Gly-Asp (RGD). This contrast agent concentrates on the tumour blood vessels with a time . As a result, the amplitude of the generated photoacoustic signal from the tumour will be increased when compared with normal tissue (De la Zerda *et al.*, 2008). Another example is drug delivering and treatment monitoring by measuring the pH value. The pH value is measured by delivering the theranostic platform (THPDINs) to the target (tumour) and generating photoacoustic emissions from it. The ratio of the amplitude of photoacoustic emissions that are generated by using 825 nm and 680 nm laser wavelengths depends on the pH value (Yang *et al.*, 2019).

8.6   Conclusion

In this study, the D-FDMAS beamformer was linearised and called D-sDMAS. This D-sDMAS beamformer was affected by the phase of the beamformed data from the DAS

beamformer and produced sidelobes. These beamforming techniques were applied to MPI using in-vivo measurements. The D-FDMAS and D-sDMAS beamformers provided more accurate measurements of oxygen saturation in veins than the DAS beamformer. In addition, the oxygen saturation value generated by using the D-FDMAS beamformer was comparable to that when using the D-sDMAS beamformer.

Chapter 9

Summary

Photoacoustic imaging provides functional and anatomical information of the body, such as depiction of the capillary density, SLN and oxygen saturation. Solid-state laser sources are commonly used in photoacoustic imaging. The unaffordability and relatively large size of these laser sources limit their widespread diagnostic use. Photoacoustic imaging will be more accessible if a more affordable and portable pulse laser source, such as the PLD, is used. The PLD suffers from low output optical energy when compared with the solid-state laser source. This limits the imaging depth and the generated photoacoustic image has a low SNR. Some techniques, such as the averaging technique, combining multiple PLDs and coded excitations, have been investigated to deal with these limitations. In this thesis, the factors that limit using PLDs for photoacoustic applications were shown. In addition, a few techniques that make PLDs more useable in photoacoustic imaging were developed.

9.1   Chapter 2

The required number of PLDs to achieve a specific SNR for photoacoustic emissions was estimated. Based on this calculation, 190 PLDs were needed to achieve a 10.02 dB SNR for a blood vessel located at a depth of 4 mm. The output energy of this number of PLDs was studied experimentally using an agar phantom. In this experiment, the Nd:YAG laser was used to simulate the output optical energy from PLD. The output optical energy from 190 PLDs achieved 7.5 dB SNR. This large number of PLDs makes PLDs suitable just for superficial imaging as the assembly of these PLDs will be complex. In

addition, the price of 190 PLDs with their drivers (£ 179k) was higher than that of the Nd:YAG laser (around £ 110k). There were some limitations in this calculation, for instance, the ultrasound attenuation was calculated based on the high frequency component within the -6 dB transducer bandwidth. In addition, the high PRF of PLDs was not investigated.

9.2   Chapter 3

The Nd:YAG laser is the most common laser source in photoacoustic imaging. This is because the output optical energy of this laser source is high. However, its PRF is within 10 to 20 Hz. As a result, this laser source is not suitable for photoacoustic applications that need a high frame rate. Therefore, PLD which has high PRF is investigated in photoacoustic applications. This PLD has low output optical energy. As a result, the photoacoustic signal generated by using PLD has low SNR. Therefore, coded excitations were investigated to improve SNR. One of the most popular coded excitations is the unipolar golay code. In the unipolar golay code that does not generate coding artefacts in photoacoustic emissions, four sequences of laser pulses are transmitted. Two sequences were for positive pulses while the others for negative pulses. This unipolar golay code was developed to transmit only two sequences of pulses with less effect on its performance. This developed unipolar golay code was compared with some photoacoustic coded excitations using simulations. This developed unipolar golay coded produced coding artefacts. In this comparison, this developed code provided a slightly higher code gain than the original unipolar golay code if the noise level was high. In addition, the acquisition time of the developed unipolar golay code was shorter than that of the original unipolar golay code by 78 μsec when the deepest imaging target had a depth of 6 cm. This is because after transmitting each pulse sequence, the time of flight of the photoacoustic wave from the deepest imaging target will be waited to receive the sequence of the generated photoacoustic waves. In the developed unipolar golay code, two sequences of pulses are transmitted, while in the original unipolar golay code, four sequences of pulses are transmitted. As a result, the developed unipolar golay code has less consumption time than the original unipolar golay code.

9.3   Chapter 4

The micro-Doppler technique was investigated by using a linear array transducer to recover the lost part of the photoacoustic image due to the limited transducer bandwidth. In addition, it was used to extract a very weak photoacoustic emission. Based on simulations, the low-frequency part of the photoacoustic image was recovered using the micro-Doppler technique. In addition, the SNR of the photoacoustic image was improved by 16.18 dB compared with the passive technique. In experiments, the SNR was improved by 15 dB compared with the passive technique. However, the low-frequency part of the photoacoustic image was not recovered. This is because the bandpass filter that was used to extract the photoacoustic emission from the small angle approximation that was the result of multiplying two sine waves. This technique will help to increase the imaging depth, and make the low output laser sources, such as the PLD, more useful in photoacoustic imaging.

The quality of the photoacoustic image was affected by clutter, phase aberration and motion artefacts. These effects will be significant, if the DAS beamformer is used, in reducing the spatial resolution and SNR of photoacoustic imaging. In addition, sidelobes will be generated. In this thesis, some beamforming techniques were investigated to improve the spatial resolution and SNR, and reduce clutter in photoacoustic imaging.

9.4   Chapter 5

The FDMAS beamformer was applied to photoacoustic imaging by using a linear array transducer. This beamformer depends on the correlation operation between the delayed RF signals. Based on experimental measurements, it improved the SNR by 6.9 dB compared with the DAS beamformer. In addition, from the point spread function of a single absorbent point (Simulation), the FDMAS beamformer enhanced the axial and lateral resolutions by 10 % and 34 %, respectively, when compared with the DAS beamformer. The FDMAS beamformer showed a reduction in side lobes compared with the DAS beamformer. This reduction was emphasised, if the beamforming step size in the lateral direction was reduced.

9.5   Chapter 6

The FDMAS beamformer was investigated in 3D photoacoustic imaging by mechanically moving a 1D linear array transducer. This beamformer improved the elevation resolution. It also reduced the clutter and background noise compared with the DAS (3D) beamformer. There were two ways to apply the FDMAS beamformer to 3D photoacoustic imaging. One of them was with the sum combination (S-FDMAS (3D)) and the other was with the multiplication combination (M-FDMAS (3D). Based on the carbon fibre rod experiment, S-FDMAS (3D) improved the elevation and lateral resolutions by 28 % and 20 %, respectively, compared with the DAS (3D) beamformer. The S-FDMAS (3D) beamformer enhanced also the SNR by 12 dB compared with the DAS (3D) beamformer. The M-FDMAS (3D) beamformer increased the elevation and lateral resolutions by 35 % and 17.5 %, respectively, compared with the DAS (3D) beamformer. In addition, it improved the SNR by 11 dB when compared with DAS (3D). When FDMAS (3D) was applied to complex structures, it improved its spatial resolution. It also provided improved depictions of the small branches in the leaf skeleton.

9.6   Chapter 7

The D-FDMAS beamformer was proposed and the SA-FDMAS beamformer was applied to photoacoustic imaging. These beamformers reduced clutter and the background noise of photoacoustic images compared with the DAS beamformer. In addition, these beamformers decreased the contrast difference between the needle and SLN compared with the FDMAS beamformer. The D-FDMAS beamformer has advantages over the SA-FDMAS beamformer in terms of simplicity and computational efficiency. Based on experimental measurements, the optimised sub-group for the D-FDMAS beamformer should have 16 to 32 elements, while for the SA-FDMAS beamformer each sub-group should have 32 to 64 elements. In the inclusion and needle experiment, the 16 D-FDMAS beamformer improved the SNR of the inclusion and needle by almost 5 and 8 dB, respectively, compared with the DAS beamformer. It reduced the contrast difference between the needle and inclusion by almost 12 dB compared with the FDMAS beamformer.

9.7 Chapter 8

The reduction of background noise and clutter with the D-FDMAS beamformer was investigated in MPI. The D-FDMAS beamformer was linearised and called D-sDMAS. The linearity effect of the D-FDMAS beamformer was studied. Based on in-vivo measurements, the oxygen saturation of a vein that the 32 D-FDMAS beamformer provided ($O_2 = 68 \pm 9$ %) was comparable to that when using the 32 D-sDMAS beamformer ($O_2 = 71 \pm 9$ %). In addition, these oxygen saturation values provided by using the 32 D-FDMAS and 32 D-sDMAS beamformers were closer to the real value than the value given by using the DAS beamformer ($O_2 = 79 \pm 17$ %).

9.8 Future Work

- In the estimation, the number of PLDs needed to achieve a specific SNR for photoacoustic emissions, ultrasound attenuation will be considered for all frequency components within the -6 dB transducer bandwidth. The PRF of PLDs will also be investigated to increase the accuracy of calculation. This is because the SNR of the photoacoustic will be improved by using the averaging technique. However, the transmitted optical energy should be reduced when the PRF is increased for safety reasons.

- The developed unipolar golay code will be compared with the original golay code experimentally.

- In micro-Doppler technique, the effect of the DC part of the small angle approximation will be reduced by applying windows to the carrier signals rather than applying a bandpass filter. As a result, the low frequency part of the photoacoustic signal will be experimentally recovered.

- The FDMAS beamformer will be applied in the real-time process by using one of the real-time processors.

- The D-FDMAS beamformer will be applied to 3D photoacoustic imaging by using a 1D linear array transducer. In addition, The D-FDMAS (3D) beamformer will be compared with the FDMAS (3D) beamformer in terms of SNR, spatial resolution and complexity.

Appendix A

1 Generating Velocity Potential and Pressure Wave

The equations of velocity potential and pressure waves was taken from (Jacques, 2004, 2014; Paltauf *et al.*, 2002). The equations for calculating the diameter of the focal point, the radius of the focal point and the half angle spread were based on (OLYMPUS, 2015). The Matlab code for generating velocity potential and pressure wave is shown below:

```matlab
%%% Generate potential velocity and pressure wave%%%
% Where:
%QQ is potential velocity (m^2/sec)
%p  is pressure wave (Pa)
%tt is time scale (sec)
%x  is x length of biological tissue [cm]
%y  is y length of biological tissue [cm]
%z  is z length of biological tissue [cm]
%dx is step size in x direction [cm]
%dy is step size in y direction [cm]
%dz is step size in z direction [cm]
%Nz is number of steps in z direction (depth)
%PLD_Number is number of PLDs that is used
function [ QQ, p, tt] = VP_and_PW(y,x,z,dy,dx,dz,Nz,F,PLD_Number)
% clear all;
%% simulation specification %%
c=1500;                              % The speed of the ultrasound ...
    in the medium (m/s)
B=2.29e-4;                           % The thermal expansion (C-1)
rho=1000;                            % Density (Khm-3)
Cp=4184;                             % Specific heat (J Kg-1)
%% Transducer Specification (1) %%
FF=(17e-3);%/10;                      % The focal point (cm)
```

A.

```
23  f=3.5e6;                                % The centre frequency of ...
        the transducer
24  D=(6.3e-3);%/10;                         % The diameter of the ...
        transducer (cm)
25  %% The diameter of the focus point %%
26  BD=(1.02*FF*c)/(f*D);                    % The diameter of the focus ...
        point
27  haf_BD=BD/2;                             % The radius of the focus point
28  % The place of the ultrasound transducer
29  tranducer=[0 0 0]*1e-2;
30  %The received point%
31  [YYY XXX ZZZ]=meshgrid(y,x,z);
32  t_for=(ZZZ.*1e-2)≥tranducer(3);
33  %% The energy absorbed on the object%%
34  % The destance between the ditector and points
35  Rkj=sqrt((XXX.*1e-2-tranducer(2)).^2+(YYY.*1e-2-tranducer(1)).^2 ...
36      +(ZZZ.*1e-2-tranducer(3)).^2);
37  %% Some calculation %%
38  dv=(dx)*(dy)*(dz)*1e-6;                  % The volume of the element
39  dt=((dx)*1e-2+(dy)*1e-2+(dz)*1e-2)/(3*c); % The time step
40  s=(((dz*Nz)-tranducer(3))*1e-2)/c;       % The depth of the ...
        scanning medium in time scale
41  NN=s/dt;                                 % The number of sampling ...
        in time scale
42  %% calculate the potential velocity%%
43  wwkj=1;        % assume the transducer have large  felid of view
44  element_number=0;
45  parfor kk=1:1:(NN)
46      Q(kk)=0;            % The initial value of the potential velocity
47      tot_dis=dt*kk*c;    % The distance that transducer sample move
48      step=tranducer(3)+(dt*kk*c);    % The step size for the sampling
49      rk=[tranducer(1) tranducer(2) step];    % The place of the ...
            sampling curve
50      tk=sqrt(((tranducer(1)-rk(1))^2)+((tranducer(2)-rk(2))^2) ...
51          +((tranducer(3)-rk(3))^2))/c; % the distance between the ...
                sample curve and the transducer in time scale
52      %% calculate the potential velocity for each sample curve %%
53      hkj=(abs(tk-(Rkj./c))<(dt/2));
54      % Calculate if the scanning element is within the field of view ...
            of the
55      % transducer
56      if (tot_dis≤FF)
57      % Transducer beam
58      pos_tranducer=[D/2 D/2 tranducer(3)]; % The positive coordinate ...
            for the transducer
```

```matlab
59        foc_tranducer=[haf_BD haf_BD (FF)]; % The positive coordinate of ...
              the focus point
60        x0=pos_tranducer(1); y0=pos_tranducer(2); z0=pos_tranducer(3);
61        x1=foc_tranducer(1);y1=foc_tranducer(2);z1=foc_tranducer(3);
62        z_test=abs(ZZZ.*1e-2);
63        x_test=(((z_test-z0)/(z1-z0))*(x1-x0))+x0;
64        y_test=(((z_test-z0)/(z1-z0))*(y1-y0))+y0;
65        wwkj=( abs(XXX.*1e-2)≤x_test)&(abs(YYY.*1e-2)≤y_test);
66        else
67        alfa=asin((0.514*c)/(f*D));
68        zz=(D/2)/tan(alfa);
69        pos_tranducer=[haf_BD haf_BD (FF)]; % The positive coordinate for ...
              the transducer
70        foc_tranducer=[D/2 D/2 (zz)]; % The positive coordinate of the ...
              focus point
71        x0=pos_tranducer(1);y0=pos_tranducer(2);z0=pos_tranducer(3);
72        x1=foc_tranducer(1);y1=foc_tranducer(2);z1=foc_tranducer(3);
73        z_test=abs(ZZZ.*1e-2);
74        x_test=(((z_test-z0)/(z1-z0))*(x1-x0))+x0;
75        y_test=(((z_test-z0)/(z1-z0))*(y1-y0))+y0;
76        wwkj=( abs(XXX.*1e-2)≤x_test)&(abs(YYY.*1e-2)≤y_test);
77   %%%%%%%%%%%%%%%%%%%%%%%%%%%%%%%%%%%%%%%%%%%
78        end
79   % Calculate potential velocity
80   Akj=-(B./(4*pi*rho*Cp).*(dv/dt).*(hkj./(Rkj)).*wwkj).*t_for;
81   Qn=(Akj.*F).*(1e6);
82   Q(kk)=sum(Qn(:));
83   % Calculate Time scale
84   tt(kk)=dt*kk;
85   end
86   %% calculate the pressure
87   PLD=PLD_Number*1.57e-5;  % The energy of PLDs (1.57e-5 J for one PLD)
88   QD=PLD*Q;
89   QQ=-QD;
90   QQ(length(Q)+1)=0;                    % Increase one point to make ...
         comparison
91   for i=1:length(Q)
92   p(i)=(rho/dt)*(QQ(i+1)-QQ(i));        % calculate the pressure (Pa)
93   end
94   end
```

After the ideal pressure wave is generated, the impulse response of the ultrasound transducer will be applied to it. In addition, this pressure will be attenuated and converted to a voltage. Then, the RMS value of the pressure wave will be calculated

A.

as shown in the below Matlab code:

```matlab
1  %% Applying Impulse response of ultrasound transducer %%
2  %Where:
3  %mean_signal is RMS value of the Pressure wave
4  %VVo  is the pressure wave after applying impulse response of ...
       transduce(Pa)
5  %p    is ideal pressure wave (Pa)
6  %dt   is time step (sec)
7  %tt   is time scale of depth (sec)
8
9  function [mean_signal,VVo ] = RMS_conv( p,dt,tt)
10 %Idea Photoacoustic Emissions%
11 Fs =(1/dt);          % Sampling frequency
12 nfft =length(tt);    % Length of FFT
13 X = fft(p,nfft);     % FFT for the signal
14 mx = abs(X);         %make absolut value for The FFT
15 mx = mx(1:nfft/2);   % use the positive part of the FFT
16 f = (0:nfft/2-1)*Fs/nfft;     % Frequency scale
17 %%%%%%%%%%%%%%%%%%%%%%%%%%%%%%%%%%%%%%%%%%%%%%%%%%%%%%%%%%%%%%%%%%%%%%%%
18 %%Transducer(1)%%
19 tc_1 = gauspuls('cutoff',3.5e6,0.6529,[],-60);
20 t_1 = -tc_1 : dt : tc_1;
21 yi_1 = gauspuls(t_1,3.5e6,0.6529);
22 nfft =length(tt);                   % Length of FFT
23 s_1 = fft(yi_1,nfft);               % FFT for the signal
24 mamp_1=s_1/max(abs(s_1));
25 f_tran_1 = (0:nfft/2-1)*Fs/nfft;    % Frequency scale
26 %%%%%
27 mx_r_s_1=X.*mamp_1;                 % Apply the impulse ...
       response of transducer on photoacoustic emissions
28 mx_r_11 = abs(mx_r_s_1);            %make absolut value for ...
       The FFT
29 mx_r_1 = mx_r_11(1:nfft/2);         % use the positive part of ...
       the FFT
30 VVo=ifft(mx_r_s_1,nfft);            %calculte the effect of ...
       the transducer on the shape of the Photoacusitic wave ( in Time ...
       domain)
31 %%%%%%%%%%%%%%%%%%%%%%%%%%%%%%%%%%%%%%%%%%%%%%%%%%%%%%%%%%%%%%%%%%%%%%%%
32 % Applying attenuation on the photoacoustic signal
33 transducer_f=4.6e6;                             % The frequency ...
       that is used to calculate the attenuation
34 for i=1:length(tt)
35     diss(i)=tt(i)*1500*100;                     % Calculate the ...
```

```
         depth in cm
36       atten_dB=0.9*diss(i)*(transducer_f/(1e6))^1.1;  % Attenuation ...
             dB/cm/MHz
37       atten_lin=10^(-atten_dB/10);
38       P_atenu(i)=VVo(i)*atten_lin;
39   end
40   %convert the pressure wave to voltage
41   for i=1:length(tt)
42       s_volt(i)=P_atenu(i)*(0.27e-6) ;
43   end
44   % calculate the RMS voltage of the received signal
45   s_volt2 = interp( s_volt,34);              % Interpolation the signal
46   ttt = interp( tt,34);                      % Interpolation time
47   ss_volt=(s_volt2.^2);
48   %%%%%%%%%%%%%%%%%%%%%%%%%%%%%%%%%%%%%%%%%%%%%%%%%%%
49   sum_ss_volt=0;
50   sum_ss_volt=sum(ss_volt((230*34):(360*34)));
51   mean_signal=sqrt(sum_ss_volt/(((360*34)-(230*34))+1)); %RMS of Pressure
52   end
```

Then, the SNR of pressure wave will be calculated based on the RMS value of the signal and the RMS value of noise that is taken from experiments.

2 Gelatine Phantom

The recipe of gelatine phantom consists of 6% of gelatin (Sigma, G2500-1KG), 2% of germall (Gracefruit, Germall Plus) and 88% of degassed and de-ionised water. This recipe, and the method for creating the gelatine phantom, was taken from (Browne *et al.*, 2003; Nie *et al.*, 2018). The inclusion was created with the same steps that were used to create the gelatine phantom but Parker ink was added to it. By adding Parker ink, the absorption of the inclusion was almost 5 cm^{-1}.

3 Coded Artefacts of Coded Excitation

Figure A.1 shows the shapes of the coded artefacts for certain coded excitations. The unipolar golay code with 512 code length did not generate coded artefacts, as seen when comparing figures A.1 (A) with (B). The legendre code sequence with 639 code length, pulse position modulation with 56 code length and developed unipolar golay code with 1024 code length generated coded artefacts in the photoacoustic signal as shown in

figures A.1 (C), (D) and (E). The distribution of these artefacts was changed based on the size of the code length for each coded excitation. In addition, the amplitude difference between the target signal and artefacts was reduced as the code length was reduced.

(A) Original Photoacoustic Signal

(B) Unipolar Golay Code ($N_L = 512$)

(C) Legendre Code Sequence ($N_L = 639$)
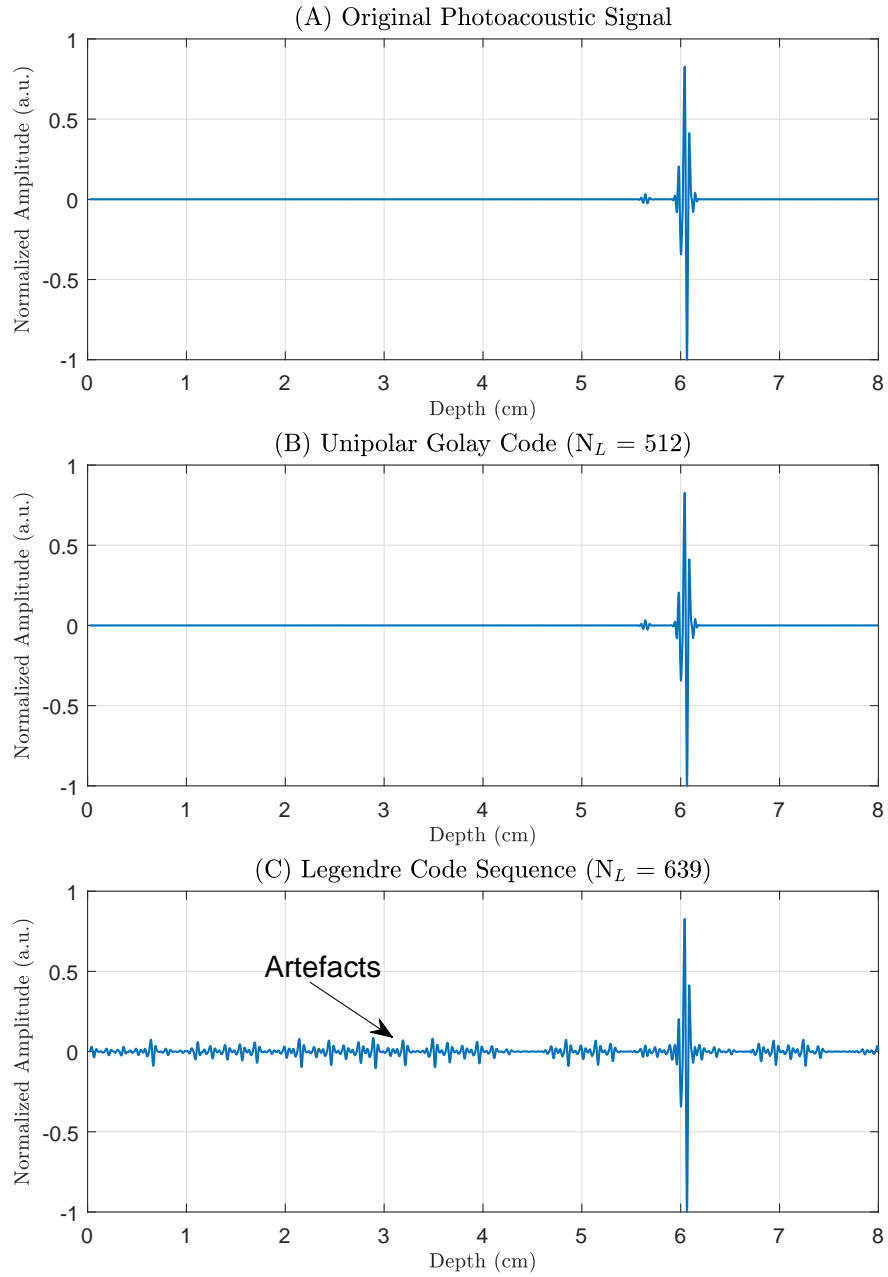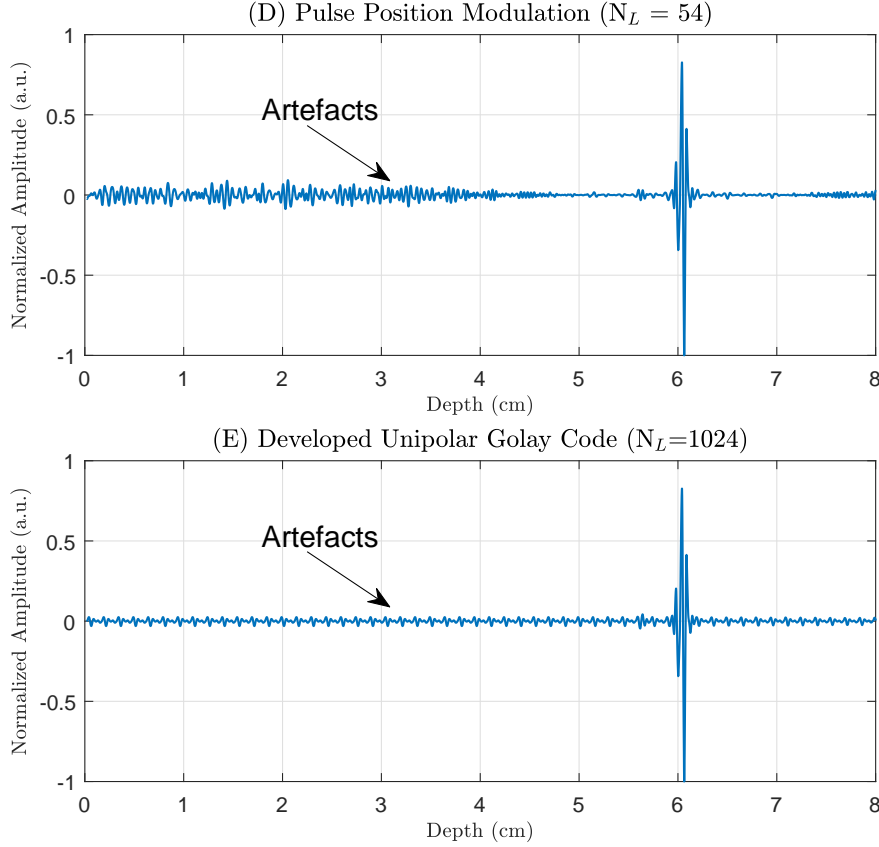
Figure A.1: Shapes of artefacts of coded excitations. (A) Original photoacoustic signal, (B) Unipolar Golay Code (N_L = 512), (C) Legendre Code Sequence (N_L = 639), (D) Pulse Position Modulation (N_L = 56) and (E) Developed Unipolar Golay Code (N_L=1024).

4 Down Conversion of the Micro-Doppler Signal

In the trigonometric identities, the product of a sine wave and a cosine wave is shown in equation A.1 (Mathematics, 2013):

$$\sin(A)\cos(B) = \frac{1}{2}(\sin(A - B) + \sin(A + B)).\tag{A.1}$$

By applying equation 4.4 to quation A.1, equation 4.4 can be written as equation A.2 (Gao *et al.*, 2016):

$$\begin{aligned}M_{mic-d} &= A_{mic-d}A_R\sin(2\pi(f_o + f_{mic-d})t)\cos(2\pi f_o t),\\ &= \frac{1}{2}A_{mic-d}A_R(\sin(2\pi f_{mic-d}t) + \sin(2\pi(2f_o + f_{mic-d})t)).\end{aligned}\tag{A.2}$$

The high-frequency part in equation A.2 will be removed by using a low-pass filter . After low-pass filtering, equation A.2 can be updated to equation A.3 (Gao *et al.*, 2016):

$$M_{mic-d} = \frac{1}{2} A_{mic-d} A_R \sin(2\pi f_{mic-d} t). \tag{A.3}$$

By investigating the small angle approximation as explained in equation A.4 (Bannison & Hall, -):

$$\sin(\theta) \approx \theta, \tag{A.4}$$

The micro-Doppler signal is obtained as given in equation A.5 (Gao *et al.*, 2016):

$$M_{mic-d} = \frac{1}{2} A_{mic-d} A_R 2\pi f_{mic-d} t. \tag{A.5}$$

By introducing equation 4.3 into equation A.5, the relation between the micro-Doppler and the photoacoustic signal is shown in equation A.6 (Gao *et al.*, 2016):

$$\begin{aligned} M_{mic-d} &= A_{mic-d} A_R \pi (\frac{2 f_o k_s R_d}{C} \frac{\partial P(t)}{\partial t} \cos\theta) t, \\ &= \alpha \frac{\partial P(t)}{\partial t} t, \end{aligned} \tag{A.6}$$

where $\alpha = \frac{2\pi A_{mic-d} A_R f_o k_s R_d \cos\theta}{C}$.

5 Experimental Down Conversion of the Micro-Doppler Signal

To down convert the micro-Doppler signal when using a linear array transducer, the modulated signal is multiplied with the carrier signal without shifting. From trigonometric identities, the product of a sine wave and another sine wave is given in equation A.7 (Mathematics, 2013):

$$\sin(A)\sin(B) = \frac{1}{2}(\cos(A - B) - \cos(A + B)). \tag{A.7}$$

Therefore, the multiplication of the modulated signal with the carrier signal is shown in equation A.8:

$$\begin{aligned} M_{mic-d} &= A_{mic-d} A_R \sin(2\pi(f_o + f_{mic-d})t)\sin(2\pi f_o t), \\ &= \frac{1}{2} A_{mic-d} A_R (\cos(2\pi f_{mic-d} t) - \cos(2\pi(2f_o + f_{mic-d})t)). \end{aligned} \tag{A.8}$$

The high-frequency part in equation A.8 can be removed by using a low-pass filter. After low-pass filtering, equation A.8 can be updated to equation A.9:

$$M_{mic-d} = \frac{1}{2} A_{mic-d} A_R \cos(2\pi f_{mic-d} t). \tag{A.9}$$

The small angle approximation of a cosine wave is shown in equation A.10 (Bannison & Hall, -):

$$\cos(\theta) \approx 1 - \frac{\theta^2}{2}. \tag{A.10}$$

By combining equationA.10 with equation A.9, equation A.11 is obtained:

$$\begin{aligned} M_{mic-d} &= A_m(1 - \frac{(2\pi f_{mic-d} t)^2}{2}), \\ &= (A_m - \frac{A_m(2\pi f_{mic-d} t)^2}{2}), \end{aligned} \tag{A.11}$$

$$A_m = \frac{1}{2} A_{mic-d} A_R,$$

where A_m is the dc part. It can be removed by using a bandpass filter as shown in equation A.12:

$$M_{mic-d} = -\frac{A_m(2\pi f_{mic-d} t)^2}{2}. \tag{A.12}$$

The micro-Doppler frequency will be extracted by applying the square root to equation A.12. To apply the square root operation, the sign operation is used to preserve the phase of the signal as shown in equation A.13:

$$\begin{aligned} M_{mic-d} &= sign(-\frac{A_m(2\pi f_{mic-d} t)^2}{2})\sqrt{|-\frac{A_m(2\pi f_{mic-d} t)^2}{2}|}, \\ &= sign(-\frac{A_m(2\pi f_{mic-d} t)^2}{2})\sqrt{|2A_m|}\pi f_{mic-d} t. \end{aligned} \tag{A.13}$$

By introducing equation 4.3(Gao $et\ al.$, 2016) into equation A.13, the relation between the micro-Doppler signal and photoacoustic emission is shown in equation A.14:

$$\begin{aligned} M_{mic-d} &= sign(-\frac{A_m(2\pi(\frac{2f_o k_s R_d}{C}\frac{\partial P(t)}{\partial t}\cos\theta)t)^2}{2})\sqrt{|2A_m|}\pi(\frac{2f_o k_s R_d}{C}\frac{\partial P(t)}{\partial t}\cos\theta)t, \\ &= \alpha\frac{\partial P(t)}{\partial t}t, \end{aligned} \tag{A.14}$$

where $\alpha = sign(-\frac{A_m(2\pi(\frac{2f_o k_s R_d}{C}\frac{\partial P(t)}{\partial t}\cos\theta)t)^2}{2})\sqrt{|2A_m|}\pi(\frac{2f_o k_s R_d}{C}\cos\theta)$. The limited number of transmitted cycles of the carrier signal makes the frequency spectrum broader.

This creates artefacts in the extracted photoacoustic emission. This broadband spectrum of the carrier signal will be extracted by multiplying the carrier signal with itself (down conversion of the broadband spectrum). Then all steps to extract the photoacoustic emission will be applied to it. By subtracting the extracted broadband signal from the extracted photoacoustic emission, the artefacts in the extracted photoacoustic emission will be reduced.

6 Spatial Resolutions of FDMAS and Sub-FDMAS Beamformers

6.1 Simulation Setup

Photoacoustic emissions were generated from three absorption points as shown in figure A.2 by using the K-Wave simulation toolbox (Treeby & Cox, 2010). The diameter of these points was 0.1 mm. Table A.1 shows the specifications of these simulations.
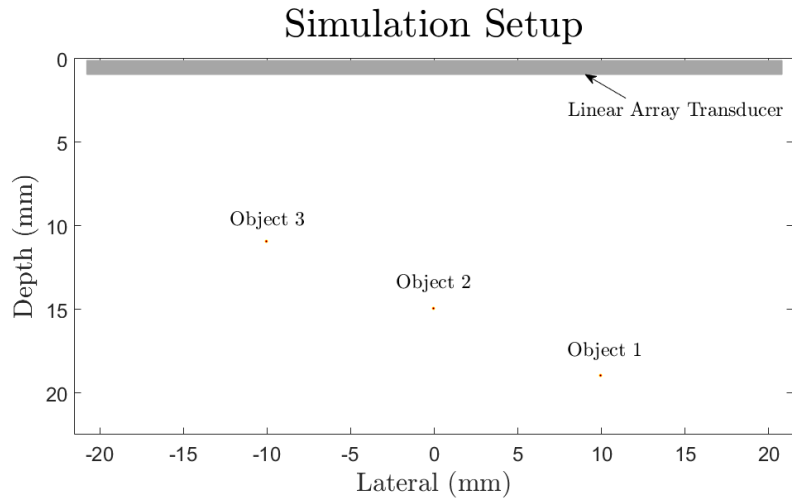
Figure A.2: Three absorbent points in the K-wave simulation to study the effect of FDMAS and Sub-FDMAS beamformers on spatial resolutions.

Specifications of the Simulation	
Grid Size (mm)	0.05
Element Number	128
Pitch Size (mm)	0.3
Centre frequency (MHz)	5
Fractional Bandwidth	60 %
Radius of the absorption target (mm)	0.05
Speed of sound in the medium (m/sec)	1500
Sampling frequency (MHz)	80

Table A.1: Specifications of the simulation to study the effect of FDMAS and Sub-FDMAS beamformers on spatial resolutions.

6.2 Simulation Results

Figure A.3 (A) shows the photoacoustic image for three absorption points when the DAS beamformer was used. In this image, the amplitudes of the sidelobes and artefacts were high when compared with the amplitudes of the targets. These sidelobes and artefacts were reduced when the FDMAS beamformer was used as shown in figure A.3 (B).
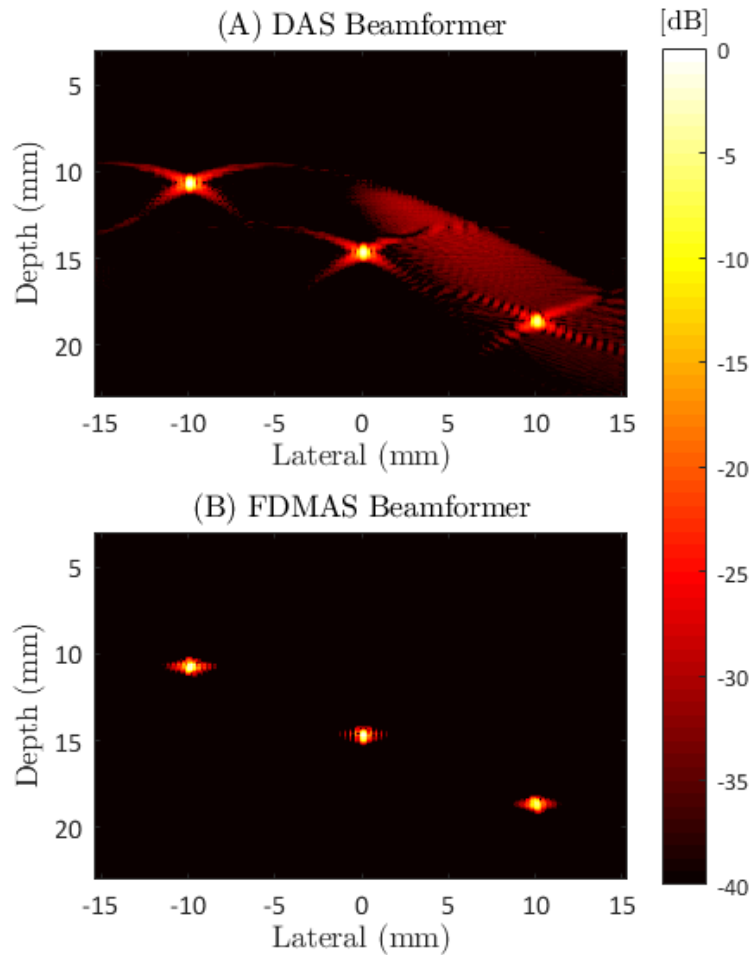
Figure A.3: Photoacoustic images of the three absorbents when using (A) DAS and (B) FDMAS beamformers. Dynamic range: 40 dB.

7 Multiple Wavelength Photoacoustic Images

Figure A.4 shows the multiple wavelength photoacoustic images for the back hand when the DAS beamformer was used. From this figure, it can be seen that the photoacoustic images had high clutter signals. In addition, the contrast of the blood vessels was increased as the wavelength of the laser was increased. This is because the percentage of oxyhemoglobin was higher than that of deoxyhemoglobin in the blood vessels. Moreover, the absorption coefficient of oxyhemoglobin was higher than that

of deoxyhemoglobin for the wavelength that was higher than 800 nm as shown in figure A.5 (Jacques *et al.*, 2014; Jacques, 2014). Figures A.6 and A.7 show the multiple wavelength photoacoustic images for the back hand when the 32D-FDMAS and 32D-sDMAS beamformers were used. From these figures, it can be seen that the clutter signals were reduced when compared with the images that were generated by using the DAS beamformer.
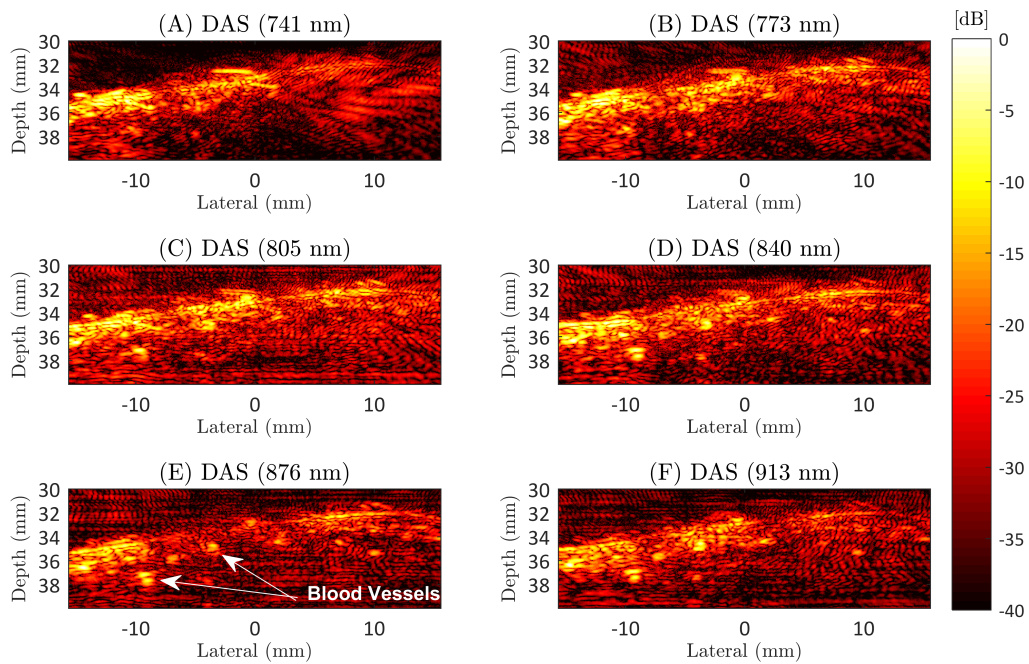
Figure A.4: Multiple wavelength photoacoustic images for the back hand when the DAS beamformer was used. Dynamic range: 40 dB.
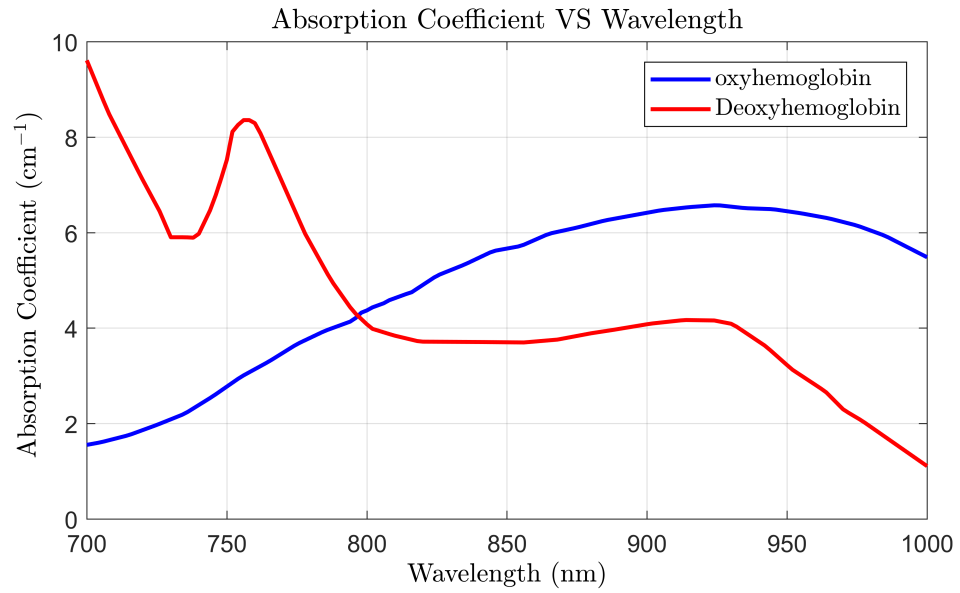
Figure A.5: Absorption coefficients of oxyhemoglobin and deoxyhemoglobin. These absorption coefficients were taken from the database of Monte Carlo simulation (Jacques et al., 2014; Jacques, 2014).
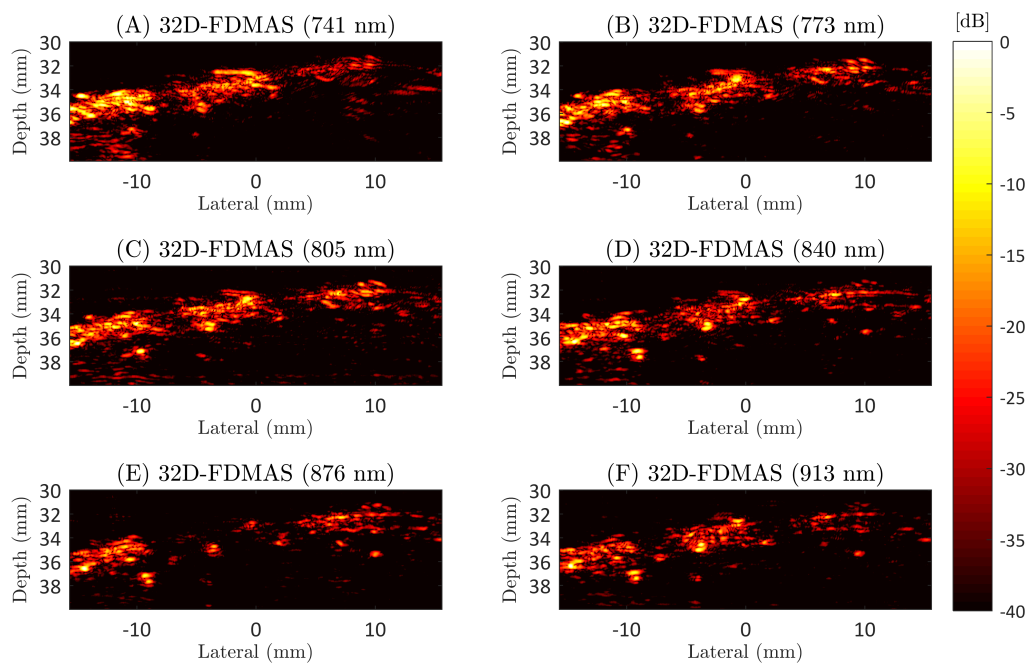
Figure A.6: Multiple wavelength photoacoustic images for the back hand when the 32D-FDMAS beamformer was used. Dynamic range: 40 dB.
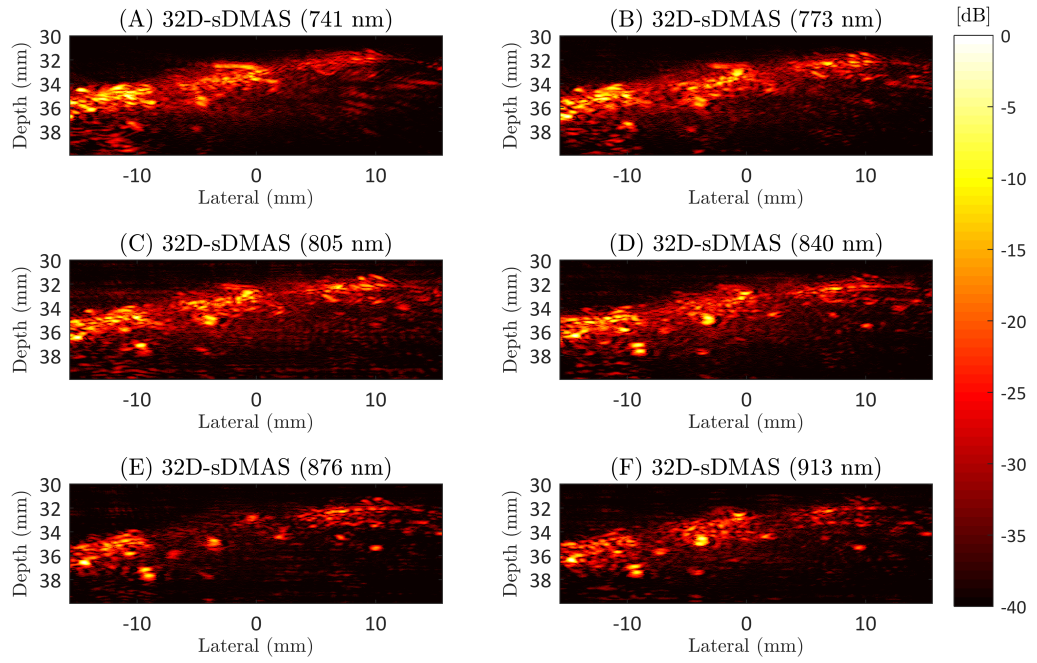
Figure A.7: Multiple wavelength photoacoustic images for the back hand when the 32D-sDMAS beamformer was used. Dynamic range: 40 dB.

References

AERNOUTS, B., VAN BEERS, R., WATTÉ, R., HUYBRECHTS, T., LAMMERTYN, J. & SAEYS, W. (2015). Visible and near-infrared bulk optical properties of raw milk. *Journal of dairy science*, **98**, 6727–6738. 186

ALLEN, T.J. & BEARD, P.C. (2006). Pulsed near-infrared laser diode excitation system for biomedical photoacoustic imaging. *Optics Letters*, **31**, 3462–3464. 2, 3, 10, 19, 38

ALLEN, T.J. & BEARD, P.C. (2007). Dual wavelength laser diode excitation source for 2d photoacoustic imaging. In *Biomedical Optics (BiOS) 2007*, 64371U–64371U, International Society for Optics and Photonics. 19

ALLEN, T.J. & BEARD, P.C. (2016). High power visible light emitting diodes as pulsed excitation sources for biomedical photoacoustics. *Biomed. Opt. Express*, **7**, 1260–1270. 40

ALLEN, T.J., COX, B. & BEARD, P.C. (2005). Generating photoacoustic signals using high-peak power pulsed laser diodes. In *Biomedical Optics 2005*, 233–242, International Society for Optics and Photonics. 2, 3, 10, 11, 18, 39

ALLES, E.J., JAEGER, M. & BAMBER, J.C. (2014). Photoacoustic clutter reduction using short-lag spatial coherence weighted imaging. In *Ultrasonics Symposium (IUS), 2014 IEEE International*, 41–44, IEEE. 3, 5, 88, 133

ALSHAYA, A., HARPUT, S., MOUBARK, A.M., COWELL, D.M.J., MCLAUGHLAN, J. & FREEAR, S. (2016). Spatial resolution and contrast enhancement in photoacoustic imaging with filter delay multiply and sum beamforming technique. In *2016 IEEE International Ultrasonics Symposium (IUS)*, 1–4. i, 5, 113, 133

REFERENCES

ALSHAYA, A., HARPUT, S., COWELL, D.M.J., CARPENTER, T., MCLAUGHLAN, J.R. & FREEAR, S. (2017). Elevation resolution enhancement in 3d photoacoustic imaging using fdmas beamforming. In *2017 IEEE International Ultrasonics Symposium (IUS)*, 1–4. i

AN, L. & COX, B.T. (2018). Estimating relative chromophore concentrations from multiwavelength photoacoustic images using independent component analysis. *Journal of biomedical optics*, **23**, 076007. 181, 195

ANDREEV, V.G., KARABUTOV, A.A. & ORAEVSKY, A.A. (2003). Detection of ultrawide-band ultrasound pulses in optoacoustic tomography. *Ultrasonics, Ferroelectrics, and Frequency Control, IEEE Transactions on*, **50**, 1383–1390. 4, 9, 11, 12, 13, 15

ANSARI, M.A. & MOHAJERANI, E. (2011). Mechanisms of laser-tissue interaction: optical properties of tissue. *Journal of Lasers in Medical Sciences*, **2**, 119–125. 7, 15

AZUMA, M., ZHANG, H.K., KONDO, K., NAMITA, T., YAMAKAWA, M. & SHIINA, T. (2015). High frame rate photoacoustic computed tomography using coded excitation. In *Photons Plus Ultrasound: Imaging and Sensing 2015*, vol. 9323, 93232O, International Society for Optics and Photonics. 50, 51

BANNISON, T. & HALL, E., eds. (-). *A-Level Mathematics A Comprehensive and Supportive Companion to the Unified Curriculum*. 212, 213

BEARD, P. (2011). Biomedical photoacoustic imaging. *Interface focus*, **1**, 602–631. 68

BECKMANN, M.F. & SCHMITZ, G. (2013). Photoacoustic coded excitation using pulse position modulation. In *Ultrasonics Symposium (IUS), 2013 IEEE International*, 1853–1856, IEEE. 4, 42, 47, 48, 49, 60

BECKMANN, M.F., MIENKINA, M.P., SCHMITZ, G., FRIEDRICH, C.S., GERHARDT, N.C. & HOFMANN, M.R. (2010). Monospectral photoacoustic imaging using legendre sequences. In *Ultrasonics Symposium (IUS), 2010 IEEE*, 386–389, IEEE. 4, 42, 45, 46, 47

BECKMANN, M.F., FRIEDRICH, C.S., MIENKINA, M.P., GERHARDT, N.C., HOFMANN, M.R. & SCHMITZ, G. (2012). Multispectral photoacoustic coded excitation using pseudorandom codes. In *Photons Plus Ultrasound: Imaging and Sensing 2012*, vol. 8223, 82231E, International Society for Optics and Photonics. 2

BRASE, C.H. & BRASE, C.P. (2013). *Understanding basic statistics*. Cengage Learning. 34

BROCHU, F.M., BRUNKER, J., JOSEPH, J., TOMASZEWSKI, M.R., MORSCHER, S. & BOHNDIEK, S.E. (2016). Towards quantitative evaluation of tissue absorption coefficients using light fluence correction in optoacoustic tomography. *IEEE transactions on medical imaging*, **36**, 322–331. 179, 180, 197

BROWNE, J., RAMNARINE, K., WATSON, A. & HOSKINS, P. (2003). Assessment of the acoustic properties of common tissue-mimicking test phantoms. *Ultrasound in medicine & biology*, **29**, 1053–1060. 152, 209

CHAN, V. & PERLAS, A. (2011). Basics of ultrasound imaging. In *Atlas of ultrasound-guided procedures in interventional pain management*, 13–19, Springer. 2

CHEN, S.L., HUANG, S.W., LING, T., ASHKENAZI, S. & GUO, L.J. (2009). Polymer microring resonators for high-sensitivity and wideband photoacoustic imaging. *IEEE transactions on ultrasonics, ferroelectrics, and frequency control*, **56**, 2482–2491. 25, 68, 112

CHEN, Z., YANG, S. & XING, D. (2012). In vivo detection of hemoglobin oxygen saturation and carboxyhemoglobin saturation with multiwavelength photoacoustic microscopy. *Optics letters*, **37**, 3414–3416. 112, 176

CHOI, M.J., GUNTUR, S.R., LEE, K.I., PAENG, D.G. & COLEMAN, A. (2013). A tissue mimicking polyacrylamide hydrogel phantom for visualizing thermal lesions generated by high intensity focused ultrasound. *Ultrasound in medicine & biology*, **39**, 439–448. 95, 116, 151

CONG, B., KONDO, K., YAMAKAWA, M. & SHIINA, T. (2014). Photoacoustic image reconstruction quality enhancement based on optimum focusing by calculating mean acoustic sound-speed. In *2014 IEEE International Ultrasonics Symposium*, 1368–1371. 88

REFERENCES

Cong, B., Kondo, K., Namita, T., Yamakawa, M. & Shiina, T. (2015). Photoacoustic image quality enhancement by estimating mean sound speed based on optimum focusing. *Japanese Journal of Applied Physics*, **54**, 07HC13. 89

Cowell, D.M.J., Smith, P.R. & Freear, S. (2013). Phase-inversion-based selective harmonic elimination (pi-she) in multi-level switched-mode tone- and frequency-modulated excitation. *IEEE Transactions on Ultrasonics, Ferroelectrics, and Frequency Control*, **60**, 1084–1097. 81, 118

Cox, B.T. & Treeby, B.E. (2010). Artifact trapping during time reversal photoacoustic imaging for acoustically heterogeneous media. *IEEE transactions on medical imaging*, **29**, 387–396. 88

Cox, B.T., Arridge, S.R., Köstli, K.P. & Beard, P.C. (2006). Two-dimensional quantitative photoacoustic image reconstruction of absorption distributions in scattering media by use of a simple iterative method. *Applied Optics*, **45**, 1866–1875. 197

Daoudi, K., Van den Berg, P., Rabot, O., Kohl, A., Tisserand, S., Brands, P. & Steenbergen, W. (2014). Handheld probe integrating laser diode and ultrasound transducer array for ultrasound/photoacoustic dual modality imaging. *Optics Express*, **22**, 26365–26374. 2, 20, 38, 40, 88

De la Zerda, A., Zavaleta, C., Keren, S., Vaithilingam, S., Bodapati, S., Liu, Z., Levi, J., Smith, B., Ma, T.J., Oralkan, O., Cheng, Z., Chen, X., Dai, H., Khuri-Yakub, P. & Gambhir, S. (2008). Carbon nanotubes as photoacoustic molecular imaging agents in living mice. *Nature nanotechnology*, **3**, 557–62. 197

De Montigny, E. (2011). Photoacoustic tomography: Principles and applications. *Department of Physics Engineering, Polytechnic School Montreal*. 1, 8, 9

Deng, Z. & Li, C. (2016). Noninvasively measuring oxygen saturation of human finger-joint vessels by multi-transducer functional photoacoustic tomography. *Journal of biomedical optics*, **21**, 061009. 2, 176, 180

Deng, Z., Yang, X., Gong, H. & Luo, Q. (2011). Two-dimensional synthetic-aperture focusing technique in photoacoustic microscopy. *Journal of Applied Physics*, **109**, 104701. 118

Fan, P. & Darnell, M. (1996). Binary sequences with optimal periodic autocorrelations. In *Sequence design for communications applications*, vol. 1, 79–111, Research Studie Press. 46

Fournelle, M., Hewener, H., Günther, C., Fonfara, H., Welsch, H.J. & Lemor, R. (2009). Free-hand 3d optoacoustic imaging of vasculature. In *2009 IEEE International Ultrasonics Symposium*, 116–119, IEEE. 113

Gao, F., Feng, X. & Zheng, Y. (2016). Micro-doppler photoacoustic effect and sensing by ultrasound radar. *IEEE Journal of Selected Topics in Quantum Electronics*, **22**, 152–157. 4, 15, 68, 69, 70, 71, 74, 83, 85, 211, 212, 213

Gao, F., Feng, X., Zhang, R., Liu, S., Ding, R., Kishor, R. & Zheng, Y. (2017). Single laser pulse generates dual photoacoustic signals for differential contrast photoacoustic imaging. *Scientific reports*, **7**, 626. 39

Garcia-Uribe, A., Erpelding, T.N., Krumholz, A., Ke, H., Maslov, K., Appleton, C., Margenthaler, J.A. & Wang, L.V. (2015). Dual-modality photoacoustic and ultrasound imaging system for noninvasive sentinel lymph node detection in patients with breast cancer. *Scientific reports*, **5**, 15748. 132

Gateau, J., Gesnik, M., Chassot, J.M. & Bossy, E. (2015). Single-side access, isotropic resolution, and multispectral three-dimensional photoacoustic imaging with rotate-translate scanning of ultrasonic detector array. *Journal of biomedical optics*, **20**, 056004–056004. 112

Harput, S., Arif, M., Mclaughlan, J., Cowell, D.M.J. & Freear, S. (2013). The effect of amplitude modulation on subharmonic imaging with chirp excitation. *IEEE Transactions on Ultrasonics, Ferroelectrics, and Frequency Control*, **60**, 2532–2544. 81, 118

Heijblom, M., Piras, D., Brinkhuis, M., van Hespen, J.C., Van den Engh, F., Van der Schaaf, M., Klaase, J., Van Leeuwen, T., Steenbergen, W.

& MANOHAR, S. (2015). Photoacoustic image patterns of breast carcinoma and comparisons with magnetic resonance imaging and vascular stained histopathology. *Scientific reports*, **5**, 11778. 132

HEINZ, C., REINER, M., BELKA, C., WALTER, F. & SÖHN, M. (2015). Technical evaluation of different respiratory monitoring systems used for 4d ct acquisition under free breathing. *Journal of Applied Clinical Medical Physics*, **16**. 32, 56, 97

HOSKINS, P.R., MARTIN, K. & THRUSH, A. (2010). *Diagnostic ultrasound: physics and equipment*. Cambridge University Press. 69, 189

HU, S. & WANG, L.V. (2010). Photoacoustic imaging and characterization of the microvasculature. *Journal of biomedical optics*, **15**, 011101–011101. 68, 112

HVERVEN, S.M., RINDAL, O.M.H., RODRIGUEZ-MOLARES, A. & AUSTENG, A. (2017). The influence of speckle statistics on contrast metrics in ultrasound imaging. In *Ultrasonics Symposium (IUS), 2017 IEEE International*, 1–4, IEEE. 154

JACQUES, S., LI, T. & PRAHL, S. (2014). Monte carlo program code. Accessed: 2015, Nov 15 Available: http://omlc.org/software/mc/mcxyz/index.html. xv, 7, 8, 20, 22, 51, 53, 181, 182, 189, 217, 218

JACQUES, S.L. (2004). Laser optoacoustic imaging. In G. Palumbo, R. Pratesi, D.P. Hader & G. Jori, eds., *Lasers and Current Optical Techniques in Biology*, vol. 4, 573–590, The Royal Society of Chemistry. 2, 10, 11, 13, 14, 15, 23, 39, 53, 54, 205

JACQUES, S.L. (2013). Optical properties of biological tissues: a review. *Physics in Medicine & Biology*, **58**, R37. 195

JACQUES, S.L. (2014). Coupling 3d monte carlo light transport in optically heterogeneous tissues to photoacoustic signal generation. *Photoacoustics*, **2**, 137–142. xv, 15, 20, 22, 23, 30, 51, 53, 54, 181, 182, 205, 217, 218

JAEGER, M., BAMBER, J.C. & FRENZ, M. (2013). Clutter elimination for deep clinical optoacoustic imaging using localised vibration tagging (lovit). *Photoacoustics*, **1**, 19–29. 133

KIM, C., ERPELDING, T.N., JANKOVIC, L., PASHLEY, M.D. & WANG, L.V. (2010a). Deeply penetrating in vivo photoacoustic imaging using a clinical ultrasound array system. *Biomedical optics express*, **1**, 278–284. 1, 2, 108

KIM, C., ERPELDING, T.N., MASLOV, K.I., JANKOVIC, L., AKERS, W.J., SONG, L., ACHILEFU, S., MARGENTHALER, J.A., PASHLEY, M.D. & WANG, L.V. (2010b). Handheld array-based photoacoustic probe for guiding needle biopsy of sentinel lymph nodes. *Journal of biomedical optics*, **15**, 046010. 132, 149

KIM, C., SONG, K.H., GAO, F. & WANG, L.V. (2010c). Sentinel lymph nodes and lymphatic vessels: noninvasive dual-modality in vivo mapping by using indocyanine green in rats volumetric spectroscopic photoacoustic imaging and planar fluorescence imaging. *Radiology*, **255**, 442–450. 2, 132

KIM, C., ERPELDING, T.N., JANKOVIC, L. & WANG, L.V. (2011). Performance benchmarks of an array-based hand-held photoacoustic probe adapted from a clinical ultrasound system for non-invasive sentinel lymph node imaging. *Phil. Trans. R. Soc. A*, **369**, 4644–4650. 68

KIRCHNER, T., SATTLER, F., GRÖHL, J. & MAIER-HEIN, L. (2018). Signed real-time delay multiply and sum beamforming for multispectral photoacoustic imaging. *Journal of Imaging*, **4**, 121. 6, 176, 177, 178, 179

KOLKMAN, R.G., STEENBERGEN, W. & VAN LEEUWEN, T.G. (2006). In vivo photoacoustic imaging of blood vessels with a pulsed laser diode. *Lasers in Medical Science*, **21**, 134–139. 3, 18

KOLKMAN, R.G., BRANDS, P.J., STEENBERGEN, W. & VAN LEEUWEN, T.G. (2008). Real-time in vivo photoacoustic and ultrasound imaging. *Journal of biomedical optics*, **13**, 050510. 88

KORNEL, P., FRENZ, M., BEBIE, H., WEBER, H.P. *et al.* (2001). Temporal backward projection of optoacoustic pressure transients using fourier transform methods. *Physics in medicine and biology*, **46**, 1863. 88

LAO, Y., XING, D., YANG, S. & XIANG, L. (2008). Noninvasive photoacoustic imaging of the developing vasculature during early tumor growth. *Physics in Medicine and Biology*, **53**, 4203–4212. 68

REFERENCES

Laser-Components (2015). Pulse laser diode datasheet. Accessed: 2015, Nov 15. 22, 38

Laser-Safety (2014). Safety of laser products. 22, 53, 54, 56, 187

Li, G., Li, L., Zhu, L., Xia, J. & Wang, L.V. (2015). Multiview hilbert transformation for full-view photoacoustic computed tomography using a linear array. *Journal of biomedical optics*, **20**, 066010. 3

Li, M., Tang, Y. & Yao, J. (2018). Photoacoustic tomography of blood oxygenation: A mini review. *Photoacoustics*. 179, 180, 181, 194

Li, W. & Chen, X. (2015). Gold nanoparticles for photoacoustic imaging. *Nanomedicine*, **10**, 299–320, pMID: 25600972. 2

Liao, C.K., Li, M.L. & Li, P.C. (2004). Optoacoustic imaging with synthetic aperture focusing and coherence weighting. *Optics letters*, **29**, 2506–2508. 90

Lim, H.B., Nhung, N.T.T., Li, E.P. & Thang, N.D. (2008). Confocal microwave imaging for breast cancer detection: Delay-multiply-and-sum image reconstruction algorithm. *IEEE Transactions on Biomedical Engineering*, **55**, 1697–1704. 5, 89

Mallidi, S., Luke, G.P. & Emelianov, S. (2011). Photoacoustic imaging in cancer detection, diagnosis, and treatment guidance. *Trends in Biotechnology*, **29**, 213–221. 2, 9, 10

Mallidi, S., Watanabe, K., Timerman, D., Schoenfeld, D. & Hasan, T. (2015). Prediction of tumor recurrence and therapy monitoring using ultrasound-guided photoacoustic imaging. *Theranostics*, **5**, 289–301. 112

Manohar, S. & Razansky, D. (2016). Photoacoustics: a historical review. *Advances in optics and photonics*, **8**, 586–617. 1

Manohar, S., Vaartjes, S.E., van Hespen, J.C., Klaase, J.M., van den Engh, F.M., Steenbergen, W. & Van Leeuwen, T.G. (2007). Initial results of in vivo non-invasive cancer imaging in the human breast using near-infrared photoacoustics. *Optics express*, **15**, 12277–12285. 68

MANSIK JEON, E.H.J.K.J.K.B.L.H.B.Y.C.L.D.E.G.G.Z.J.O.J.F.L.C.K., WEN-TAO SONG (2014). Methylene blue microbubbles as a model dual-modality contrast agent for ultrasound and activatable photoacoustic imaging. *Journal of Biomedical Optics*, **19**, 1 – 9 – 9. 2

MARI, J.M., XIA, W., WEST, S.J. & DESJARDINS, A.E. (2015). Interventional multispectral photoacoustic imaging with a clinical ultrasound probe for discriminating nerves and tendons: an ex vivo pilot study. *Journal of biomedical optics*, **20**, 110503. 176

MATHEMATICS, S. (2013). Table of trigonometric identities. Accessed: 05-Mar-2019. 211, 212

MATRONE, G., SAVOIA, A.S., CALIANO, G. & MAGENES, G. (2015). The delay multiply and sum beamforming algorithm in ultrasound b-mode medical imaging. *IEEE transactions on medical imaging*, **34**, 940–949. 5, 6, 89, 90, 91, 113, 114, 133

MCLAUGHLAN, J., COWELL, D., HARPUT, S. & FREEAR, S. (2014). Diagnostic imaging of molecular-targeted nanorods simultaneously exposed to light and sound. In *Ultrasonics Symposium (IUS), 2014 IEEE International*, 1626–1629, IEEE. 4, 69

MEHRMOHAMMADI, M., JOON YOON, S., YEAGER, D. & Y EMELIANOV, S. (2013). Photoacoustic imaging for cancer detection and staging. *Current molecular imaging*, **2**, 89–105. 132

MIENKINA, M.P., FRIEDRICH, C.S., GERHARDT, N.C., WILKENING, W.G., HOFMANN, M.R. & SCHMITZ, G. (2010). Experimental evaluation of photoacoustic coded excitation using unipolar golay codes. *Ultrasonics, Ferroelectrics, and Frequency Control, IEEE Transactions on*, **57**, 1583–1593. 2, 4, 18, 42, 43, 44, 45, 47, 49, 64

MOEIN MOZAFFARZADEH, M.M.B.M., YAN YAN (2018). Enhanced linear-array photoacoustic beamforming using modified coherence factor. *Journal of Biomedical Optics*, **23**, 1 – 10 – 10. 176

MONTILLA, L.G., OLAFSSON, R., BAUER, D.R. & WITTE, R.S. (2012). Real-time photoacoustic and ultrasound imaging: a simple solution for clinical ultrasound systems with linear arrays. *Physics in Medicine & Biology*, **58**, N1. 88

REFERENCES

MOUBARK, A.M., ALOMARI, Z., HARPUT, S., COWELL, D.M.J. & FREEAR, S. (2016). Enhancement of contrast and resolution of b-mode plane wave imaging (pwi) with non-linear filtered delay multiply and sum (fdmas) beamforming. In *2016 IEEE International Ultrasonics Symposium (IUS)*, 1–4. 113, 114

NIE, L., HARPUT, S., COWELL, D.M.J., CARPENTER, T.M., MCLAUGHLAN, J.R. & FREEAR, S. (2018). Combining acoustic trapping with plane wave imaging for localized microbubble accumulation in large vessels. *IEEE Transactions on Ultrasonics, Ferroelectrics, and Frequency Control*, **65**, 1193–1204. 152, 209

NIKOLOV, S.I. & JENSEN, J.A. (2000). 3d synthetic aperture imaging using a virtual source element in the elevation plane. In *2000 IEEE Ultrasonics Symposium. Proceedings. An International Symposium (Cat. No.00CH37121)*, vol. 2, 1743–1747 vol.2. 119

NOUNOU, M.I., ELAMRAWY, F., AHMED, N., ABDELRAOUF, K., GODA, S. & SYED-SHA-QHATTAL, H. (2015). Breast cancer: conventional diagnosis and treatment modalities and recent patents and technologies. *Breast cancer: basic and clinical research*, **9**, BCBCR–S29420. 132

NTZIACHRISTOS, V. (2010). Going deeper than microscopy: the optical imaging frontier in biology. *Nature methods*, **7**, 603–614. 112

OH, J.T., LI, M.L., ZHANG, H.F., MASLOV, K. & WANG, L.V. (2006). Three-dimensional imaging of skin melanoma in vivo by dual-wavelength photoacoustic microscopy. *Journal of biomedical optics*, **11**, 034032. 68, 176

OLYMPUS (2015). Olympus ultrasonic transducers for nondestructive testing. Accessed: 2015, Nov 15. 25, 27, 205

ORAEVSKY, A.A., SAVATEEVA, E.V., SOLOMATIN, S.V., KARABUTOV, A.A., ANDREEV, V.G., GATALICA, Z., KHAMAPIRAD, T. & HENRICHS, P.M. (2002). Optoacoustic imaging of blood for visualization and diagnostics of breast cancer. 88, 176

PALTAUF, G., VIATOR, J., PRAHL, S. & JACQUES, S. (2002). Iterative reconstruction algorithm for optoacoustic imaging. *The Journal of the Acoustical Society of America*, **112**, 1536–1544. 13, 14, 25, 54, 205

PARK, S., MALLIDI, S., KARPIOUK, A.B., AGLYAMOV, S. & EMELIANOV, S.Y. (2007). Photoacoustic imaging using array transducer. In *Photons Plus Ultrasound: Imaging and Sensing 2007: The Eighth Conference on Biomedical Thermoacoustics, Optoacoustics, and Acousto-optics*, vol. 6437, 643714, International Society for Optics and Photonics. 133

PARK, S., KARPIOUK, A.B., AGLYAMOV, S.R. & EMELIANOV, S.Y. (2008a). Adaptive beamforming for photoacoustic imaging. *Optics letters*, **33**, 1291–1293. 88, 133, 170

PARK, S., KARPIOUK, A.B., AGLYAMOV, S.R. & EMELIANOV, S.Y. (2008b). Adaptive beamforming for photoacoustic imaging using linear array transducer. In *2008 IEEE Ultrasonics Symposium*, 1088–1091, IEEE. 3, 5

PIRAS, D., HEIJBLOM, M., XIA, W., VAN LEEUWEN, T.G., STEENBERGEN, W. & MANOHAR, S. (2012). Adapted directivity approach for photoacoustic imaging reconstruction. In *Photons Plus Ultrasound: Imaging and Sensing 2012*, vol. 8223, 82231Z, International Society for Optics and Photonics. 112

POUREBRAHIMI, B., YOON, S., DOPSA, D. & KOLIOS, M.C. (2013). Improving the quality of photoacoustic images using the short-lag spatial coherence imaging technique. In *Photons Plus Ultrasound: Imaging and Sensing 2013*, vol. 8581, 85813Y, International Society for Optics and Photonics. 88

PRAHL, S. (2017). Mie scattering calculator. 116, 151

PREISSER, S., HELD, G., AKARÇAY, H.G., JAEGER, M. & FRENZ, M. (2016). Study of clutter origin in in-vivo epi-optoacoustic imaging of human forearms. *Journal of optics*, **18**, 094003. 133

RAJIAN, J.R., FABIILLI, M.L., FOWLKES, J.B., CARSON, P.L. & WANG, X. (2011). Drug delivery monitoring by photoacoustic tomography with an icg encapsulated double emulsion. *Optics express*, **19**, 14335–14347. 68

SACKS, G.S. (2004). The abc's of acid-base balance. *The Journal of Pediatric Pharmacology and Therapeutics*, **9**, 235–242. 195, 196, 197

REFERENCES

SCHWARZ, M., BUEHLER, A. & NTZIACHRISTOS, V. (2015). Isotropic high resolution optoacoustic imaging with linear detector arrays in bi-directional scanning. *Journal of biophotonics*, **8**, 60–70. 5, 112

SIVASUBRAMANIAN, K., PERIYASAMY, V. & PRAMANIK, M. (2018). Non-invasive sentinel lymph node mapping and needle guidance using clinical handheld photoacoustic imaging system in small animal. *Journal of biophotonics*, **11**, e201700061. 2, 132

SMITH, P.R., COWELL, D.M.J., RAITON, B., KY, C.V. & FREEAR, S. (2012). Ultrasound array transmitter architecture with high timing resolution using embedded phase-locked loops. *IEEE Transactions on Ultrasonics, Ferroelectrics, and Frequency Control*, **59**, 40–49. 81, 118

SMITH, P.R., COWELL, D.M.J. & FREEAR, S. (2013). Width-modulated square-wave pulses for ultrasound applications. *IEEE Transactions on Ultrasonics, Ferroelectrics, and Frequency Control*, **60**, 2244–2256. 81, 118

SONG, K.H., STEIN, E.W., MARGENTHALER, J.A. & WANG, L.V. (2008). Noninvasive photoacoustic identification of sentinel lymph nodes containing methylene blue in vivo in a rat model. *Journal of biomedical optics*, **13**, 054033. 2

SU, T., LI, D. & ZHANG, S. (2018). An efficient subarray average delay multiply and sum beamformer algorithm in ultrasound imaging. *Ultrasonics*, **84**, 411–420. 133, 134, 135, 136

SYNNEVAG, J.F., AUSTENG, A. & HOLM, S. (2007). Adaptive beamforming applied to medical ultrasound imaging. *IEEE Transactions on Ultrasonics, Ferroelectrics, and Frequency Control*, **54**, 1606–1613. 170

TARUTTIS, A. & NTZIACHRISTOS, V. (2015). Advances in real-time multispectral optoacoustic imaging and its applications. *Nature photonics*, **9**, 219. 68, 176

TIAN, C., XIE, Z., FABIILLI, M.L., LIU, S., WANG, C., CHENG, Q. & WANG, X. (2015). Dual-pulse nonlinear photoacoustic technique: a practical investigation. *Biomedical optics express*, **6**, 2923–2933. 4, 68

TREEBY, B.E. & COX, B.T. (2010). k-wave: Matlab toolbox for the simulation and reconstruction of photoacoustic wave fields. *Journal of biomedical optics*, **15**, 021314–021314. 72, 79, 92, 100, 136, 148, 182, 183, 214

TREEBY, B.E., ZHANG, E.Z. & COX, B. (2010). Photoacoustic tomography in absorbing acoustic media using time reversal. *Inverse Problems*, **26**, 115003. 88

TREEBY, B.E., JAROS, J. & COX, B.T. (2016). Advanced photoacoustic image reconstruction using the k-wave toolbox. In *Photons Plus Ultrasound: Imaging and Sensing 2016*, vol. 9708, 97082P, International Society for Optics and Photonics. 72, 79, 182, 183

UPPUTURI, P.K. & PRAMANIK, M. (2015). Performance characterization of low-cost, high-speed, portable pulsed laser diode photoacoustic tomography (pld-pat) system. *Biomedical optics express*, **6**, 4118–4129. 2, 38, 108

UPPUTURI, P.K. & PRAMANIK, M. (2018). Fast photoacoustic imaging systems using pulsed laser diodes: a review. *Biomedical engineering letters*, **8**, 167–181. 2

VO-DINH, T. (2003). *Biomedical Photonics Handbook*. CRC Press. 4, 6, 7, 15

WANG, D., WANG, Y., ZHOU, Y., LOVELL, J.F. & XIA, J. (2016a). Coherent-weighted three-dimensional image reconstruction in linear-array-based photoacoustic tomography. *Biomedical optics express*, **7**, 1957–1965. 5, 112, 113

WANG, D., WANG, Y., WANG, W., LUO, D., CHITGUPI, U., GENG, J., ZHOU, Y., WANG, L., LOVELL, J.F. & XIA, J. (2017). Deep tissue photoacoustic computed tomography with a fast and compact laser system. *Biomed. Opt. Express*, **8**, 112–123. 79, 149, 162, 194

WANG, L.V. (2008). Tutorial on photoacoustic microscopy and computed tomography. *Selected Topics in Quantum Electronics, IEEE Journal of*, **14**, 171–179. 2, 12

WANG, L.V. & HU, S. (2012). Photoacoustic tomography: in vivo imaging from organelles to organs. *Science*, **335**, 1458–1462. 112

WANG, L.V. & YAO, J. (2016). A practical guide to photoacoustic tomography in the life sciences. *Nature methods*, **13**, 627. 2

REFERENCES

Wang, T., Nandy, S., Salehi, H.S., Kumavor, P.D. & Zhu, Q. (2014). A low-cost photoacoustic microscopy system with a laser diode excitation. *Biomedical Optics Express*, **5**, 3053–3058. 3, 18, 20

Wang, Y., Wang, D., Zhang, Y., Geng, J., Lovell, J.F. & Xia, J. (2016b). Slit-enabled linear-array photoacoustic tomography with near isotropic spatial resolution in three dimensions. *Optics letters*, **41**, 127–130. 3, 5, 112

Wang, Z., Ha, S. & Kim, K. (2012). A new design of light illumination scheme for deep tissue photoacoustic imaging. *Opt. Express*, **20**, 22649–22659. 4, 68

Wei, C.W., Nguyen, T.M., Xia, J., Arnal, B., Wong, E.Y., Pelivanov, I.M. & O'Donnell, M. (2015). Real-time integrated photoacoustic and ultrasound (paus) imaging system to guide interventional procedures: ex vivo study. *IEEE transactions on ultrasonics, ferroelectrics, and frequency control*, **62**, 319–328. 3, 18, 42, 112

Wells, P., Halliwell, M., Skidmore, R., Woodcock, J. & Webb, A. (1977). Tumour detection by ultrasonic doppler blood-flow signals. *Ultrasonics*, **15**, 231–232. 69

Wiendelt, S. (2013). Photoacoustic tomography. In S.P. Morgan, F.R. Rose & S.J. Matcher, eds., *Optical Techniques in Regenerative Medicine*, 329–354, Taylor and Francis. 12

Xi, L., Grobmyer, S.R., Zhou, G., Qian, W., Yang, L. & Jiang, H. (2014). Molecular photoacoustic tomography of breast cancer using receptor targeted magnetic iron oxide nanoparticles as contrast agents. *Journal of Biophotonics*, **7**, 401–409. 108

Xia, J. & Wang, L.V. (2014). Small-animal whole-body photoacoustic tomography: a review. *IEEE Transactions on Biomedical Engineering*, **61**, 1380–1389. 112

Xia, J., Guo, Z., Maslov, K.I., Wang, L.V., Aguirre, A., Zhu, Q. & Percival, C. (2011). Three-dimensional photoacoustic tomography based on the focal-line concept. *Journal of biomedical optics*, **16**, 090505. 113

Xia, J., Yao, J. & Wang, L.V. (2014). Photoacoustic tomography: principles and advances. *Electromagnetic waves (Cambridge, Mass.)*, **147**, 1. 2

XIA, W., WEST, S.J., NIKITICHEV, D.I., OURSELIN, S., BEARD, P.C. & DESJARDINS, A.E. (2016). Interventional multispectral photoacoustic imaging with a clinical linear array ultrasound probe for guiding nerve blocks. 197

XIA, W., KUNIYIL AJITH SINGH, M., MANEAS, E., SATO, N., SHIGETA, Y., AGANO, T., OURSELIN, S., J WEST, S. & E DESJARDINS, A. (2018). Handheld real-time led-based photoacoustic and ultrasound imaging system for accurate visualization of clinical metal needles and superficial vasculature to guide minimally invasive procedures. *Sensors*, **18**, 1394. 40

XU, M. & WANG, L.V. (2005). Universal back-projection algorithm for photoacoustic computed tomography. *Physical Review E*, **71**, 016706. 113

XU, M. & WANG, L.V. (2006). Photoacoustic imaging in biomedicine. *Review of scientific instruments*, **77**, 041101. 1, 88

YANG, Z., SONG, J., TANG, W., FAN, W., DAI, Y., SHEN, Z., LIN, L., CHENG, S., LIU, Y., NIU, G., RONG, P., WANG, W. & CHEN, X. (2019). Stimuli-responsive nanotheranostics for real-time monitoring drug release by photoacoustic imaging. *Theranostics*, **9**, 526–536. 197

YAO, J. & WANG, L.V. (2011). Photoacoustic tomography: fundamentals, advances and prospects. *Contrast media & molecular imaging*, **6**, 332–345. 68

YOON, C., KANG, J., HAN, S., YOO, Y., SONG, T.K. & CHANG, J.H. (2012). Enhancement of photoacoustic image quality by sound speed correction: ex vivo evaluation. *Optics express*, **20**, 3082–3090. 88, 89

ZACKRISSON, S., VAN DE VEN, S. & GAMBHIR, S. (2014). Light in and sound out: emerging translational strategies for photoacoustic imaging. *Cancer research*, **74**, 979–1004. 132

ZEMP, R.J., BITTON, R., SHUNG, K.K., LI, M.L., STOICA, G. & WANG, L.V. (2007). Photoacoustic imaging of the microvasculature with a high-frequency ultrasound array transducer. *Journal of Biomedical Optics*, **12**, 1 − 3 − 3. 3, 5

ZENG, L., LIU, G., YANG, D. & JI, X. (2012). 3d-visual laser-diode-based photoacoustic imaging. *Optics express*, **20**, 1237–1246. 2

REFERENCES

ZENG, L., LIU, G., YANG, D. & JI, X. (2013). Portable optical-resolution photoacoustic microscopy with a pulsed laser diode excitation. *Applied Physics Letters*, **102**, 053704. 3, 19, 40

ZENG, L., LIU, G., YANG, D. & JI, X. (2014). Cost-efficient laser-diode-induced optical-resolution photoacoustic microscopy for two-dimensional/three-dimensional biomedical imaging. *Journal of Biomedical Optics*, **19**, 076017–076017. 3, 19

ZHANG, H., KONDO, K., YAMAKAWA, M. & SHIINA, T. (2012). Simultaneous multispectral coded excitation using gold codes for photoacoustic imaging. *Japanese Journal of Applied Physics*, **51**, 07GF03. 42

ZHANG, H.F., MASLOV, K., SIVARAMAKRISHNAN, M., STOICA, G. & WANG, L.V. (2007). Imaging of hemoglobin oxygen saturation variations in single vessels in vivo using photoacoustic microscopy. *Applied physics letters*, **90**, 053901. 180, 181

ZHANG, Y., HONG, H. & CAI, W. (2011). Photoacoustic imaging. *Cold Spring Harbor Protocols*, **2011**, pdb–top065508. 2

ZHONG, H., DUAN, T., LAN, H., ZHOU, M. & GAO, F. (2018). Review of low-cost photoacoustic sensing and imaging based on laser diode and light-emitting diode. *Sensors*, **18**, 2264. 40